Control Strategies for the More Electric Aircraft Starter-Generator Electrical Power System

Seang Shen Yeoh (BEng, MSc)

Thesis submitted to the University of Nottingham

for the degree of Doctor of Philosophy

March 2016

Abstract

The trend towards development of More Electric Aircraft (MEA) has been driven by increased fuel fossil prices and stricter environmental policies. This is supported by breakthroughs in power electronic systems and electrical machines. The application of MEA is expected to reduce the aircraft mass and drag, thereby increasing fuel efficiency and reduced environmental impact. The starter-generator (S/G) scheme is one of the solutions from the MEA concept that brings the most significant improvement to the electrical power generation system. A S/G system is proposed from the possible solutions brought by the MEA concept in the area of electrical power generation and distribution. Due to the wide operating speed range, limited controller stability may be present. This thesis contributes to the control plant analysis and controller design of this MEA S/G system. The general control requirements are outlined based on the S/G system operation and the control structure is presented. The control plants are derived specifically to design the controllers for the S/G control scheme. Detailed small signal analysis is performed on the derived plant while taking into consideration the aircraft operating speed and load range. A safe range for the controller gains can then be determined to ensure stable operation throughout the S/G operation. Adaptive gain and a novel current limit modifier are proposed which improves the controller stability during S/G operation. Model predictive control is considered as an alternative control strategy for potential control performance improvements with the S/G system. The technical results and simulations are supported by Matlab®/Simulink® based models and validated by experimental work on a small scaled drive system.

Claims and Novelty

In this Thesis:

- The control design process for a novel MEA S/G system is introduced which takes into account its control requirements (speed for starter mode, DC link bus for generator mode, flux weakening (FW) for high speed operation). The designed controllers (PI based) can ensure stable operation of the S/G system throughout the speed and load operating ranges.

- A novel current limit modifier is proposed to eliminate an unstable region identified during generator mode FW operation. Adaptive FW controller gain is employed in combination with this method for stable control in generator mode.

- A hybrid PI and modulated model predictive control method is presented for the S/G system that showed improvements in PI controller stability and reduced current ripples when compared to the full PI solution.

Acknowledgements

A million thanks to my friends and colleague, especially to Mr. Fei Gao and Dr. Tao Yang. Over the years, I have learnt many things from them, and hopefully they too from me. Special mentions to Dr. Shuai Shao, Bob (Dr. Ponggorn Kulsangcharoen), Miss. Sharmila Sumsurooah, Mr. Wasseem Mohammed, Dr. Rashed Mohamed, Dr. Luca Tarisciotti, Dr. Eduardo Reyes Moraga, and Dr. David Hind for their technical and emotional support. My PhD experience has been enhanced by getting to work and know them. There is also my appreciation to Mr. Yinjen Ng for convincing me to pursue my PhD.

Not to forget, I would like to thank my family for supporting me throughout the way. I am grateful to my parents Mr. Chong Hoeo Yeoh and Ms. Yew Kuan Lim for encouraging me to carry on my PhD even during my low times. With their help I was able to advance and focus on my research to a successful PhD.

Table of Contents

List of Figures

List of Tables

List of Acronyms

AC	Alternating Current
ADC	Analogue to Digital Conversion
AEGART	Aircraft Electrical Generation Active Rectifier Technology
AFE	Active Front End rectifier
APU	Auxiliary Power Unit
CF	Constant Frequency
CFD	Computational Fluid Dynamics
CFS	Carbon Fibre Sleeve
CSD	Constant Speed Drive
DAC	Digital to Analogue Conversion
DC	Direct Current
DSP	Digital Signal Processor
DTC	Direct Torque Control
ECS	Environmental Control System
EMI	Electromagnetic Interference
EU	European Union
FEM	Finite Element Model
FOC	Field Oriented Control
FP7	7th Framework Programme
FPGA	Field Programmable Gate Array
FW	Flux Weakening
H.P	High Pressure
I.P	Intermediate Pressure
IGBT	Insulated Gate Bipolar Transistors

IM	Induction Machine
IPM	Interior mounted Permanent magnet Machine
ITD	Integrated Technology Demonstrator
JTI	Joint Technology Initiatives
L.P	Low Pressure
LCD	Liquid Clear Display
LHP	Left Hand Plane
LUT	Look-Up Table
M^2PC	Modulated Model Predictive Control
MEA	More Electric Aircraft
MOET	More Open Electrical Technologies
MOSFET	Metal Oxide Semiconductor Field Effect Transistor
MPC	Model Predictive Control
MS	Metallic Sleeve
MTPA	Maximum Torque Per Ampere
NPC	Neutral Point Clamped
PI	Proportional plus Integral
PID	Proportional plus Integral plus Derivative
PM	Permanent Magnet
PMM	Permanent Magnet Machine
POA	Power Optimized Aircraft
PWM	Pulse Width Modulation
RAT	Ram Air Turbine
RH	Routh Hurwitz
RHP	Right Hand Plane
S/G	Starter-Generator
SiCMos	Silicon Carbide MOSFET

SISO	Single Input Single Output
SM	Synchronous Machine
SPM	Surface mounted Permanent magnet Machine
SRM	Switched Reluctance Machine
SVM	Space Vector Modulation
THD	Total Harmonic Distortion
THD	Total Harmonic Distortion
TIMES	Totally Integrated More Electric Systems
TRU	Transformer Rectifier Unit
VF	Variable Frequency
VSCF	Variable Speed Constant Frequency
VSD	Variable Speed Drive
ZOH	Zero Order Hold

List of Symbols

$|V|$	Stator voltage magnitude
$|V|_{max}$	Maximum stator voltage magnitude
C	DC link capacitor
d	Duty cycle
E_{dc}	DC link voltage
E_{dcmax}	Maximum DC link voltage
E_{dcmin}	Minimum DC link voltage
$E_{dcrated}$	Rated DC link voltage
f	Transfer function
f_c	Frictional force
g, J_c	Predictive control cost function
G_v	Transfer function open loop gain
H_T	Electromagnetic torque control signal
H_ψ	Stator flux control signal
$i_{a,b,c}$	Three phase AC currents
$I_{d,q}$	Current vector in dq frame
$i_{d,q}$	Three phase AC currents in dq frame
i_{dc}	DC link current
i_{dcmax}	Maximum DC link current
i_f	Permanent magnet field current
i_L	Load current
i_{lmt}	Current modifier limit
i_{max}	Maximum current
I_{MC}	Current vector

i_{NP}	Neutral point current
$i_{qcrt\text{-}lmt}$	q-axis current critical limit
i_{qlim}	q-axis current reference limit
i_s	Stator current
J	Combined machine and engine inertia
k	Discrete time step
k_{droop}	Droop gain
$k_{id,q}$	Current controller integral gain in dq frame
k_{ii}	DC link current controller integral gain
k_{is}	Speed controller integral gain
k_{iv}	Flux weakening controller integral gain
$k_{iv\text{-}adapt}$	Adaptive flux weakening controller integral gain
$k_{iv\text{-}lmt}$	Flux weakening controller integral term limit
$k_{pd,q}$	Current controller proportional gain in dq frame
k_{pi}	DC link current controller proportional gain
k_{ps}	Speed controller proportional gain
k_{pv}	Flux weakening controller proportional gain
k_t	Torque constant
L	Inductive element
$L_{d,q}$	Machine inductance in dq frame
$L_{ld,q}$	Leakage inductances in dq frame
$L_{md,q}$	Magnetizing inductances in dq frame
m_s	Modulation step
N	Number of state variables
P	Active power
p	Pole pairs
$p_{1,2}$	Transfer function poles

P_{rated}	Rated active power
P_{RH}	Hurwitz polynomial
Q	Reactive power
R	Resistive element
r	Reference signal
R_{dc}	DC link resistor
R_s	Stator resistance
S	Complex power
$S_{1,2,3,4}$	Power switches
$S_{a,b,c}$	Three phase switching states
T_e	Electromagnetic torque
T_L	Load torque
T_m	Modulation period
T_s	Sampling period
u	Error of predicted variables
$v_{01,02}$	Zero active vector
$v_{1,2}$	Active space vectors
$v_{a,b,c}$	Three phase AC voltages
V_C	Converter voltage vector
$v_{d,q}$	Three phase AC voltages in dq frame
$V_{d,q}$	Voltage vector in dq frame
V_M	Machine voltage vector
V_{MC}	Voltage vector
w	Cost function weighing factors
$W_{cd,q}$	dq current controller
W_{fw}	Flux weakening controller
W_{idc}	DC link current controller

W_s	Speed controller
x	State variable
y	Output signal
z_1	Transfer function zeroes
z_l	Transfer function zero during limited i_q^* case
z_{nl}	Transfer function zero during unlimited i_q^* case
γ	Stator current angle
ζ	Damping ratio
θ	Electrical angle
θ_r	Mechanical angle
ϕ	Current limit angle
$\psi_{d,q}$	Flux linkage in dq frame
ψ_m	Machine flux linkage
ψ_s	Stator flux
ω_b	Base speed
ω_e	Electrical speed
ω_{gmax}	Maximum generation speed
ω_{gmin}	Minimum generation speed
ω_n	Natural bandwidth
ω_r	Mechanical speed

Chapter 1   Introduction

Evolution over more than a hundred years has led to the modern aircraft that we see today. What started as a curiosity to achieve manned flight made famous by the Wright brothers, later on developed for military warfare due to its speed and aerial superiority [1]. During World War I, aircraft were mainly used for combat and many prototypes were built and flown with the aim of developing a better flying war machine. After the war ended, the development of aircraft slowed down as there was little incentive for civil aviation. Existing military aircraft were used for flight entertainment such as air races and stunts. Then World War II started in 1939, and aircraft development activity restarted with emphasis on combat capabilities, size, and efficiency. As a result, the aircraft could cover larger distances and carry greater payloads such as heavy bombs or military equipment. After World War II, commercial air transportation grew rapidly by the use of these ex-military aircraft [1]. Aircraft became safer and better equipped to be commercialised for passengers to travel vast distances within reasonable periods of time. Aircraft have become a convenient method of transportation and this trend is likely to continue in the future.

The advantages of air travel have attracted more and more passengers over the years which have led to more aircraft being deployed. It has led to the development of aircraft with larger capacity such as the A380 that can seat up to 853 passengers in single class configuration [2]. As a comparison, the previous highest capacity civilian aircraft was the B747 capable of seating up to 415 passengers [3]. In addition, services and facilities on board the aircraft have needed to be improved to meet the demands of air passengers. Having to do so while trying to maintain or reduce emissions and costs is very difficult and therefore requires the design and development of aircraft systems to be reconsidered.

With the increased price of fossil fuels in the early 21st century, airline companies became interested in more efficient aircraft. In order to achieve significant difference in efficiency, the whole aircraft would need to be optimised in terms of weight, aerodynamics, power generation, management, distribution, and

utilisation [4]. A state-of-the-art aircraft designed with these criteria in mind is the B787. It is built from lighter weight composite materials and has better aerodynamic design for the nose and wings. The engines have improved architecture that reduces fuel consumption and increases thrust power. The aircraft has a more electrical based power system that has five times more power output than a typical large civil aircraft and some of the important aircraft loads such as the cabin pressurisation system are converted to rely on electricity [5]. The potential benefits of using more electrical based power systems for aircraft will be discussed later in this Chapter. Overall, the B787 achieved up to 3% improvement in fuel consumption [5].

Aside from material selection and aerodynamics, better efficiency could be achieved with changes to the aircraft power system by looking at ways for on-board energy management optimisation. This Chapter will look at the potential solutions brought by adopting a more electrical aircraft power system and its advantages.

1.1   Overview of Existing Aircraft Power Systems

The main source of power for state-of-the-art aircraft comes from the gas turbine engines. Fig. 1.1 shows the power sources produced from the engine for an aircraft power system. Jet fuel is used for propulsive power and a small percentage in the form of mechanical, pneumatic, hydraulic, and electrical power. These different power mediums are used for loads on-board the aircraft, as depicted in Fig. 1.3a. Mechanical power is extracted via a shaft which is driven by the aircraft engine and distributed via an accessory gearbox, as shown in Fig. 2.5. This gearbox also helps produce hydraulic power by driving the hydraulic pumps which is then distributed to the flight actuators and landing gears.

The electrical power is generated from electrical machines that are coupled to the accessory gearbox connections. It is used to power electrical loads such as flight control equipment, lighting, and galleys. An auxiliary power unit (APU) generator is located at the aft of the aircraft to provide electrical power when the aircraft is on ground and to assist in the main engine start-up. A ram air turbine (RAT) is also available in conventional aircraft to provide emergency power in the event of main engine failures. 'Bleed air' is extracted as pneumatic power from the engines for

wing de-icing, cabin pressurisation, and Environmental Control Systems (ECS) [6]. For a large sized civilian aircraft such as the A330 or B777, it is estimated that a total 1.7MW of power output is used for all of these loads. This output power compared to other forms of transportation is very large in relation to the size of its platform [7].
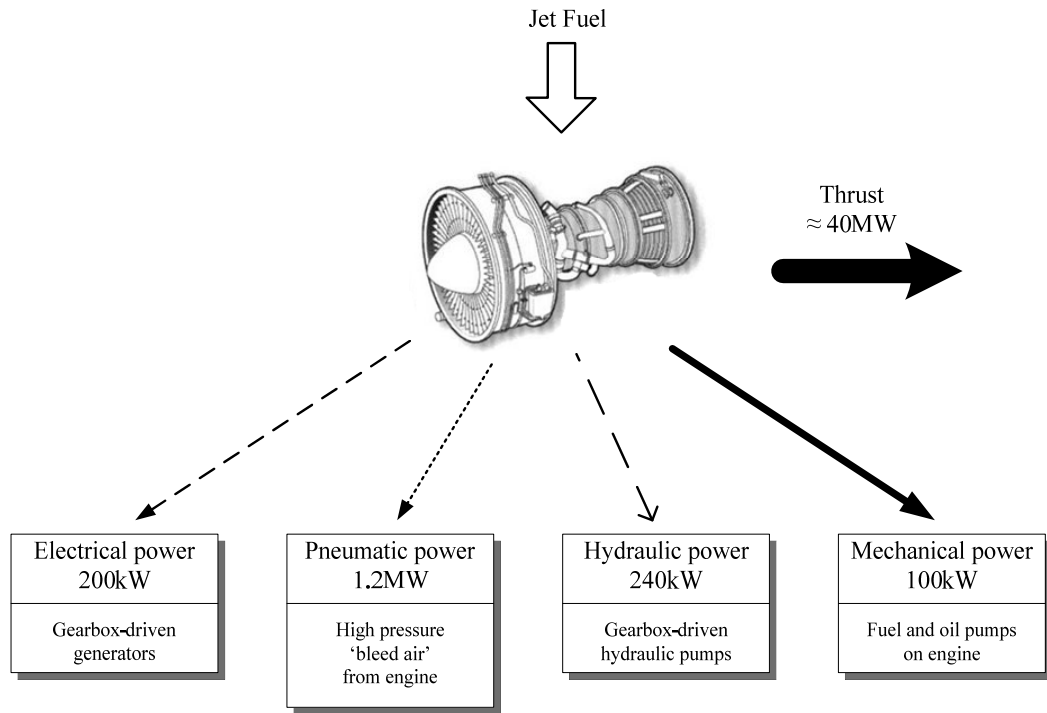
Fig. 1.1. Typical power output of a large civil aircraft [7].

1.2 Motivation for Aircraft Advancement

The following are reasons to improve the current aircraft power system:

- Hydraulic systems may be robust and have high power density; however the transmission pipe connections to the required loads are heavy, inflexible, and susceptible to leaks. The pipes may cover significant distances from the engine all the way back to the aft of the aircraft. These systems have no leak detection which makes maintenance more difficult.
- Pneumatic systems are known to have low efficiencies, especially the bleeding compressors used for start-up operation and cabin pressurisation. The placement of the compressors within the aircraft

engine and the bleed air extraction disrupts the internal air flow aerodynamics. This significantly affects the efficiency of the engine and leads to more fuel consumption [8].

- The accessory gearbox used to produce mechanical power is very complex and the entire component needs to be replaced if faults are found within it [6]. In addition, it is the crucial medium which transmits power for the hydraulic and electrical systems.

- The RAT is designed for deployment during engine-failure conditions. It can only be used once and therefore requires replacement after each use [6].

- Having different power mediums makes the aircraft power system very complex, reducing the efficiency as a whole and it can be quite difficult to locate and fix faults. As a result, interaction between the power sources may lead to reduced reliability and hence increased maintenance downtime.

- The trend of increased air traffic is estimated to increase 5% per year in the near future and it is supported by the eventual emergence of new commercial aircraft manufacturers in North America and Asia [9]. This would lead to increased carbon dioxide emissions which have an impact on the environment. Stricter environmental policies are enforced to reduce carbon emissions from aircraft.

All the mentioned issues drive the research for a more efficient and simpler aircraft to reduce the overall costs and fuel consumption [8]. A possible solution to the current issues is realisation of the More Electric Aircraft (MEA). The aim of this next generation aircraft is to reduce the complexity of the existing aircraft system by removing non-electrical power sources and using only electrical power. The use of electrical power with an appropriate distribution system provides options for re-configurability, prognostics and diagnostics. It is possible then to monitor the health condition of the power system and predict end of life, rather than relying on the life span of connected equipment. These features offer increased flexibility and availability of the power system plus reduced unscheduled downtime [7].

The advantages of using electrical power for the various functions of an aircraft system have led to the increased amount of power being required and hence needs to be generated. Fig. 1.2 shows the electrical power generated by several civilian aircraft in the past decade. The amount of electrical power generated increases as the years advance. The B787 has electrical power generation capabilities that are much higher than most commercial aircraft and reaches up to 1.45MVA. This trend will probably continue as electrical power becomes more important on board future aircraft.
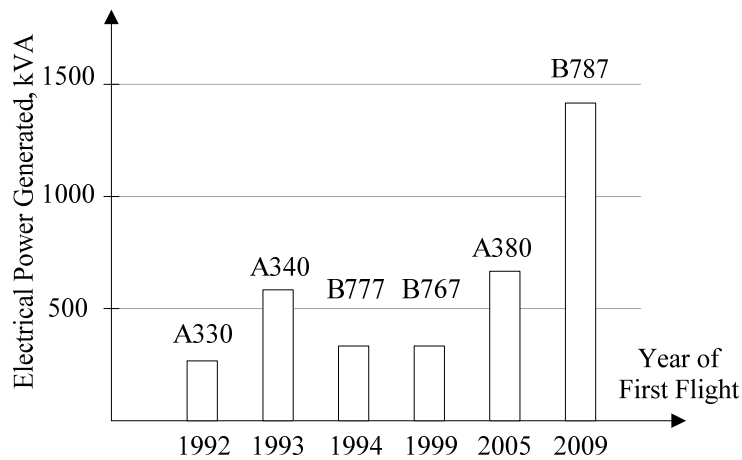
Fig. 1.2. Electrical power levels generated for various civil aircraft [10, 11].

1.3   More Electric Aircraft

While the idea to develop aircraft that primarily rely on electrical power has been thought of since World War II, such as the Vickers Valiant V-Bombers, it was not a popular idea. However there have continually been debates about its advantages compared to the other power sources. Technological constraints in terms of power generation and conditioning were also an issue in the past. This idea only resurfaced in the 1990s with the emergence of power electronic devices that could support and provide such a power demand. In addition to that, breakthroughs in fault tolerant electrical machines and electrical power systems support the revival of the MEA concept. Several projects were dedicated to expanding research in this field, such as the Totally Integrated More Electric Systems (TIMES) [4], Power Optimised Aircraft (POA) [12], More Open Electrical Technologies (MOET) [13], Cleansky [14], and

recently Clean Sky 2 [15]. These projects are devoted to the research of relevant technologies required to develop the next generation of aircraft.

Fig. 1.3 shows the potential difference between a conventional and a MEA aircraft power system [6, 10]. The hydraulic systems could be localised and be controlled electrically. Bleed air may not be required if electrical air pumps are used for the ECS and high resistivity wires for wing de-icing. If all loads are to be converted to rely on electrical power, it is estimated that only 60% of the output power is required to perform the same operation as a similarly sized conventional aircraft [7]. Electrification of the loads would mean that the engine could be modified to be more efficient and less complex. One modification would be the 'bleed-less' engine structure which improves the internal aerodynamics. A fan shaft generator can be added into the engines to replace the RAT as the more reliable emergency power source. The engines can also utilise advanced magnetic bearings to allow for oil and gear-free operation [16]. The overall effect of the changes mentioned above would result in improved aircraft reliability, complexity, costs, efficiency and aircraft- empty weight [4, 6, 7].
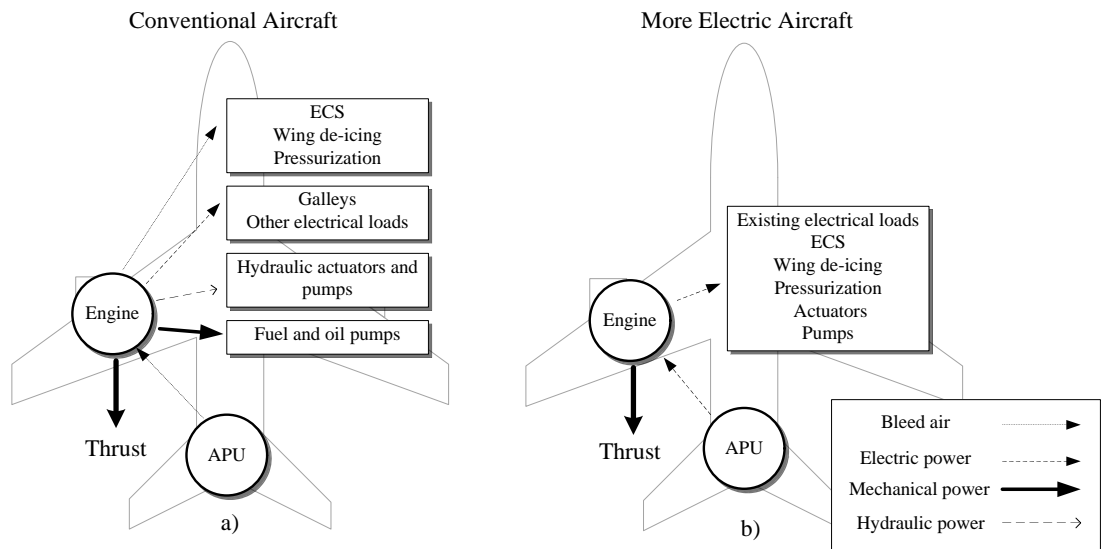
Fig. 1.3. Difference between conventional and MEA types of load [6].

The adoption of the MEA concept has already started in recent years. The B787 is a prime example of an aircraft that has implemented several of the MEA solutions. The engines on-board this aircraft have a 'bleed-less' architecture while the ECS, cabin

pressurisation, and wing de-icing rely on electrical power [5]. The backup wing actuators are also electrically powered [10].

1.3.1   Starter-Generator Concept

One of the core ideas of the MEA involves integrating multiple aircraft functions in a system for reduced mass that would lead to fuel savings and improved efficiency. It is one of the key changes brought by the MEA concept and is called the starter-generator (S/G) scheme. The start-up process of a large aircraft engine requires assistance from a starter to provide smooth acceleration until the engine achieves a self-sustaining speed. For example, air starter motors run with air supplied from a ground cart or APU to rotate the starter turbine which drives the engine. Once the engine achieves a certain threshold speed, the air compressors can channel sufficient bleed air for the ignition process to further accelerate the engine speed. The engine power is then harnessed and distributed through the accessory gearbox for different types of power sources. If the starter function can be done electrically with an electrical machine while being able to use the same machine to generate electrical power, there would be significant advantages in terms of weight and volume reduction.

The S/G scheme involves a simpler connection between the electrical machine and the engine. The engine tower shaft, power take-off shaft, and the accessory gearbox may no longer be required. This therefore has the potential to greatly reduce the complexity of the power system. A power converter is used to replace the accessory gearbox and interface between the electrical machine and the aircraft main bus [17]. By controlling the electrical machine via the power converter, it is possible to direct the power flow in and out of the machine, thereby determining its role as a starter or generator. Fig. 1.4 shows the power flow and a brief description of each mode of operation.

Electrical power could be supplied from the ground power supply or APU through the main bus to the electrical machine in order to perform its start-up function. The electrical machine then acts as a starter and drives the engine. At high

speeds, the machine acts as a generator to supply electrical power to the on-board loads.
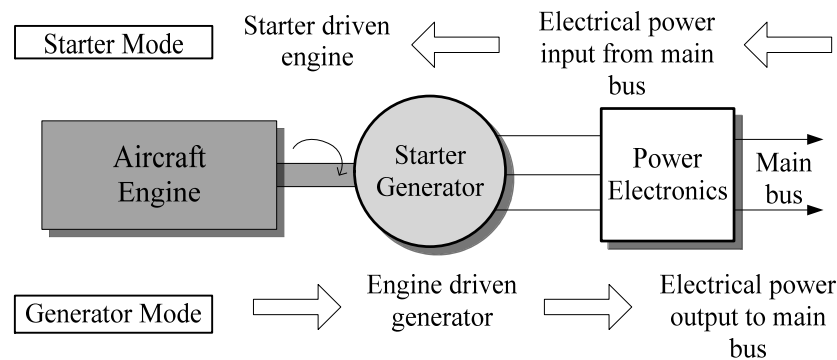
Fig. 1.4. General starter-generator mode of operation.

The electric S/G function is present within the B787. The generators supply electrical power from the APU, via power converters, to drive the engine. Once the start-up operation is complete, the power converters function as motor controllers for the ECS and the generators resume their role [5]. The topology is not identical to the S/G concept as there is no dedicated power converter and the accessory gearbox is still present. To date, the S/G concept has been demonstrated in the frame of POA project [12] to gauge the feasibility of electrical machine integration within a large civil sized aircraft engine [18]. A S/G is incorporated in the middle part of the engine and an additional generator towards the rear end. They are controlled by separate power converters which are also situated within the engine. The placement of the S/G within the engine enables the advantages mentioned earlier in this Sub-section. More robust and reliable power electronics and conductors are needed as the engine operating temperature is the limiting factor to realising this integration. Alternatively, the S/G could be connected from outside the engine which removes the issue of high temperature engine environment. Doing so can accelerate the development of S/G systems as part of improving the efficiency of future aircraft.

The control of S/Gs also has to be reanalysed as it will need to take into account both modes of operation. Research into the control of such novel systems is lacking at the beginning of this PhD programme; hence it shall be the core area of research in this thesis. Detailed explanation on aircraft starter and power generation systems will be given in Chapter 2.

1.4 Aims and Objectives of the Thesis

The aim of this research is to investigate the control design aspects of a novel type of S/G system for future MEA.

The specific objectives are as follows:

- The design of a control system, based on linear control methods, for the specified S/G system. The design requirements include coordinated control of machine speed, DC bus voltage/current, and machine flux. These requirements are specified in order to establish good control performance over the entire speed range conversing both motoring and generation modes. As the key element towards this objective, the control plant should be investigated and a mathematical model suitable for advanced control design should be developed.

- Investigation into dynamic performance, electric power quality, and stability of the designed control system in order to meet the specified technical requirements.

- Development of simulation models in support of the aim. These include the plant, the control scheme, and representative loads models at different levels (architectural, functional, and behavioural) for S/G system analysis.

- Investigation into possibilities offered by advanced control approaches (including non-linear ones) for further enhancement of S/G system control performance.

- Construction of a scaled prototype test rig to enable experimental support to the achieved analytical design results.

1.5   Structure of Thesis

This thesis is structured as follows:

Chapter 2 starts with an overview of existing aircraft engine starting procedures and methods. Then, the electrical power generation systems on-board aircraft are discussed and potential advancements brought by the MEA concept are considered. The advantages of each option are assessed and a novel S/G system topology used in this research is detailed. An initial control strategy is formulated based on the combined starter and generator operation. A literature review is conducted to cover various control methods that were found to be crucial for S/G operation with the selected power system topology.

Chapter 3 considers the control approach for the S/G system and the reference frame is defined. The control structure is then detailed for S/G operation in both starter and generator modes. Following this, the relevant mathematical equations representing the S/G system are established to derive the controlled plant. The equations are linearised in order to simplify the control design process using linear design methods. The control plant models are then derived and verified against non-linear models built in Matlab®/Simulink®.

Chapter 4 deals with the detailed control design for starter mode operation. The control plant models are specifically re-formulated for speed and flux weakening controller design. Due to the employed flux weakening method, two states are created by the use of a dynamic limiter. Hence, two distinct control plants are derived for flux weakening control design. The control plants are verified against non-linear equivalent models at different operating points. The worst case scenario for starter mode is considered for the design of the flux weakening controller. Following the controller design time-domain simulations across the whole starter mode operation are performed in order to confirm the achieved control performance.

Chapter 5 focuses on the detailed control structure for generator mode operation. The control plants are specifically re-derived for DC link bus voltage and flux weakening controller design. They are then verified against non-linear equivalent models at different operating points. The worst case scenario for generator mode is considered for the design of the DC link bus voltage controller. Analysis on the flux weakening control plant is repeated to investigate the stability of the controller designed in the previous Chapter when operating in generator mode. The controllers are simulated across the whole generator mode of operation in order to validate the achieved control performance.

Chapter 6 discusses an alternate control scheme based on model predictive control as a non-causal type controller to investigate possible advantages for the S/G power system. The control strategy is a hybrid structure of linear controllers with a variant of model predictive control with an inherit modulation scheme. The performance of this hybrid control scheme is compared with the full proportional plus integral (PI) control structure. Parameter variation tests are also performed to determine the robustness of the hybrid control scheme.

Chapter 7 reports experimental validation of theoretical results accumulated from the previous Chapters. The experimental setup is explained in detail with its relevance to the aircraft S/G system. The capabilities of the rig are described and the controllers are designed following the design process suggested in this Thesis. The results are shown to validate the analytical findings.

Finally, Chapter 8 concludes the Thesis with the overall work and main outcomes. Possible future research work is also discussed in this Chapter. A list of publications which resulted from the research is also given.

1.6 Conclusion

In this Chapter, the present state of conventional aircraft power system architectures has been outlined. Due to the pressure of environmental policies, a more efficient energy management of aircraft power systems is required to reduce fuel consumption and hence reduce carbon emissions. The implementation of MEA aims for improved aircraft weight, efficiency, running costs, safety and reliability. MEA is an attempt to 'electrify' the aircraft power system by replacing pneumatically and hydraulically driven on-board systems by those which are electrically-driven. The benefit of electric power for aircraft with appropriate distribution systems is that it provides convenience of use, options for re-configurability, prognostics and diagnostics. The increasing reliance on electrical power would therefore require major enhancement to the electrical power generation system. The most significant improvement to the electrical power generation system brought by the MEA is the S/G scheme. An electrical machine can be used as an engine starter or generator depending on the mode of operation with the help of state-of-the-art power electronics. The implementation of MEA S/G on board aircraft is fairly new and this Thesis shall focus on the controller design aspects. The aims and objectives of this Thesis have been formulated in this Chapter along with the outline of this Thesis.

Chapter 2　More Electric Aircraft Electrical Starter-Generator System

2.1　Introduction

Before the S/G system is proposed and investigated for this Thesis, existing methods for aircraft engine start and power generation will be discussed. These are accompanied by solutions proposed within the MEA concept. A topology for the S/G system is selected from the array of candidates. Key factors in this selection process are the reduction of overall weight, safety/reliability and efficiency. Existing controls for the generator are examined and a control strategy is proposed based on combining both generation and the engine start-up functions.

2.2　Aircraft Engine Starter

The primary source of power for an aircraft is its engines; they make flight possible due to the thrust they create. The use of engines for aircraft was introduced due to the fact that it is difficult to achieve manned flight without the help of an external thrust source. Steam powered engines were considered for aircraft in the early 19th century, after they were successfully used within trains, ships, and ground vehicles. A notable aircraft steam engine was built by Stringfellow in 1868. This engine managed to power a flying model for about 120 feet [19]. However, steam powered engines did not flourish due to power density issues and problems related to keeping the burner operational with high wind speeds. It was at the end of the 19th century that these problems were partially solved, but by then internal combustion aircraft engines had been made popular by the Wright brothers [19]. Combustion engines offer much better power density than the steam variant, which secured the future of manned flight. At that time, the engines were driven by pistons, much like the ones in modern automotive vehicles.

Towards the end of World War II, the jet engine emerged as a revolutionary type of propulsion. The speed and range of aircraft increased dramatically as a result of using the jet engine. It also had a major impact on the commercialisation of air transportation as aircraft were able to cover great distances with economical costs [1].

Turbofan and turbojet type gas turbine engines are commonly used on jet propelled aircraft today. The difference between these two types of jet engine is that turbofan engines do not fully utilise all of the air flowing into the engine [1]. They generally have the same structure as shown in Fig. 2.1. This is comprised of air compressors, a combustion chamber, and a turbine. The working principle of a jet engine is that by manipulating the pressure of the air flow into the combustion chamber higher kinetic energy can be accumulated for thrust power. The operation of this kind of engine can be simplified into three stages and described with respect to Fig. 2.1:

- Air passing through the engine is accelerated by the compressors in order to increase the kinetic energy. They function to increase the speed of the air by increasing its pressure. Some of the air flows into the engine passing through the low pressure (L.P) compressor. The air is further compressed through the intermediate (I.P) and high pressure (H.P) compressors before being sent to the combustion chamber. Note the size of the air channel for each of the compressors contributes to the compression process.

- The compressed air is pushed into the combustion chamber to be mixed together with jet fuel and ignited. The combustion process produces propulsive force that accelerates the aircraft forwards [20].

- The exhaust is channelled out of the engine with the help of a nozzle. There are turbines along the channel that are driven by the exhaust while it is being expelled from the engine. This turbine provides mechanical power to the compressors to keep them spinning and to the accessory gearbox for power distribution.

Air

Exhaust

L.P
Compressor

I.P
Compressor

H.P
Compressor

Combustion
Chamber

Turbine

Nozzle
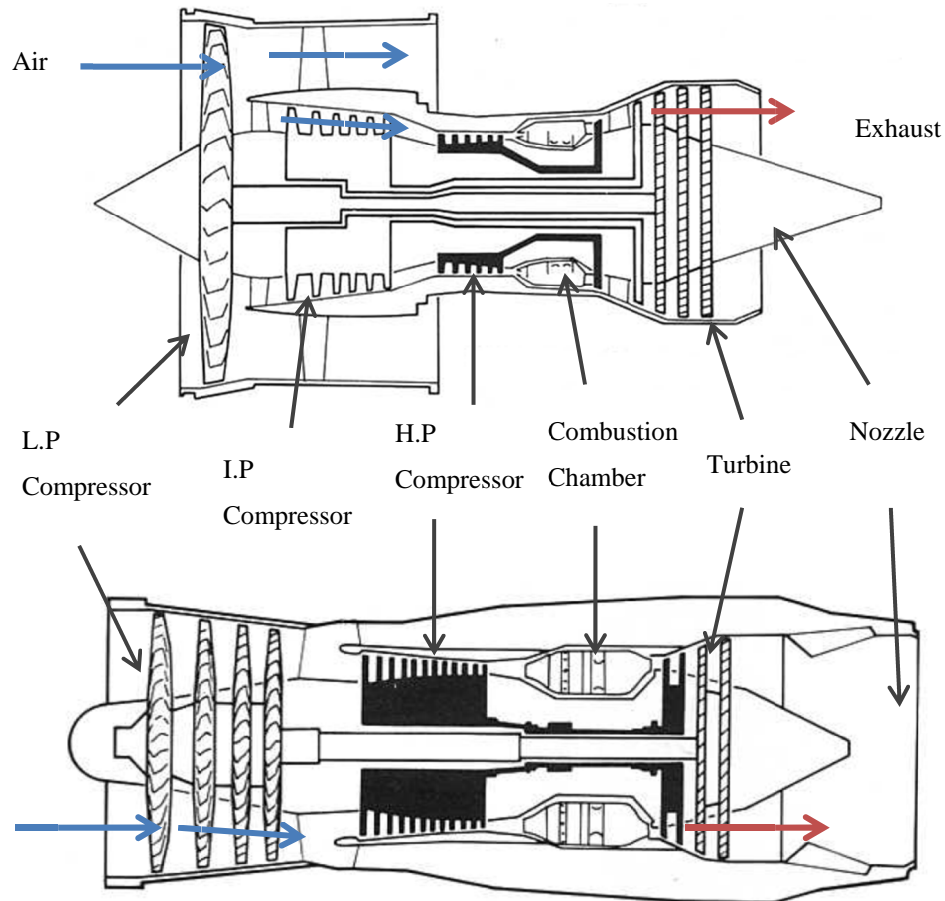
Fig. 2.1. Cross section of a turbofan (top) and a turbojet (bottom) aircraft engine [20].

2.2.1 Engine Start-up Process

Thrust can be generated with these three steps when the engine compressors are rotating. However at standstill, air needs to be forced into the engine for air compression and combustion to happen. Therefore, a starter system is used to aid with start-up of the engine [20]. The function of the starter system is to bring the engine to an optimal speed where the start-up process is more efficient. For conventional civil aircraft, the function of a starter motor is to provide high torque and transmit it such that smooth acceleration can be achieved until the engine reaches self-sustaining speed.

Aircraft engines usually require two separate systems for the start-up process. The first process requires the air compressor and turbine to be accelerated to a certain speed with assistance so that the optimal fuel to air ratio can be achieved. The second

part involves the ignition of the air and fuel mixture in the combustion chambers. Both of these systems operate side by side automatically depending on the current speed of the engine. A start-up sequence of an aircraft engine is illustrated in Fig. 2.2.

- When the ignition switch is turned on, the starter motor performs its function to start driving the engine.
- Air starts to flow into the engine with help from the compressors.
- As the speed reaches about 10% of the engine maximum speed, fuel is injected into the combustion chamber.
- The air and fuel mixture is ignited to aid the engine to reach self-sustaining speed.
- Once a self-sustaining speed is reached, the starter circuit is cancelled. The engine continues to accelerate by itself until the idle speed is reached.

This completes the start-up process of the engine [17]. The engine speed can be accelerated further in order to provide the necessary thrust for the take-off and cruising stages of the aircraft's flight profile.
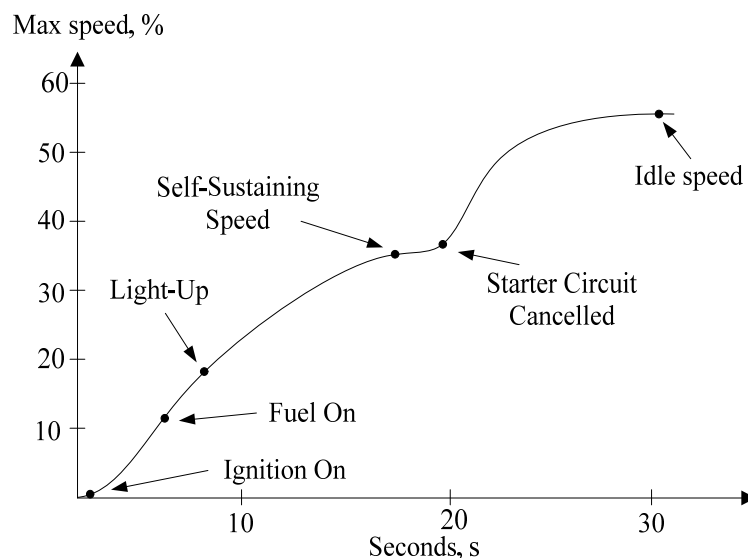
Fig. 2.2. General starting sequence of a turbo-jet engine [20].

The starter should be designed according to the engine torque-speed characteristics. These vary depending on the environmental temperature. Fig. 2.3 shows the typical profile of these characteristics and it can be seen that more torque

is required at colder temperatures. In order to provide acceleration for the start-up process, the starter should be able to overcome the torque requirements for these temperature ranges.
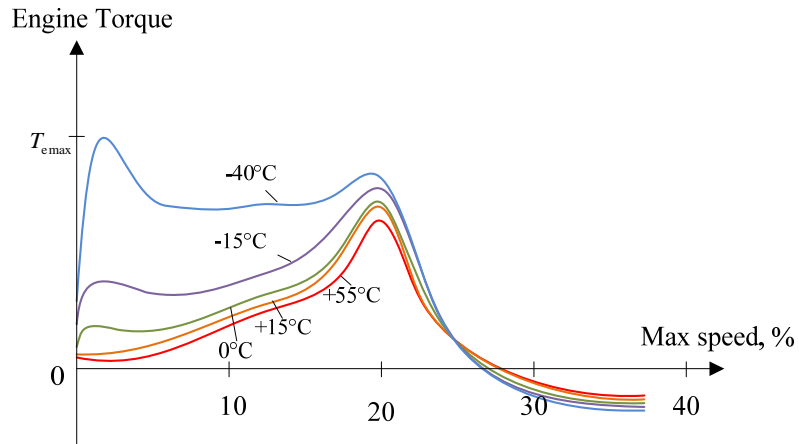
Fig. 2.3. Typical aircraft engine torque-speed characteristics at different temperatures.

2.2.2   Engine Start-up Methods

Various methods can be used to drive an aircraft starter. Some aircraft use air, while others use hydraulics, gas, or electrical power [20]. Whichever way is used, they all achieve the starting requirements shown in Fig. 2.2. Each type of available power source for starters is outlined below:

Engine start by means of hydraulics uses hydraulic pressure provided from a ground supply unit. It is transferred to the hydraulic pumps that are part of the accessory gearbox. The difference in hydraulic pressure rotates the pumps which drives the engine via the gearbox. The starter is controlled by an electrical circuit and is disconnected when the required engine speed is reached. This method is usually used on small aircraft.

Cartridges offer a quick and independent way of starting an aircraft engine. A cartridge is placed within an impulse-type turbine and this acts as the engine starter. When ignited with a remote detonator, the cartridge releases high velocity gases to rotate the turbines. A mechanism disconnects the starter from the engine once the

self-sustaining speed is reached. It is usually used for military aircraft as the main requirement for engine start is to be as fast as possible.

The most common start-up method for most aircraft, due to its simple and economical methodology, is to employ pneumatic power [20]. Fig. 2.4 shows the location of an air starter system on an aircraft engine. Several ways could be used to supply air for pneumatic starting; either by transferring 'bleed air' produced from an APU, cross fed from another already running engine or from the ground air start supply. The air is sent into the starter turbine which drives the engine via a series of reduction gears and clutches. The air flow is controlled by pressure valves that are situated on the engine and are closed when self-sustaining speed is achieved. The clutch also disconnects the starter turbine from the engine to allow further speed acceleration.
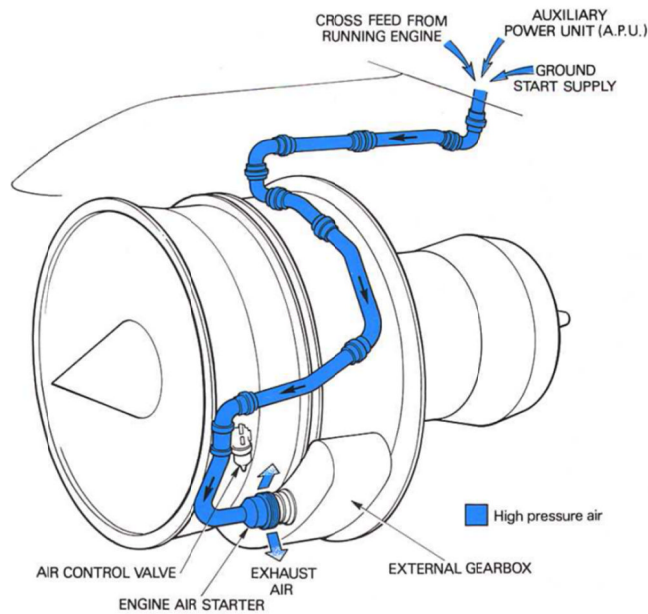
Fig. 2.4. An aircraft engine with air starting system [20].

Gas powered starters work by combusting fuel to drive the engine. Using its own contained system (fuel, ignition, and starter motor), the gas turbine is driven to a certain speed. The exhaust which is produced as a result of combustion is channelled to a free-power turbine. This is also part of the starter to drive the engine. Similar to the other starters, a mechanism disconnects the starter once self-sustaining speed is

reached. This type of starter has a high power output for a low weight as it is running on fuel [20].

Electrical starters can also be utilised to initially drive aircraft engines. A DC electric motor functions as an electrical starter which can be supplied from different power sources such as the aircraft DC bus or ground power supply. With the help of relays and resistors, the voltage is gradually built up as the starter speed increases. The starter power supply is cut off when the engine is successfully brought to self-sustaining speed, or after the time cycle for this function is complete [20]. The advantage of using an electrical based starter is that the power generated as a result of being driven by the engine could be sent back to the aircraft bus. Doing so can enable the S/G concept that is based on a single electrical machine performing both starter and generator functions.

2.3   Accessory Gearbox

Once the engine has started successfully, one of the components it drives is an external/accessory gearbox that is located on the engine, as seen in Fig. 2.4. Through an internal gearbox that is connected to the drive shaft of the engine, mechanical power is transmitted to the accessory gearbox [10]. Typical accessories that rely on this gearbox are shown in Fig. 2.5.

The mechanical power is converted to power services such as:

- Fuel pumps for the engine.
- Oil pumps for lubrication purposes.
- Auxiliary electrical power alternator for engine control functions.
- Oil breather to regulate the pressure within the gearbox.

Other than that, the accessory gearbox also provides interface for:

- Engine speed measurements from the tachometer for aircraft control.
- Input power source for starter function as discussed earlier.
- Hydraulic power supply from the hydraulic pumps.
- Primary generator to supply electrical power for the aircraft [21].
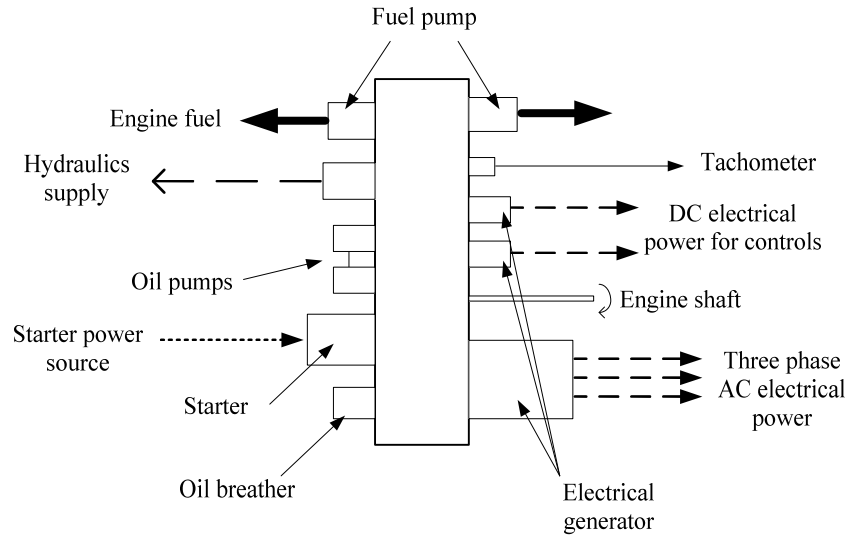
Fig. 2.5. Accessory gearbox inputs and outputs [10].

The engine rotation is translated into various power sources with the help of gears, turbines, and electrical machines. The electrical machine plays the role of a generator and supplies AC power for most modern aircraft. The next Section will explain how the electrical power is generated, distributed, and utilised.

2.4   Aircraft Electrical Power System

Electrical power generation has made significant progress ever since aircraft become more dependent on electrical loads. DC machines were introduced as generators when aircraft started using electrical powered flight controls. The generators are usually self-excited; they contain electromagnets to generate electrical power when driven by the aircraft engines. The DC power output is transferred via a commutator to the loads and is supported by on-board batteries to maintain the voltage level [10].

Then the introduction of V-Bombers during World War II, with their greater electrical power requirements, led to a radical change in aircraft power generation systems [10]. Four AC generators were utilised which were connected to four separate engines. These were used to power loads such as radar and electronic jamming equipment. The AC generators generated sine wave output voltages at constant frequency and were directly distributed to the electrical loads.

The evolution of AC generators over the years has led to the state-of-the-art machine that is commonly used in modern conventional aircraft today: the three stage wound field synchronous machine (SM) shown in Fig. 2.6. Based on the equivalent electrical circuit, it can be regarded as three machines sharing the same rotor. On the left side is a permanent magnet (PM) generator where variable frequency voltage is generated that is dependent on the engine speed. The control scheme detects the voltage levels at the PM generator armature and provides an appropriate DC current reference for the exciter field. The voltage level of the exciter armature is therefore controlled according to the exciter field and rectified into DC form with a rotating diode rectifier. This creates a main excitation field to induce AC voltage through the main armature windings for aircraft utilisation. The control scheme also monitors and regulates the output AC voltage.
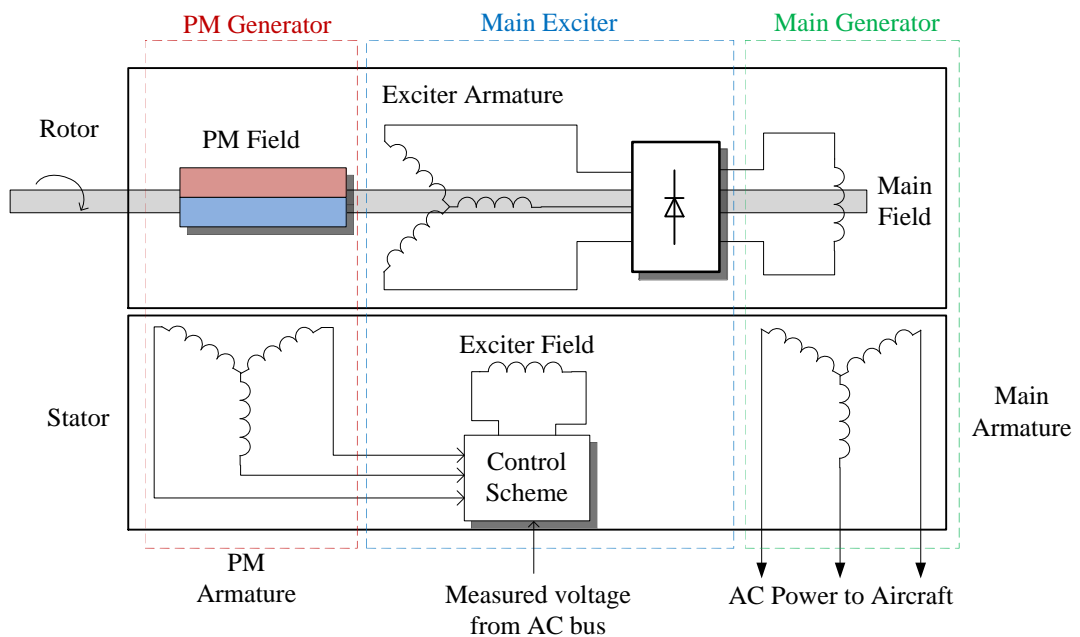
Fig. 2.6. Electrical diagram of a three stage wound field synchronous machine.

The main advantages of using this type of generator are:

- For its high reliability and safety. The exciter field is controlled and could be turned off during emergency situations.
- Voltage control can be easily achieved by only varying the excitation field.

However, the three stage SM can be quite complex due to multiple windings and electronic components on the rotor. Additional windings and larger diodes are then required for a higher power density machine which increases system weight and complexity. The heavier rotor limits the speed achievable by the machine. Hence, one of the ways to optimise the machine in terms of weight, i.e. by increasing its speed range, cannot be utilised. In addition, more windings are required if electrical engine start functionality is desired for the three stage SM. Size and weight are crucial factors for future aircraft components as environmental policies are imposing tighter restrictions on emissions. This means that the three stage SM has severe limitations for power rating improvement and more efficient electrical machines are required for future MEA S/G systems.

Adoption of a different type of machine may allow for more power to be generated as the limitations of SM could be overcome. Therefore, alternative machines such as induction (IM), permanent magnet (PMM), and switched reluctance (SRM) machines are considered [21, 22].

The SRM has been known to be the most robust and fault tolerant among the possible choices of electrical machines. In addition, it has a simple design (windings only on stator part) as can be seen in Fig. 2.7 and can operate over a wide speed range. Due to its build structure, the output three phase voltages are not sinusoidal, indicating high harmonic content which may influence the power quality of the main bus. Moreover, SRM produces a high torque ripple that has an adhere effect on the mechanical gearboxes and the engine. Filters are then required to ensure that the power quality meets the aircraft standards which affect the overall aircraft weight [22].
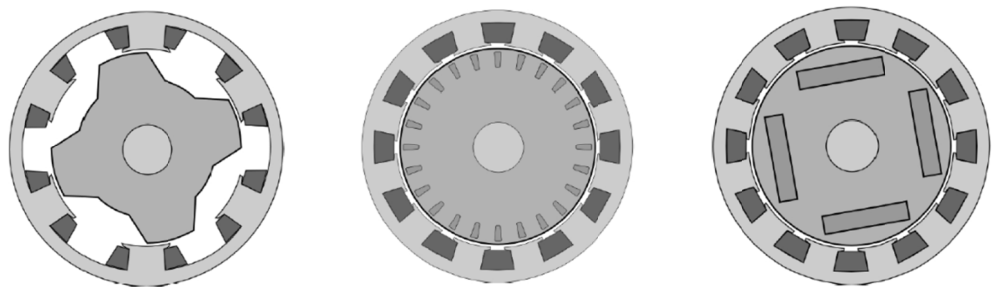
Fig. 2.7. Cross section of a typical SRM (left), IM (middle), and PMM (right) [23].

The IM is one of the most commonly used electrical machines in industry, partly due to its simplicity and robust characteristics. It is also cheap to manufacture as it has been an established technology for many years. In general, there are two types of IM which are the wound type and the squirrel cage. The latter is widely used in industry for its reliability and economical build. Its rotor core is built with steel laminations and is slotted with aluminium or copper conductors. The core serves to carry the magnetic field through the rotor conductors. The cross section of the IM can be seen in Fig. 2.7. However, it has mediocre power density partly due to currents flowing within the rotor [21]. For typical IM topologies, there would be mechanical constraints when operating at high speeds. The rotor cage starts to expand when the rotational speed increases which may result in conflict with the stator component [24]. Fortunately, carefully designed IM considering the rotor would be able to operate at high speeds.

PMM are recent choices for many applications due to their power density, efficiency, and existing self-excitation from using magnets [6]. The magnets are usually attached to the rotor of the machine and either surface or interior mounted, as shown in Fig. 2.7. Despite the favourable advantages, several key drawbacks of using PMM need to be addressed before it is applicable for aerospace applications. Cooling systems are required to ensure the magnets are within safe operating temperatures. The inability to disable the magnetic field is also a safety issue to be considered [6].

Overall, when being utilised as a S/G, the key advantages of each of the three machine types detailed above can be summarised as follows:

- SRM for its robustness.
- IM for its mature technology and economical build.
- PMM for its power density and high performance.

The next Sub-section overviews the electric power generation system topologies on-board existing and future MEA.

2.4.1   Power Generation Topologies

Fig. 2.8 shows one of the most common electric power generation topologies used on many modern aircraft such as the A320 and B747 [10]. Since the engine is running at a wide speed range, a constant speed drive (CSD), which is part of the accessory gearbox, is used to output constant speed output regardless of the engine speed. As a result, the speed fed into the generator produces constant frequency (CF) AC power typically at 400Hz to be distributed to the aircraft electrical loads.

However, the gearbox itself is very costly and has to perform an assortment of functions which results in a highly complex component. This results in frequent maintenance to ensure reliability which in turn can cause delays to planned flights. This limitation drives the need to look into alternate topologies which do not require the accessory gearbox for power generation. There are two topologies that are considered as alternatives to CF power generation method.
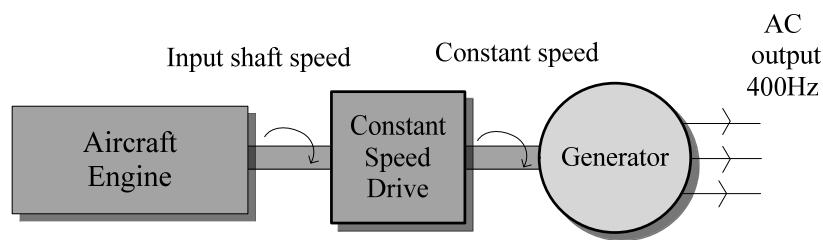
Fig. 2.8. Constant frequency topology.

The variable speed constant frequency (VSCF) topology is similar to the CF topology as three-phase AC power with constant frequency is produced irrespective of the shaft speed. The difference is that power electronic converters are used to regulate the power output which can be much more efficient. In Fig. 2.9a, a diode rectifier is used to convert the AC output electrical power from the generator into DC form. An inverter is then used to convert that DC power into AC power with fixed frequency to the main bus. It has been used on existing aircraft such as the B777 as a backup power generation system although its reliability has yet to be better than the CF topology [10].

Another option is to use a cycloconverter where the AC power and frequency is regulated directly without transitioning to DC power, as shown in Fig. 2.9b. Six

phases are generated at high frequencies and are carefully regulated with power switches such that constant 400Hz three phase AC power is produced. This method has been used on military aircraft successfully as an alternative to the CF topology. However, the input frequency has to be much higher than the output; hence a fixed turns ratio gearbox may be required to interface the engine and generator. The typical configuration of a cycloconverter requires a significant number of power devices and this may influence the reliability and control complexity in general. Despite the disadvantages, its output power is likely to be more efficient than CF since the CSD is excluded from the topology [6].
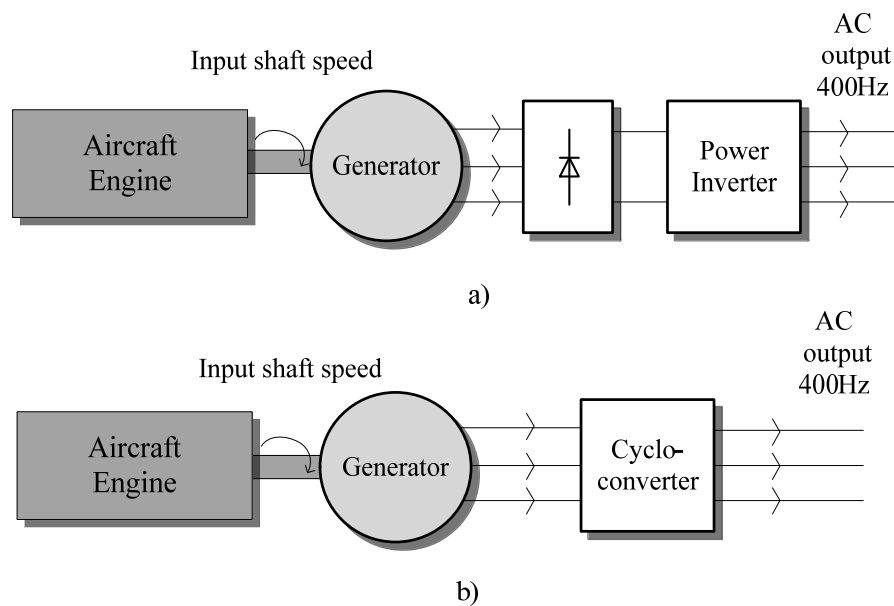
Fig. 2.9. Variable speed constant frequency with a) diode rectifier and b) cycloconverter topologies.

The second topology is referred to as variable frequency (VF), also known as "frequency-wild". This has been getting a lot of attention in the field of future aircraft power generation research as it is a very promising potential methodology. It is the simplest and most reliable topology for power generation [10]. As shown in Fig. 2.10, the generator is coupled to the engine shaft via a variable speed drive (VSD) and outputs three phase VF power ranging between 300Hz to 900Hz depending on the engine speed.

The wide VF range affects frequency sensitive aircraft loads such as the AC electric motors. When fed electrical power directly from the generator, the motor speed is dependent on the frequency of the AC power. This may cause inconsistent

25

performance within the loads that utilise these electrical motors [10]. Localised power converters may be employed on the inputs to such loads in order to prevent this possible issue and at the same time provide electrical control over them. VF topologies have been widely used for business jets and recently been adopted for larger sized commercial aircraft such as the A380 and B787.
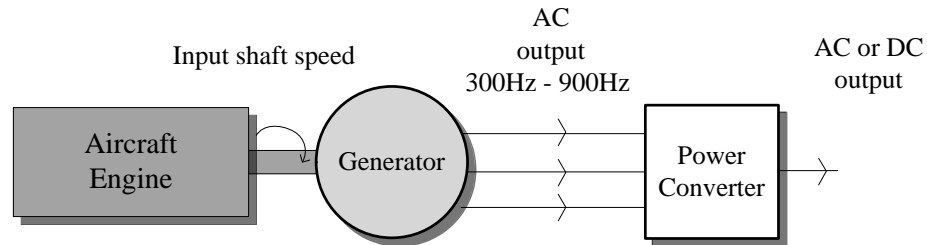
Fig. 2.10. Variable frequency topology.

2.4.2   Generator Control

The main control objectives of conventional power generation systems are to regulate the output voltage and provide some protective functions. For DC generator systems, the stator field can be controlled by varying the stator resistance which therefore influences the output voltage, as seen in Fig. 2.11. The variation of resistance takes into account the number of connected loads and engine speed. The DC generators are controlled to supply constant DC voltage even with variable engine speed and electrical loads. This control also needs to satisfy aircraft standards in order to ensure compatibility between the aircraft electrical power system and other loads (refer to MIL-STD-704F [25]). The control of AC generator systems is similar, except for the addition of a separate DC power source for field excitation. Additional regulators are also required to control this DC power source which makes the control slightly more complex.
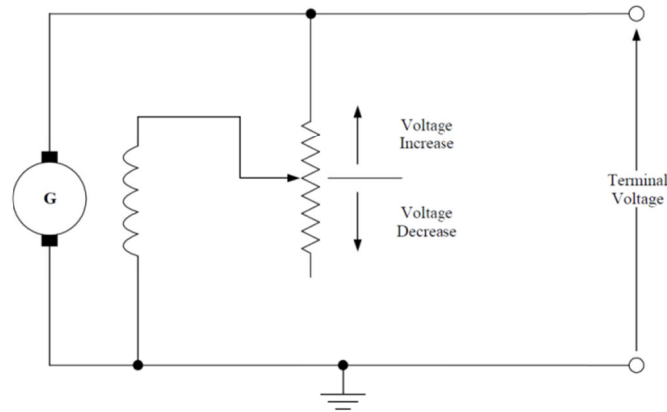
Fig. 2.11. DC generator voltage regulator [10].

For a multi-engine aircraft, usually there is more than one generator in operation. Parallel control between all of the generators could be done so that the electrical loads could be distributed evenly [10]. The advantage of parallel control is that uninterrupted power can be supplied even in the worst cases of engine/generator failure. Each generator would have their own voltage regulators to compensate for load changes.

Parallel operation of AC generators is also possible, but only with CF power. Both active and reactive power from each generator would need to be controlled simultaneously in order to achieve effective load sharing. While parallel control performance relies on the accuracy of CF regulated by the CSD, the actual control makes use of current measurements from the electrical power output of each generator, as shown in Fig. 2.12. Active loads are distributed equally using the current error sensed from current transformers with respect to the load demand and is used to trim the torque applied by all generators. Reactive load sharing is established by altering the DC excitation current which will vary the generator output voltage. A combination of generator speed and DC excitation current control yields sharing of both active and reactive power equally between the connected generators [10]. In the case of generator failure, there would be no change-over transients as all the generators are synchronised.

Parallel control could still be applied to VSCF topologies as their power outputs are CF. However it is not possible to do so with the VF topology as the method of regulating the active and reactive loads, as detailed earlier, may not be

optimal or fast enough to accommodate the effect of wide varying frequencies between multiple generators.

It is possible to control the electrical power when employing the VF topology by utilisation of power converters on the output the generator. The power transmission is controlled directly using the power switches. This technique is much more efficient and faster than the conventional method of control. However a different control strategy may be required to control the power converter while taking into account the functions of the S/G.
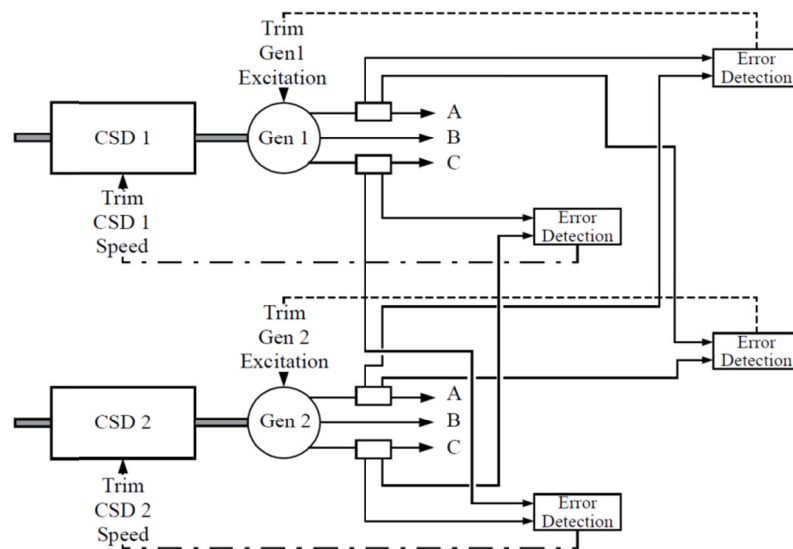
Fig. 2.12. AC generator parallel operation [10].

2.4.3 Electrical Power Distribution

From the twin 28VDC to the current 230V frequency-wild AC system on the B787, there is a trend indicating that the voltage level of power generation is increasing in order to meet the increased electrical load demands on the aircraft, as shown in Fig. 2.13. Most conventional civil aircraft output 115VAC with a CF of 400Hz, a voltage level that has not changed since the 1950s. During the past decade, higher voltage level electrical systems have been investigated. 230VAC VF systems have been adopted on the B787, while 270VDC systems have been developed for military aircraft such as the Lockheed Martin F-22 [6, 10]. Higher voltage levels give the advantage of lower current transfer at the same power level, thereby reducing voltage drop and copper losses in the distribution wires.

There is also a move towards utilising different power generation systems, for example the VF topology, due to its significant advantages as discussed earlier. The VF topology could potentially reduce the number of power converters; especially as certain AC loads, such as wing de-icing, can accept wide voltage frequencies. Also, most legacy loads are still compatible with such voltage levels and existing protection circuits can be re-used for this power system. However, having three phases (or more) would mean the main bus would require more connections which would in turn increase aircraft weight.
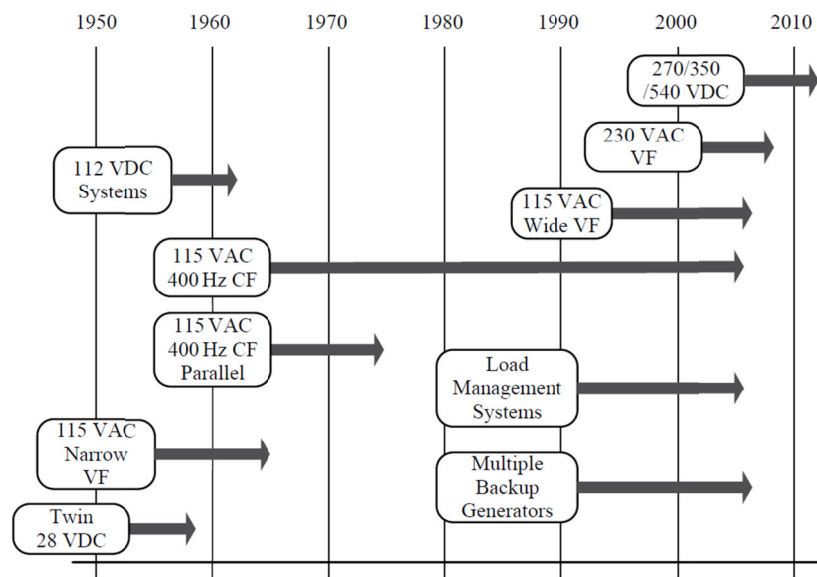
Fig. 2.13. Aircraft electrical power system trend timeline [10].

The DC current limit for state-of-the-art systems has been found to be about 400A due to limitations imposed by the contactor and feeder size [10]. So for a 28VDC system the maximum power that can be transmitted is about 12kW, hardly enough to meet most of the modern aircraft power requirements. The logical approach is therefore to increase the DC voltage level. High DC voltage bus systems have been used mostly in military aircraft, typically at 270V, which are converted from the CF 115VAC voltage level using a rectifier. These aircraft could generate up to 300kW per bus which is several times more than the typical power level today. By employing new power generation topologies such as VF, it is possible to implement DC link buses without the need for the accessory gearbox but instead with active rectification. Furthermore, less overall system weight could be achieved from less

wiring, although this may be counter-balanced by the amount of converters used for each AC load. The voltage levels are determined by the circuit protection level and risk of corona discharge at high altitudes. High voltage buses also pose a risk in terms of safety, hence circuit protection may need to be improved before such system were to be used in civil aircraft [4, 6, 26-29]. With implementation of different power generation topologies, the DC bus system looks more promising compared to AC bus system [30].

Not all electrical loads connected to the main aircraft bus can directly use the generated power. If the voltage level of the aircraft bus is 115VAC or 270VDC, power conversion is required from one form to another for loads such as backup batteries that operate at 28VDC. Transformer rectifier units (TRU) are commonly used in modern aircraft to convert from 115VAC to 28VDC for such loads [10]. However, they are uncontrolled converters and the DC voltage level changes according to the load intensity. TRUs also require filters in order to smooth the DC output voltage and require forced cooling as the required heat dissipation is quite significant. This makes the TRU quite bulky as a whole. The 28VDC is sometimes converted to 115VAC single phase as emergency power for flight controls [31]. This is achieved by using inverters based on silicon controlled rectifiers which are half controlled to produce AC power from DC.

Advanced power electronics can be used to replace the existing electrical converters on the aircraft power systems to achieve higher power density and fault tolerance. Power electronics such as insulated gate bipolar transistors (IGBT) have been commonly used in power convertors for high power applications [32, 33]. Additionally, the bi-directional power flow capabilities of power electronic converters enable the function of regeneration for potential electrical loads such as the aircraft actuators.

The present converters used on aircraft are typically either passive or half-controlled in terms of electrical power conversion. Fully controlled converters have yet to be implemented on aircraft and this could soon be implemented due to the recent developments in power electronics. Full control of the power flow, in terms of active and reactive components, could now be achieved which opens up new possibilities for MEA concepts such as the S/G scheme.

This change in the power generation system will facilitate more efficient electrical generators, and more reliable ways of generating power, by bypassing the accessory gearbox. The generator could be interfaced with power electronic converters to provide full flexibility of power conversion including different forms (AC or DC) according to the load requirements. It also opens up the possibility of controlling the generator as an engine starter using a power converter which would further optimise the functionality of the power generation system.

2.4.4   Starter-generator System

There has been research contributing to novel MEA S/G topologies for the past 25 years [34]. Extensive work on using IM as a S/G has been done in [22]. S/G operation has been investigated with a resonant converter fed IM in [35]. Experimental results showed that use of an IM as a S/G is feasible in both modes with the help of a DC machine that represents the aircraft engine. Further work could include assessing the S/G in an actual aircraft operating environment to determine its limitations.

SRMs have also been considered and investigated as a S/G in [34, 36, 37]. A 250kW SRM was tested in [36] in accordance with the aircraft starter and generator requirements. The machine was capable of operating in both starter and generator modes up to 13.5krpm. Dynamic load impact/dispatch of up to 102.5kW was also performed on this setup with successful bus voltage recovery at the point of regulation.

Existing three stage SM were also looked at as potential aircraft S/G. In [38], a SM is designed and built as a solution for integral S/G. The results show credibility of the prototype SM as a S/G due to its good efficiency at high speed low torque operations. Griffo [39] presented a sensorless control strategy for the SM. Results showed that the S/G can operate a starter function although parameter variations can influence the performance of the control scheme. A three stage SM fed by a multilevel back-to-back converter was reported in [40]. The concept was tested with a prototype which demonstrated the system is capable of S/G operation.

The state-of-the-art solution is the integral S/G in the frame of the POA [6, 16, 18]. The aim was to demonstrate the feasibility of a more electric engine that is more efficient than a conventional aircraft jet engine. A 150kW PMM is integrated directly into the high pressure engine shaft as a S/G. Towards the end of the engine is a 120kW SRM for additional electrical power generation, as shown in Fig. 2.14. The accessory gearbox is not in use and its functions were performed by electrical ancillary systems instead. Even active magnetic bearings were used to reduce the oil consumption of the lubrication systems [18]. The demonstration of this more electric engine marks a significant step towards the development of MEA.
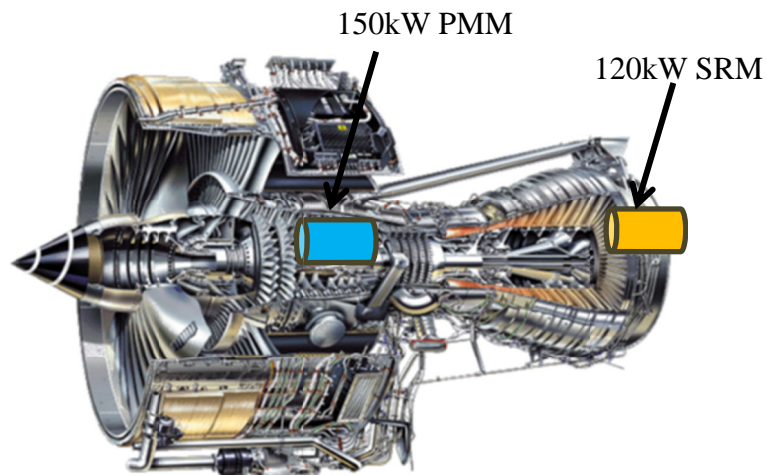
Fig. 2.14. Trent 500 aircraft engine with locations of the embedded S/G machines [18].

Recently, several studies looked into the control aspects of the MEA S/G. For example, [39] and [41] implemented vector control schemes that regulate the S/G system via a power converter. Classic PI controllers were used and the speed of the machine was controlled during starter mode to drive the engine. In generator mode, the DC link voltage is controlled to 270VDC. The control strategies met the requirements for both modes successfully. However, there is the lack of detailed control analysis especially in generator mode. The wide operating range of S/G together with high electrical power circulating between the machine and converter would require rigorous analysis to ensure the performance and stability of the designed control system. Furthermore, there are only a few reported studies in this area and many control aspects related to an integrated starter-generator system remain unanswered. These gaps in knowledge demonstrate the need, and basis, for the research detailed in this Thesis.

2.5   Power System Topology

From the MEA options discussed earlier in this Chapter, the S/G topology that will be studied in this Thesis can now be established. The criteria on which this was decided were weight, volume, and power losses which are crucial to aircraft overall efficiency. Safety and hence reliability were also crucial factors that needed to be taken into consideration. The system will be as follows:

- The generator will be a PMM. This decision is based on its power density, as it is the most efficient machine among the three choices.
- VF will be utilised as it is the simplest and most reliable topology that excludes the accessory gearbox.
- High voltage DC power distribution will be implemented but to its advantages in terms of weight reduction and lower copper losses. Loads which do not need regulated power could be connected directly without power converters to reduce weight further.

This S/G topology is considered to be one of the most promising possible solutions for future MEA S/G systems and is also currently being investigated by the University of Nottingham within the frame of the AEGART project; a part of Clean Sky JTI EcoDesign ITD EU FP7 framework program [42]. The acronym AEGART stands for "Aircraft Electrical Generation with Active Rectification Technology". The project has conducted intensive trade-off studies of potential S/G topology candidates [43] and the topology based on a surface-mounted PMM (SPM) fed by three level IGBT active rectifier has been selected. This PhD research is a part of the AEGART project. The main aim here is to investigate control aspects in order to establish high-performance operation in both starter and generator mode.

The AEGART project looks for the optimal solution for more-electric business-jets, and the overall electric power system topology is shown in Fig. 2.15. It is comprised of a PMM connected to a three level active front end rectifier (AFE) and coupled to an aircraft engine. The other end of the AFE is connected to the aircraft main bus which is DC in nature and is parallel to connecting electrical loads. To simplify the representation of on-board electrical loads, they are grouped

generally into two; constant power and resistive loads. Not shown in Fig. 2.15 is the thermal management system which allows the PMM to operate in high temperatures.
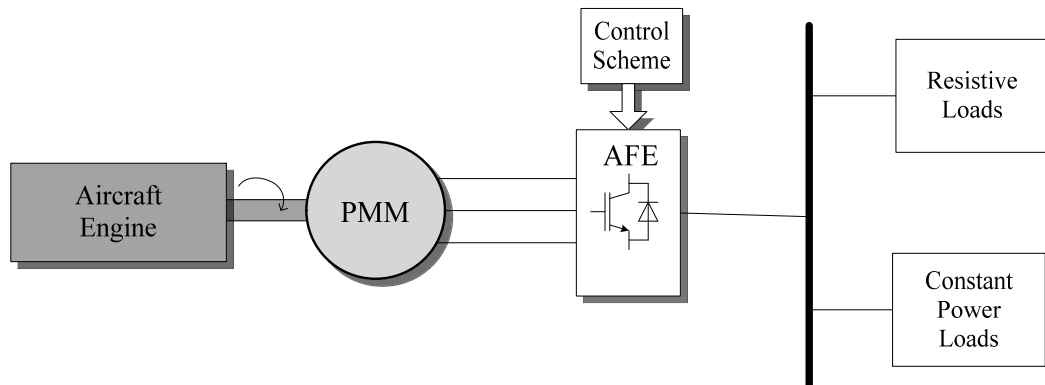
Fig. 2.15. AEGART S/G power system topology.

The AEGART S/G system was designed to meet the following technical specifications:

- Generator speed in motoring mode - up to 12krpm, in generating mode – 19.2k…32krpm

- In starter mode, the engine should be driven up to self-sustaining speed at ambient temperatures that can vary between -40°C to +55°C. The torque-speed engine characteristics are depicted in Fig. 2.16 as coloured lines.

- In generation mode, the system should provide up to 45kW of electrical power to the 270VDC bus.

- The electric power quality should meet MIL-STD-704F requirements.

- The output DC current should be controlled according to the droop characteristics shown in Fig. 2.32.

As mentioned, several potential S/G system topologies were considered and were passed through a detailed trade-off procedure [43, 44]. IM and SRM based S/G were part of the consideration together with SPM and interior mounted PMM (IPM). The SPM configurations utilise either metallic sleeves (MS), carbon fibre sleeves (CFS), or are designed for flux weakening (FW). The IPM configuration is also considered with FW capabilities. On the power converter side, two-level and three-level topologies are considered for most of the machine configurations. The combinations were evaluated in terms of machine geometry (mass, volume),

converter (mass, losses), and thermal management (machine and converter temperatures). The overall mass, weight, efficiency, control performance and safety of the S/G topologies were also assessed. Table 2.1 shows some of the trade-off results between the considered machine-converter topologies, while the summary of different machine advantages and disadvantages when utilised as S/G is shown in Table 2.2. SPM/CFS has the lightest machine mass, while the SPM/FW combination with a three-level converter generates the least losses for both the converter and machine. Due to the minimal losses and slight weight difference compared to the SPM/CFS, the latter was selected for further investigation and development into a working prototype.

Table 2.1. Trade-off comparison between the considered machine-converter topologies.

Topology		IM		SRM	SPM/MS	SPM/CFS	SPM/FW		IPM/FW	
		2L	3L	C	2L	2L	**2L**	**3L**	2L	3L
Machine Active Mass		14.1kg		21.4kg	14.4kg	13.9kg	**14.4kg**		15.2kg	
Machine Losses	20krpm	1.87kW		1.63kW	0.99kW	0.91kW	**0.86kW**		1.06kW	
	32krpm	1.77kW		1.63kW	0.93kW	0.83kW	**1.85kW**		1.11kW	
Converter Losses	20krpm	2.1kW	1.3kW	9.5kW	5.4kW	5.4kW	**1.6kW**	**1.3kW**	2.1kW	1.8kW
	32krpm	2.2kW	1.4kW	2.1kW	3.7kW	3.7kW	**2.1kW**	**1.5kW**	1.5kW	1.3kW
Worst Case Temp.	Stator	231°C		170°C	170°C	169°C	**223°C**		179°C	
	Rotor	268°C		196°C	199°C	186°C	**195°C**		201°C	
	Speed	20k		20k	20k	20k	**32k**		20k	

Table 2.2. Summary of trade-off comparison between different machines as S/G.

Machine	Gains	Losses
IM	- Robust - High power factor - Reliable	- Significant rotor losses - Limited fault tolerance
SR	- Inherently safe - Reliable	- High mass - High losses from torque ripples
SPM	- Low overall mass - High performance	Fault detection
IPM	- Low overall mass - High power density	Limited fault tolerance

2.5.1 AEGART Electrical Machine

The SPM was designed to achieve the torque-speed characteristic shown by a bold black line in Fig. 2.16. P and T_e are the power and electromagnetic torque output of the SPM. ω_b is the base speed of the machine which is the last speed that can utilise the maximum torque. Beyond this speed, the torque output is reduced in order to maintain a constant power output. ω_{gmax} and ω_{gmin} are the maximum and minimum generation speed of the machine as mentioned earlier in the S/G requirements. During starter mode the machine has to supply constant torque and constant power when operating in generator mode. The maximum torque output from the SPM is selected to satisfy the torque requirement of the engine at the defined ambient temperature range. The positive torque requirements are met when the SPM is operating in starter mode. This includes the constant torque region and a small portion of the constant power region. When the engine torque is negative, the SPM operates in generator mode.

Considering the S/G would operate as a generator most of the time on an average flight cycle, the SPM is optimised for operation within the generation speed region indicated in Fig. 2.16. As a result, the size of the SPM could be minimised which involves compromising the machine design for operating both as a starter and generator. Fault tolerance is considered by adopting double layer stator windings (redundancy solution) in the event of a failure [43].
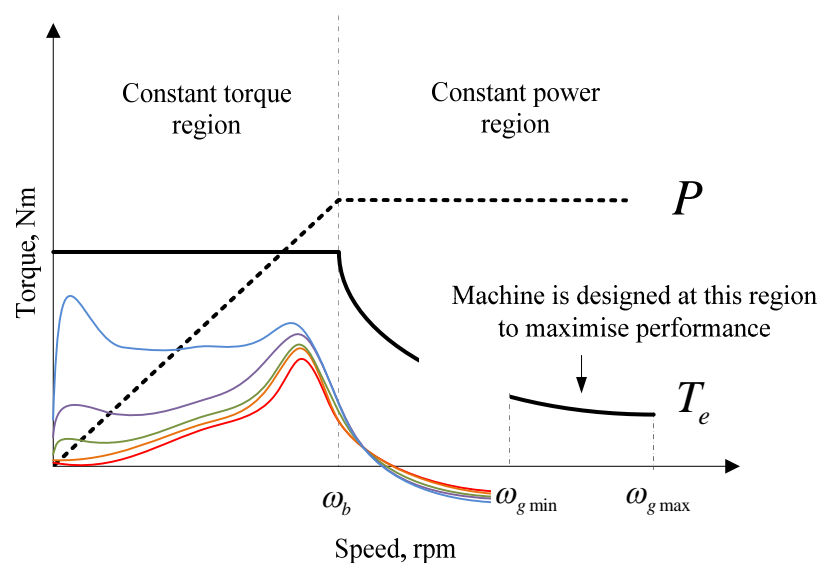
Fig. 2.16. Torque-speed characteristic of the AEGART PMM.

The following is a brief description on the electrical machine design and more details can be found in [44]. A number of design aspects were assessed, such as the pole/slot combinations of the machine casing. The pole/slot combinations have to be selected properly as higher number of poles could lead to more converter related losses at higher power levels. Taking into account the power electronic converter losses and switching frequency limitations, a six-pole, thirty six-slot machine is chosen. The magnets are made from JNHF silicon steel due to its more affordable price and comparable magnet losses compared to the other material of choice, cobalt alloy.

Since the magnets are surface mounted, a sleeve is used in order to keep the magnets in place at high speeds. Carbon fibre was selected for the sleeve material with sufficient thickness to cover up to a 110% speed margin. With a customised machine housing, the oil can be channelled between the slots and along the stator outer diameter for a more distributed and efficient cooling. Roller and angular contact bearings are used to support the machine rotor. This SPM has been modelled as a finite element model (FEM) to verify its capability and estimated losses. Once that has been done, it is built and is currently being tested at the time of writing. The completed prototype pictures can be seen in Fig. 2.17. The nominal parameters of the machine relevant for this research are listed in Table 2.3.
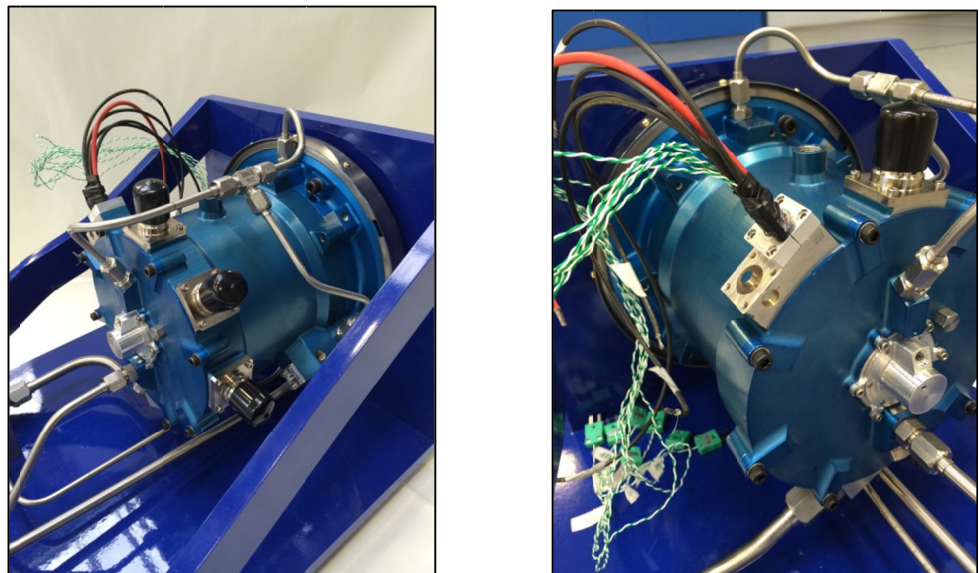
Fig. 2.17. Overview of the AEGART SPM.

Table 2.3. SPM parameters.

Parameter	Value
Stator resistance, R_s	$1.058m\Omega$
Stator inductance in rotating frame, $L_d = L_q$	$99\mu H$
Pole pairs, p	3
Magnet flux-linkage, ψ_m	$0.03644Vs$
Rated power, P_{rated}	$45kW$
Combined machine and engine inertia, J	$0.403kgms^2$

2.5.2   Power Converter

From the SPM preliminary design, the converter limits were defined as 400A peak output current, 1.2kV DC-link peak voltage, and 1.6kHz electrical frequency; which correspond to 32krpm on a three-pole pair machine. Two options were considered for the converter; the two-level AFE and three-level neutral point clamped (NPC) converter shown in Fig. 3.6 and Fig. 2.18 respectively. E_{dc} is the DC link voltage, C is the DC link capacitor, i_{NP} is the neutral point current, and S_1 to S_4 are the power switches on one leg of the converter. $v_{a,b,c}$ and $i_{a,b,c}$ are the three phase voltages and currents respectively.
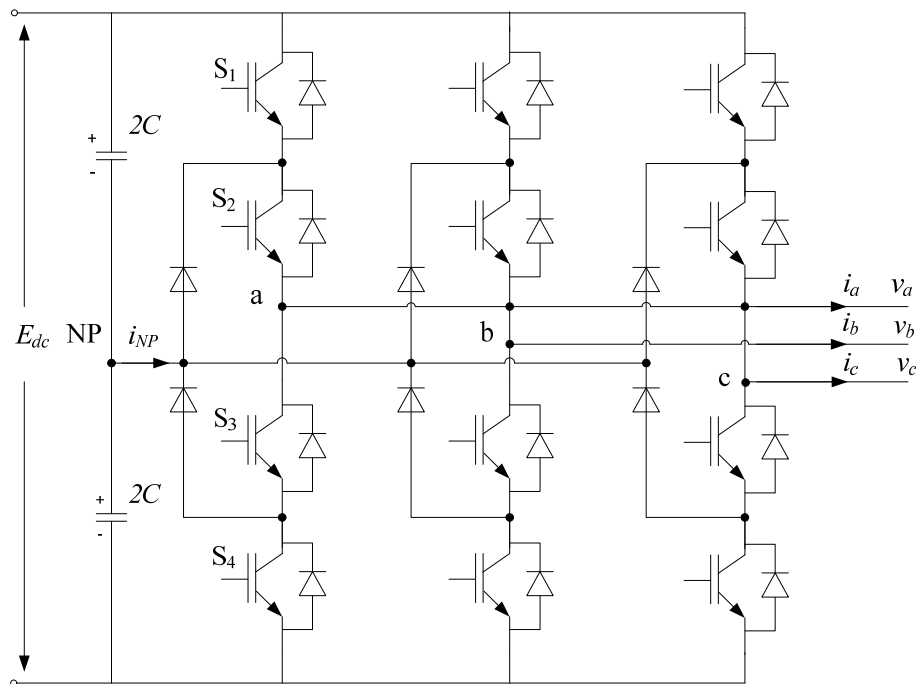
Fig. 2.18. Three-level NPC converter.

Three types of power devices were considered for the power converter; the metal oxide semiconductor field effect transistor (MOSFET), silicon carbide MOSFET (SiCMos), and IGBT. Simulation results of the first two options showed very low power losses but they were not capable of meeting the maximum current requirement. Complex solutions would be required to enable these devices. Hence, commercially available IGBTs are selected as the power devices for this S/G power system. The key consideration in selecting the power devices and converter topologies is the total power loss when operating the machine for S/G functions at steady state conditions. Both of these converters are simulated in the Matlab/Simulink environment with the PLECS toolbox [45] to analyse the losses and total harmonic distortion (THD) at different S/G load conditions. It was found that the NPC converter generates less overall losses compared to the two-level converter [43]. This is due to the more sinusoidal output voltage waveform of the NPC converter compared to the two-level converter. The former was therefore chosen for the AEGART system. Moreover this choice had additional advantages such as lower electromagnetic interference (EMI) emissions and current harmonics. With smaller losses, the volume and weight of the heatsinks can be reduced as well, which is crucial in aircraft applications. The capacitors are designed to allow enough current and are shaped to fit the IGBT layouts. The final converter design is also equipped with its own gate drivers, transducers, and resolver interface to provide a compact solution. Finally, the converter is prototyped and is currently being tested with the SPM for S/G operation. Table 2.4 shows the parameters of the converter and DC link bus.

Table 2.4. Converter parameters.

Parameter	Value
DC link capacitance, C	$1.2mF$
Rated DC link voltage, $E_{dcrated}$	$270V$
Converter maximum AC current, i_{max}	$400A$

2.5.3 Thermal Management System

The AEGART machine is designed to be oil-cooled with the oil supplied from the auxiliary gearbox. The nominal oil temperature is 120°C. Two methods of oil distribution were considered; indirect and direct cooling. Preliminary simulations show direct oil cooling as the optimal solution where significant temperature reduction can be achieved. Computational fluid dynamics (CFD) is applied as a numerical simulation to investigate the fluid flow within the SPM. Using another numerical method based on lumped parameters, information on the temperature distribution within the SPM can be obtained. The analysis confirms that the designed cooling system is able to maintain the SPM temperature below the limit.

The thermal management of the converter was designed as a forced air cooling solution. The size of the fan and heatsink are designed for converter losses based on the worst case scenario. CFD simulations showed that the converter cooling system was able to dissipate the heat generated from power loss throughout the S/G operation and maintain the temperature well below the maximum value. Both cooling systems are built together with the machine and converter to enable the prototype testing of the S/G system.

In comparison to the state-of-the-art electrical power generation solution which utilises a three stage SM, the AEGART system offers advantages in terms of reduced mass and velocity, while having increased power density, and efficiency. The reliability as a whole power generation system is also increased due to the removal of the CSD. A power converter is used to control the PMM and its bi-directional power flow regulation offers both capabilities of starter and generator.

2.6 S/G Control Scheme

Based on the S/G operation, the general control aspects could be determined. In starter mode, speed or torque control is important to rotate the air compressors of the engine. In generator mode, the speed of the engine is controlled externally and control of the DC link bus power is the primary objective. Both starter and generator

modes are separate and there is no need to control them both at the same time. Due to the wide speed range that the S/G is operating within, the power converter may be subjected to very high levels of back-emf from the machine at high speeds. Flux weakening is employed to ensure that the back-emf is within the converter limits. More details on flux weakening will be discussed in Sub-section 2.6.3. If the S/G system is investigated as a stand-alone system, it would be sensible that control of the DC link voltage is fixed at 270VDC to ensure the uninterrupted operation of the electrical loads. However, if multiple S/G or electrical power sources are connected in parallel, then another control variable has to be considered as there might be conflict in maintaining the DC link voltage. For this case droop control is applied where multiple sources mutually manage power sharing according to droop characteristics. The general idea will be discussed in Section 2.6.5 although multiple source topologies are not the subject of the research reported in this Thesis.

The general control scheme for the S/G can be seen in Fig. 2.19. ω_r is the mechanical speed, S_{abc} are the three phase switching states and all variables with the $*$ notation denote the reference value of controlled variable.
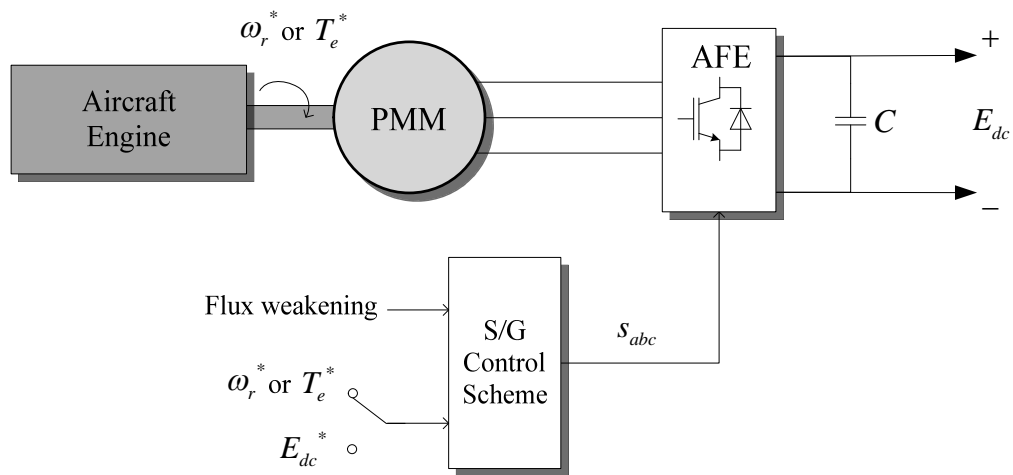
Fig. 2.19. Conceptual control scheme of S/G system.

The topology of this S/G, controlled directly by power electronics, is similar to VF drive systems widely used in industrial applications [46, 47]. An electrical machine (usually AC in nature) is interfaced with a controllable power converter that is connected to an electrical power source. The switching signals derived from the drive controller are sent the power converter. Most VF drive systems use one of the

two feedback controls; field-oriented (FOC) or direct torque control (DTC). Both of these control methods are briefly explained and one shall be selected for this S/G system.

2.6.1 Direct Torque Control

As the name suggests, DTC is a control method that controls the torque of AC electrical machines. This is done by estimating the torque and stator flux from the measured voltage and current of the machine. The stator flux could be regulated for more advanced control requirements. These estimated variables are compared to their reference values and are regulated as fast as possible if the error between them exceeds a tolerance band. DTC therefore effectively utilises hysteresis control within the core structure [48]. The general DTC configuration can be seen in Fig. 2.20. ψ_s is the machine stator flux. H_ψ and H_T are the control output signals for each control variable. The control signals are then interpreted within a voltage vector look-up table (LUT) to output appropriate switching states for the converter.
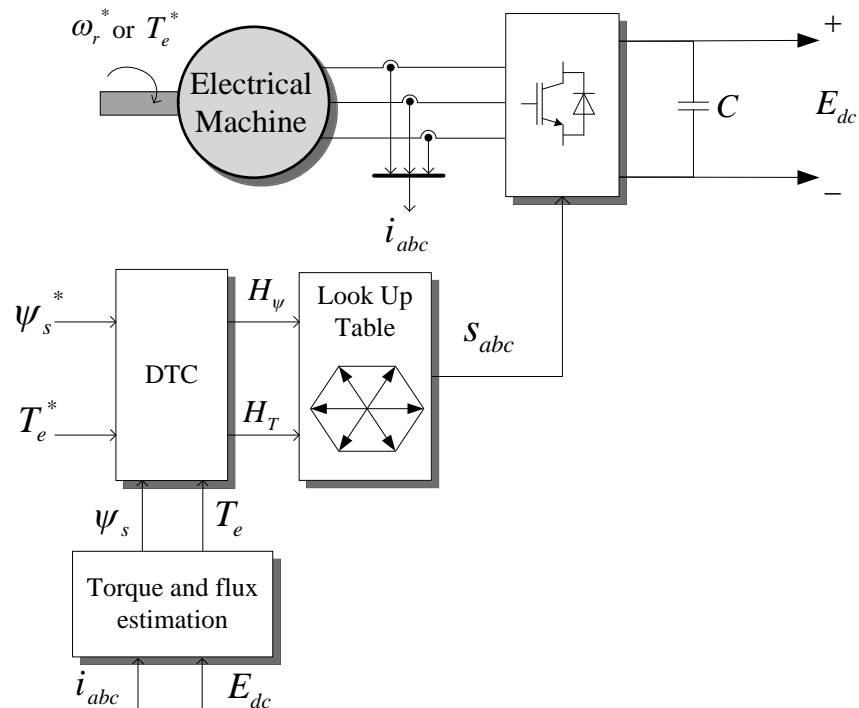
Fig. 2.20. General DTC structure.

The advantage of using DTC is that it has very fast dynamic response and does not require PI regulators, coordinate transformations, or pulse width modulation (PWM) signals for control operation [49-51]. However, due to the use of hysteresis control, there can be significant current ripple in the outputs from the power converter. The ripples can affect the torque performance of the machine, especially during starter mode, and hence provide less smooth engine acceleration. The power quality of the main bus is also jeopardised due to the current ripple. Hence, this type of control is not considered for this S/G system.

2.6.2   Field Oriented Control

FOC is based on drive (machine + converter) control, utilising a rotating reference frame, which is aligned with the machine flux. The rotating reference frame is the result of direct quadrature transformation that attempts to simplify time varying AC variables into DC type constant steady state values. Easier analysis and control design can be performed on the DC variables before performing an inverse transformation back to AC signals [46].

Decoupled control of active and reactive current or voltage components could be achieved in the direct and quadrature axes, also known as the *dq* frame [46]. When aligned with the rotor flux, the *d*-axis current controls the reactive power or flux while the *q*-axis current controls the active power or torque. The general control structure can be seen in Fig. 2.21 where $v_{d,q}$ and $i_{d,q}$ are the machine stator voltages and currents in *dq* frame. PI regulators are usually used to control the *dq* currents and output the corresponding *dq* voltage reference. The voltage references are converted back into the three phase frame and are passed through a PWM scheme which synthesises switching signals for the converter. An outer control loop is added to regulate speed or torque and outputs the necessary current references for the *dq* currents.
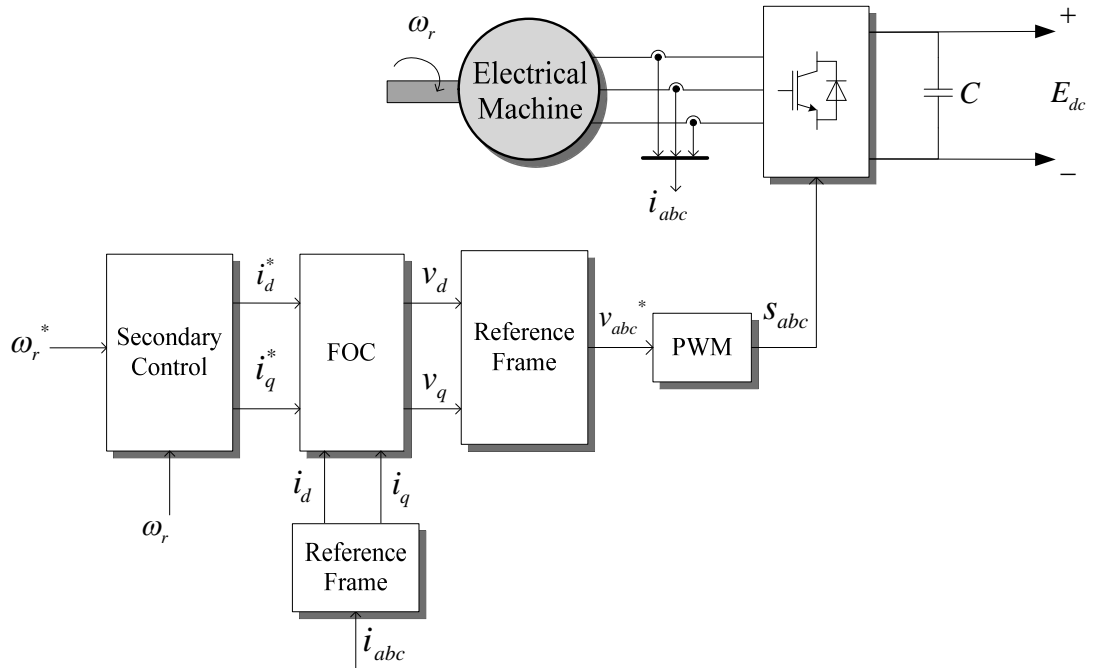
Fig. 2.21. General FOC structure.

The FOC may be more complex by having a cascaded loop structure, but the controlled current quality can be better compared to DTC with properly tuned PI controllers. Furthermore, it is more convenient to control the *dq* currents directly rather than going through an estimation process to determine the stator flux. The cascaded loop of the FOC allows the secondary control to be conveniently changed according to S/G operational mode; hence FOC is chosen as the main control scheme. Details on the control scheme and the design approaches are detailed in the following Chapters 3, 4, and 5. The next Sub-section discusses the role of flux weakening for the subject application and will overview the ways of establishing flux weakening control.

2.6.3   Flux Weakening Control

Field or flux weakening (FW) is a control method of enabling electric machines to achieve a wider speed range above their rated value. Some applications such as the aerospace and automotive sectors require its electrical machine to operate at high speed regions. Appropriate machine selection and sizing should suffice to meet the speed requirements within nominal operation; however an alternative is to

have a lower rating machine capable of FW. This may reduce the overall system size and cost but achieve the same requirements [52].

In principle, FW works by injecting de-magnetising current which 'weakens' the flux of the electrical machine. The weakened flux reduces the back-emf produced by the machine which determines the AC stator voltage level. With proper control of this de-magnetising current, the process results in a regulated AC stator voltage level [53].

The FW operating region can be illustrated using the torque speed characteristics shown in Fig. 2.22. Below ω_b, the machine operates in the constant torque region. In this region, P increases linearly with respect to speed and is usually within the converter current limits. The maximum torque of the machine can be achieved in this region. Beyond ω_b, the machine operates in the constant power region where FW is utilised to not exceed the operational limits of the converter. This would also ensure that the converter does not reach overmodulation and effective control can be maintained throughout operating within this region. At the expense of keeping P constant, the torque is reduced in proportion to the increasing speed.
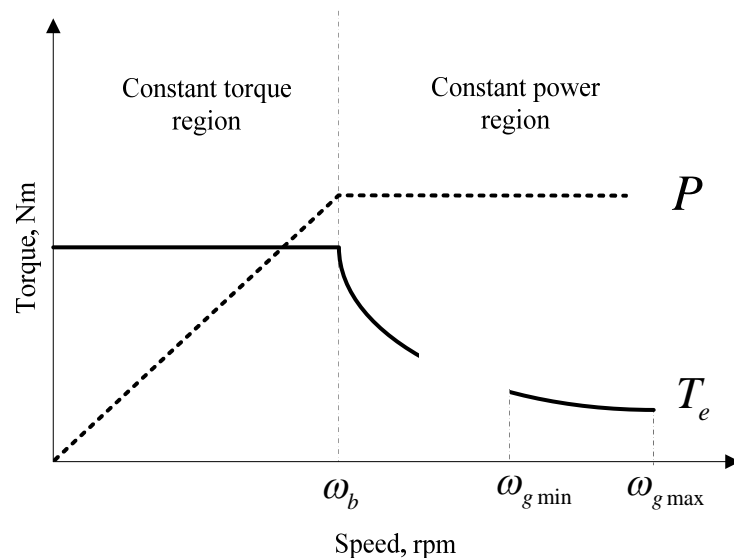
Fig. 2.22. A typical electrical machine torque-speed characteristic.

The designed PMM will be able to operate at a wide speed range that covers both constant torque and power regions. Furthermore, the main task for the PMM is

to function as a generator when the aircraft is cruising in the air. During that period, the operating speed of the PMM is between 19.2krpm to 32krpm which is within the constant power region. There is a wide speed range from ω_b to ω_{gmax}, hence FW control is crucial and critical for the operation of this S/G power system.

A considerable amount of research has been done over the recent decades on FW. All types of potential S/G electrical machines which were discussed earlier have been investigated under FW operation [54-56]. Furthermore, the majority of published papers analyse FW mainly for industrial applications where the drive is operated in motoring mode, while a few considered generator mode [57-67]. There is very little literature dealing with the rigorous analysis of FW operation and control design for generator mode. More research has yet to be done in the field, including analysis in generator mode for specific aircraft applications.

Based on the S/G system under consideration, a literature review has been performed to establish current state-of-the-art in the area of FW control for PMM-based applications. For consistency, the control approaches are described in terms of FOC in motoring mode where FW is controlled as the reactive component on the d-axis, while speed/torque is controlled as active component on the q-axis. The following are the generalised FW methods from the compiled literature that could be considered for the S/G power system.

2.6.3.1   Analytic Method

This method uses equations to relate relevant variables. Variables such as ω_r, or stator voltage magnitude, $|V|$, could be used as reference for the equations to determine the appropriate FW region. Fig. 2.23 shows, in general, the control structure of the drive system with the equations for FW situated in the calculation block. W_s represents the general form of the speed regulator.
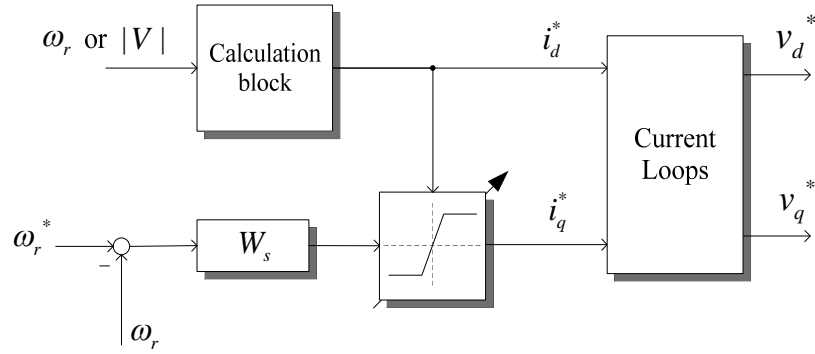
Fig. 2.23. Control structure with analytic method.

The output of the calculation block would be the reference for the direct axis current, i_d^*. i_d^* could differ between the speed operating regions, hence two or more sets of equations can be used. For SPM, no i_d is required in the constant torque region. i_d^* would use (2.1) in order to satisfy that condition.

$$i_d^* = 0 \tag{2.1}$$

Within the constant power region, equations such as (2.2) are used to determine appropriate i_d in order to maintain $/V/$ within its limits [68]:

$$\left(\frac{|V|_{\text{max}}}{p\omega_r} \right)^2 \leq \left(L_d i_d + \psi_m \right)^2 + \left(L_q i_q \right)^2 \tag{2.2}$$

where $/V/_{max}$ is the maximum stator voltage magnitude, p is the machine pole pairs, and ψ_m is the machine flux. $L_{d,q}$ are the machine inductances in dq frame. Logic commands could then be used to switch between the required references.

By adding measured or predicted values of i_q and ω_r during operation, an appropriate value of i_d^* could be calculated for FW. Additional limits could be imposed onto the q-axis control loop in order to limit the maximum allowable current going through the converter. The most common solution is using a dynamic limiter that limits i_q^* with respect to i_d^* and the maximum current seen in Fig. 2.23.

A large number of papers utilise the analytic method in drive systems [57, 59, 69-88]. The analytic method is also used with direct torque control (DTC) as shown in [89-94]. The implementation of FW in DTC structures can be more complex compared to FOC due to the need of observers for parameter estimation.

Advantages of the analytic method include its simple derivation process and flexibility to accommodate additional control variables. This is supported by the large amount of papers utilising this method. However, dependency on system parameters would mean that it is sensitive towards parameter variations and could affect system performance. The machine torque cannot be utilised properly in the FW region due to current controller saturation. This affects the voltage reference during transient FW operations. Feedforward decoupling and voltage compensators based on the modulation scheme are used to optimise the voltage output; hence improving the torque performance [76, 95].

2.6.3.2   Advanced Angle Method

The concept of this method is that it assumes angle modification of the current or voltage magnitude vector to determine the appropriate $i_q{}^*$ and $i_d{}^*$. Fig. 2.24 shows the control scheme with an advanced current angle method that determines both speed and FW controller outputs. $/V/$ is controlled by means of varying the angle of stator current, γ, which would influence both $i_d{}^*$ and $i_q{}^*$. $\Delta\gamma$ is the perturbation of γ resulting from the regulation of $/V/$ and i_s is the stator current. W_{fw} is the general form of the FW controller.
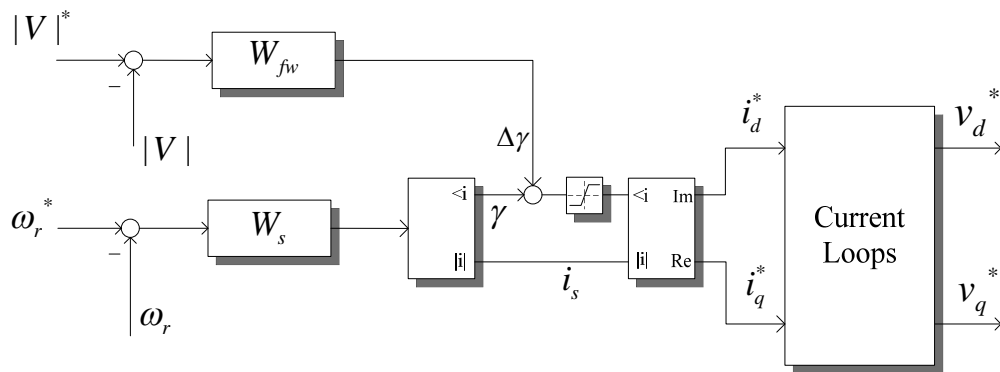
Fig. 2.24. Control structure with advanced angle method.

This can be clearly illustrated on an i_d - i_q plane, where i_s is rotated by $\Delta\gamma$ as seen in Fig. 2.25. The current magnitude vector of i_s and $\gamma + \Delta\gamma$ would determine the values of $i_d{}^*$ and $i_q{}^*$ [60, 96, 97].
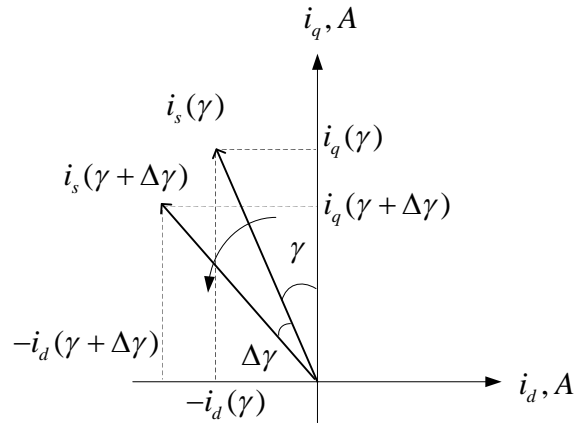
Fig. 2.25. i_s vector rotation in *dq* current plane.

The advanced angle method could also be used to vary the stator voltage angle for a simpler control approach or to combine with space vector modulation (SVM) technique [98-102]. The advantage of this method is that it is less sensitive towards system parameter variations due to the use of integrator based regulators. The application of such controllers enables FW control without critical dependency on accurate parameters.

However, there are some inherent disadvantages with this control strategy as it is unable to operate under no load conditions. Because i_s, in terms of magnitude, is mostly determined by active load power demand, then this FW method is unable to regulate either *d* or *q* currents. This can be especially disadvantageous for the considered application if the system is unable to operate at no load condition within the FW region. Another disadvantage is due to the linear controller; its performance is dependent on the operating point and system complexity. Kitamura [102] proposed a variable gain controller that is updated according the system frequency. Hatsuse [100] added electrical frequency compensation to control the impact of speed difference in the system. Bolognani [103] proposed a voltage based angle control method with analytical equations to provide a smooth transition between normal and optimised torque regions.

2.6.3.3   Direct Current Method

Another proposed FW control strategy is the direct current method. The control structure is shown in Fig. 2.26, where the magnitude of $i_d{}^*$ is controlled directly by a FW controller in order to regulate $|V|$. With reference to Fig. 2.25, both i_d and i_q would determine the magnitude and angle of vector i_s when using this control method. A dynamic limiter could be used to limit $i_q{}^*$ based on maximum allowable current and $i_d{}^*$ [95].
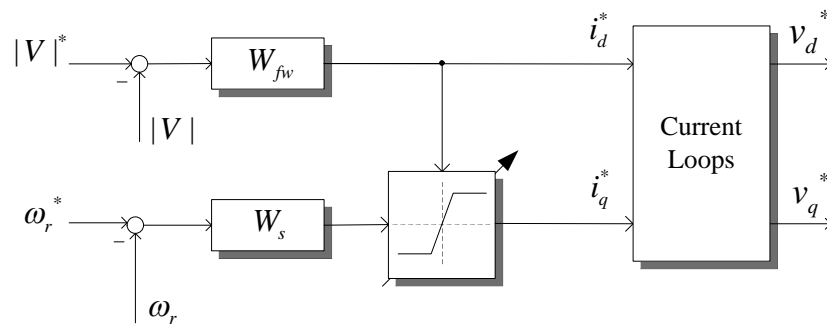
Fig. 2.26. Control structure with direct current FW method.

Studies in [61, 95, 104-114] looked into this method, while [115] and [116] did research into DTC. Radovan [117] introduced a hybrid method of FW control using direct current and analytical methods. Similar work has been done by Tae-Suk where a novel anti-windup strategy is proposed to improve the torque and voltage output of an SPM drive system [110]. Research has also been done on a five-phase PMM in [114].

The advantages are similar to the advanced angle method. It also solves the no load control disadvantage but introduces a new challenge: a cross link interaction may exist between $i_d{}^*$ and $i_q{}^*$ due to the use of the dynamic limiter. If more $i_d{}^*$ is requested when the maximum i_s has been reached during steady state operation, the dynamic limiter gives priority to $i_d{}^*$ and $i_q{}^*$ is reduced. This would affect the performance of the controller as insufficient active power is supplied to the loads.

2.6.3.4   Current Reference Modification Method

This method is mainly used in combination with additional control functions and can be divided into two parts; current optimisation and current reference modification. The first part makes use of model based equations for optimal current control within the constant torque region. The current optimisation function is used as part of the speed or torque drive control. Depending on the type of machine that is controlled, for example the IPM, there would be reluctance torque components that can be utilised if some i_d is provided. This current optimisation method is also known as maximum torque per ampere (MTPA). The second part determines the region where FW is required according to the voltage limit equations (2.2). i_d^* can then be determined based on the operating speed or $/V/$. Appropriate current changes denoted as Δi_d^* and Δi_q^* are injected into the respective reference current loops as shown in Fig. 2.27. Linear controllers can also be used for this current modification function.
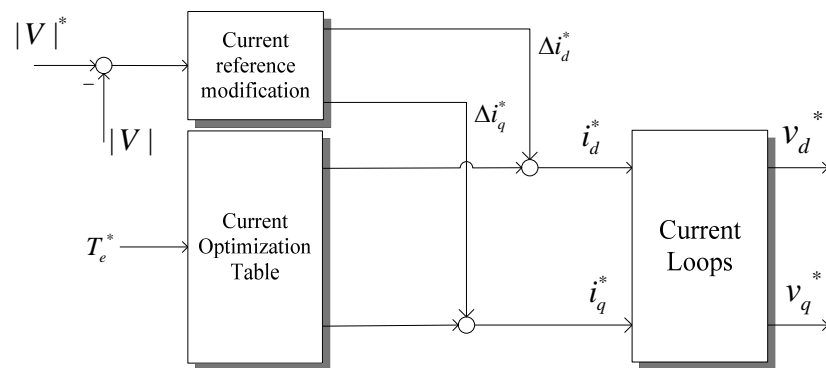
Fig. 2.27. Control structure with current reference modification method.

This FW method for high speed drive systems have been investigated in [62, 68, 118, 119]. Modification of both *dq* current references simultaneously provides flexibility in determining the current vector. However it is possible to achieve maximum torque during FW without using linear controllers. As this method uses model based equations similar to the analytic method, it has the same disadvantages.

2.6.3.5   Look-up Table Method

The look-up table method can be considered a variation of the analytic method, using equations to determine the control output. The difference is that the output values are computed beforehand and stored in look-up tables programmed into the microcontroller. When the drive system is in operation, the measured values are used to cross reference the appropriate reference values in the look-up tables. Appropriate reference values are then used for the inner current loops.

Control structures with current optimisation solutions such as MTPA can consider this method since they can easily be implemented in look-up tables. The tables can also be modified or expanded to consider the FW region [120-123]. It is also possible to create multi-dimensional tables to consider various control variables. An additional controller could be used to determine the value of machine flux for two dimensional look-up table based control schemes [120, 121, 123] as shown in Fig. 2.28.
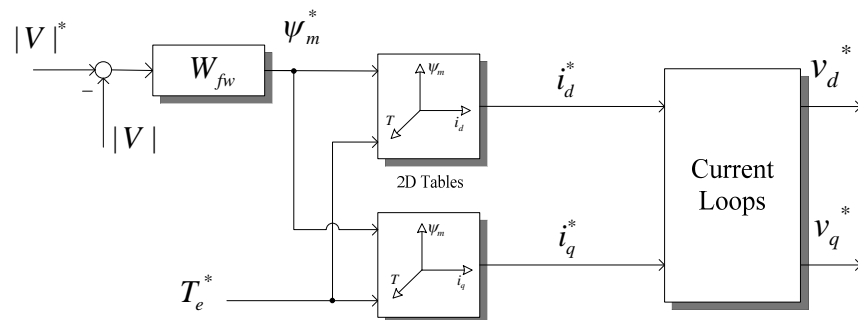
Fig. 2.28. Control structure with look up table method.

The advantage of this method is the reduced microcontroller computational time due to use of pre-calculated values. Its accuracy is defined by the resolution of the look-up table. However, if high accuracy is required, the large number of data to store would mean high memory requirements for the microcontroller. In addition, the data values are derived from parameter-dependent equations; hence this method would be sensitive to parameter variations.

2.6.3.6 Single Current Regulator Method

The methods detailed above control both active and reactive vectors using the *dq* current references. However, for high speed ratio FW (or deep FW), there may be instability issues resulting from current controller saturation and/or cross coupling effects [63]. A control method is proposed where only a single current regulator is used [63-65, 124, 125] as shown in Fig. 2.29. The regulator is designed to control active power while being capable of operating in deep FW regions. The single regulator also takes into account the total required current based on i_d^* and i_q^* to prevent controller saturation. The other current reference is not required and a constant output value is implemented. Usually it is set for a particular FW speed such that the drive system operates with optimal voltage and current levels when that operating point is reached.
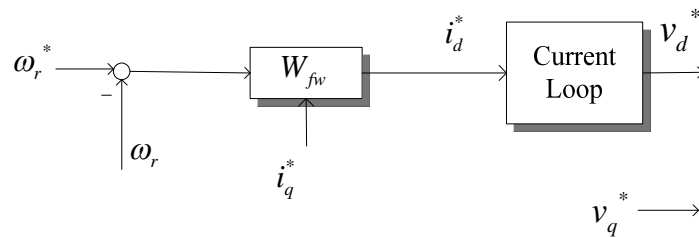
Fig. 2.29. Control structure with single current regulator method.

The advantage of this method is its simple structure, and utilisation of the cross coupling effect present in electrical machines in the control process. Furthermore, with an appropriate value of v_q^*, the electrical machine is capable of achieving high speed ratio FW. The downside of using a constant value of v_q^* is the efficiency and operational performance of the drive system, particularly around the base speed operating point. The torque capabilities would be limited, causing a slower acceleration process. Taiyuan [64] introduced a voltage limit equation in order to obtain variable v_q^* based on the maximum output voltage to alleviate this issue.

2.6.3.7   Model Predictive Control Method

The model predictive control (MPC) method is based on the mathematical equations of the drive system that is being controlled. The present state variables are used, with the drive system equations, to predict the future state of the control variables. The predicted states are then compared with their reference value using a cost function, *g, as* shown below:

$$g = \sum \left| x^* - x(k+n) \right| \tag{2.3}$$

where $x(k + n)$ is the predicted future state n sampling periods ahead and x^* is the reference value for that particular state in the discrete domain. For each possible switching state of the converter, there would be a different value of g. The switching state with the lowest g, which would therefore yield the lowest state variable error, is then selected and the corresponding switching combination is applied to the converter. This process can generally be considered the core process within MPC and the general control diagram can be seen in Fig. 2.30.
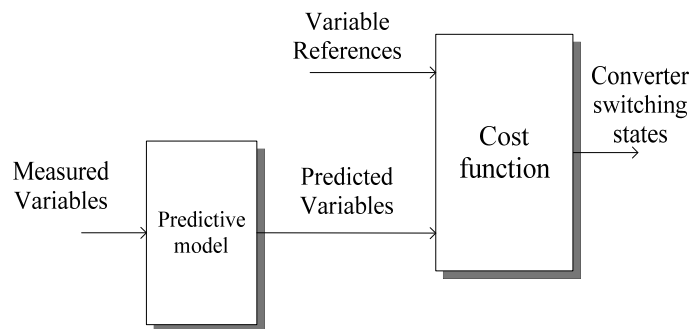
Fig. 2.30. Control structure with MPC method.

The advantages of this method are that no linear controller is required since it is replaced with the cost function and there is a high flexibility which allows modifications or extensions to control functions. It also has a very fast control response and is capable of controlling multiple variables within a single control loop [126, 127].

FW control using MPC is similar to the analytic method, relying on mathematical equations and its accuracy compared to the real plant. These equations

are added into the predictive model to predict the future state variables. [128] and [129] proposed combining this method with FOC and DTC respectively.

The main disadvantage of this approach is sensitivity towards parameter variations since it is model-based control. The accuracy of the model used for prediction affects the control performance. There are heavy computational requirements depending on the complexity of equations and depth of predictability.

2.6.4   Summary of Reviewed FW Methods

The advantages and disadvantages of the different FW methods are summarised in Table 2.5 for comparison purposes. Because of the possible parameter variations that could occur due to the wide operating range of the S/G power system, in terms of speed and temperature, model based FW methods are not considered. In addition, this may complicate the control scheme by adding estimators for parameter adaptation. The best candidates are the advanced angle and direct current methods due their robustness during parameter variations. Together with the use of linear controllers, load disturbances to the S/G system can be managed. Since the S/G may operate without load, especially in generator mode, the direct current method is chosen as the FW control method for the S/G power system investigated in this Thesis.

All published papers that use linear controllers for FW control provide a lack of detailed information regarding the implemented control design. Control schemes are introduced and stability analysis is performed but the design criteria for the FW controllers are often not clearly explained and the controller parameters are selected using "trial and error" methods [107]. This PhD study will address this gap by looking at different aspects of the FW control design for S/G systems, based-on a PMM machine fed by an AFE. This will be reported in Chapter 4 and 5.

Table 2.5. Advantages and disadvantages of various FW methods.

Method	Advantages	Disadvantages
Analytic	• Simple control implementation. • Expandable control structure.	• Sensitive towards parameter variations. • Cross coupling at high speeds (or extreme load cases).
Advanced angle	• Robust towards parameter variations.	• Unable to operate at no load conditions in FW zone.
Direct current	• Robust towards parameter variations.	• Cross coupling at high speeds (or extreme load cases).
Current reference modification	• Maximum torque control without linear controller.	• Sensitive towards parameter variations. • Filters may affect system performance.
Look up table	• Reduce offline computational time.	• High memory requirements. • Sensitive towards parameter variations.
Single current regulator	• Simple control structure. • Achieve high speed ratio FW.	• Lower operational efficiency below reference speed. • No current optimisation.
Model predictive control	• Expandable control structure. • No linear controller required.	• Heavy computational requirements. • Sensitive towards parameter variations. • Accuracy of mathematical model.

2.6.5   DC Link Voltage Control

When the electrical machine functions as a generator, the output voltage has to be controlled to maintain appropriate voltage levels for the electrical loads. The voltage is regulated to a constant reference value even when subjected to different load levels. In addition to that, the voltage transient has to reach steady state within a limited amount of time while not exceeding the voltage limits as defined in MIL-STD-704F. For 270VDC aircraft power systems the required transient envelope is shown in Fig. 2.31 [25].
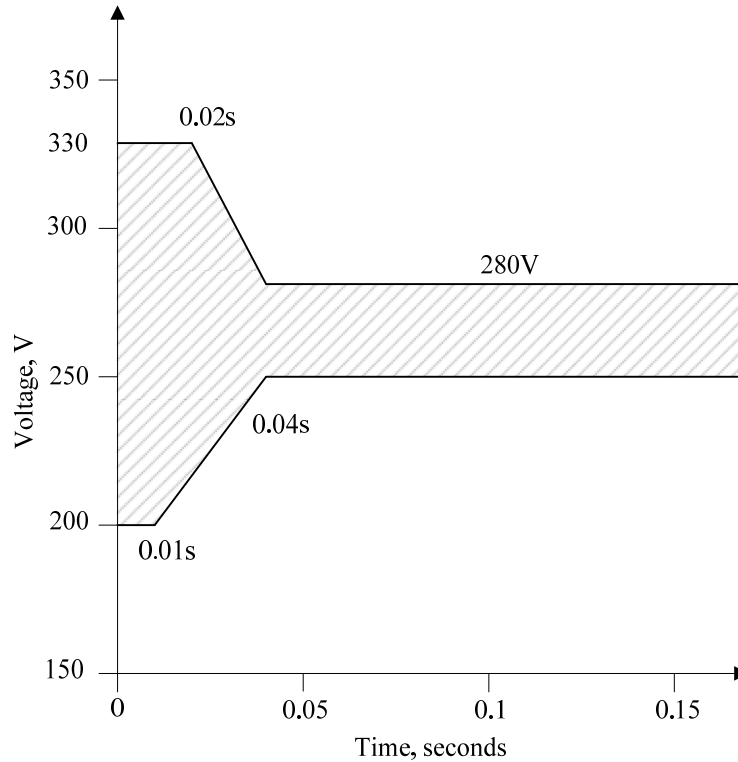
Fig. 2.31. Envelope of normal voltage transient for 270VDC system from MIL-STD-704F.

Studies of constant DC link voltage control have been done in [57, 62, 130]. The generator systems were fed by an AFE and demonstrated good DC link voltage control [62, 130]. After the voltage controller is established, analysis of the power system is investigated for potential stability issues. Stability analysis of aircraft power generation systems under varying electrical loads was investigated in [130]. Other parameters of the power system such as the DC link capacitance and speed were also varied to observe the operational limits with respect to the loads. Using the results of this analysis, the power system can then be optimised in order to improve stability margins. Constant DC link voltage control is effective for single power source systems, but multiple power sources in parallel require a different approach. Since the AEGART system will require the capability of operation in parallel with other on-board sources, appropriate control methods will also be investigated in this Thesis.

To prepare the S/G control scheme for possible parallel operation with multiple controlled power sources, droop control is used. Droop control allows multiple power sources to vary their power output based on dynamically changing loads [131]. The power variation for the AEGART S/G system can be expressed by the

current-voltage characteristic shown in Fig. 2.32. E_{dcmax} and E_{dcmin} are the maximum and minimum allowable voltage. i_{dcmax} is the maximum DC current at the rated active power, P_{rated}, when E_{dc} drops to E_{dcmin}. Their values are selected to meet the requirements of MIL-STD-704F and are stated in Table 2.6.
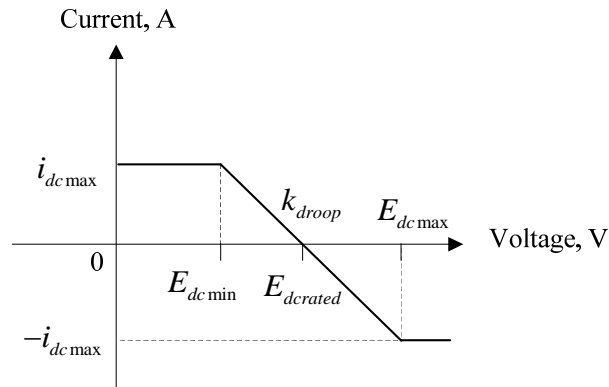
Fig. 2.32. Droop characteristic for AEGART power system.

The electrical loads of the aircraft are expressed in terms of current demand and then droop control is applied according to Fig 2.32. The voltage is allowed to vary within a tolerance band to avoid control conflict between multiple power sources. The variation of droop gain, k_{droop}, influences the power sharing ratio between the power sources shown in Fig. 2.33. For example, as k_{droop} increases, the voltage tolerance band becomes smaller, which restricts the amount of power to be shared by the system using this droop coefficient.

Table 2.6. Droop control parameters for AEGART power system.

Parameter	Value
Maximum DC link voltage, E_{dcmax}	280V
Minimum DC link voltage, E_{dcmin}	250V
Droop gain, k_{droop}	8.5
Maximum DC current at P_{rated}, i_{dcmax}	170A
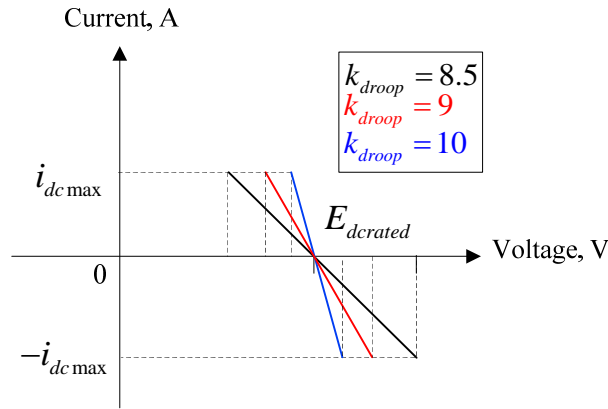
Fig. 2.33. Droop characteristics at different k_{droop}.

Droop control has been widely used in terrestrial microgrid systems [131-133] but has not yet been researched within aircraft applications. A possible configuration for parallel operation would involve multiple AEGART S/G systems, and other electrical power sources, being connected to a single aircraft DC bus. Power sharing between the sources would be achieved using droop control. This decentralised control method (each source having its own independent controller) would also have the advantage of no additional supervisory regulation being required for the overall power system. Electrical loads could be connected to the main aircraft bus and power would be inherently shared between the sources. However, some loads such as the motor controllers for ECS and flight actuators utilise power electronics that are tightly controlled. Such loads often behave like constant power loads and exhibit negative impedance characteristics that may influence the overall power system stability and power quality [134]. For this reason, studies of stability analysis have been performed during the AEGART project which considers multiple source topologies. At the time of writing, stability analysis of multiple S/G power systems utilising droop control is currently being investigated by Mr. Fei Gao at the University of Nottingham [135-137]. The work reported in this Thesis is related to [135-137] but focuses on S/G control design to enable multi-feed operation within an on-board electrical power system. This will be reported in Chapter 5.

In summary, the key points for the overall proposed control scheme are as follows:

- Speed control is required in starter mode to drive the aircraft engine to self-sufficient speed.

- When ω_{gmin} is achieved, the system should switch to generator mode with DC link control (voltage is controlled in standalone operation, or output current in paralleled operation).

- FW control is required for the investigated S/G system due to its wide speed operation range and machine-converter system design constraints.

- The direct current FW method is selected due to its robustness under parameter variation. There are no reports on rigorous and detailed procedures for FW controller design across both starter and generator modes.

- Analysis of DC link control during generator mode in S/G application is also lacking in current publications and will therefore be thoroughly investigated.

- Droop control will be utilised within the DC link control. This will facilitate parallel S/G operation in future aircraft electrical power systems.

These points are the main subjects of study in this Thesis and the key findings are reported in following Chapters.

2.7   Conclusion

This Chapter provided an overview of the current state-of-the-art in the area of aircraft electrical S/G systems. Electrical power generation has traditionally been performed by electric machine(s) interfaced to an accessory gearbox which is typically very costly, requires intensive maintenance and is unreliable. This Chapter has discussed solutions offered by the MEA concept including approaches to electric power generation, distribution and utilisation. For each of these categories, conventional solutions have been described and potential future alternatives, together with their potential advantages, have been overviewed. As discussed, the AEGART project will develop a novel power generation system. This will be based on a PMM due to its high power density. VF will be adopted due to its simplicity and ability to generate the required DC power with the help of an AFE. It also allows the PMM to be utilised as a S/G by controlling the electrical power flow to/from the aircraft electrical bus, depending on mode of operation. The electrical machine and power converter designed within the AEGART project form the subject of control design in this Thesis; these have been described along with its capabilities and operational limits. Based on the S/G operation, the general control requirements have been outlined in this Chapter i.e. speed has to be controlled in starter mode while DC link power is controlled in generator mode. For both cases FW control is important in order to maintain controllability of the power system. A detailed literature review has been performed for a selection of both FW control approaches and for DC link control methods. The latter is required to provide system capability for parallel operation with other sources. For FW control, the direct current method has been chosen for this application based on its given advantages. Overall, this Chapter has detailed the key targets of research in this Thesis and established the methodologies and topologies that will be used as a basis for the investigations in the following Chapters.

Chapter 3   PMM based Starter-Generator System as a Controlled Plant

3.1   Introduction

As discussed in Chapter 2, the S/G power system will utilise FOC. As part of the control design process, this Chapter will outline the control scheme (FW, speed, and DC link control) for FOC. The core plant for the FW and DC link control will be identified and corresponding mathematical models suitable for subsequent control analysis and design will be derived. Small signal analysis is used to linearise the plant of control. The derived plant models are verified by time-domain simulations against full-order non-linear models developed in Matlab®/Simulink®.

3.2   Reference Frame

The control scheme utilised in this research will be FOC, as discussed in the previous Chapter. The rotating reference, (or dq) frame, which is part of FOC will be detailed in this Section. Fig. 3.1 shows the phasor diagram of the three phase stationary and two phase rotating dq frames. $x_{a,b,c}$ represent the three phase frames, $x_{d,q}$ represent the dq frames, and θ is the angle between both frames.

The frame transformation from three phase to dq can be interpreted into a set of mathematical equations. If the d-axis is aligned with phase a ($x_d = x_a$) as a reference point for both frames, then:

$$\begin{bmatrix} x_d \\ x_q \end{bmatrix} = k_{dq} \begin{bmatrix} x_a \\ x_b \\ x_c \end{bmatrix} \tag{3.1}$$

$$k_{dq} = \frac{2}{3} \begin{bmatrix} \cos(\theta) & \cos\left(\theta - \dfrac{2\pi}{3}\right) & \cos\left(\theta + \dfrac{2\pi}{3}\right) \\ -\sin(\theta) & -\sin\left(\theta - \dfrac{2\pi}{3}\right) & -\sin\left(\theta + \dfrac{2\pi}{3}\right) \end{bmatrix} \tag{3.2}$$
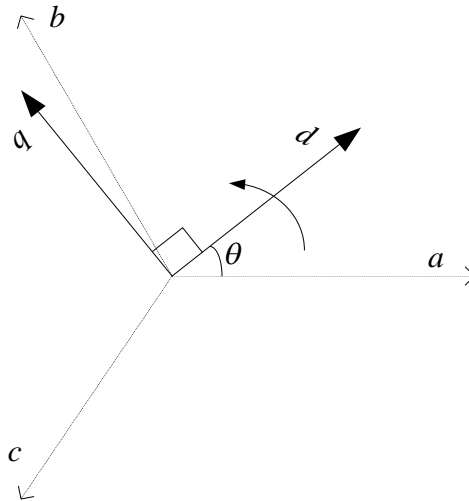
Fig. 3.1. Three phase and *dq* phasor diagram.

The transformation that is used for this control assumes balanced three phase components. Peak notation is used where the *dq* peak values are equal to the variable three phase magnitudes. It is then easier to analyse the magnitude of the control variables in the power system between both frames. However, it is the power variant which means that the power calculated in the *dq* frame is 2/3 of the power in three phase frame. The inverse transformation back to three phase frame is in Appendix A. The next Section explains the control approach utilised for the S/G system.

3.3   Control Approach

The control concept for the S/G system can be explained with the help of an *RL* circuit connected between two AC voltage sources V_C and V_M, as shown in Fig. 3.2. *R* and *L* represent the resistive and inductive elements between AC voltage sources.
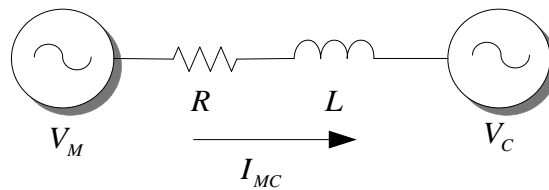
Fig. 3.2. *RL* circuit with two voltage sources.

The phasor diagram shown in Fig. 3.3 represents the current vector I_{MC} when the dq reference frame is aligned with voltage vector V_M. V_{MC} is the voltage across RL resulting from current I_{MC}. V_d, V_q, I_d, and I_q are the voltages and currents in the dq frame.
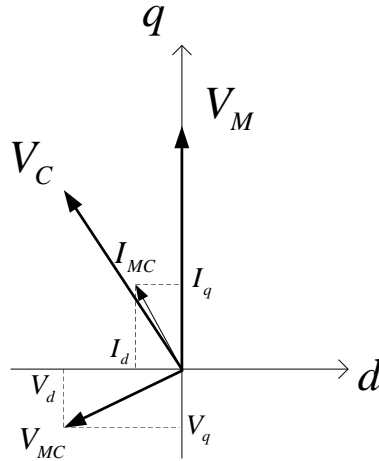
Fig. 3.3. Phasor diagram of RL circuit.

The complex power, S, can be written as [138]:

$$S = V_{MC} I_{MC}^* = P + jQ \tag{3.3}$$

where P and Q are the active and reactive components of S. V_{MC} and I_{MC} can be equated as:

$$V_{MC} = -V_q - jV_d \tag{3.4}$$

$$I_{MC}^* = I_q - jI_d \tag{3.5}$$

The product of these vectors yields:

$$S = -\left(V_q I_q + V_d I_d\right) + j\left(V_q I_d - V_d I_q\right) \tag{3.6}$$

For power converter systems, it is common to orient the active voltage vector (V_M in this case) to the d-axis. Drive systems however usually have the rotor flux aligned with the d-axis as in this case the θ used for the dq transformation can refer to the machine rotor position. This is useful as it is usually measured [46, 138]. When the q-axis is aligned to V_M, then V_d is seen to be zero and the powers are simplified to:

$$P = -V_q I_q \tag{3.7}$$

$$Q = V_q I_d \tag{3.8}$$

This means that active and reactive power can be independently controlled by I_d and I_q assuming constant voltage magnitude. The values of I_d and I_q can be set to produce the desired complex power through the RL circuit. Changing the direction of I_q changes the direction of active power flow between V_C to V_M. This is important for the control of the S/G system. If V_M is the machine and V_C is the power converter, then active power can be controlled towards the direction of the machine (starter) or to the power converter (generating).

In the S/G system, the machine stator currents should be controlled in order to achieve the required power flow control as explained earlier. Using classic PI controllers, the machine stator currents are controlled in the *dq* frame as shown in Fig. 3.4. In starter mode, speed is controlled by the outer control loop which determines i_q^* for the internal current loop. It is then replaced by a DC link control loop to regulate E_{dc} when the power system goes into generator mode. The FW loop regulates the stator magnitude voltage, |V|, during both modes and its output determines i_d^*. |V| is calculated from the control output *dq* voltages with the assumption that the actual voltages are similar to the reference signals.

The controllers can be designed to achieve specific performance if the plant of control is known [139]. The plant can be mathematically formed if the equations of the power system are known. As mentioned in Section 2.5, the difference in control structure for S/G operation is the outer control loops. Hence, the core plant of control to be derived should also include the current loops. The core plant is depicted in Fig. 3.4. It includes the machine, the converter, and the current control loops. The engine model is not part of this research with the assumption that the mechanical dynamics are much slower than the electrical response. Hence the engine is considered as an external ideal speed source.
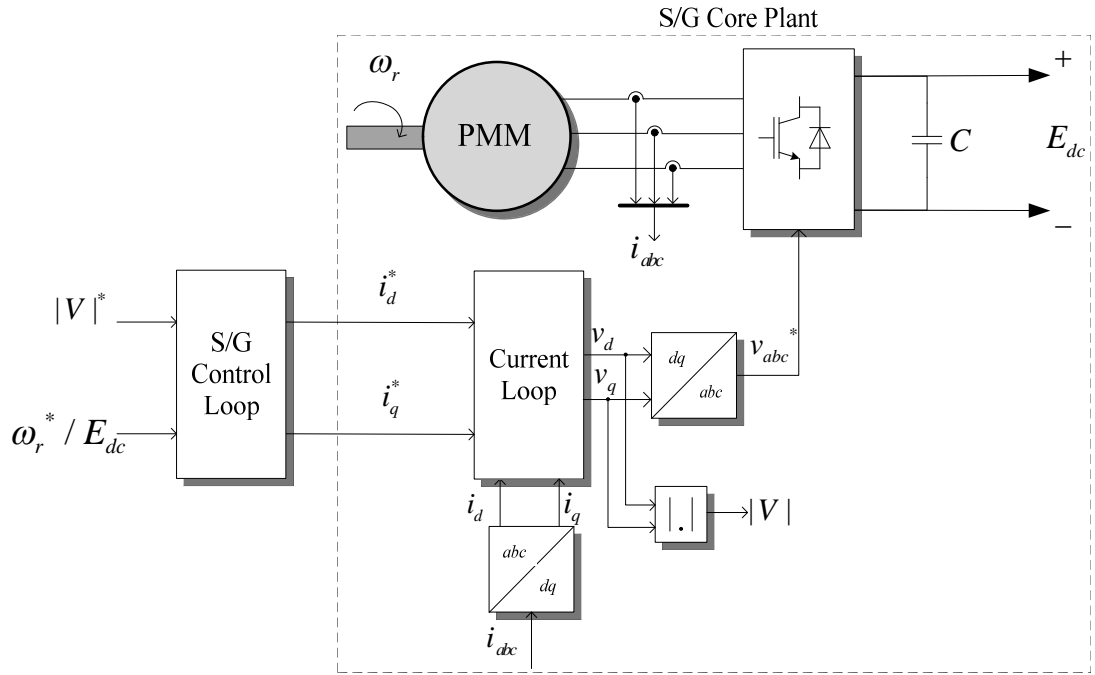
Fig. 3.4. Control scheme for proposed S/G system.

3.4   S/G System Model in *dq* Frame

The equations of the machine, converter, DC link, and current loops are introduced below in order to prepare for the core plant derivation. The equations of the power system are all written with respect to the *dq* frame for consistency of analysis. Fig. 3.5 shows the equivalent circuit of the PMM after conversion to *dq* frame [140]. R_s is the stator resistance, i_f is the equivalent permanent magnet field current, and ω_e is the electrical speed of the machine. $L_{ld,q}$ and $L_{md,q}$ are leakage and magnetising inductances in *dq* frame. $\Psi_{d,q}$ are the flux linkages in *dq* frame. Since the PMM is surface mounted, it is non-salient and the *dq* inductances are the same ($L_d = L_q$).
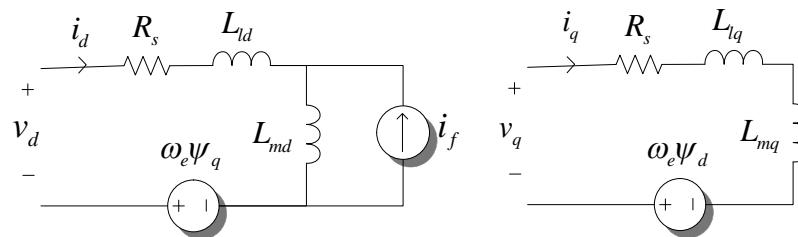
Fig. 3.5. Equivalent electrical circuit of a PMM aligned at *d*-axis (left) and *q*-axis (right).

The machine electrical equations can be re-arranged and represented by the following equations [140]:

$$L_d = L_{ld} + L_{md} \tag{3.9}$$

$$L_q = L_{lq} + L_{mq} \tag{3.10}$$

$$\psi_m = L_{md} i_f \tag{3.11}$$

$$\psi_d = (L_{ld} + L_{md})i_d + L_{md} i_f \tag{3.12}$$

$$\psi_q = (L_{lq} + L_{mq})i_q \tag{3.13}$$

to obtain [46]:

$$v_d = R_s i_d + L_d \frac{di_d}{dt} - L_q \omega_e i_q \tag{3.14}$$

$$v_q = R_s i_q + L_q \frac{di_q}{dt} + (L_d i_d + \psi_m)\omega_e \tag{3.15}$$

The machine torque and speed can be derived as [46]:

$$T_e = \frac{3}{2} p\left(\psi_m i_q + i_d i_q \left(L_d - L_q\right)\right) \tag{3.16}$$

$$k_t = \frac{3}{2} p\psi_m \tag{3.17}$$

$$J\frac{d\omega_r}{dt} = T_e - T_L \tag{3.18}$$

$$\omega_e = p\omega_r \tag{3.19}$$

where k_t is the torque constant, J is the machine inertia, and T_L is the load torque.

For this Thesis, a two-level converter (Fig. 3.6) is considered instead of a three-level converter (Fig. 2.18) in order to simplify the S/G system since the purpose of this research is to design and test the designed control scheme. Another reason is the availability of the two-level converter for experimental validation, as will be detailed

in Chapter 7. The current control procedure for a two-level and three-level converter may be slightly different, but the overall function is the same.
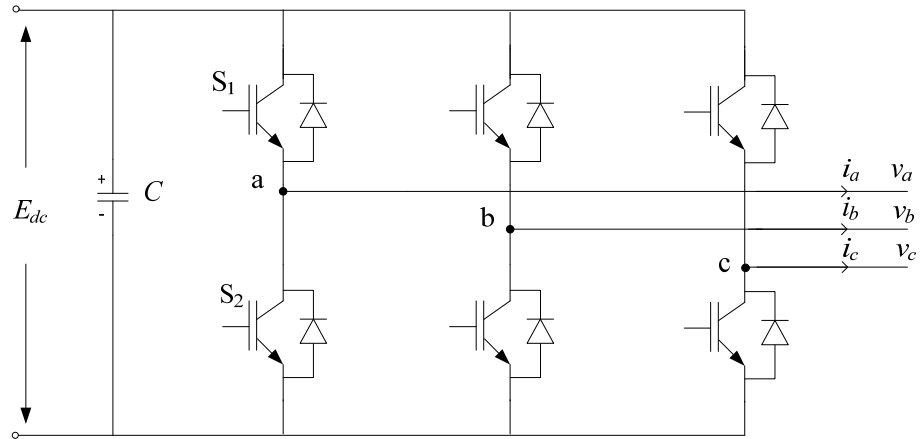
Fig. 3.6. Two-level AFE converter.

The switching power converters are discontinuous in nature and could complicate the control design process. However, analysis of the power converter can be simplified if only the average model is considered. The average model equation of a power converter can be represented by a complex power equation in the *dq* frame [138]:

$$E_{dc}i_{dc} = -\frac{3}{2}\left(v_d i_d + v_q i_q\right)$$
(3.20)

The negative sign denotes the direction of i_{dc} when it is measured. Positive i_{dc} is defined as power supplied to the DC link bus while negative is towards the machine side. The DC link bus equation can be equated as:

$$C\frac{dE_{dc}}{dt} = i_{dc} - i_L$$
(3.21)

where i_L is the general notation for electrical loads connected to the DC link bus. $|V|$ can be determined by:

$$|V| = \sqrt{v_d^2 + v_q^2}$$
(3.22)

The next Sub-section will detail the design of the current controllers. This is important for the main control scheme and also for derivation of the core plant.

3.4.1 Current Controller Design

The next stage is to design the current controllers of the S/G power system. Fig. 3.7 shows the *dq* current loops and their respective control plant. The plants are based on the machine equations (3.14) and (3.15). If the feedforward terms within the current control plant are compensated, then it can be reduced to a first order transfer function:

$$\frac{i_d}{v_d} = \frac{1}{L_d s + R_s} \tag{3.23}$$

$$\frac{i_q}{v_q} = \frac{1}{L_q s + R_s} \tag{3.24}$$

The current PI controllers can be represented in the transfer function form:

$$W_{cd}(s) = k_{pd} + \frac{k_{id}}{s} \tag{3.25}$$

$$W_{cq}(s) = k_{pq} + \frac{k_{iq}}{s} \tag{3.26}$$

where k_{pd}, k_{pq}, k_{id} and k_{iq} are the current controller proportional and integral gains.
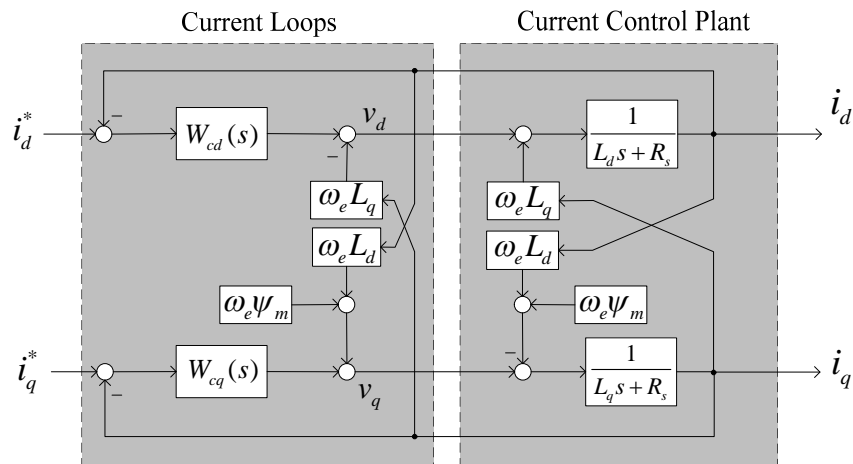
Fig. 3.7. Current loops with corresponding control plant.

The plant with the controller, in a negative feedback loop, creates a closed loop transfer function.

$$\frac{i_d}{i_d^*} = \frac{k_{pd}s + k_{id}}{L_d s^2 + \left(R_s + k_{pd}\right)s + k_{id}} \tag{3.27}$$

$$\frac{i_q}{i_q^*} = \frac{k_{pq}s + k_{iq}}{L_q s^2 + \left(R_s + k_{pq}\right)s + k_{iq}} \tag{3.28}$$

The denominator of the closed loop transfer function mainly determines the dynamic response of the controlled variable. The controller gains can then be tuned such that it is similar to a desired second order response generally written as:

$$\frac{\omega_n^2}{s^2 + 2\zeta\omega_n s + \omega_n^2} \tag{3.29}$$

$$2\zeta\omega_n = \frac{R_s + k_{pd}}{L_d} = \frac{R_s + k_{pq}}{L_q} \tag{3.30}$$

$$\omega_n^2 = \frac{k_{id}}{L_d} = \frac{k_{iq}}{L_q} \tag{3.31}$$

where ζ is the damping ratio and ω_n is the natural bandwidth. In general, the selection of control bandwidth for the currents is preferred to be as fast as possible in order to achieve good performance for the outer loop controllers. For this system, the current controllers are designed to have 1kHz bandwidth. The selection of this bandwidth is well within the power converter switching frequency of 16kHz. Current control design for drive systems with linear controllers is well established [43]. The desired current response requirements are $\zeta =0.707$ and $\omega_n =2\pi \times 1000$Hz and the controller gains are calculated to be $k_{pd} = k_{pq} = 0.8785$ and $k_{id} = k_{iq} = 3908$. Fig. 3.8 shows the *dq* current responses to a step reference. It shows that the designed response is achieved as the current reaches steady state within 1ms (or 1kHz). The damping ratio was found to be about 0.5 due to the presence of a zero in the transfer function of the controller, as seen in (3.27) and (3.28), this results in a greater overshoot within the transient response.
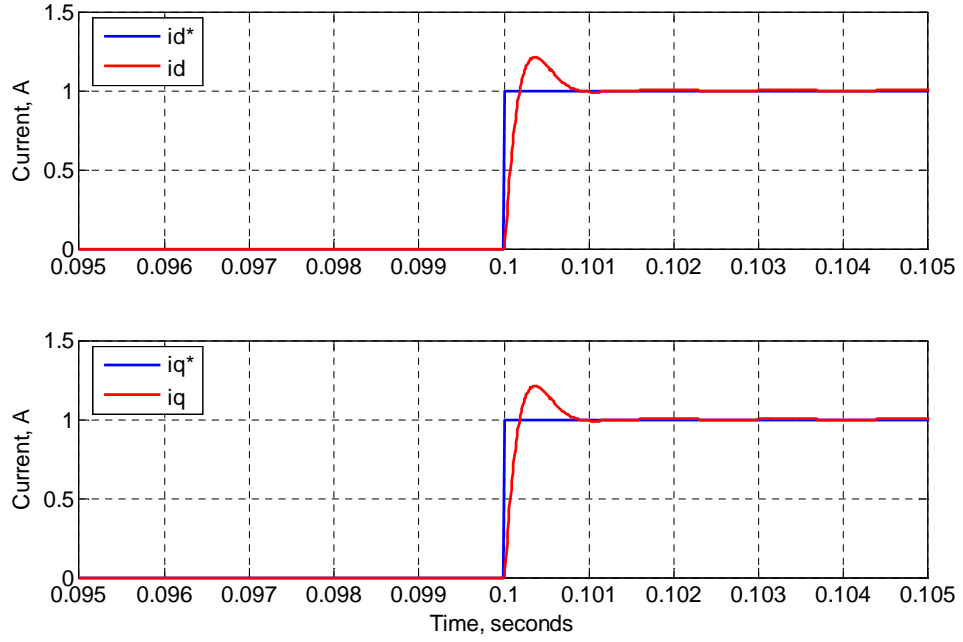
Fig. 3.8. Closed loop response of the *dq* current controllers to a step of 1A at $t = 0.1$s.

3.5 Core Plant Model

The equations of the machine, converter, DC link, and current loops have now been established. Therefore the core plant for the S/G control loop can be derived. Due to non-linearities in (3.14), (3.15), (3.20) and (3.22), the equations are linearised using Taylor's series expansions around a particular operating point. The equations that have non-linearities are therefore linearised to:

$$\partial v_d = R_s \partial i_d + L_d s \partial i_d - L_q \omega_{eo} \partial i_q - L_q i_{qo} \partial \omega_e \tag{3.32}$$

$$\partial v_q = R_s \partial i_q + L_q s \partial i_q + L_d \omega_{eo} \partial i_d + \left(L_d i_{do} + \psi_m \right) \partial \omega_e \tag{3.33}$$

$$\partial \left| V \right| = \frac{v_{do}}{\left| V \right|_o} \partial v_d + \frac{v_{qo}}{\left| V \right|_o} \partial v_q \tag{3.34}$$

$$\partial i_{dc} = \begin{bmatrix} -\dfrac{3}{2E_{dco}} \left(i_{do} \partial v_d + v_{do} \partial i_d + i_{qo} \partial v_q + v_{qo} \partial i_q \right) \\[2mm] +\dfrac{3}{2E_{dco}^{\ 2}} \left(i_{do} v_{do} + i_{qo} v_{qo} \right) \partial E_{dc} \end{bmatrix} \tag{3.35}$$

71

The variables with subscript o represent steady state values around a particular operating point. The linearised equations for the core plant are split according to the starter and generator modes shown in Fig. 3.9 and Fig. 3.11 respectively. The starter mode FW and speed controllers are included. In generator mode, FW and DC link voltage controllers are included. FW control is therefore always be active for both modes; hence only the DC link voltage control plant needs to be derived in generation mode.
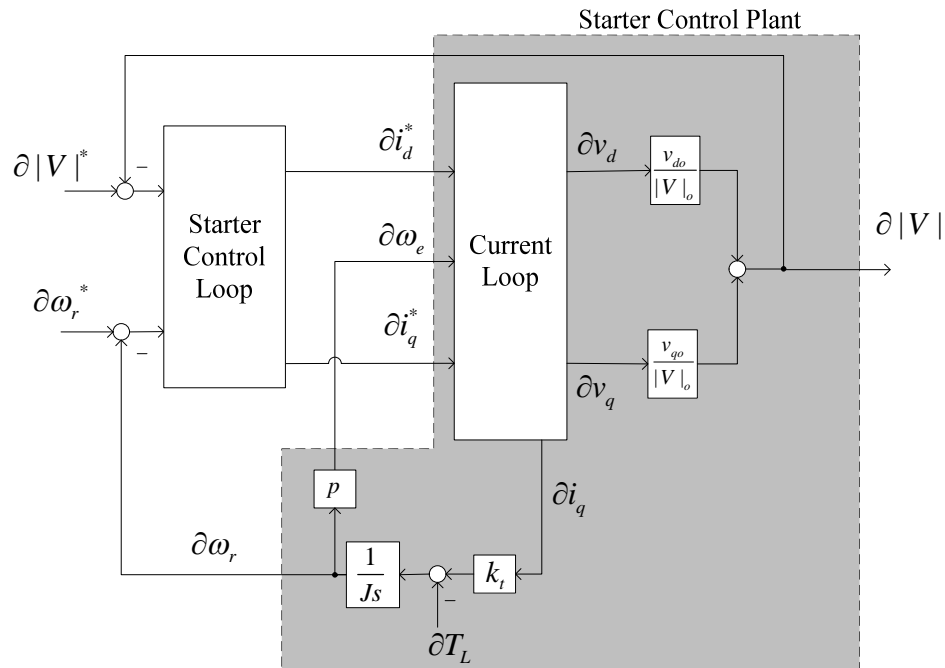
Fig. 3.9. Starter mode controls.

3.5.1 Speed Control Plant

From Fig. 3.9, it can be seen that the control plant for speed loop requires the electromechanical torque equation along with the i_q current loop. Some assumptions are customary when deriving the control plant for the speed loop [47]:

- The bandwidth of the speed controller is chosen to be much slower than the i_q loop, hence i_q for the speed control design is assumed to be equal to i_q^*.

- There is no reluctance torque generated since the machine is non-salient ($L_d = L_q$), which means that T_e is proportional to i_q.

- No form of disturbance is introduced during the control design, e.g., $T_L = 0$.

The equation for the speed control plant can then be derived as:

$$\frac{\partial \omega_r}{\partial i_q^*} = \frac{k_t}{Js}$$
(3.36)

The structure of the speed control plant can be seen in Fig. 3.10.

$$\partial i_q^* \quad \boxed{\dfrac{k_t}{Js}} \quad \partial \omega_r$$
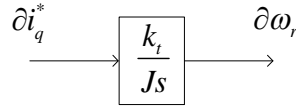
Fig. 3.10. Plant of control for speed controller.

3.5.2 FW Control Plant

The plant for the FW loop is more complex, covering dynamics of the machine and full current loops. Since the output of the plant is $|V|$, equation (3.34) can be used as a starting point to derive the plant. Replacing ∂v_d and ∂v_q yields:

$$\partial |V| = \frac{1}{|V|_o} \begin{bmatrix} v_{do}\left(\left(R_s + L_d s\right)\partial i_d - \omega_{eo}L_q \partial i_q - i_{qo}L_q \partial \omega_e\right) + \\ v_{qo}\left(\left(R_s + L_q s\right)\partial i_q + \omega_{eo}L_d \partial i_d + \left(L_d i_{do} + \psi_m\right)\partial \omega_e\right) \end{bmatrix}$$
(3.37)

The equation can be rearranged in terms of ∂i_d, ∂i_q, and $\partial \omega_e$:

$$\partial |V| = \frac{1}{|V|_o} \begin{bmatrix} \left(v_{do}\left(R_s + L_d s\right) + v_{qo}\omega_{eo}L_d\right)\partial i_d \\ +\left(-v_{do}\omega_{eo}L_q + v_{qo}\left(R_s + L_q s\right)\right)\partial i_q \\ +\left(-v_{do}i_{qo}L_q + v_{qo}\left(L_d i_{do} + \psi_m\right)\right)\partial \omega_e \end{bmatrix}$$
(3.38)

Since the closed loop current dynamics are related to the plant, ∂i_d and ∂i_q can be changed to ∂i_d^* and ∂i_q^* respectively. Considering the closed loop current transfer functions (3.27) and (3.28):

$$\frac{\partial i_d}{\partial i_d^*} = \frac{1}{L_d} \frac{\left(2\xi\omega_n L_d - R_s\right)s + \omega_n^2 L_d}{s^2 + 2\xi\omega_n s + \omega_n^2}$$

(3.39)

$$\frac{\partial i_q}{\partial i_q^*} = \frac{1}{L_q} \frac{\left(2\xi\omega_n L_q - R_s\right)s + \omega_n^2 L_q}{s^2 + 2\xi\omega_n s + \omega_n^2}$$

(3.40)

$\partial|V|$ would then be a function of ∂i_d^*, ∂i_q^*, and $\partial\omega_e$. The overall transfer function can be visualised in Fig. 3.11.
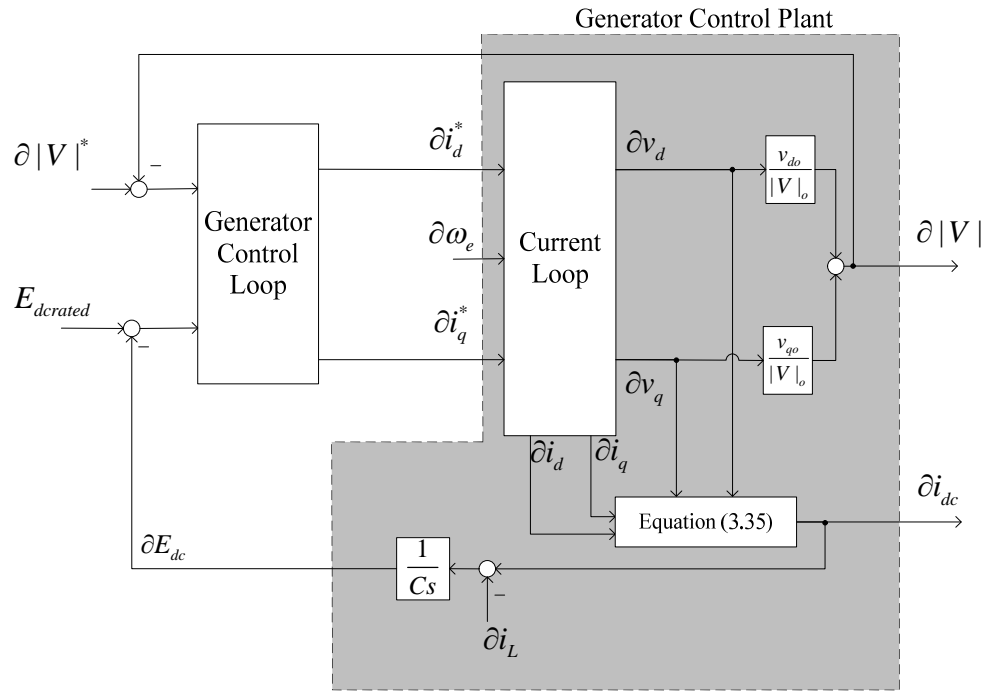
Fig. 3.11. Generator mode controls.

3.5.3   DC Link Control Plant

The DC link controller will utilise droop control, as defined earlier in Section 2.6.5. The control variable will be i_{dc} in order to regulate changes caused by load currents. E_{dc} is monitored to provide droop reference to the DC link controller based on the load changes. Therefore, the output of this control plant will be i_{dc} instead of E_{dc}. Details of the DC link controller will be presented in Chapter 5. The plant for DC link control can be derived from equation (3.35) and then be expanded by using (3.32), (3.33), and (3.21):

74

$$\left(\frac{2E_{dco}^2 Cs - 3\left(v_{do}i_{do} + v_{qo}i_{qo}\right)}{2E_{dco}^2 Cs} \right) \partial i_{dc} = \frac{3}{2E_{dco}} \left[\begin{array}{c} -\left(v_{do}\partial i_d + i_{do}\left(\begin{array}{c} \left(R_s + L_d s\right)\partial i_d - \omega_{eo}L_q \partial i_q \\ -i_{qo}L_q \partial \omega_e \end{array} \right)\right) \\ -\left(v_{qo}\partial i_q + i_{qo}\left(\begin{array}{c} \left(R_s + L_q s\right)\partial i_q + \omega_{eo}L_d \partial i_d \\ +\left(L_d i_{do} + \psi_m\right)\partial \omega_e \end{array} \right)\right) \end{array} \right]$$

$$(3.41)$$

Rearranged in terms of ∂i_d, ∂i_q, and $\partial \omega_e$:

$$\partial i_{dc} = \frac{3E_{dco}Cs}{2E_{dco}^2 Cs - 3\left(v_{do}i_{do} + v_{qo}i_{qo}\right)} \left[\begin{array}{c} -\left(-i_{do}\omega_{eo}L_q + v_{qo} + i_{qo}\left(R_s + L_q s\right)\right)\partial i_q \\ -\left(i_{qo}\omega_{eo}L_d + v_{do} + i_{do}\left(R_s + L_d s\right)\right)\partial i_d \\ -\left(-i_{do}i_{qo}L_q + i_{qo}\left(L_d i_{do} + \psi_m\right)\right)\partial \omega_e \end{array} \right] \quad (3.42)$$

∂i_d and ∂i_q are changed to ∂i_d^* and ∂i_q^* respectively using transfer function (3.39) and (3.40). Overall, the control plants derived for FW and DC link control can be arranged as a multivariable matrix relating the outputs to the inputs:

$$\begin{bmatrix} \partial |V| \\ \partial i_{dc} \end{bmatrix} = \begin{bmatrix} f_{11} & f_{12} & f_{13} \\ f_{21} & f_{22} & f_{23} \end{bmatrix} \begin{bmatrix} \partial i_d^* \\ \partial i_q^* \\ \partial \omega_e \end{bmatrix} \quad (3.43)$$

where

$$f_{11} = \frac{\partial |V|}{\partial i_d^*} = \frac{1}{L_d} \frac{\left(2\xi\omega_n L_d - R_s\right)s + \omega_n^2 L_d}{s^2 + 2\xi\omega_n s + \omega_n^2} \left[\frac{v_{do}}{|V|_o}\left(R_s + L_d s\right) + \frac{v_{qo}}{|V|_o}\omega_{eo}L_d \right]$$

$$f_{12} = \frac{\partial |V|}{\partial i_q^*} = \frac{1}{L_q} \frac{\left(2\xi\omega_n L_q - R_s\right)s + \omega_n^2 L_q}{s^2 + 2\xi\omega_n s + \omega_n^2} \left[-\frac{v_{do}}{|V|_o}\omega_{eo}L_q + \frac{v_{qo}}{|V|_o}\left(R_s + L_q s\right) \right]$$

$$f_{13} = \frac{\partial |V|}{\partial \omega_e} = \frac{1}{|V|_o} \left[-v_{do}i_{qo}L_q + v_{qo}\left(L_d i_{do} + \psi_m\right) \right]$$

$$f_{21} = \frac{\partial i_{dc}}{\partial i_d^*} = \frac{1}{L_d} \frac{\left(2\xi\omega_n L_d - R_s\right)s + \omega_n^2 L_d}{s^2 + 2\xi\omega_n s + \omega_n^2} \left[\frac{-3E_{dco}Cs\left(i_{qo}\omega_{eo}L_d + v_{do} + i_{do}\left(R_s + L_d s\right)\right)}{2E_{dco}^2 Cs - 3\left(v_{do}i_{do} + v_{qo}i_{qo}\right)} \right]$$

$$f_{22} = \frac{\partial i_{dc}}{\partial i_q^{\cdot *}} = \frac{1}{L_q} \frac{\left(2\xi\omega_n L_q - R_s\right)s + \omega_n^2 L_q}{s^2 + 2\xi\omega_n s + \omega_n^2} \left[\frac{-3E_{dco}Cs\left(-i_{do}\omega_{eo}L_q + v_{qo} + i_{qo}\left(R_s + L_q s\right)\right)}{2E_{dco}^2 Cs - 3\left(v_{do}i_{do} + v_{qo}i_{qo}\right)} \right]$$

$$f_{23} = \frac{\partial i_{dc}}{\partial \omega_e} = \frac{-3E_{dco}Cs\left(-i_{do}i_{qo}L_q + i_{qo}\left(L_d i_{do} + \psi_m\right)\right)}{2E_{dco}^2 Cs - 3\left(v_{do}i_{do} + v_{qo}i_{qo}\right)}$$

It can be seen in Fig. 3.12 that the plants to be controlled have cross linked interaction between ∂i_d^*, ∂i_q^*, and $\partial \omega_e$. This is due to the feed forward terms in the PMM electrical equations creating closely coupled dynamics between the *dq* currents. As a result, the plant may be more complex when the interactions are combined together to accommodate single input single output (SISO) controllers.
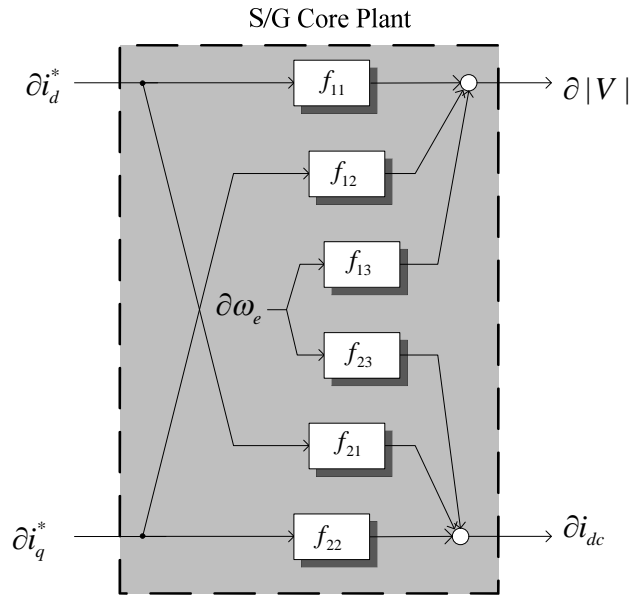
Fig. 3.12. Block diagram of the derived S/G plant.

3.5.4 S/G Plant Model Verification

Before the plants for the FW and DC link controllers are further analysed, they will be verified with non-linear equivalent models. These models are simulated in the Matlab®/Simulink® environment. The block diagrams used to represent the S/G power system can be found in Appendix C. The non-linear model is built with relevant non-linear equations and the PMM block available in the Simpower Systems toolbox. An operating point is usually selected with respect to the speed of the PMM because in drive systems it determines the electrical frequency of the system. The

operating points are obtained from the equations in steady state operation ($s = 0$). The derived plants are verified by comparison with the non-linear model built in Simulink. The operating points are given in Table 3.1.

Table 3.1. Operating point for plant verification.

Parameter	Operating point for f_{11}, f_{12}, f_{13}	Operating point for f_{21}, f_{22}, f_{23}
v_{do}	-38.1V	48.8V
v_{qo}	151.2V	148V
$|V|_o$	155.9V	155.9V
i_{do}	-125.2A	-129.9A
i_{qo}	61A	-78.7A
ω_{eo}	6283rad/s	6283rad/s
E_{dco}	270V	270V

At those operating points, the transfer functions are calculated to be:

$$f_{11} = \frac{-0.21452(s - 2.494 \times 10^4)(s + 4449)}{s^2 + 8884s + 3.948 \times 10^7} \tag{3.44}$$

$$f_{12} = \frac{0.8519(s + 1593)(s + 4449)}{s^2 + 8884s + 3.948 \times 10^7} \tag{3.45}$$

$$f_{13} = 0.0248 \tag{3.46}$$

$$f_{21} = \frac{0.63426s(s + 21.37)(s + 4449)}{(s + 308.6)(s^2 + 8884s + 3.948 \times 10^7)} \tag{3.47}$$

$$f_{23} = \frac{0.016s}{(s + 308.6)} \tag{3.48}$$

$$f_{22} = \frac{0.38421s(s - 2.936 \times 10^4)(s + 4449)}{(s + 308.6)(s^2 + 8884s + 3.948 \times 10^7)} \tag{3.49}$$

The step response verification for the multivariable plant can be seen in Fig. 3.13. It can easily be seen that the outputs are identical to the non-linear model. This verifies the multivariable plant.

It can be seen in f_{11} and f_{22} that there are fast positive zeros at 2.494×10^4 and 2.936×10^4 respectively. A positive zero causes an opposing response to the input and its dynamics depend on its position on the plane [138]. This effect can be seen in Fig. 3.13 for f_{11} and f_{22}. The non-minimum phase characteristic may limit the stability range of the entire system and hence it is all the more important to analyse the plant during the control design phase in the following Chapters.

Summarising this Section, the core S/G plant has been derived for speed, FW, and DC-link control design. Verification of the plant has been carried out by comparing the step response of the plant with the non-linear equivalent model in Matlab®/Simulink®. The plant derivation is important as it will allow detailed analysis of the S/G controllers to be developed in Chapter 4 and 5. Non-minimum phase characteristics were observed in part of the S/G plant, which may limit the stability range of the entire system. Investigation of the plant across the whole S/G operational range will be carried out in Chapter 4 and 5 in order to study its behaviour. The information obtained will then be used to design the controllers and ensure a stable response throughout the S/G operational range.
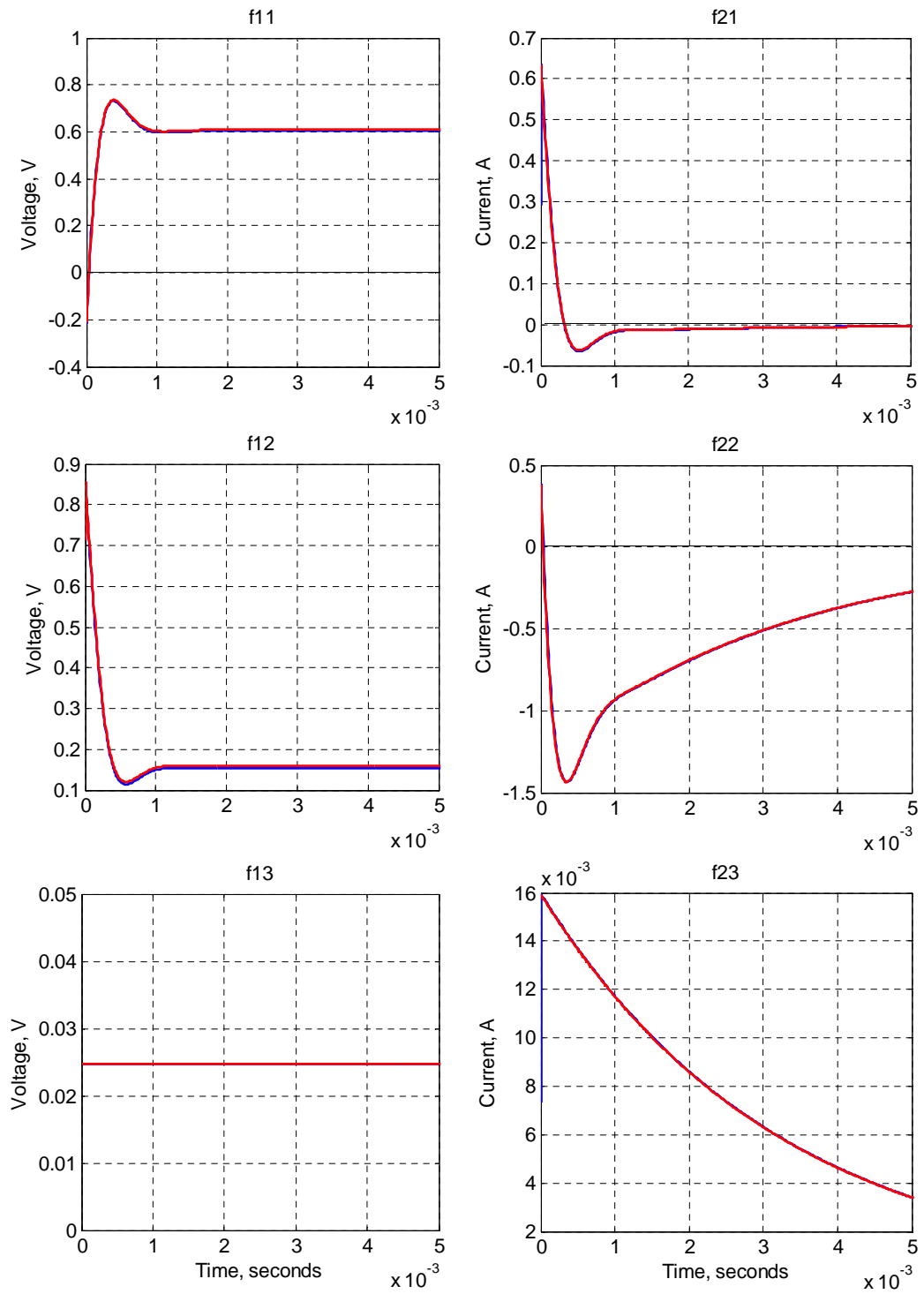
Fig. 3.13. Step response comparison between the S/G core plant transfer functions (blue) and the equivalent non-linear model (red). The step inputs are $\partial i_d^* = \partial i_q^* = 1\text{A}$, $\partial \omega_e = 1\text{rad/s}$.

3.6   Analysis of Sampling Time and Delay Effects

So far, the current controller design and the overall S/G plant analysis has assumed ideal feedback control using continuous time transfer functions without delays. For some systems, the effect of having discrete time plants with delays maybe negligible while for others it could be significant. The control performance can be affected due to a delayed control signal or a delayed measurement of a variable. The dynamic response of the plant can differ when the calculated control signal is applied at a later time period where it is no longer optimal. For discrete time systems, the sample ratio is also important as it relates the sampling time to the frequency of the controlled plant. A high sample time ratio yields more sample points which yields better control performance compared to a lower ratio. Since the AEGART S/G system can operate up to 32krpm, signals with equivalent electrical frequencies of 1.6kHz have to be processed by the controller. In relation to the selected PWM switching frequency of 16kHz, the lowest sample time ratio is therefore 10. The combination of low sample time ratio and delay effects results is lesser control accuracy due to the small number of sample points and hence more significant delays.

Furthermore, the S/G system has non-minimum phase elements, as seen by the positive zero in (3.44) and (3.49), these result in a limited stability range for the controllers. The characteristics of discretised positive zeroes are similar to zeroes in the continuous domain, i.e. they cause an opposite initial response as seen in Fig. 3.13 for f_{11} and f_{22}. Depending on the S/G operating point, the position of the zero varies. In combination the effect of discretisation, delay and the presence of this positive zero may worsen the stability of the designed controllers.

Fig. 3.14 shows a typical digital control negative feedback loop with delay blocks. k represents the current instant time, t, in discrete domain. r, u, and y are the reference, input, and output signals respectively. A synchronous clock triggers the data measurement and conversion process at fixed intervals according to the sampling period. There are three identified delays:

- Computational delay in the controller. In ideal situations, there is the assumption that the variable measurement, computation, and control signal output have been performed and completed at the beginning of each sampling

period. However, in practise this is not possible and the signal output is usually applied one sampling period later.

- Communication delay between the controller and the plant due to digital to analogue conversion (DAC) and zero order hold (ZOH). A short delay is present when the digital control output converts to analogue signals before being sent to the plant. Delays associated with the PWM signals in power electronics systems are normally represented by a ZOH.

- Communication delay between the sensor and the controller due to analogue to digital conversion (ADC). A short delay is present when the sensor measures the variable and sends the information to the controller.
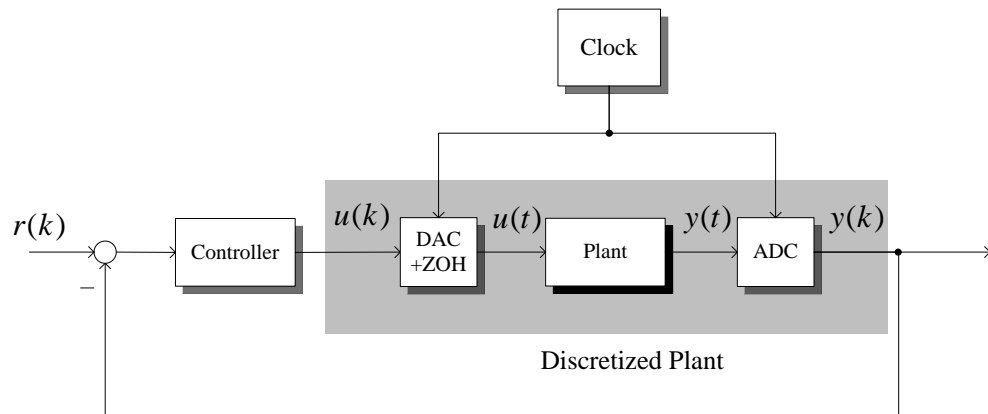
Fig. 3.14. Digital control feedback loop [141].

Estimation of the overall delay provides a simple solution as modelling the delays accurately requires complex algorithms that takes into account the PWM carrier signal and converter switching frequency. One sample delay usually occurs within the controller while the other delays have variable sample delays depending on the sample time ratio. The total delay is hence approximated to 1.5 sample periods. The effect of this delay can be seen in Fig. 3.15 for the S/G closed loop current response at different bandwidths. A pure delay of 1.5 sample periods was applied at the output of the plant within the current loop. There was a difference in dynamic response between the closed loop with and without the delay. Due to the presence of the delay, the plant dynamics changed and thus the closed loop response also changed. As the current loop bandwidth was increased, the dynamic response was seen to become more oscillatory. This therefore establishes that there is a limit to how fast the current loop bandwidth can be before the S/G system becomes unstable.

As a result, the sampling time for discretisation and the current loop bandwidth utilised within the S/G has to be chosen carefully in order to prevent instability.
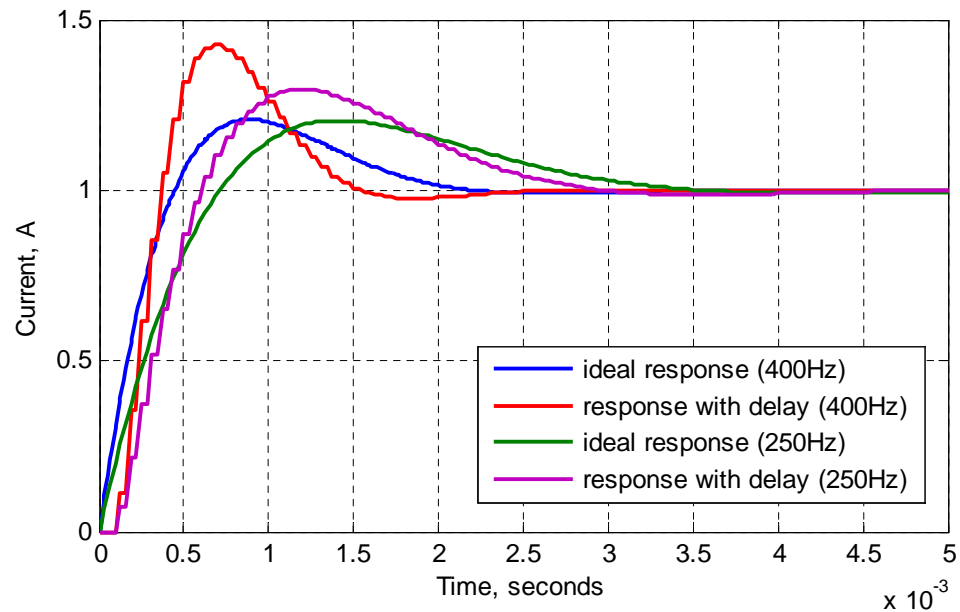
Fig. 3.15. Closed loop current step response to reference of 1A for ideal and non-ideal feedback loop with 400Hz and 250Hz bandwidth.

The impact of this digital delay on the plant (3.43) under FW and DC link voltage control is shown in Fig. 3.16. The delay was positioned within the current loops. It can be seen that the delay also has impact on the multivariable plant, affecting mostly the off diagonal terms. The effect of the delay on the system can be reduced either by decreasing the closed loop bandwidth or by utilising a Smith predictor [141].

Based on the simulation results presented above, the effect of the inherent delays within digital control has to be considered in order to avoid instability in the S/G system. If required to maintain stability, the current loop bandwidth can be further reduced in order to minimise the impact of the delay. However, the main focus of the analysis in this Thesis is to fully understand the overarching issues when utilising FW and DC link control. The effect of delays on the control response is therefore neglected during the control design process. Furthermore, the theoretical findings resulting from the control design of this S/G system will be confirmed with a small prototype test bench. The sampling time ratio is much higher for the

prototype than the AEGART S/G due to a smaller electrical frequency of up to 180Hz. As a result the effect of the digital delay can be ignored.
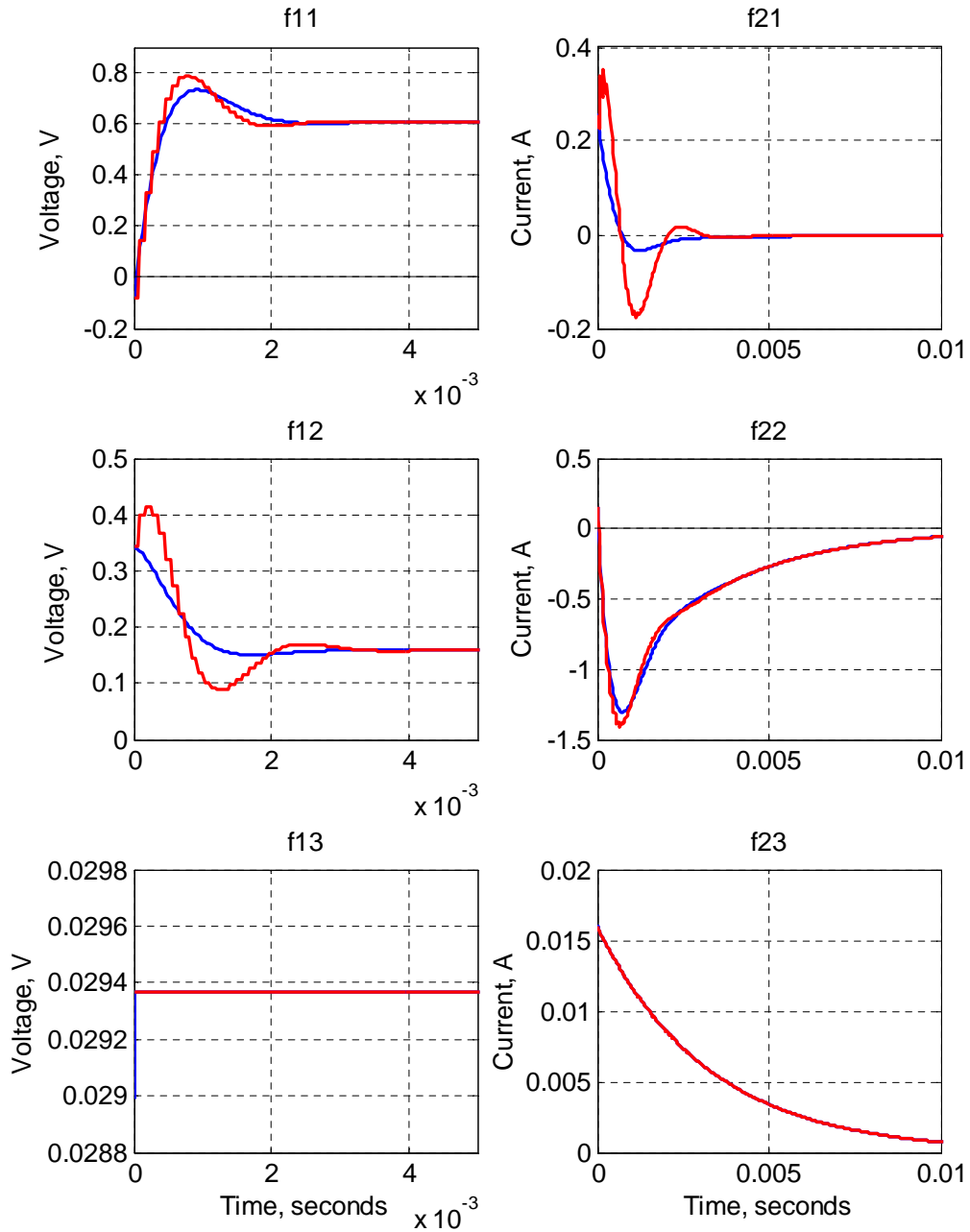
Fig. 3.16. Step response comparison between the S/G core plant ideal transfer functions (blue) and the transfer functions with delay (red) with 400Hz current loop bandwidth.

3.7 Conclusion

This Chapter detailed the control strategy that will be implemented within the S/G system. FOC was selected as the primary control method and the control structure was detailed with reference to the S/G mode of operation. In starter mode, separate controllers were used for FW and speed control. When the S/G system operates in generator mode, the speed controller is replaced with a DC link controller. The FW controller is active at all times for both mode of operation. Equations that represent the core parts of S/G system (machine, converter, DC link bus) were also introduced in this Chapter. The current control loops for the S/G were designed and included into the core part of the control scheme. It was shown that the plant included non-linearities; hence small signal models were derived using a linearisation technique. The necessary control plant models were derived for each mode of S/G operation. It was found that the plants for FW and DC link control have cross-link dynamics due to the machine feedforward terms and these cross-couplings increased the complexity of the plant. The derived plant transfer functions have been verified against non-linear models created in Matlab®/Simulink®. Furthermore, the presence of positive zeroes within those plants was shown to result in non-minimum phase characteristics. This may cause the S/G system to have a limited stability range. Therefore, these limits will be investigated in detail within the following Chapters. The effect of digital delays within the control system was also considered as they can influence the performance of the designed controllers. However, the delay was neglected with the assumption that it does not have a significant impact and that the key focus of this research is to understand the overarching issues related to FW and DC link control design within the S/G system.

Chapter 4   Starter Mode Operation: Analysis and Control Design

4.1   Introduction

This Chapter will deal with control design analysis for the S/G system operation in starter mode based on the plant models derived in Section 3.5. The capabilities of the S/G system are identified beforehand in order to aid with the control design process. The plant specifically for FW control will be derived and verified against a non-linear equivalent model. The speed and FW controllers shall be designed to achieve good overall performance. Finally, the designed controllers will be tested together in simulation to confirm the control performance.

4.2   S/G System Capabilities and Limitations

The operating conditions of the S/G system will now be considered before the design process. A more detailed control scheme than was previously considered is depicted in Fig. 4.1. It shows a cascaded control structure with the FW and speed controllers connected to the i_d and i_q control loops respectively. A dynamic limiter is also shown for the chosen direct current FW method as discussed in Section 2.6.3. i_{qlim} is the i_q^* limit of the dynamic limiter and i_{max} is the maximum stator current.

There are two factors that limit the performance of the S/G electrical system. The first is the maximum current flowing through the converter IGBTs. The control scheme needs to ensure that the current demand does not go beyond the limit in order to maintain safe operation. According to the AEGART converter design, the maximum current is 400A. The following equation represents the current limit in terms of *dq* frame currents:

$$i_{\max}{}^2 \geq i_d{}^2 + i_q{}^2 \tag{4.1}$$
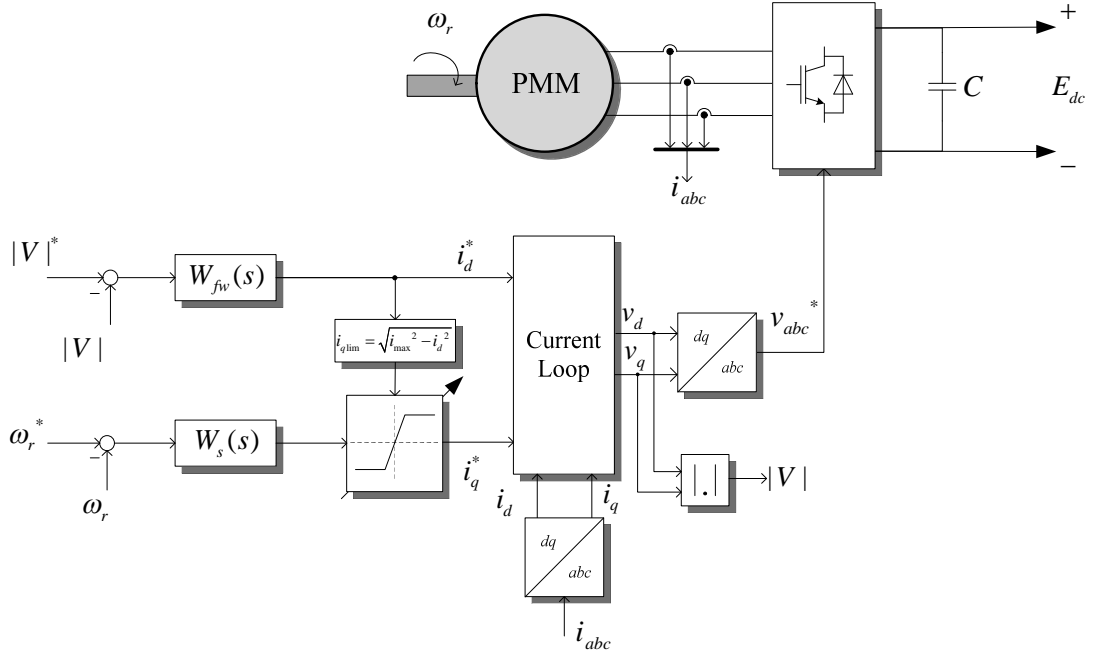
Fig. 4.1. Detailed control scheme for starter mode.

The second factor is the AC side voltage limit which is utilised to avoid converter over modulation. When operating at high speeds, the machine back-emf can reach very high levels. Hence, the S/G system requires FW to ensure that the back-emf is within $|V|_{max}$. Using SVM, $|V|_{max}$ can be related to the DC link voltage with the following equation [138]:

$$|V|_{max} = \frac{E_{dcrated}}{\sqrt{3}} = 155.9V \tag{4.2}$$

Assuming steady state operation and ignoring R_s, the machine electrical equations (3.14) and (3.15) can be reduced to:

$$v_d = -L_q \omega_e i_q \tag{4.3}$$

$$v_q = (L_d i_d + \psi_m) \omega_e \tag{4.4}$$

The voltage limit equation can be derived using (3.22), (4.3), and (4.4) to form:

$$\left(\frac{|V|_{max}}{\omega_e L_q} \right)^2 = \left(\frac{L_d}{L_q} i_d + \frac{\psi_m}{L_q} \right)^2 + i_q^2 \tag{4.5}$$

The voltage and current limit circles can be plotted based on (4.1) and (4.5) on an i_d-i_q plane. The radius of the voltage circle decreases as the speed is increased from 8krpm to 32krpm, as shown in Fig. 4.2. The centre point of this circle is the critical current at $-\psi_m/L_q$ or -368A using the machine parameters from Table 2.3. Theoretically, infinite speed can be achieved as the centre point is within the current limit circle. The blue circle represents the current limit while the others are the voltage limits at different operating speeds. The light green circle is at the intersection point when i_q is maximum and i_d is zero to represent ω_b. If the speed has to be further increased, FW may be applied. This is considered the lower speed limit for ω_b. Using the voltage limit equation, the operating speed was found to be 9.22krpm. The point where FW always has to be online is the red circle touching the origin, O. Once again with (4.5), the operating speed at this point was found to be 13.62krpm as the upper limit for ω_b. At 32krpm, the required i_d is -211.45A at no load, as a significant amount of current required to de-flux the PMM. This indicates the importance of FW for this S/G system. As mentioned in Section 2.5, even though significant levels of i_d are required for this type of machine for FW, the overall trade-off studies have shown that the benefits of this S/G topology outweigh this disadvantage.

The current trajectory of the current during start-up is shown in Fig. 4.2. From standstill until ω_b, the machine operates within the constant torque region and is capable of utilising maximum torque. This is characterised by the straight line from O to point A. When the machine further accelerates to a higher speed, the voltage limit circle limits the current trajectory. At speeds above ω_b, the machine is operating in the constant power region where the current operating point needs to be within the intersectional area of both current and voltage limit circles. As a result, the current trajectory moves along the current limit circle to the left side (point A to B). When the operating speed reaches up to 32krpm, the importance of FW is more apparent for this S/G power system.

Once the S/G system capabilities have been identified, the speed controller will be designed first followed by the FW controller with reference to the plants derived in the previous Chapter. The latter controller will be analysed in detail as the control design is more elaborate.
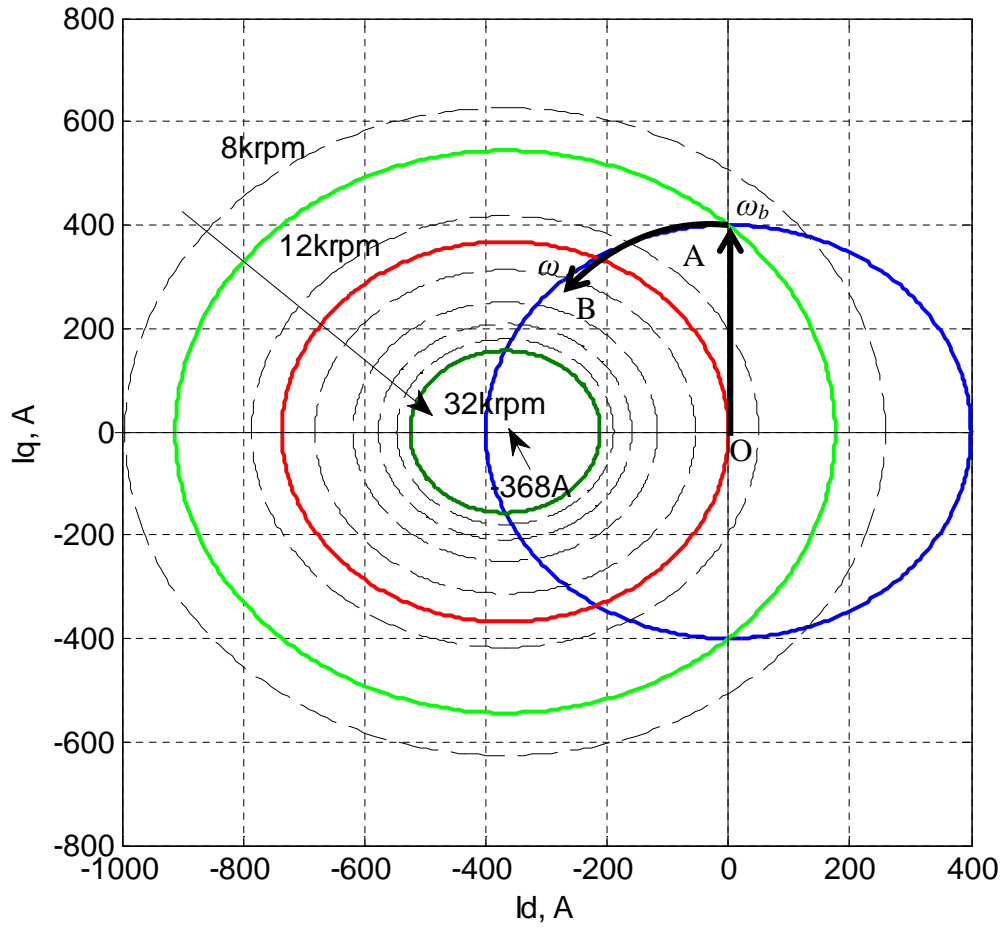
Fig. 4.2. AEGART system voltage and current limit circles.

4.3 Speed Controller Design

The speed controller will be designed utilising the plant given in (3.36) which was derived in Section 3.5.1. PI control is used for the speed controller in the form of:

$$W_s(s) = k_{ps} + \frac{k_{is}}{s} \tag{4.6}$$

where k_{ps} and k_{is} are the speed controller proportional and integral gains. A common practise in industry is to select the speed bandwidth to be at least 10 times slower than the current loop bandwidth to ensure good control performance of both loops. This gives sufficient time for the current loop to react to changes based on the speed loop. A speed bandwidth of 10Hz was chosen as the S/G system due to the slow dynamics of the mechanical system. The speed controller was designed with a

damping ratio of 0.707 and the controller gains were calculated to be $k_{ps} = 216$ and $k_{is} = 9702$.

The controller dynamic response cannot be determined during acceleration due to the high inertia of the machine and the converter current limit. A fast rate of change of speed with this high inertia system would require more power than the converter can provide. Nevertheless, the machine will be accelerated, just not at the designed bandwidth, until it reaches the speed reference.

The designed controller dynamics can be observed instead through i_q as the speed reaches steady state at about $t = 5.17$s or at $t = 5.5$s with a very small speed step of 5rpm as shown in Fig. 4.3. When the speed reference has been reached for either scenario, active power is no longer required and i_q is reduced to zero. The change of i_q is within the converter current limits ($\pm$ 400A) and hence the 0.1s settling time (or 10Hz) was observed at $t = 5.17$s. In addition, the i_q response at $t = 5.5$s showed the same settling time while not being saturated by the current limit. The current loop being much faster than the speed loop allowed the latter i_q response to be clearly observed, as shown in Fig. 4.3.
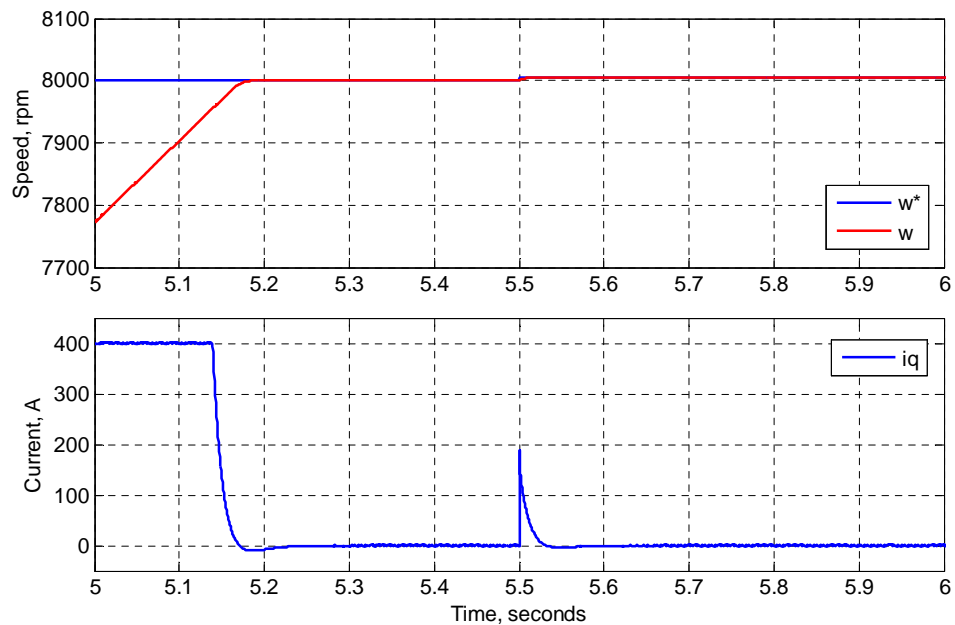
Fig. 4.3. i_q response when speed reaches reference of 8krpm at $t = 5.17$s and to a step change of 5rpm at $t = 5.5$s.

4.4 Flux Weakening Controller Design

The design of the FW controller utilises the plant derived earlier in Chapter 3. Specifically, transfer functions f_{11}, f_{12}, and f_{13} in (3.43) represent the plant for FW control design. Note that two cases of FW operation can be observed during this mode depending on the state of the dynamic limiter shown in Fig. 4.1. The output of the limiter (which will be i_q^*) is either from the speed controller or according to the current limit equation (4.1). The transition between both of these inputs happens when the total magnitude of the dq currents reaches i_{max}. Hence, these cases can be referred to as unlimited i_q^* and limited i_q^* respectively.

The control plants for each of these cases will be derived and analysed by operating speed and load variation. Depending on the results of this analysis, the controller will be designed for the worst case scenario given the speed and load limits in starter mode.

4.4.1   Control Design during the Unlimited i_q^* Case

For this case, since the limiter is not acting, the output of the speed controller sets the reference for i_q^*, and i_d^* according to the FW controller. The control plant under these conditions is depicted in Fig. 3.9. For design of the FW control, a plant relating $\partial|V|$ to ∂i_d^* has to be formed. The following assumptions are made:

- Perturbation in i_d^* does not affect i_q^* since they have separate controllers. Hence, i_q^* terms (f_{12}) can be considered as disturbances for the unlimited i_q^* case.

- The ω_e term (f_{13}) is neglected in this plant derivation since a perturbation of this term is dictated by i_q^*.

The control plant for unlimited i_q^* was found to be f_{11} and it is rewritten here for convenience:

$$\frac{\partial|V|}{\partial i_d^*} = \frac{1}{L_d} \frac{\left(2\xi\omega_n L_d - R_s\right)s + \omega_n^{\ 2}L_d}{s^2 + 2\xi\omega_n s + \omega_n^{\ 2}} \left[\frac{v_{do}}{|V|_o}\left(R_s + L_d s\right) + \frac{v_{qo}}{|V|_o}\omega_{eo}L_d\right] \tag{4.7}$$

This second order plant has already been verified against a non-linear equivalent model, as detailed in Section 3.5.4. The characteristics of this plant were analysed with differing operating points at various speeds and loads. The three operating speeds that were considered were; 8krpm, 15krpm, and 20krpm which should cover the entire starter mode speed range. The load demands investigated were at 10Nm, 25Nm, and 40Nm to cover the effect of different levels of load torque on the S/G system. The plants at the three operating speeds were calculated to observe any difference in pole zero locations, as shown below:

$$f_{s\_nl\_8krpm} = \frac{9.6011 \times 10^{-6}(s + 2.298 \times 10^{8})(s + 4449)}{(s^2 + 8884s + 3.948 \times 10^{7})} \tag{4.8}$$

$$f_{s\_nl\_15krpm} = \frac{-2.0232 \times 10^{-4}(s - 2.045 \times 10^{7})(s + 4449)}{(s^2 + 8884s + 3.948 \times 10^{7})} \tag{4.9}$$

$$f_{s\_nl\_20krpm} = \frac{-6.9881 \times 10^{-4}(s - 7.897 \times 10^{6})(s + 4449)}{(s^2 + 8884s + 3.948 \times 10^{7})} \tag{4.10}$$

Fig. 4.4 shows that one of the transfer function zeros changes when subjected to different operating speeds with no load. All other poles and zeroes did not change due to the speed variation. As no load was used this ensures that the transfer functions were purely influenced by speed. As the speed increases, the zero travelled towards the left hand plane (LHP) when operating below ω_b (13.62krpm). ω_b is the border operating speed that requires FW for any further increase in speed. Above ω_b, the zero appears in the right hand plane (RHP) and moves towards the origin.

Similarly, the pole zero movements were analysed for load impacts of T_L at a constant speed and their transfer functions were found to be:

$$f_{s\_nl\_10Nm} = \frac{-0.21452(s - 2.494 \times 10^{4})(s + 4449)}{(s^2 + 8884s + 3.948 \times 10^{7})} \tag{4.11}$$

$$f_{s\_nl\_25Nm} = \frac{-0.53546(s - 8160)(s + 4449)}{(s^2 + 8884s + 3.948 \times 10^{7})} \tag{4.12}$$

$$f_{s\_nl\_40Nm} = \frac{-0.85698(s - 1406)(s + 4449)}{(s^2 + 8884s + 3.948 \times 10^{7})} \tag{4.13}$$
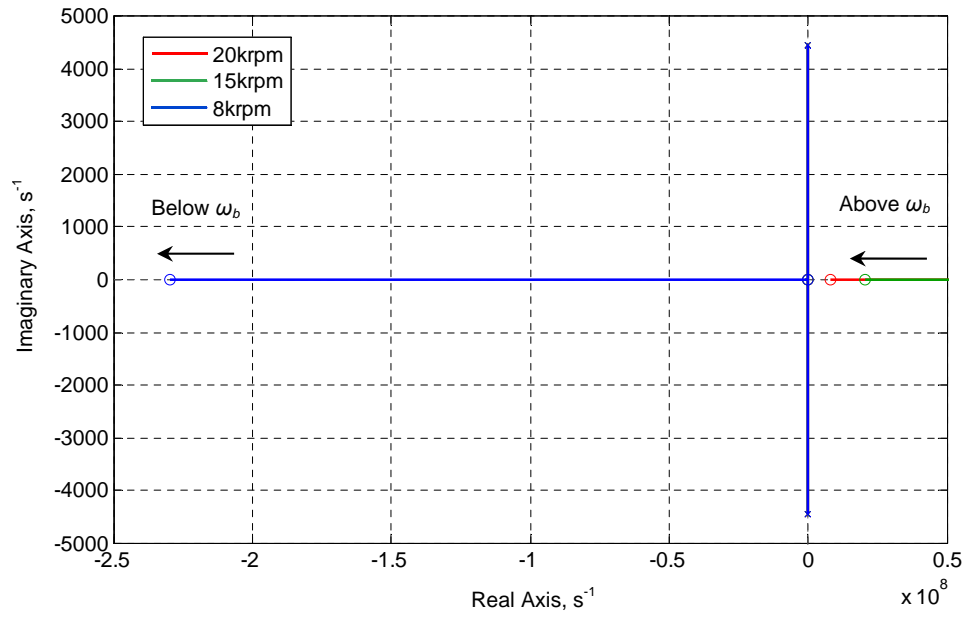
Fig. 4.4. Pole zero location at operating speeds of 8krpm, 15krpm, and 20krpm with no load, starter mode, unlimited i_q^*.

The root locus of these transfer functions can be seen in Fig. 4.5. Once again, the zero position changed, moving towards the origin as the load impact increases.
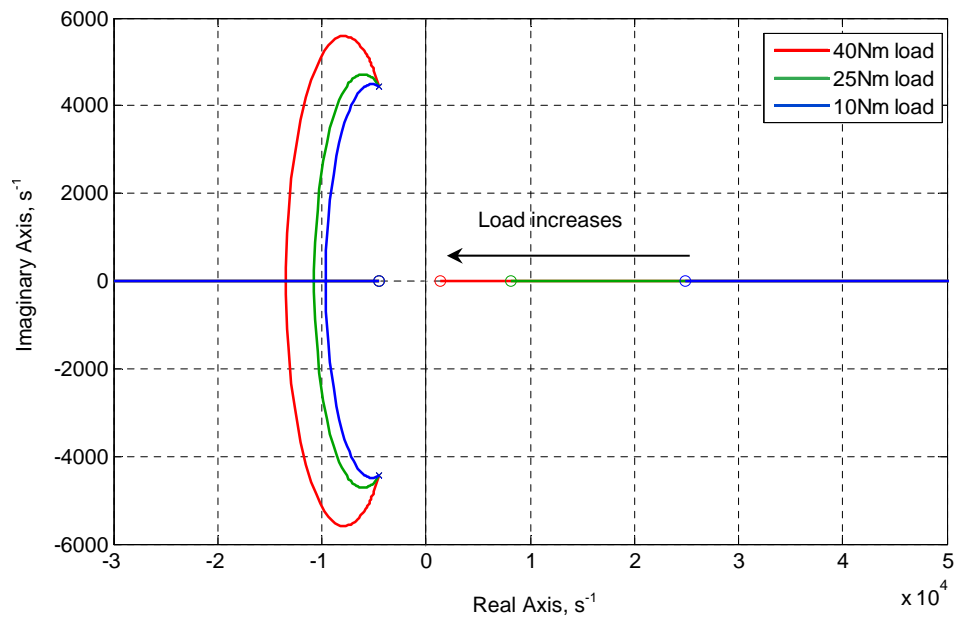
Fig. 4.5. Pole zero movement for load increment of 10, 25, 40Nm at 20krpm, starter mode, unlimited i_q^*.

This positive zero has the most significant change compared to the other poles and zero when subjected to different speeds and load impact. The equation of the zero is known from (4.7) as:

$$z_{nl} = -\frac{(v_{do}R_s + v_{qo}\omega_{eo}L_d)}{v_{do}L_d}$$

(4.14)

Its position at different speeds and loads was calculated and is shown in Fig. 4.6. Since the load demand during starter mode is defined by load torque from the aircraft engine, the unit can be translated to i_q for consistency with the analysis that will be performed in Chapter 5 for generator mode. At 15Nm, 25Nm, and 40Nm load, the demanded i_q is 91A, 152A, and 244A respectively. It can be seen that across different speeds and load conditions, the zero remains positive. As the load increases, the zero position moves closer to the origin. The red line at nearly zero current indicates that the transition of the zero from the LHP to RHP happens for speeds above ω_b.
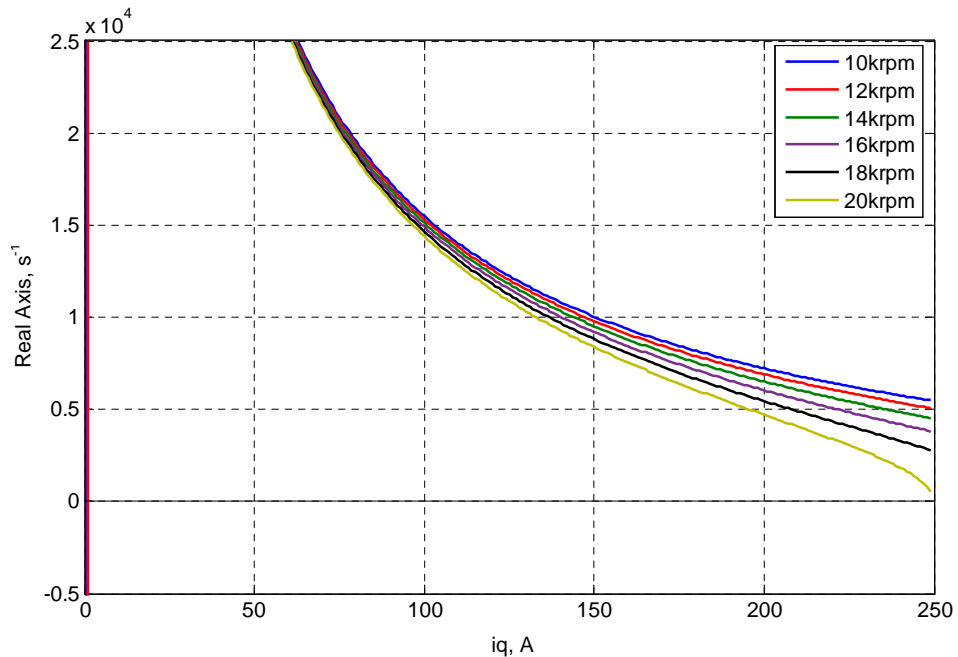
Fig. 4.6. Zero trajectories across load range in terms of current at different speeds, starter mode with unlimited i_q^*.

In order to achieve accurate control with no error between the measured and reference value, integrative action is required. After adding an integrator as part of the controller, the root locus of the closed loop plant (4.7) is shown in Fig. 4.7 for different speeds. When the speed is above ω_b, most of the root loci are located on the

RHP due to the positive zero. As the closed loop gain increases as determined by the integrator gain, k_{iv}, the eigenvalues of the plant move towards the RHP. These eigenvalues should remain on the LHP to ensure stability. As a result, a range for the k_{iv} gain can be defined where instability occurs if k_{iv} exceeds the limit. An increase in operating speed reduces the range of gain k_{iv} that can be utilised before the system becomes unstable, as seen in Fig. 4.7.
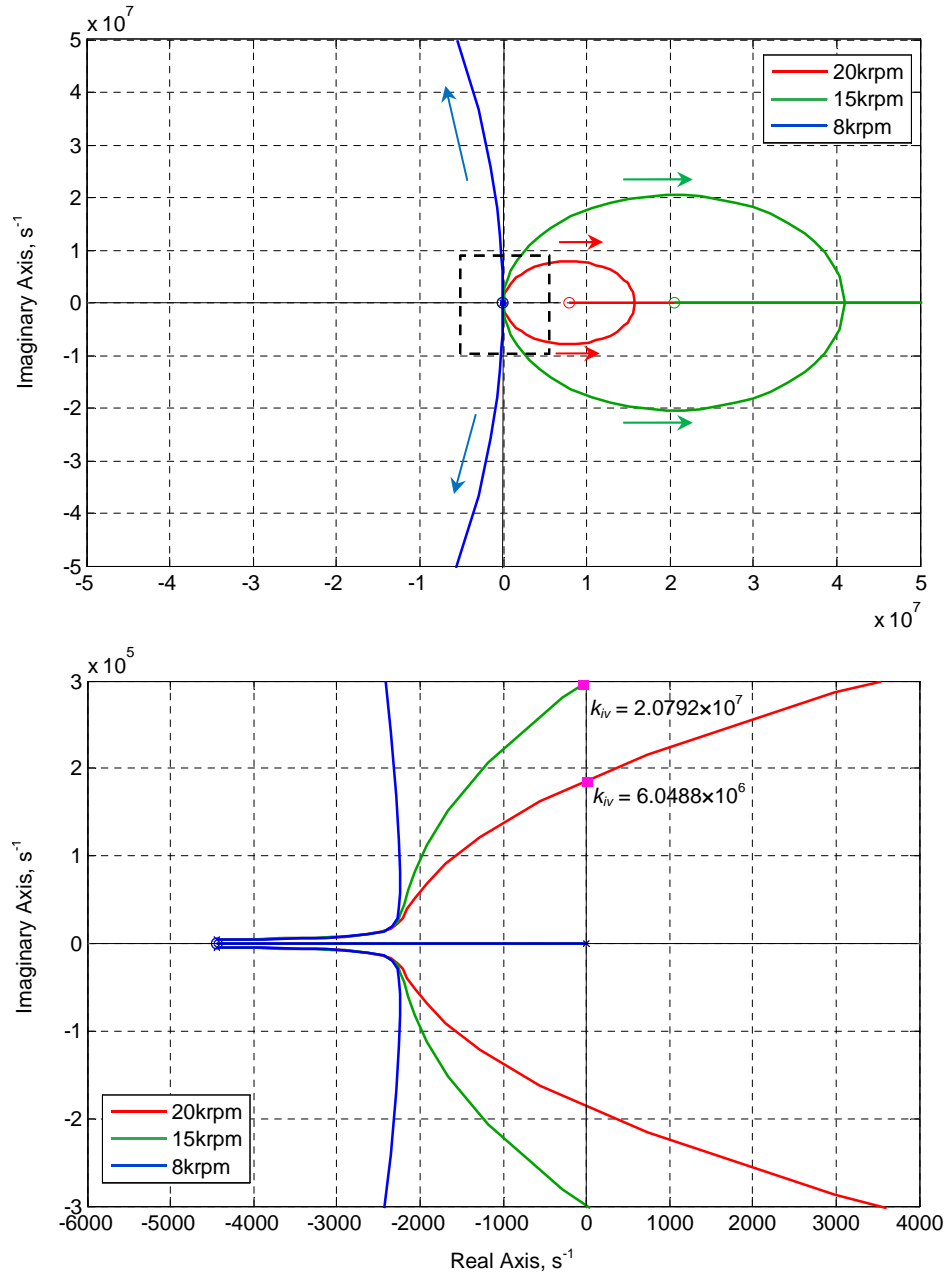
Fig. 4.7. Closed loop root locus at different speeds (top) and the zoomed area (bottom), starter mode, unlimited i_q^*.

At the border of the imaginary axis, the limits for the k_{iv} gain were found to be 2.0792×10^7 and 6.0488×10^6 at speeds of 15krpm and 20krpm respectively. Below ω_b, the root locus is always on the LHP which allows a wider range of gain to be selected for the controller. The closed loop feedback plant was also tested at different loads and the root loci are depicted in Fig. 4.8. Due to the slower positive zero at higher loads, the allowable range for k_{iv} gain is reduced. In this case, at 20krpm the stable range for k_{iv} gain reduces to 7650.
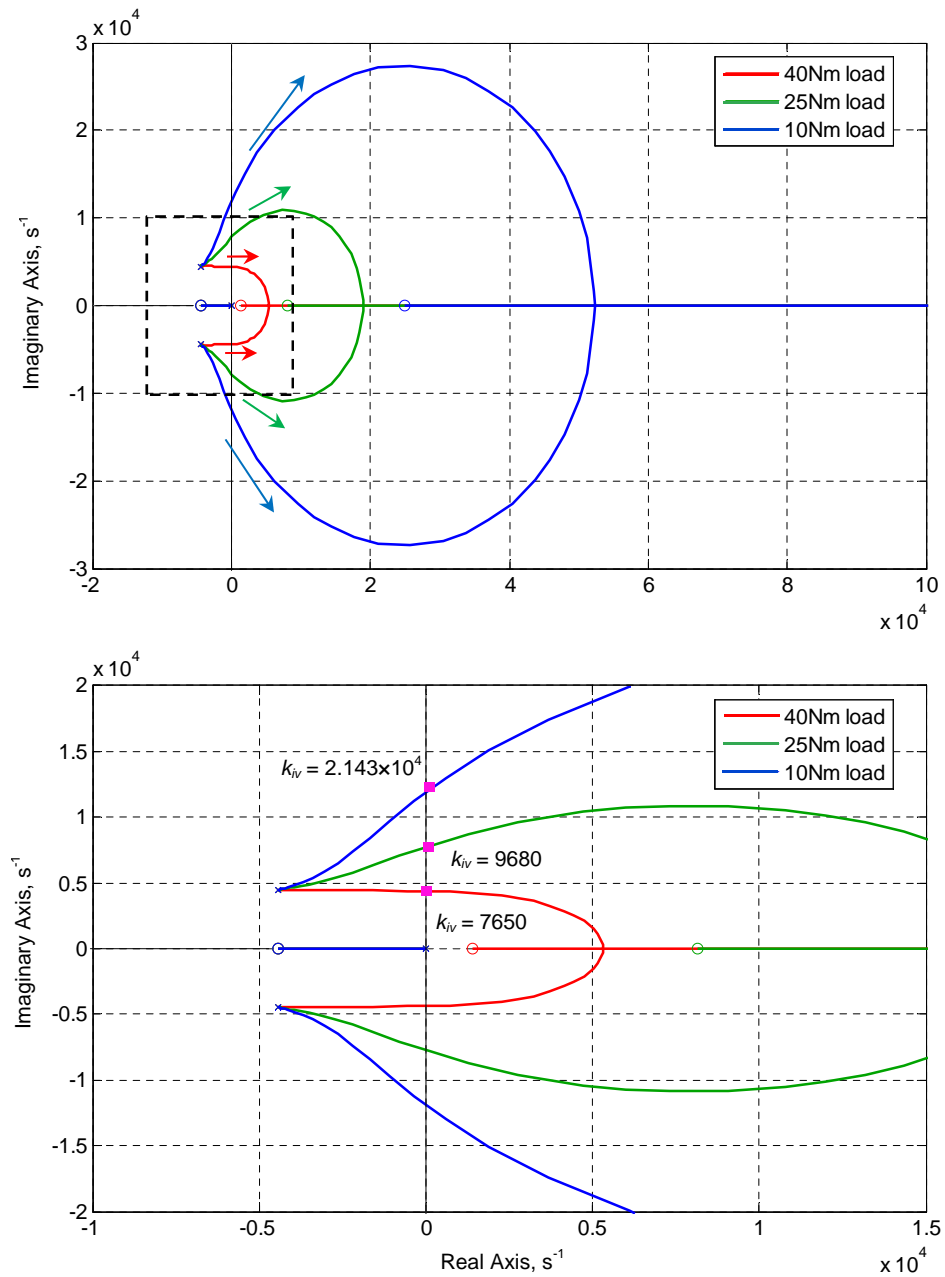
Fig. 4.8. Closed loop root locus at different loads at 20krpm (top) and zoomed area (bottom), starter mode, unlimited $i_q{}^*$.

Taking into account the smallest k_{iv} range for this case, based on operating speed and load, a reasonable response can still be achieved when k_{iv} is selected as 1500. This is shown in Fig. 4.9. The addition of a proportional gain, k_{pv}, to form a PI controller can often improve the dynamic response of the closed loop control. Fig. 4.9 shows the step response of the designed closed loop control with k_{pv} included. It can be seen from Fig. 4.9 that a significant undershoot response was observed with the addition of k_{pv}.
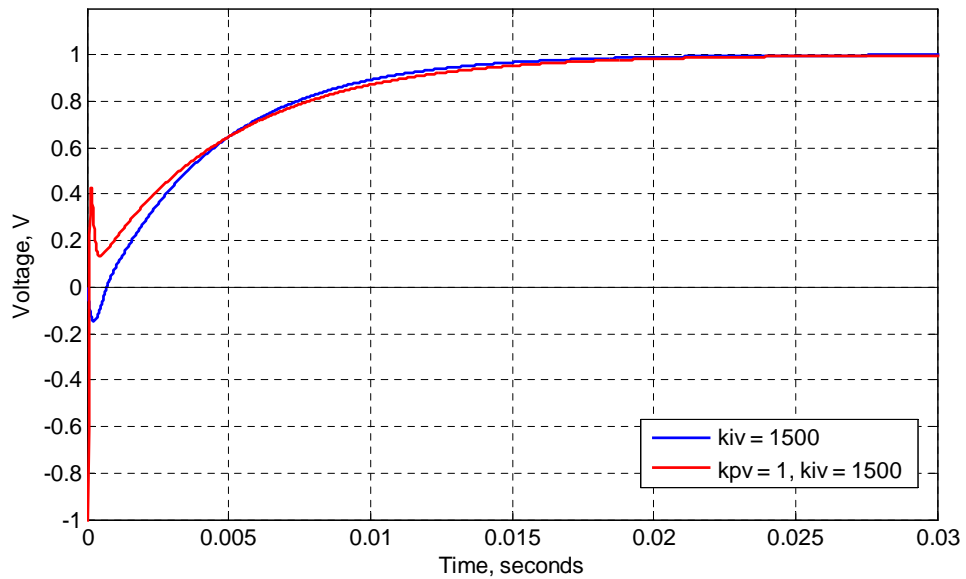
Fig. 4.9. Closed loop step response of FW integral based (blue) and PI based (red) controller operating at 20krpm, starter mode, unlimited $i_q{}^{*}$.

Fig. 4.10 shows the closed loop root locus with a PI controller. The trajectory of the closed loop poles remain within the LHP as the controller gains increase. However, the allowable range of k_{pv} was found to be very small for this control plant. The closed loop poles reach the real axis at $k_{pv} = 1$. When k_{pv} increases to 1.2, one of the poles moves into the RHP and causes instability. Hence, only small values of k_{pv} can be used as part of the controller for this power system.
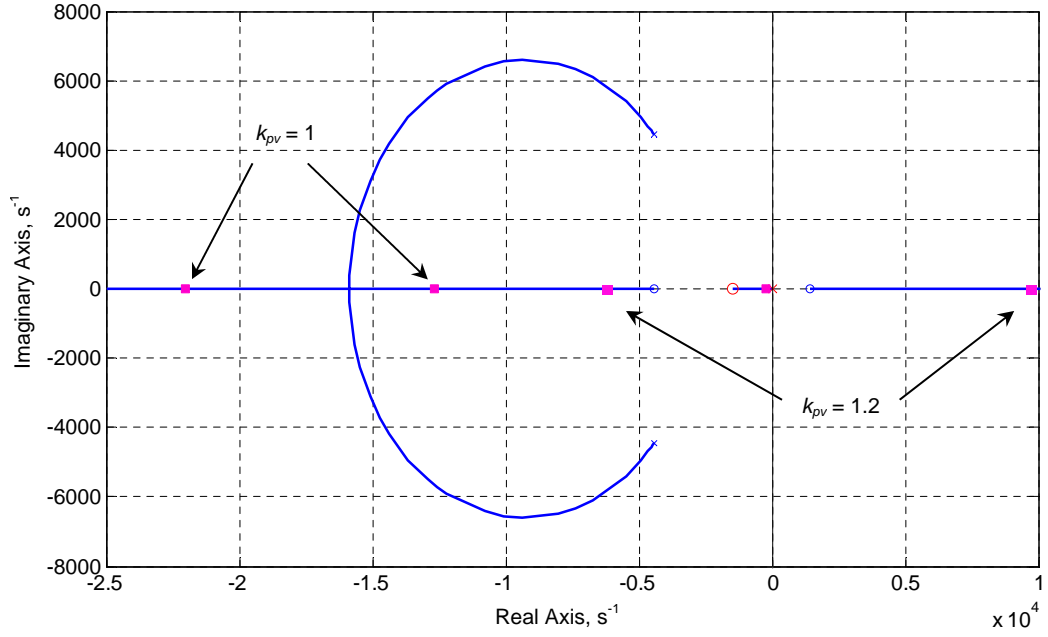
Fig. 4.10. Root locus of FW plant with PI controller (k_{pv} = 1 or 1.2, k_{iv} = 1500) operating at 20krpm, starter mode, unlimited $i_q{}^*$.

4.4.2   Control Design during Limited $i_q{}^*$ Case

This scenario happens when $i_q{}^*$ from the speed controller exceeds the current dynamic limit. Figuratively, this case can be depicted as shown in Fig. 4.11 where $i_q{}^*$ is completely dependent on $i_d{}^*$. Since the dynamic limit is non-linear in nature (see (4.1)), its linearised equivalent can be written as:

$$\partial i_q{}^* = \frac{-i_{do}{}^*}{\sqrt{i_{max}{}^2 - i_{do}{}^{*2}}} \partial i_d{}^* = \frac{-i_{do}{}^*}{i_{qo}{}^*} \partial i_d{}^* \tag{4.15}$$

The FW plant can be derived for the limited $i_q{}^*$ case by relating $\partial /V/$ to $\partial i_d{}^*$. The assumptions that were listed in the unlimited case do not apply here since there is a connection between $i_d{}^*$ and $i_q{}^*$. The ω_e terms are related to i_q through the mechanical equations (3.16), (3.18), and (3.19) in linear form:

$$\partial \omega_e = \frac{3p^2\psi_m}{2Js} \partial i_q \tag{4.16}$$

97
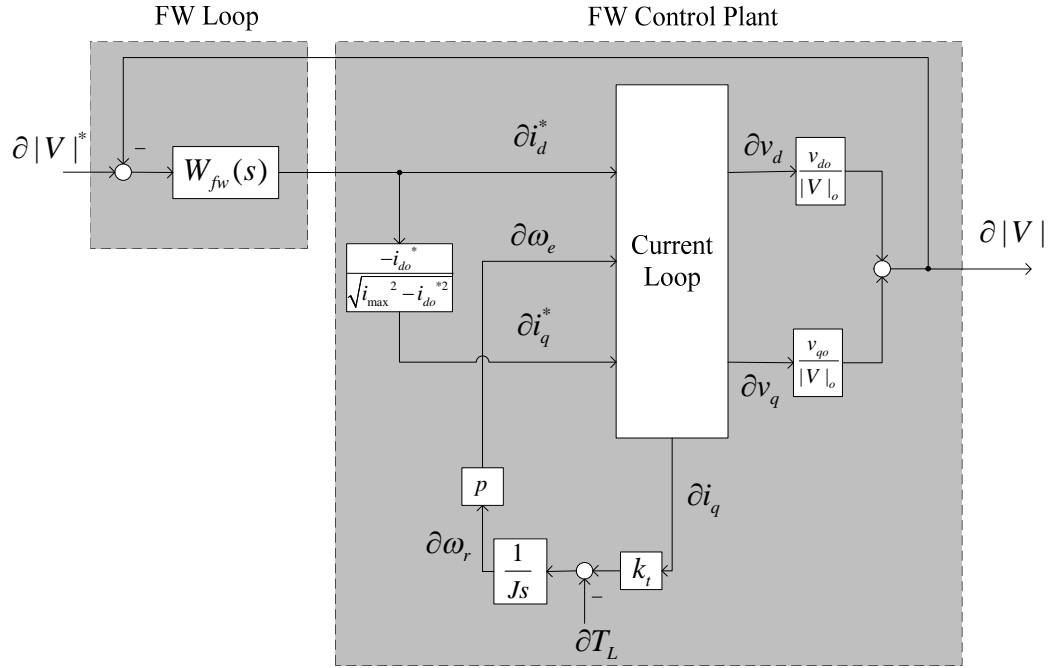
Fig. 4.11. Linearised block diagram for starter mode, limited i_q^*.

f_{12} and f_{13} terms can be merged together with f_{11} using equations (3.27), (4.15), and (4.16). The transfer function can therefore be derived as:

$$\partial |V| = \frac{k_{id} + k_{pd}s}{L_d s^2 + (R_s + k_{pd})s + k_{id}} \left[\frac{a_{1l}s^2 + a_{2l}s + a_{3l}}{a_{4l}s} \right] \partial i_d^* \qquad (4.17)$$

where

$$a_{1l} = 2J\left(i_{qo}^* v_{do} L_d - i_{do}^* v_{qo} L_q \right)$$

$$a_{2l} = 2J\left(i_{qo}^* R_s v_{do} - i_{do}^* R_s v_{qo} + i_{do}^* L_q v_{do} \omega_{eo} + i_{qo}^* L_d v_{qo} \omega_{eo} \right)$$

$$a_{3l} = 3i_{do}^* p^2 \psi_m \left(i_{qo} L_q v_{do} - i_{do} L_d v_{qo} - \psi_m v_{qo} \right)$$

$$a_{4l} = 2i_{qo}^* J |V|_o$$

Fig. 4.12 shows a comparison of the step responses of the linear plant (blue line) and the non-linear model (red line) for an operating speed of 20krpm. This operating point was selected such that the speed and load requirements would force the control system to reach the maximum limit of 400A. For this S/G system, the operating point was found to be v_{do} = -152.47V, v_{qo} = 32.43V, $/V/_o$ = 155.9V, i_{do} = -316.25A, i_{qo} = 245A, ω_{eo} = 6283rad/s. A step reference of $i_d{}^*$ = 1A was applied as the input and the output $/V/$ was observed. Perfect correlation was observed which hence verified the derived plant. The effect of the non-minimum phase is more apparent in this condition. The response shows significant undershoot after the initial step. Numerically at this operating point, the transfer function is:

$$f_{s\_l\_20krpm} = \frac{-0.62328(s - 1.301 \times 10^4)(s + 4449)(s + 0.1673)}{s(s^2 + 8884s + 3.948 \times 10^7)} \tag{4.18}$$

From (4.17), it is clear that the nature of the controlled plant has changed in the limited case with one additional zero and pole in the transfer function compared to the unlimited $i_q{}^*$ case. Upon testing at different operating points, the zero was found to be very close to the pole, thus their interaction cancelled each other's effect. The source of this pole and zero can be attributed mainly towards the mechanical dynamics. If that dynamics are assumed constant, as the mechanical time response is much slower than the electrical system [101, 103], then equation (4.17) can be simplified to:

$$\frac{\partial |V|}{\partial i_d{}^*} = \frac{k_{id} + k_{pd}s}{L_d s^2 + (R_s + k_{pd})s + k_{id}} \left[\frac{a_{5l}s + a_{6l}}{i_{qo}{}^* |V|_o} \right] \tag{4.19}$$

where

$$a_{5l} = i_{qo}{}^* L_d v_{do} - i_{do}{}^* L_q v_{qo}$$

$$a_{6l} = i_{do}{}^* \left(L_q v_{do} \omega_{eo} - R_s v_{qo} \right) + i_{qo}{}^* \left(L_d v_{qo} \omega_{eo} + R_s v_{do} \right)$$
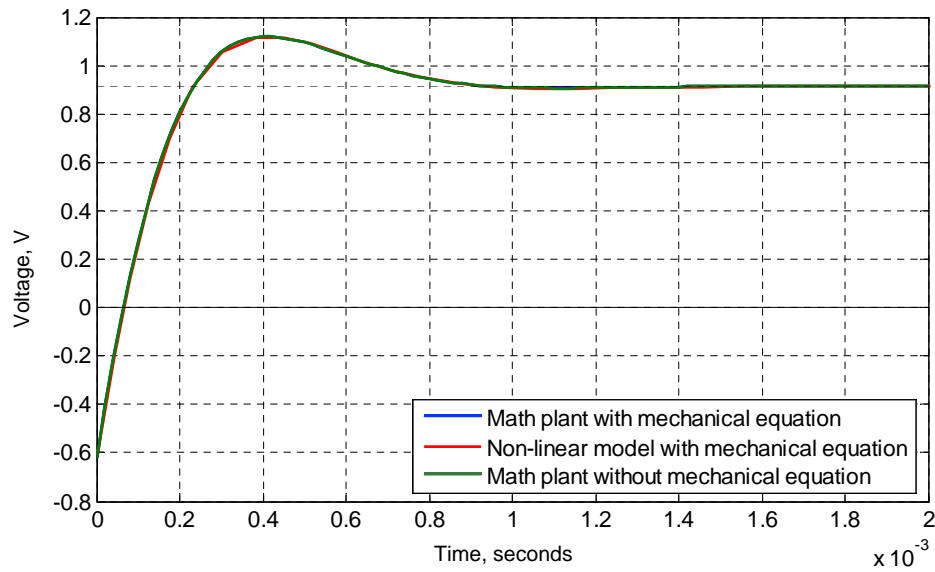
Fig. 4.12. Open loop FW plant step verification at 20krpm, starter mode, limited $i_q{}^*$.

The plant, in the case of limited $i_q{}^*$, can therefore be reduced to a single zero in addition to the current closed loop dynamics. Fig. 4.12 shows a comparison of the step responses of the transfer functions with and without the mechanical dynamics (green line). No significant difference was identified and hence the simpler transfer function was used as the plant for control design during the limited $i_q{}^*$ case.

Speed analysis was not considered for 8krpm (or speeds below ω_b) due to the improbable operating point that was required to achieve limited $i_q{}^*$. Fig. 4.13 and Fig. 4.14 show the pole zero movement due to change in operating speeds and loads respectively. It can be seen from the figures that the response is opposite to the unlimited $i_q{}^*$ case. The positive zero moves further away from the origin as the speed increases. Assessment of the impact of load variation had to be performed slightly differently in this case as limited $i_q{}^*$ only happens when the current demand exceeds the maximum current. This was therefore done by adjusting the maximum current in order to achieve the desired operating point based on the load. The zero was found to be located in the LHP for 10Nm (blue) and 25Nm (green) loads and that the trend is to move to the far left. As the load increased to 40Nm (red), the zero appeared in the RHP moving towards the origin.
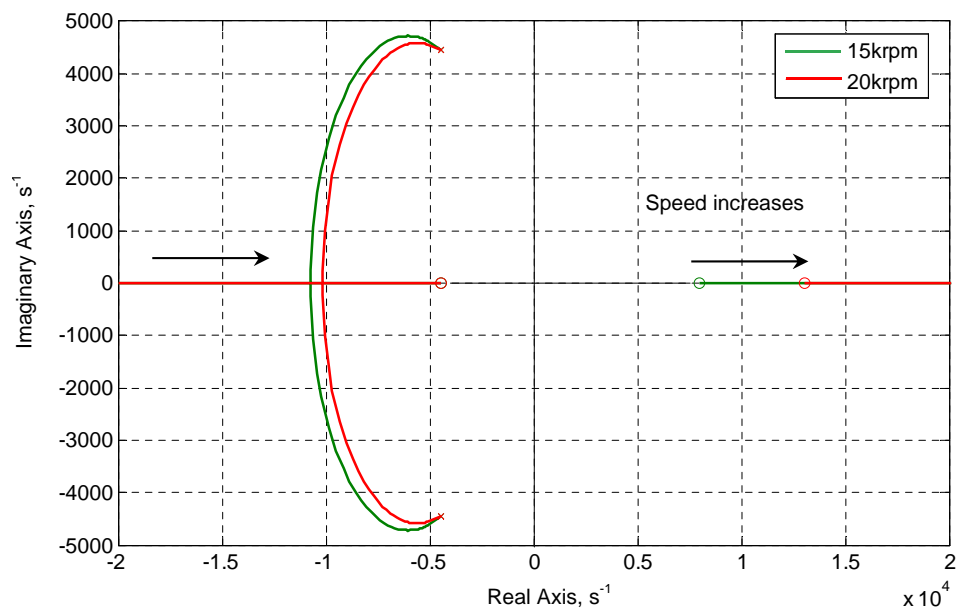
Fig. 4.13. Pole zero location at operating speeds of 15krpm and 20krpm, starter mode, limited i_q^*.
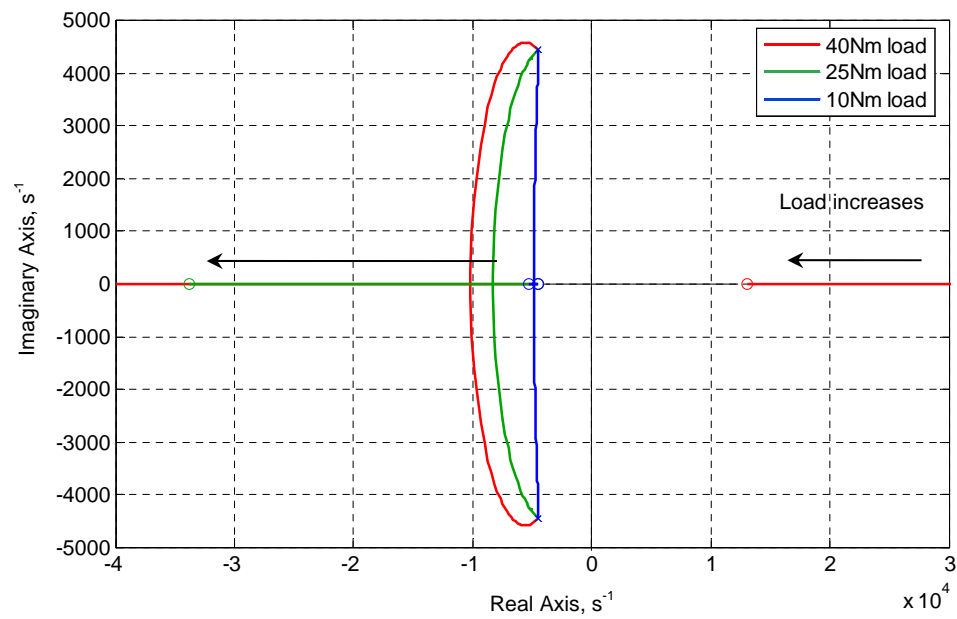
Fig. 4.14. Pole zero movement for load increment of 10, 25, and 40Nm at 20krpm, starter mode, limited i_q^*.

The movement of the zero therefore has different characteristics compared to the unlimited i_q^* case. This can be analysed using the equation of the zero obtained from (4.19):

$$z_l = -\frac{i_{do}^*\left(L_q v_{do}\omega_{eo} - R_s v_{qo}\right) + i_{qo}^*\left(L_d v_{qo}\omega_{eo} + R_s v_{do}\right)}{i_{qo}^* L_d v_{do} - i_{do}^* L_q v_{qo}} \tag{4.20}$$

The zero trajectories can be seen in Fig. 4.15 at different operating speeds and loads. As the speed increases the zero moves to the RHP at higher load values and has similar zero movement to that shown in Fig. 4.14. There is a non-linear relationship between the transition of the zero to the RHP and the operating speed. Hence the conclusion is that the FW plant is non-minimum phase during limited i_q^* only when significant loads are applied.
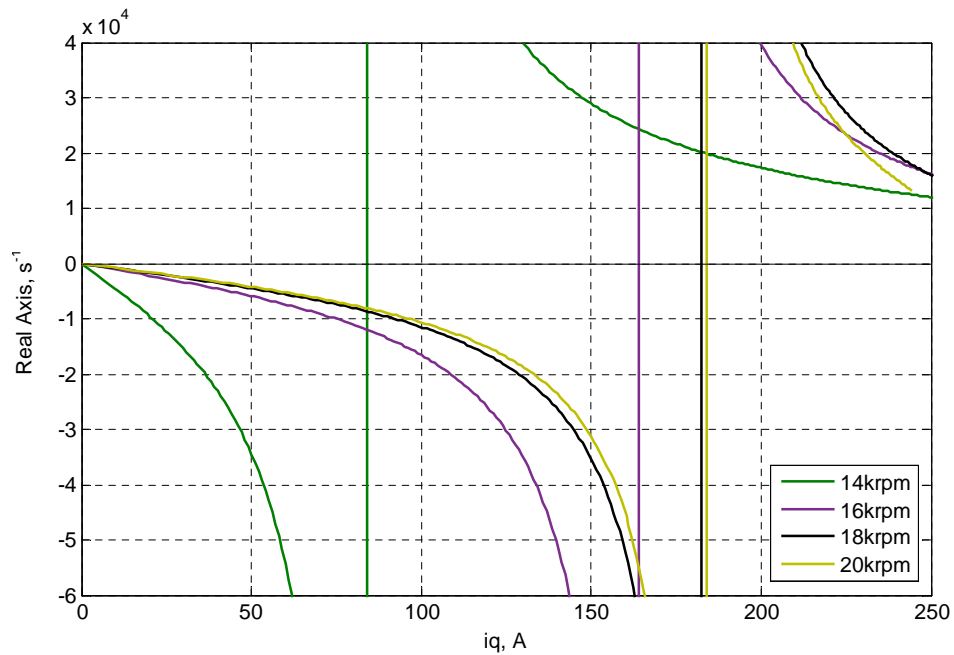
Fig. 4.15. Zero trajectories across load range in terms of current at different speeds, starter mode, limited i_q^*.

When an integrator was added to form a feedback closed loop, a similar trend was seen to that observed in the unlimited i_q^* case. The eigenvalues of the plant moved towards the RHP as the speed increased, as shown in Fig. 4.16. The difference in the allowable range for the integral gain was not significant between the two speed examples.
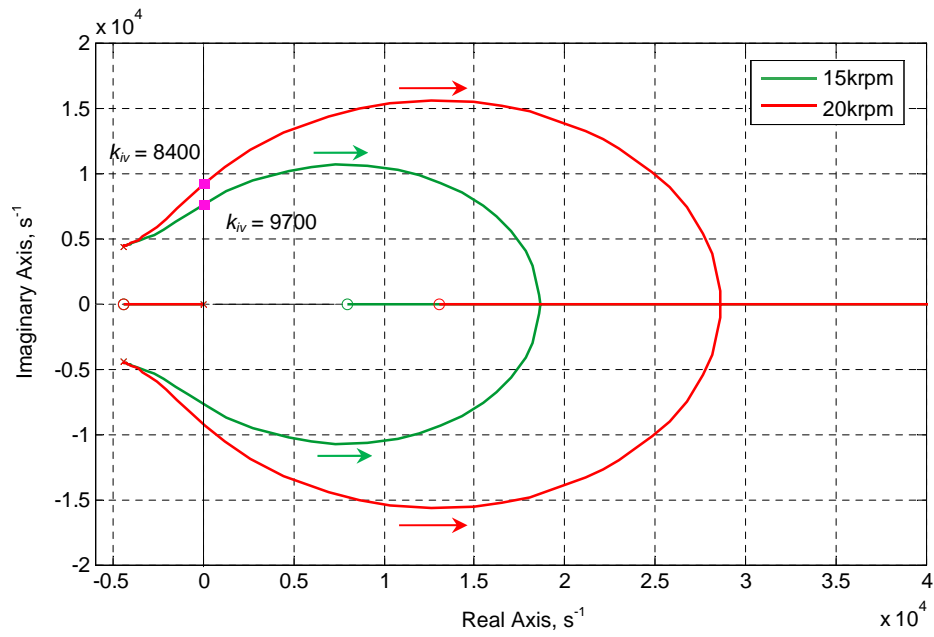
Fig. 4.16. Closed loop zero stability range at different speeds, starter mode, limited i_q^*.

Different loading-based operating points yielded different allowable gain ranges, as depicted in Fig. 4.17. It can be seen that the controller gain has a more restricted stability range as the load increases. The gain range reduced to 7650 at 40Nm load which was the same as the gain range from Fig. 4.8 due to the similarity of operating point.
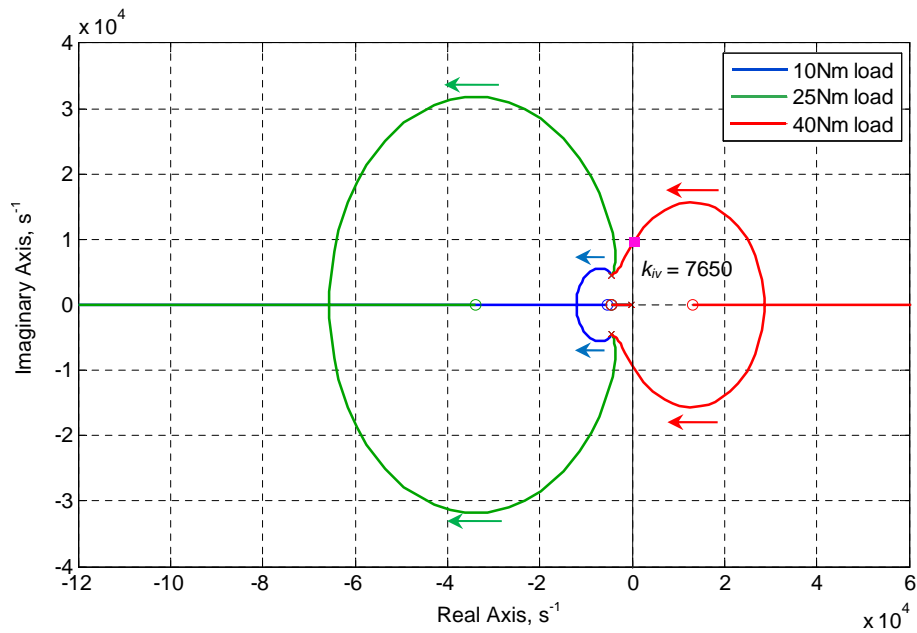
Fig. 4.17. Closed loop zero stability range at different loads at 20krpm, starter mode, limited i_q^*.

Considering the most restricted gain range based on load (which is 7650 for the unlimited $i_q{}^*$ case) k_{iv} was selected as 1500 to ensure stable operation and reasonable closed loop step response. The response is shown in Fig. 4.18.
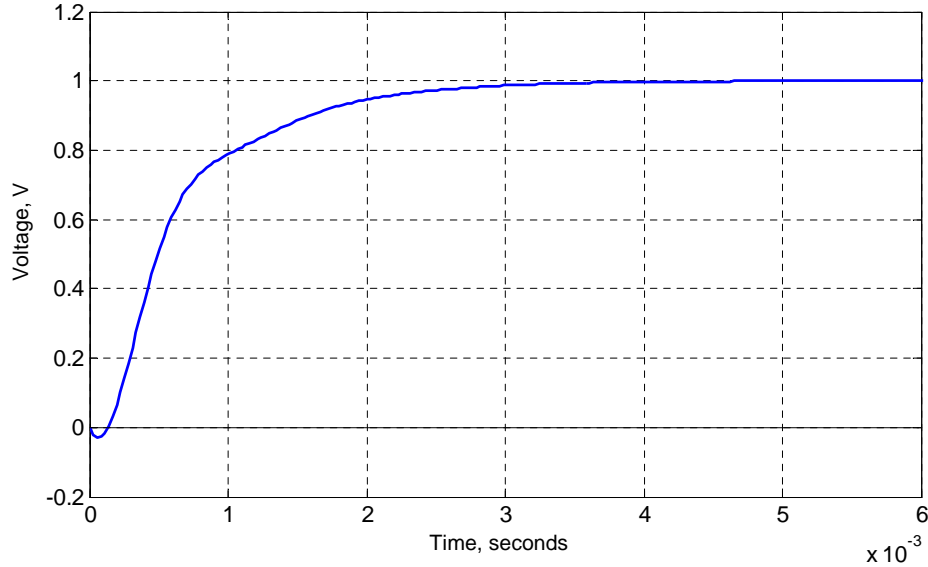
Fig. 4.18. Closed loop step response when k_{iv} = 1500 operating at 20krpm, starter mode, unlimited $i_q{}^*$.

k_{pv} was also considered and analysed in this case. Similar to the unlimited $i_q{}^*$ case, it was found that k_{pv} should be carefully selected otherwise instability may occur.

4.5   Analysis of Starter Mode Control Scheme

The frequency domain analysis results reported in the previous Section were verified by time-domain simulations using equivalent non-linear models around the selected operating point.

The closed loop gain range and stability verification reported in Fig. 4.16 at 20krpm were verified by time-domain simulation. The results are shown in Fig. 4.19. In the simulation T_L was increased in step increments of 5Nm every 0.5s until it reached 40.5Nm at t = 6.5s. At this point the power system went into the limited $i_q{}^*$ case. At t = 7s, k_{iv} was increased gradually from 8000 to 8700. Instability was observed when the controller gain reached about 8400 in accordance with the

analytical results. When k_{iv} was reduced back to 8000 stability was restored, as shown in Fig. 4.19.
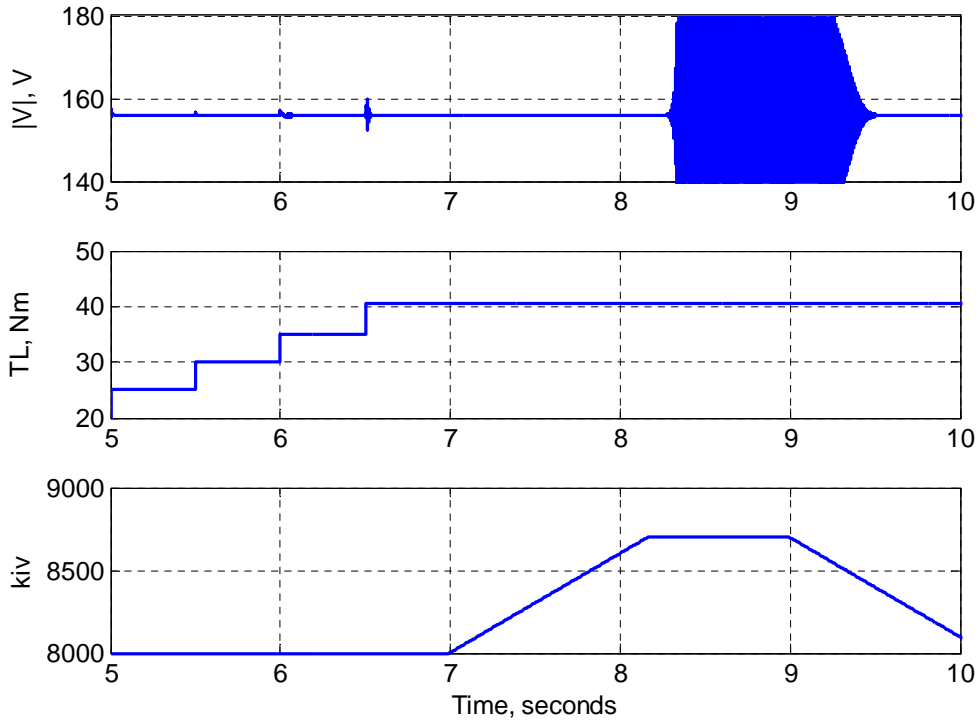
Fig. 4.19. Closed loop gain stability when k_{iv} changes between 8000 and 8700 operating at 20krpm.

The analysis of the derived plants (4.7) and (4.19) predicted that the load had more of an impact on stability margin compared to the effect of speed, especially at small loads. This can be seen by comparing the gain range in Fig. 4.7 and Fig. 4.16 at 20krpm. The gain range was reduced significantly from 6.0488×10^6 to 8400 after the transition into limited i_q^* case. As the load increased, the difference between the two influences becomes smaller.

In order to determine the gain range across operating points related to system load, the Routh Hurwitz criterion (RH) was employed [142]. RH utilises the eigenvalues to determine the stability of the closed loop system. If the coefficients of these eigenvalues are either positive or negative, then the closed loop system is assumed to be stable. As the FW plant was found to be third order, a third order Hurwitz polynomial should be used. This is given by:

$$P_{RH}(s) = x_3 s^3 + x_2 s^2 + x_1 s + x_0 = 0 \tag{4.21}$$

where x_3 to x_0 are the coefficients with respect to the order of the polynomial. To be stable under closed loop control, the coefficients must satisfy the following conditions:

$$x_3 > 0 \tag{4.22}$$

$$x_2 x_1 > x_3 x_0 \tag{4.23}$$

The FW plant for both current limited and unlimited cases can be expressed as:

$$\frac{\partial |V|}{\partial i_d^{\,*}} = \frac{G_v(s - z_1)(s - z_v)}{(s - p_1)(s - p_2)} \tag{4.24}$$

where p_1, p_2, z_1 are the poles and zeroes of the current closed loop transfer function, G_v and z_v are the gain and zero of the plant. Upon adding the integral controller, the closed loop transfer function can be found. With respect to (4.21), the coefficients can be calculated as according to:

$$x_3 = 1 \tag{4.25}$$

$$x_2 = k_{iv} G_v - p_1 - p_2 \tag{4.26}$$

$$x_1 = p_1 p_2 - k_{iv} G_v (z_1 + z_v) \tag{4.27}$$

$$x_0 = k_{iv} G_v z_1 z_v \tag{4.28}$$

Evaluating the coefficients to satisfy the conditions (4.22) and (4.23) yields:

$$k_{iv-lmt1} = \frac{p_1 + p_2}{G_v} \tag{4.29}$$

$$k_{iv-lmt2} = \frac{p_1 p_2}{G_v(z_1 + z_v)} \tag{4.30}$$

$$k_{iv-lmt3} = 0 \tag{4.31}$$

$$k_{iv-lmt4} = \frac{-B - \sqrt{B^2 - 4AC}}{2A} \tag{4.32}$$

$$k_{iv-lmt5} = \frac{-B + \sqrt{B^2 - 4AC}}{2A}$$

(4.33)

where

$$A = -G_v^{\ 2}(z_1 + z_v)$$

$$B = G_v[(z_1 + z_v)(p_1 + p_2) - z_1 z_v + p_1 p_2]$$

$$C = -(p_1 + p_2)p_1 p_2$$

The k_{iv} limits according to (4.29), (4.30), (4.31), (4.32), and (4.33) were derived at 20krpm and plotted in Fig. 4.20 for both unlimited and limited i_q^* respectively. A stable region was mapped considering all the limits in order to satisfy the RH stability conditions. In the unlimited i_q^* case, the k_{iv} gain range was largely determined by $k_{iv\text{-}lmt3}$ and $k_{iv\text{-}lmt5}$. The k_{iv} range verified the analysis of different levels of load done previously presented in Fig. 4.8. When i_q^* is limited, the boundaries were also constrained by $k_{iv\text{-}lmt3}$ and $k_{iv\text{-}lmt5}$. For loads less than 180A, the stable gain region was larger than the unlimited i_q^* case. Beyond that point, the stable gain region was almost the same.

The main conclusion from the analysis above is as follows; the FW controller for the S/G system in starting mode should be designed with consideration of the worst case operating point which corresponds to full load and unlimited i_q^*. Coincidently, the smallest k_{iv} gain range for both limited and unlimited i_q^* cases was similar (about 7650). This can be explained by both conditions sharing the same operating point at which the greatest restriction occurs. Since the initial k_{iv} selection for both cases resulted in a satisfactory control response, the final decision on the FW controller is to employ a pure integrator with the gain $k_{iv} = 1500$:

$$W_{fw}(s) = \frac{k_{iv}}{s}$$

(4.34)
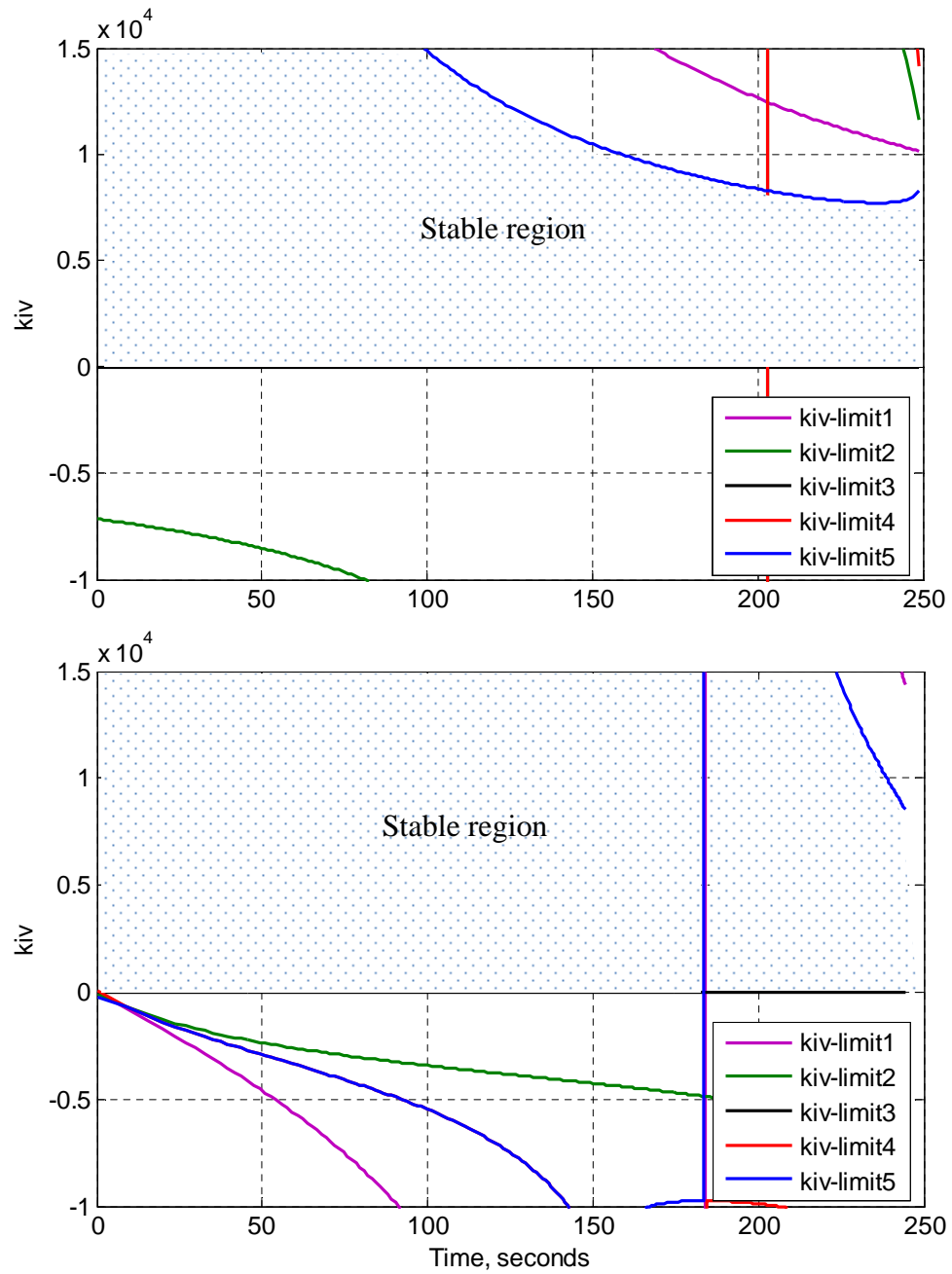
Fig. 4.20. k_{iv} range for stable operation in starter mode operating at 20krpm, unlimited (top) amd limited (bottom) i_q^* case.

4.5.1   Steady State Operation

The speed and FW controllers that were designed in the previous sections will now be compared against a non-linear model built in Matlab®/Simulink®. Fig. 4.21 shows the time domain simulation of the power system with the designed speed and FW controllers. ω_r^* and $/V/^*$ were set to 20krpm and 155.9V at the beginning of the

simulation. The difference between ω_r^* and ω_r at the start of the simulation means that maximum i_q is demanded which accelerated the PMM. $/V/$ also starts to increase due to the PMM back-emf. No i_d is required as $/V/$ is still within $/V/^*$. This is achieved by changing the output limit of the controller from 0A to -400A. Negative i_d is injected in order to maintain $/V/$ at $/V/^*$. i_q is reduced by the limiter due to the requested injection of i_d. The stator current response, i_s, shows that the total magnitude is always kept constant at 400A. When ω_r^* is reached, i_q drops to zero as the torque is no longer required. i_d reaches a steady state value dependent on ω_r. At t = 17s, a step impact of load T_L = 20Nm is demanded and the machine voltage is controlled to return to its rated value. This simulation confirms the stable operation of the designed speed and FW control in starting mode. The overall control performance was shown to be satisfactory for the required S/G system operation when used as a starter.
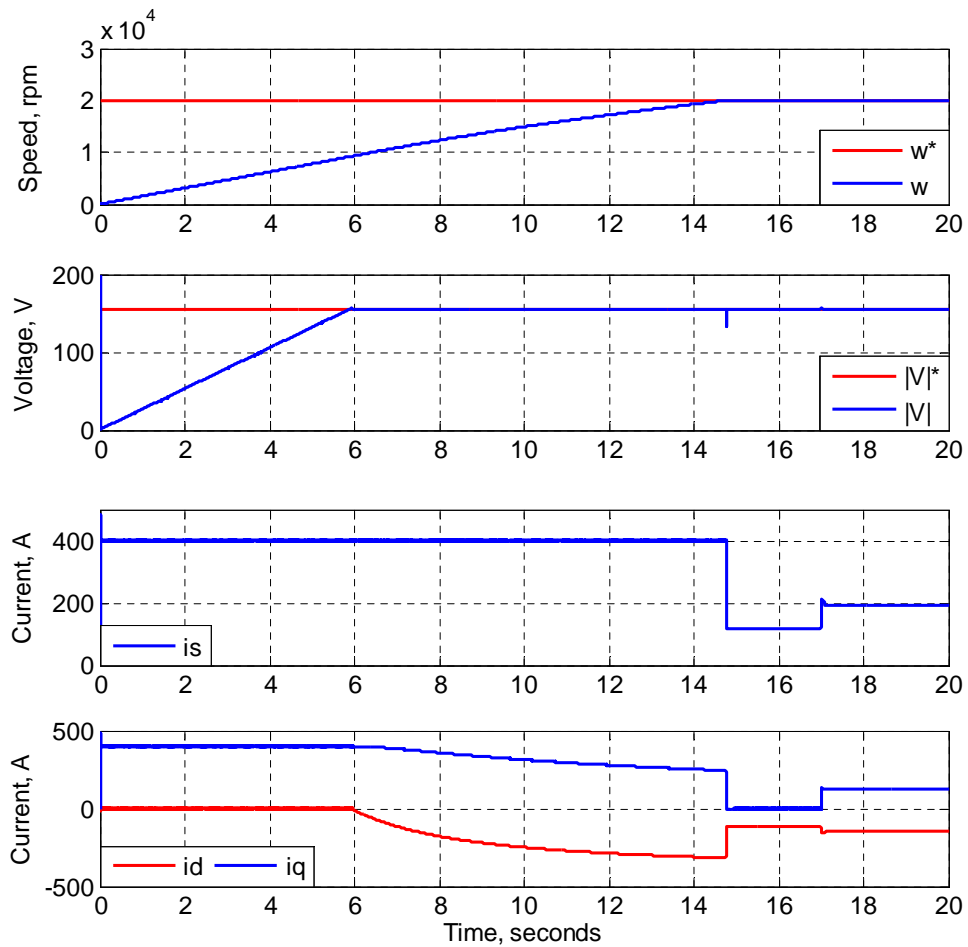
Fig. 4.21. Time domain simulation results of S/G system with designed controllers in starter mode.

The FW control analysis and design for starting mode which was conducted in this Chapter can be summarised as follows:

- To begin, the plant for FW control was derived. It was shown that the plant properties depend on the state of the dynamic current limiter which limits i_q^* according to the machine speed (i.e. i_d^*) and maximum current capability of the S/G system.

- The plant's transfer function included a zero in both cases that was influenced by the operating speed and/or load. Depending on the specific operating conditions, the zero could belong either to LHP or RHP of the complex plane making the plant either minimal or non-minimal phase.

- When the zero is located in the RHP (a non-minimum phase plant), there is a limited range that can be selected for the gain of the FW controller in order to ensure the stability of the control loop.

- The operating point corresponding to the fastest machine speed and full load was found to be the worst-case design point for the S/G in starter mode. Hence, the FW controller should be designed for this operating point in order to ensure effective control throughout starter mode operation.

- It was found that only small values of proportional gain can be used if required; otherwise a pure integrative controller is sufficient for FW control.

4.6   Conclusion

This Chapter dealt with the analysis and design of a FW mode controller for an AEGART-type S/G system. The design of the outer control loops was based on the control plant models derived in Chapter 3. The implementation of a direct current FW method into the control scheme of the S/G opened investigation of two states created by the dynamic current limiter. Hence, two distinct control plants were derived for subsequent FW control design. The plants were verified with non-linear equivalent time-domain models in Matlab$^®$/Simulink$^®$ at different operating points. It was shown that the plant properties were generally influenced by speed and load torque. The non-minimum phase nature of the derived plants limited the stability range and this was analysed. This stability range was analysed with respect to operating speed or load and the appropriate FW controller gains were derived. It was found that the nature of the open loop plant was very sensitive towards the controller's proportional gain, particularly for the limited i_q^* case. Additionally, it was shown that the wide speed range of the S/G system could cause more complications when using PI controllers; hence a pure integral controller was chosen for FW control in the subject application. Time domain simulation of the designed controllers with the S/G system showed satisfactory control performance in starter mode.

Chapter 5   Generator Mode Operation:

Analysis and Control Design

5.1   Introduction

This Chapter will detail the control design and analysis for the S/G system in generator mode based on the plant models derived in Section 3.5. Following the discussion in Chapter 3, the detailed control scheme for generator mode is introduced in Fig. 5.1. The FW controller remains active during generator mode in order to maintain $|V|$ at the required level and avoid overmodulation of the converter. The speed controller employed in starter mode will be replaced by a DC link controller, W_{idc}, acting along the q-axis.
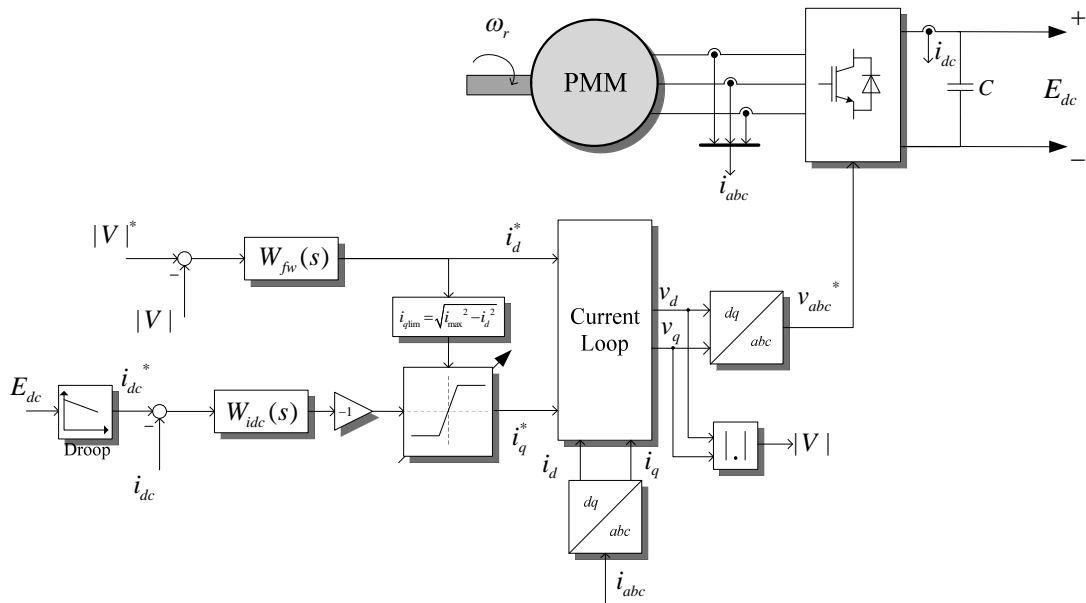
Fig. 5.1. Detailed control scheme for generator mode.

Referring back to Fig. 1.4, the active power flow was towards the DC link in generator mode. This means that i_q^* has to be inverted in order to re-direct the power flow towards the DC link. The droop gradient, or gain, $k_{droop,}$ based on Fig. 2.32 can be calculated and the line expressed mathematically as:

$$i_{dc}{}^* = k_{droop}(E_{dcrated} - E_{dc}) \tag{5.1}$$

As can be seen from (5.1) E_{dc} is compared to the rated DC link voltage reference, $E_{dcrated}$, in order to provide an appropriate value for the DC link current reference, $i_{dc}{}^*$. A linear controller can then be used to regulate i_{dc} based on this reference in order to meet the electrical load demands.

Within Fig. 5.1, i_{dc} is measured before the capacitor in order to attempt fast current control. Practical (commercial) power converters are normally constructed with a laminated bus bar arrangement (or equivalent printed circuit board) between the power switches and the DC link capacitor. This is done to reduce the commutating inductance and to minimise voltage overshoot and ringing on the devices voltages at commutation. Placing a current transducer in this path would not only be physically difficult and inconvenient, but may also increase the inductance unacceptably. However as an alternative, i_{dc} can be derived from the measurement of i_a, i_b, and i_c along with their corresponding switching signals [143]. This method allows i_{dc} to be calculated without using a dedicated sensor.

The plant for the DC link controller will be derived in the following Sub-section. In a similar way to the control design process used for the FW controller in the previous Chapter, the control plant will be studied at different operating speeds and loads. The controller gain values will then be selected based on the worst case operating point. The FW plant will then be analysed in generation mode to determine any changes in the plant nature that might affect the stability of the FW controller designed in the previous Chapter for starter mode. In a similar way to the analysis performed in starter mode, two distinct modes shall be considered in this analysis due to the presence of a dynamic limiter.

5.2   DC Link Controller Design

In order to properly analyse and design the controller, the plant relating ∂i_{dc} to $\partial i_q{}^*$ has to be derived. The linearised plant block diagram can be seen in Fig. 5.2. Since k_{droop} has already been defined as part of the AEGART S/G system design requirements, only the i_{dc} controller needs to be designed.

The assumptions when the plant was derived were:

- Constant speed at each operating point. During this mode, the speed is externally controlled by the aircraft engine. The speed dynamics are assumed to be much slower than the electrical system, hence the speed can be considered constant.

- In the case of limited i_q^*, the control value of i_q^* is determined by the FW controller due to function of the dynamic limiter prioritising FW control signals. Therefore this case was not considered for DC link control design analysis.
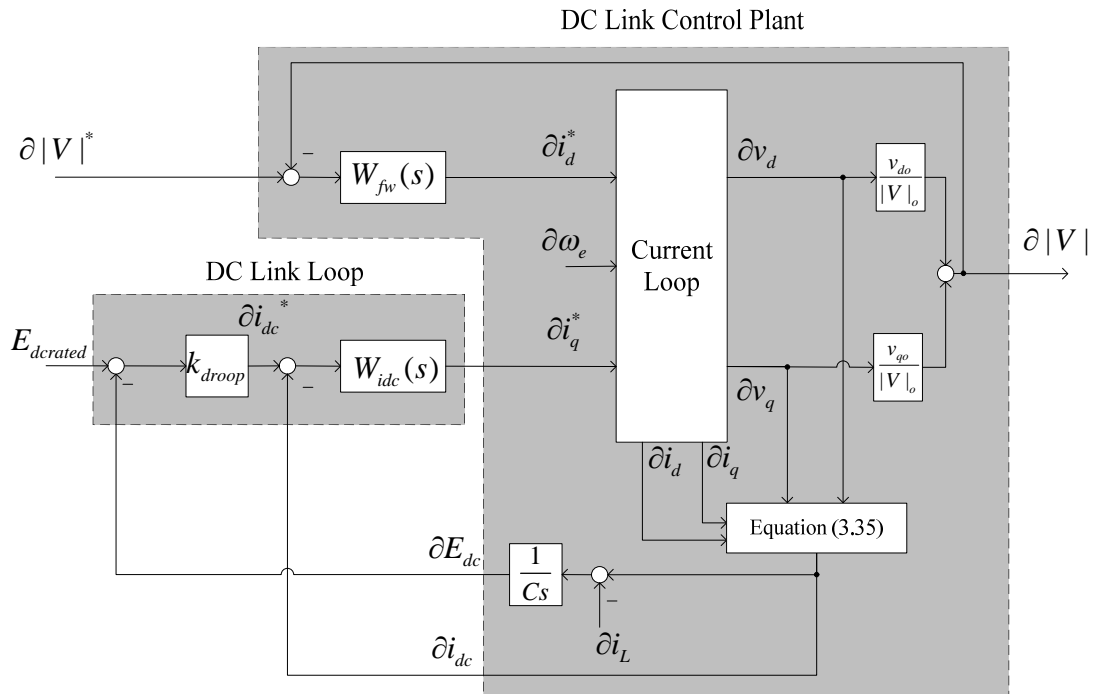
Fig. 5.2. Linearised block diagram for generator mode, unlimited i_q^*.

The derivation process of the DC link voltage control plant starts with f_{21} and f_{22}, derived earlier in (3.43). The output ∂i_{dc} affects both by ∂i_d^* and ∂i_q^*. Usually an assumption can be made here that power is only supplied from the q-axis controllers. However, it is most effective on systems that prefer zero reactive power (controlled by the d-axis in this system). The presence of the FW controller influences ∂i_d^* which affects ∂i_q^* indirectly within the feed forward terms, especially when FW is in effect. The influence of ∂i_d^* on ∂i_{dc} cannot generally be ignored and should be investigated.

Hence, the dynamics of f_{21} is also considered here. f_{21} is related to output ∂i_{dc} via the FW controller. The FW controller can be equated as:

$$i_d{}^* = \frac{k_{iv}}{s}\left(\left|V\right|^* - \left|V\right|\right)$$

(5.2)

In linearised form, the controller becomes:

$$\partial i_d{}^* = -\frac{k_{iv}}{s}\partial\left|V\right|$$

(5.3)

Using the linearised voltage limit (3.34) and machine voltage equations (3.32), (3.33), one can derive:

$$\partial i_d{}^* = -\frac{k_{iv}}{s}\left[\begin{array}{c}\left(\dfrac{v_{do}}{\left|V\right|_o}\left(R_s + L_d s\right) + \dfrac{v_{qo}}{\left|V\right|_o}\omega_{eo}L_d\right)\partial i_d \\[4mm] +\left(-\dfrac{v_{do}}{\left|V\right|_o}\omega_{eo}L_q + \dfrac{v_{qo}}{\left|V\right|_o}\left(R_s + L_q s\right)\right)\partial i_q\end{array}\right]$$

(5.4)

To reduce the complexity of the transfer function, the current closed loop transfer functions (3.27) and (3.28) are used instead of (3.39) and (3.40). Therefore equation (5.4) can be transformed into:

$$\frac{\partial i_d{}^*}{\partial i_q{}^*} = \frac{-k_{iv}\left(k_{pq}s + k_{iq}\right)\left(-v_{do}\omega_{eo}L_q + v_{qo}\left(R_s + L_q s\right)\right)\left(L_d s^2 + \left(R_s + k_{pd}\right)s + k_{id}\right)}{\left[\left(L_q s^2 + \left(R_s + k_{pq}\right)s + k_{iq}\right)\left(\begin{array}{c}\left|V\right|_o s\left(L_d s^2 + \left(R_s + k_{pd}\right)s + k_{id}\right) \\[2mm] +k_{iv}\left(k_{pd}s + k_{id}\right)\left(v_{do}R_s + v_{do}L_d s + v_{qo}\omega_{eo}L_d\right)\end{array}\right)\right]}$$

(5.5)

This transfer function is substituted into f_{21} and then combined with f_{22}. The plant for the i_{dc} controller is therefore:

$$\frac{\partial i_{dc}}{\partial i_q{}^*} = \frac{-3CE_{dco}s\left(k_{iq} + k_{pq}s\right)\left(b_{1nl}s^4 + b_{2nl}s^3 + b_{3nl}s^2 + b_{4nl}s + b_{5nl}\right)}{\left(L_q s^2 + \left(R_s + k_{pq}\right)s + k_{iq}\right)\left(2CE_{dco}{}^2 s + 3i_{do}v_{do} + 3i_{qo}v_{qo}\right)\left(b_{6nl}s^3 + b_{7nl}s^2 + b_{8nl}s + b_{9nl}\right)}$$

(5.6)

The terms from b_{1nl} to b_{9nl} can be found in Appendix B. An operating point of 32krpm was selected in order to verify the mathematical plant with the non-linear equivalent model in Simulink®. It can be seen from Fig. 5.3 that an identical step

responses produced by both the mathematical plant and the equivalent model. The plant, with $i_L = 50$A was operating at $v_{do} = 23.8$V, $v_{qo} = 154$V, $|V|_o = 155.9$V, $i_{do} = -213.27$A, $i_{qo} = -24.17$A, and $\omega_{eo} = 10048$rad/s. Numerically, (5.6) can be equated as:

$$f_{g\_nl\_32} = \frac{-0.12059s(s-1.641\times10^5)(s+4449)(s+1381)(s^2+7272s+3.932\times10^7)}{(s+1355)(s+189.2)(s^2+8884s+3.948\times10^7)(s^2+7731s+4.299\times10^7)} \quad (5.7)$$
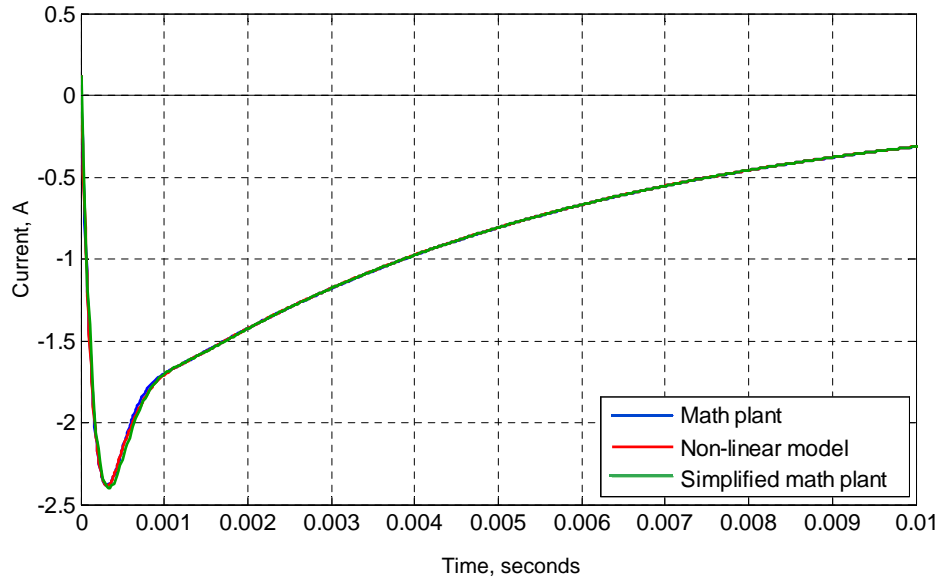
Fig. 5.3. Open loop plant step response at 32krpm with a 50A load in generator mode with unlimited i_q^*.

At the selected operating point, equation (5.7) contains a positive zero which indicates the plant is non-minimum phase. Furthermore, there are four pole/zero pairs which can be clearly seen within root locus, as shown in Fig. 5.4. These poles and zeroes are located close to one another and so as such they cancel each other's dynamics. The plant is sixth order which can be difficult to analyse and use when trying to design a simple linear controller.

Therefore additional assumptions were made in order to simplify the plant:

- The dominant dynamics are contributed by the ∂i_q terms in transfer function (5.4). Hence, the influence of ∂i_d terms is assumed to be negligible and is not considered for the plant derivation.

The plant can therefore be simplified to transfer function f_{22}:

$$\frac{\partial i_{dc}}{\partial i_q^*} = \frac{-3E_{dco}Cs\left(k_{pq}s+k_{iq}\right)\left(-i_{do}\omega_{eo}L_q+v_{qo}+i_{qo}\left(R_s+L_qs\right)\right)}{\left(L_qs^2+\left(R_s+k_{pq}\right)s+k_{iq}\right)\left(2E_{dco}^2Cs-3\left(v_{do}i_{do}+v_{qo}i_{qo}\right)\right)} \qquad (5.8)$$
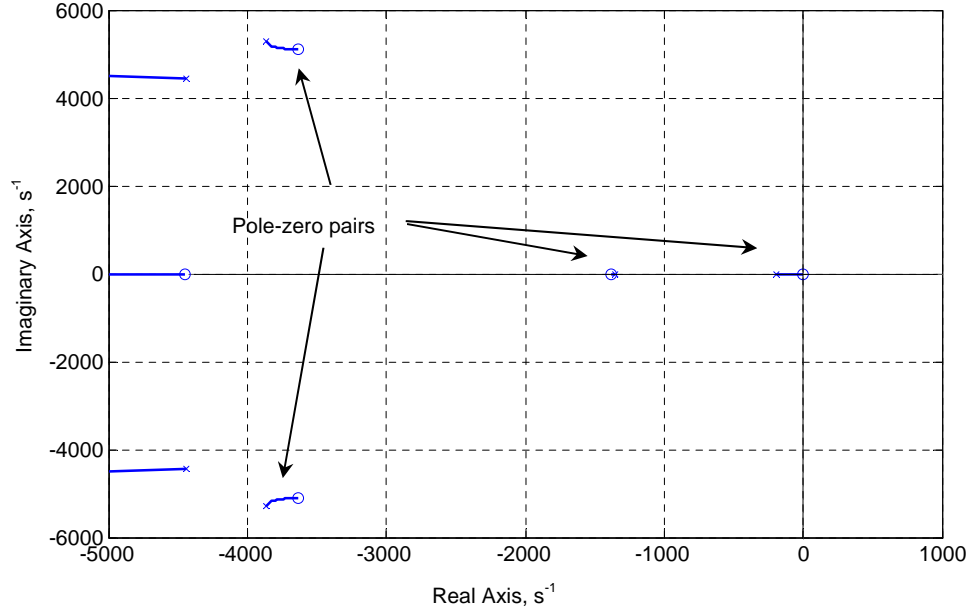
Fig. 5.4. Pole-zero pairs from transfer function (5.7).

At the same operating point as above, transfer function (5.8) can be written numerically as:

$$f_{g\_nl\_32s} = \frac{-0.12059s(s-1.531\times10^5)(s+4449)}{(s+189.2)(s^2+8884s+3.948\times10^7)} \qquad (5.9)$$

The plant is now represented by just a third order transfer function when the effect of ∂i_d^* is assumed to be negligible. It can be seen that the RHP zero is slightly different compared to (5.7). The difference in the effect on the overall plant dynamics is not significant as the zeroes are at very high frequencies. This can be seen in Fig. 5.3 where there was a slight difference at the beginning of the step response. Hence, this simplified plant is used for control design of the i_{dc} controller.

The plant was observed at different operating points that are influenced by speed and load. During generation, the speed range is between 20krpm and 32krpm while the load, i_L, can be up to 170A. This was calculated based on the rated power of the PMM (45kW) when $E_{dc} = 270$. It was assumed that the electrical loads connected to the DC bus were referred to in terms of current. Fig. 5.5 shows the location of the

117

zero on the root locus at three different speeds. It can be seen that the positive zero moves towards the origin as the speed increases. The approximate representation of this zero is known from equation (5.8) as:

$$z_{gen} = \frac{-(v_{qo} + i_{qo}R_s - i_{do}\omega_{eo}L_q)}{i_{qo}L_q} \tag{5.10}$$
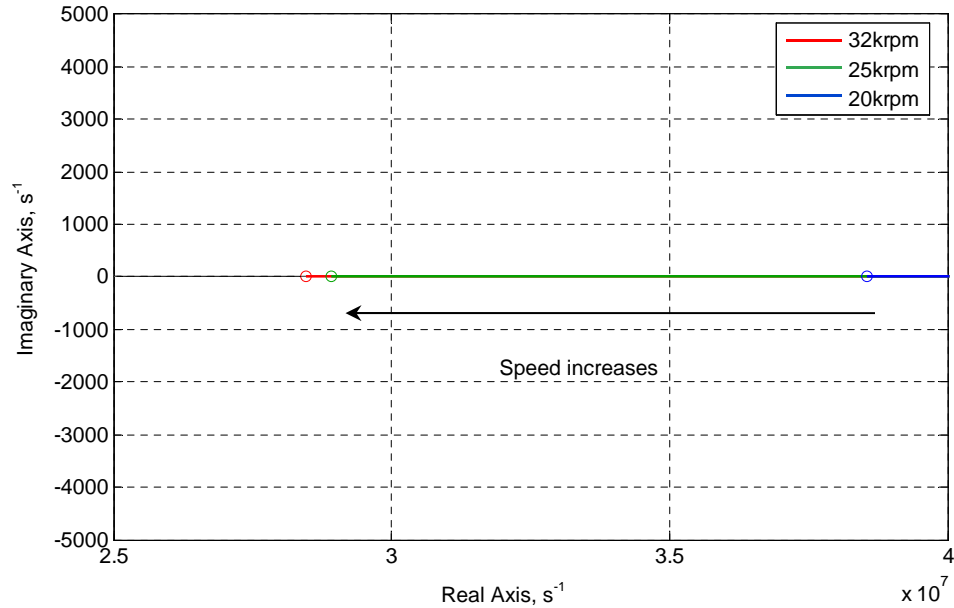
Fig. 5.5. Zero movement when speed increases from 20krpm to 32krpm, generator mode, unlimited i_q^*.

The movement of this zero can be seen in Fig. 5.6 for different electrical load demands of 50A, 100A, and 170A. The other poles and zeroes of the plant do not change significantly at different operating speeds or loads.

The trajectory of the zero at different speeds and loads can be seen in Fig. 5.7. The zero remains on the RHP throughout the operating speed and load range in generator mode with unlimited i_q^*. Fig. 5.7 also shows that the zero moves closer to the origin as the load increases and when the operating speed is reduced.

The closed loop response of the plant when utilising an integrative controller was also investigated. Fig. 5.8 shows the closed loop root locus at different operating speeds. It can be seen that the poles move towards the RHP when the controller's integral gain, k_{ii}, is increased. The allowable range for k_{ii} can therefore be determined

as the poles must not cross the imaginary axis in order to guarantee system stability. This k_{ii} range reduces as the operating speed increases, as seen in Fig. 5.8.
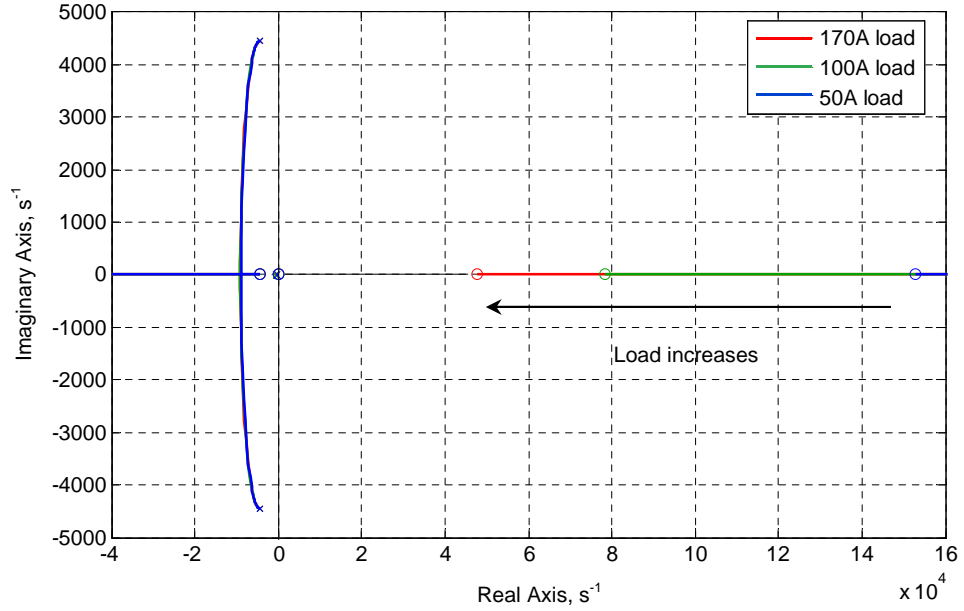
Fig. 5.6. Pole zero movement when load increases from 50A to 170A at 32krpm, generator mode, unlimited i_q^*.
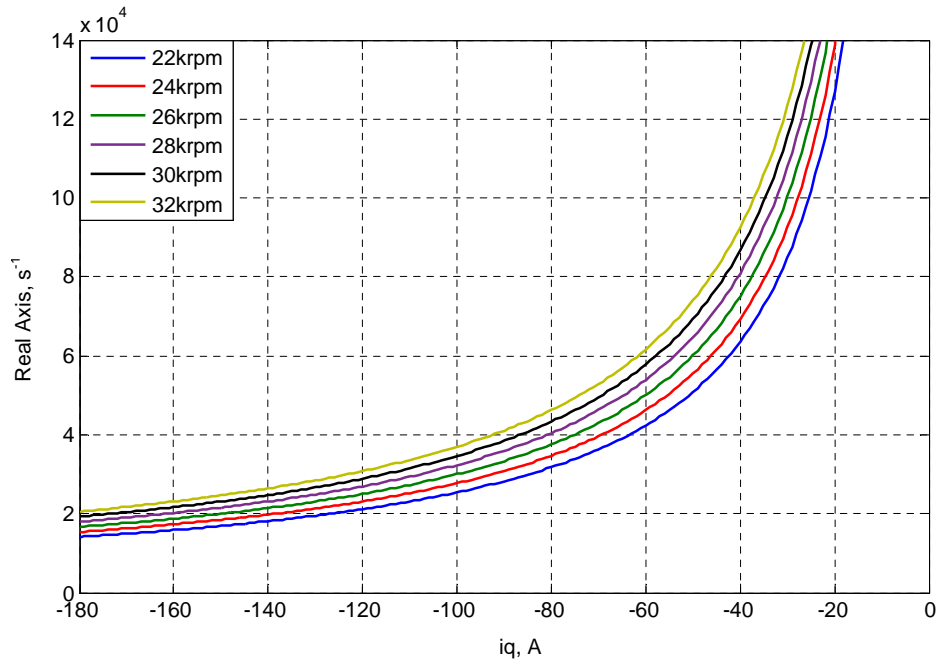
Fig. 5.7. Zero trajectories across load range at different speeds in generator mode, unlimited i_q^*.
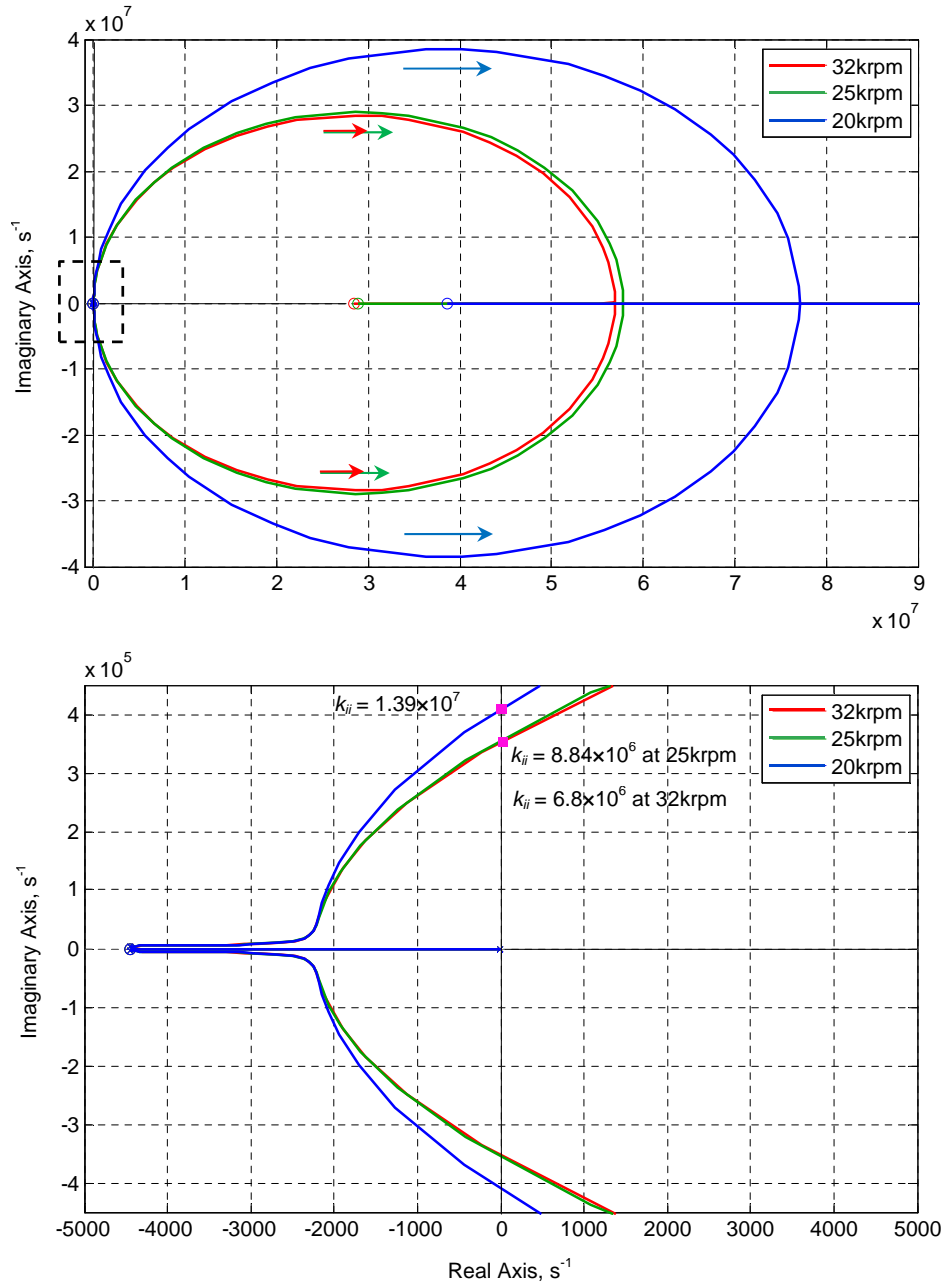
Fig. 5.8. Closed loop root locus of i_{dc} plant at different speeds (top) and the zoomed area (bottom), in generator mode with unlimited i_q^*.

A similar trend can also be seen in Fig. 5.9 for closed loop root locus at different load levels. The slower positive zero reduces the effective k_{ii} range significantly from 6.8×10^6 (no load) to 1.2×10^4 (full load). The range of k_{ii} due to load variations is therefore smaller compared to the k_{ii} range due to speed changes. Overall, the plant for DC-link control was found to be significantly affected by speed and load variations. From the analysis above, it has become clear that the worst case

scenario corresponded to the highest speed at full load. The i_{dc} controller can therefore be designed based on this operation point.
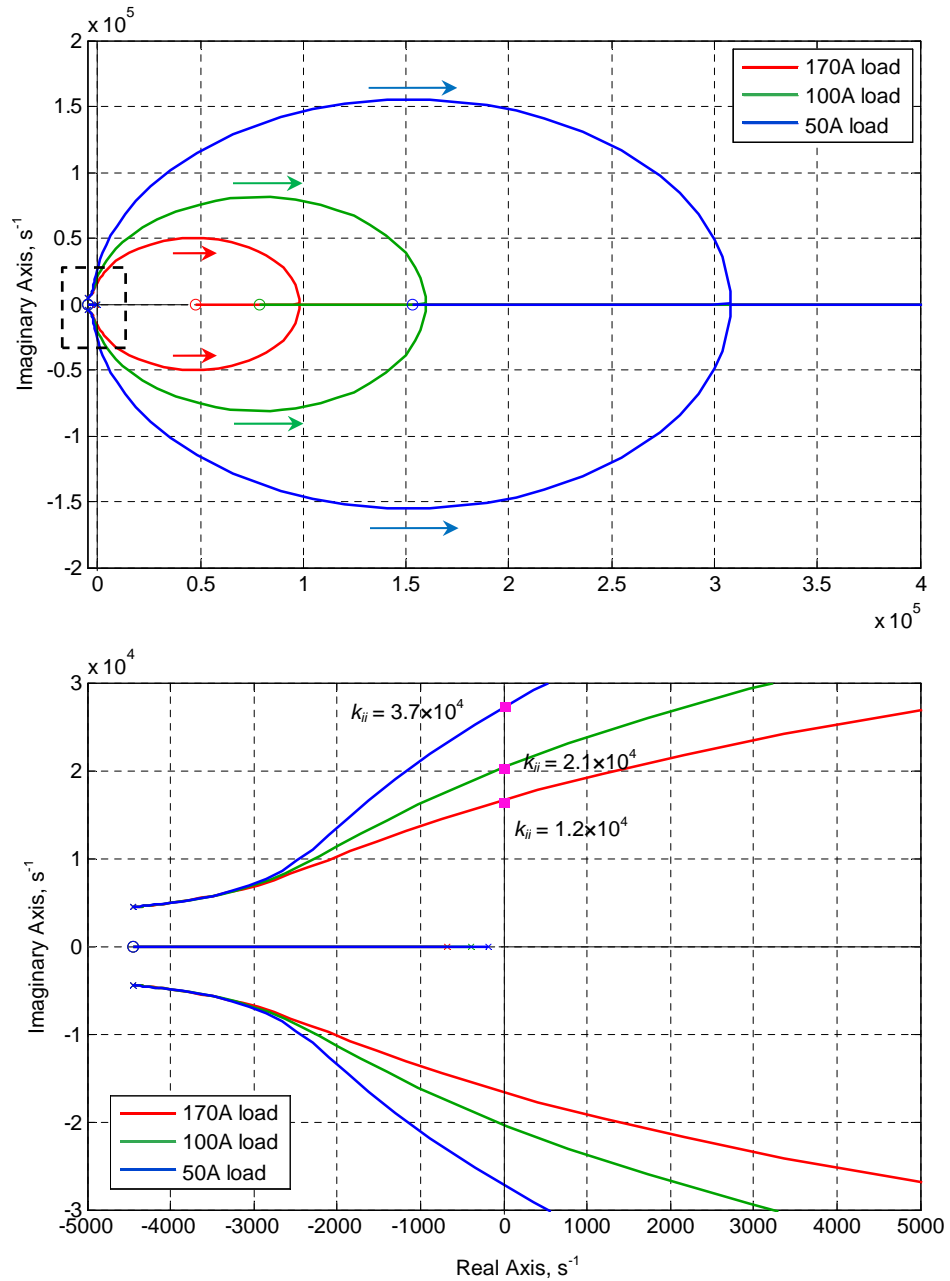
Fig. 5.9. Closed loop root locus of i_{dc} plant at different loads operating at 32krpm (top) and zoomed area (bottom) in generator mode with unlimited $i_q^{\ *}$.

The addition of proportional term, k_{pi}, was also considered during the design phase. The root locus of k_{pi} at the worst case operating point (full load, maximum speed) in generator mode can be seen in Fig. 5.10. The locus is mostly on the LHP which indicated a more stable closed loop plant. However, when the k_{pi} gain is increased, one of the poles moves towards the positive zero and appears on the RHP.

Therefore k_{pi} cannot be too large as this plant is very sensitive towards this gain and can become unstable. As shown in Fig. 5.10, when k_{pi} was increased from 2.2 to 2.5, the pole appeared on the RHP and caused instability. Careful use of k_{pi} is possible within the i_{dc} controller but a pure integral configuration is an alternative solution.
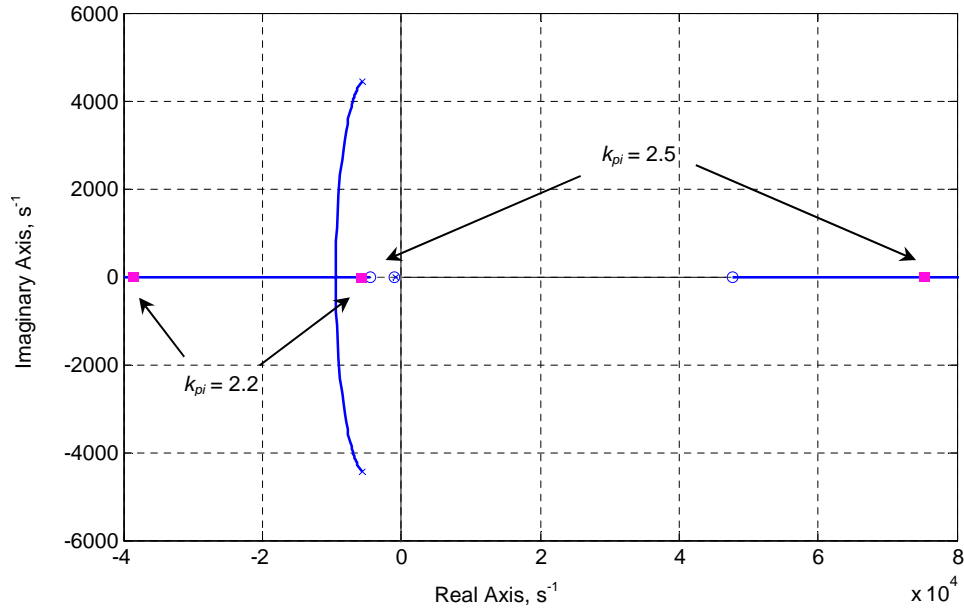
Fig. 5.10. Closed loop root locus with PI controller at different k_{pi}, generator mode unlimited i_q^*.

Fig. 5.11 shows the closed loop step response of the derived plant with different k_{pi} for the i_{dc} controller. Increasing k_{ii} decreases the settling time, and makes it possible to achieve very fast bandwidths (higher than 1kHz when $k_{ii} > 1500$). When k_{pi} is increased, the undershoot response due to the non-minimum phase nature becomes more significant.

For the S/G system in this study, the i_{dc} controller with both proportional and integral terms can be written as:

$$W_{idc}(s) = k_{pi} + \frac{k_{ii}}{s} \tag{5.11}$$

The value of k_{ii} was selected to be 200 in order to avoid conflict with the fast bandwidth of the inner current loops. k_{pi} was selected to be 0.5 so that it was well below the limit of 2.2. With $k_{pi} = 0.5$ and $k_{ii} = 200$, a fast output response with little

overshoot can then be obtained without exceeding the inner current loop bandwidth, as shown in Fig. 5.11.
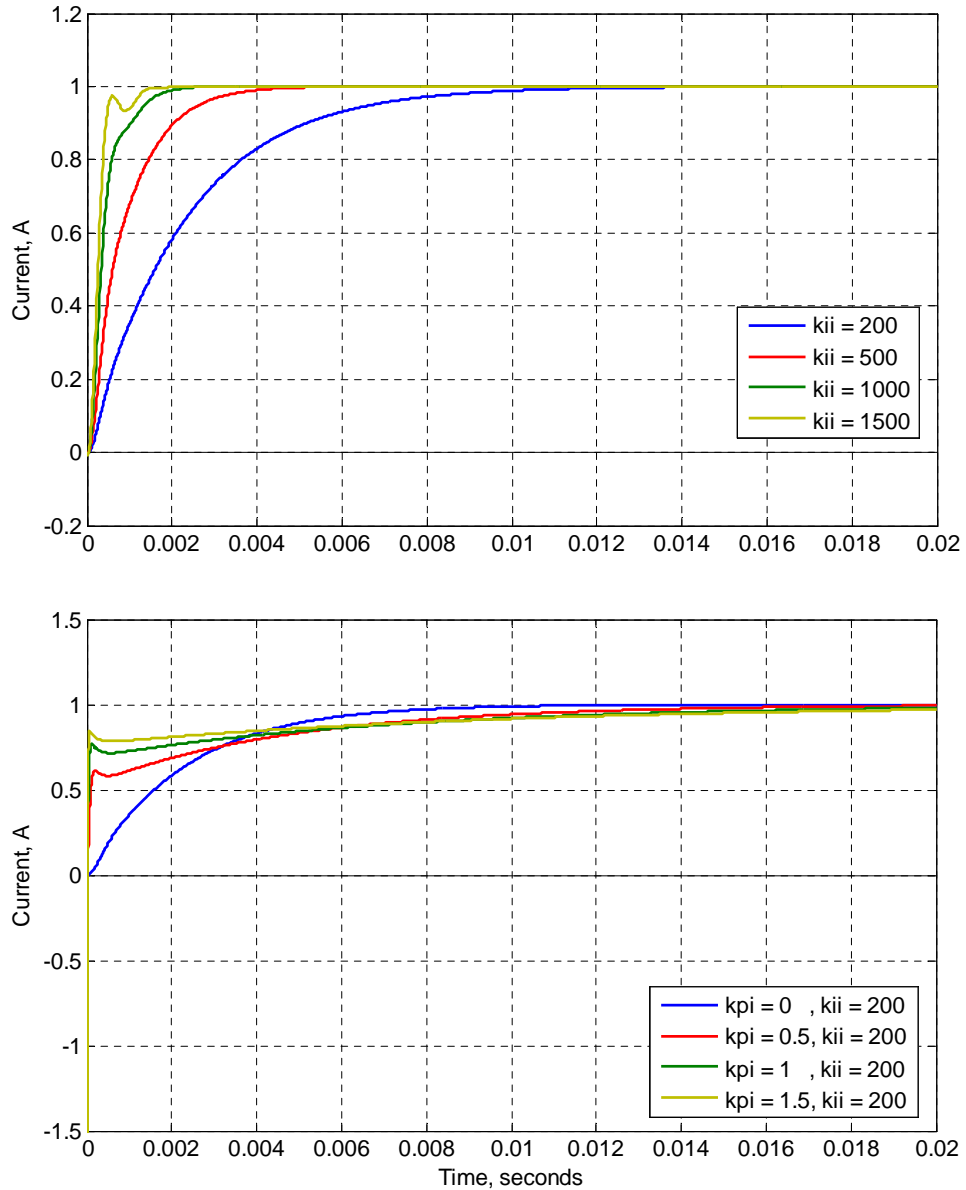
Fig. 5.11. Closed loop step response to $i_{dc}^* = 1A$ with variation of i_{dc} controller k_{ii} (top) or k_{pi} (bottom) operating at 32krpm, in generator mode with unlimited i_q^*.

After completing the i_{dc} controller design, the droop coefficient can be added to the overall DC link voltage controller. Since droop control can be regarded as a proportional gain, based on the linear droop characteristic, and as it is part of the S/G design requirement, the control can be demonstrated in time domain simulations. The results shown in Fig. 5.12 were obtained using a non-linear model built in Simulink®. The controller was tested with a full step load of 170A as this is the

worst case scenario. This test was carried out in order to determine if the E_{dc} response complies with MIL-STD-704F. It can be seen from Fig. 5.12 that E_{dc} initially drops from 270V to 250V when the load step is applied at $t = 0.04$s. It is obvious from Fig. 5.12 that the droop control response to a full load step is well within the limits specified by MIL-STD-704F.
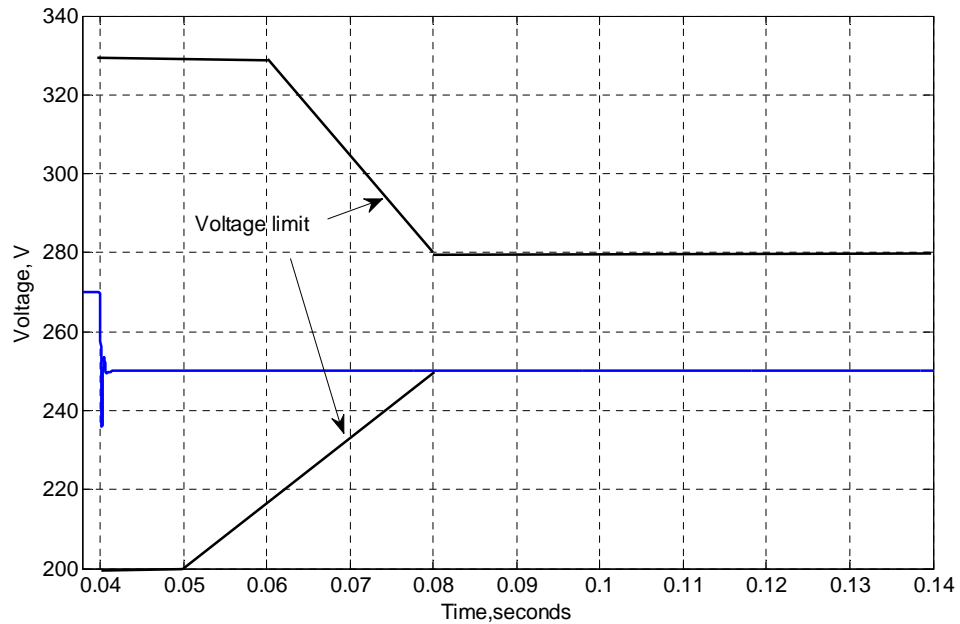
Fig. 5.12. E_{dc} to a step of $i_L = 170$A for comparison with 270VDC voltage transient limit from MIL-STD-704F.

Summarising the i_{dc} controller design process, the following should be noted:

- The i_{dc} control plant is non-minimum phase in generator mode, as indicated by a positive zero. The controller gain range is not as critical as the FW controller because of the assumption that the S/G system only operates with unlimited i_q^*.
- The i_{dc} plant can be simplified by only considering the dynamics that are influenced by the perturbation of i_q^*.
- The worst case operating point for the i_{dc} plant is at the highest operating speed (32krpm) with full load (170A).
- There is a limited range for the controller gain due to the positive zero in the plant. The i_{dc} controller therefore has to be designed based on the worst case

operating point in order to ensure stable control across all operating points within generator mode.

- The designed i_{dc} controller works well with the defined S/G droop coefficient and easily complies with the 270VDC voltage transient limit requirements as stated in MIL-STD-704F.

5.3 Flux Weakening Plant Analysis in Generator Mode

The purpose of analysing the FW plant in generator mode is to ensure the system stability when the q-axis controller changes from speed to DC-link control. The plant will now be re-derived with the DC link controller providing q-axis control signals. In this mode, it is again assumed that the speed is constant at each operating point. As before, the two cases created from the use of dynamic limitation are considered within the control design process.

5.3.1 Unlimited i_q^* Case

Fig. 5.13 shows the linearised FW plant and its controller for the unlimited i_q^* case. The DC link controller was replaced with a speed controller in generator mode. The plant was derived from f_{11} and f_{12} as was the case in the previous Chapter. The following were assumptions made during the derivation of the FW plant in generation mode with unlimited i_q^*:

- ∂i_q^* has an influence on ∂i_{dc} which affects ∂i_d^* as part of the plant input. Therefore, the converter functional model (3.35), droop equation (5.1) and the connecting i_{dc} controller are considered to derive the appropriate transfer function.

The linearised form of the i_{dc} controller and the droop coefficient are shown below:

$$\partial i_q^* = -\frac{k_{pi}s + k_{ii}}{s}\left(\partial i_{dc}^* - \partial i_{dc}\right) \qquad (5.12)$$

$$\partial i_{dc}^* = -k_{droop}\partial E_{dc} \qquad (5.13)$$
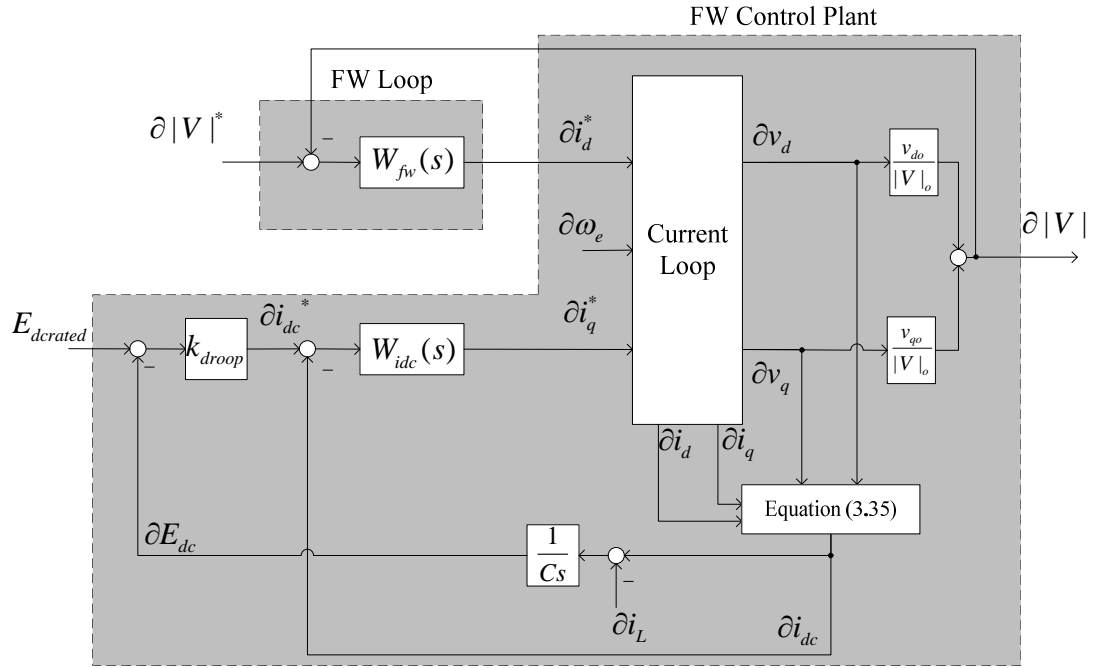
Fig. 5.13. Linearised block diagram for FW plant analysis in generator mode with unlimited $i_q{}^*$.

The ∂i_{dc} term in (5.12) can be represented by equation (3.42) without the $\partial \omega_e$ term:

$$\partial i_{dc} = \frac{3E_{dco}Cs}{2E_{dco}{}^2Cs - 3\left(v_{do}i_{do} + v_{qo}i_{qo}\right)} \begin{bmatrix} -\left(-i_{do}\omega_{eo}L_q + v_{qo} + i_{qo}\left(R_s + L_q s\right)\right)\partial i_q \\ -\left(i_{qo}\omega_{eo}L_d + v_{do} + i_{do}\left(R_s + L_d s\right)\right)\partial i_d \end{bmatrix} \quad (5.14)$$

The $\partial i_{dc}{}^*$ term can then be expanded by using (3.21), (5.13) and (5.14):

$$\partial i_{dc}{}^* = \frac{3k_{droop}E_{dco}}{2CsE_{dco}{}^2 - 3\left(v_{do}i_{do} + v_{qo}i_{qo}\right)} \begin{bmatrix} \left(i_{do}L_d s + v_{do} + R_s i_{do} + \omega_{eo}i_{qo}L_d\right)\partial i_d \\ +\left(i_{qo}L_q s + v_{qo} + R_s i_{qo} - \omega_{eo}i_{do}L_q\right)\partial i_q \end{bmatrix} \quad (5.15)$$

Equations (3.27), (5.14) and (5.15) can be substituted into (5.12) to derive the transfer function relating $\partial i_q{}^*$ to $\partial i_d{}^*$. Substitution of the resultant transfer function into f_{12} and combination with f_{11} forms a sixth order plant:

$$\frac{\partial |V|}{\partial i_d{}^*} = \frac{\left(k_{id} + sk_{pd}\right)\left(a_{1nl}s^5 + a_{2nl}s^4 + a_{3nl}s^3 + a_{4nl}s^2 + a_{5nl}s + a_{6nl}\right)}{|V|_o\left(L_d s^2 + \left(R_s + k_{pd}\right)s + k_{id}\right)\left(a_{7nl}s^4 + a_{8nl}s^3 + a_{9nl}s^2 + a_{10nl}s + a_{11nl}\right)} \quad (5.16)$$

The coefficients for the plant can be found in Appendix B. The analysis was performed for both cases in the same way as detailed in Sub-sections 4.4.1 and 4.4.2. The plant was verified at various operating points related to speed and load. Fig. 5.14

shows the open loop step response verification between the derived plant and the non-linear model. The operating point selected was full speed, 32krpm, and v_{do} = -0.76V, v_{qo} = 155.88V, $|V|_o$ = 155.9V, i_{do} = -211.46A, i_{qo} = -1.03A, ω_{eo} = 10048rad/s. At this point, the plant can be evaluated numerically as:

$$f_{fw\_nl\_32} = \frac{0.45018(s+2.029\times10^4)(s+4449)(s+3044)(s+290.1)(s^2+9339s+1.05\times10^8)}{(s+2997)(s+290.1)(s^2+8884s+3.947\times10^7)(s^2+1.464\times10^4 s+1.102\times10^8)}$$

(5.17)
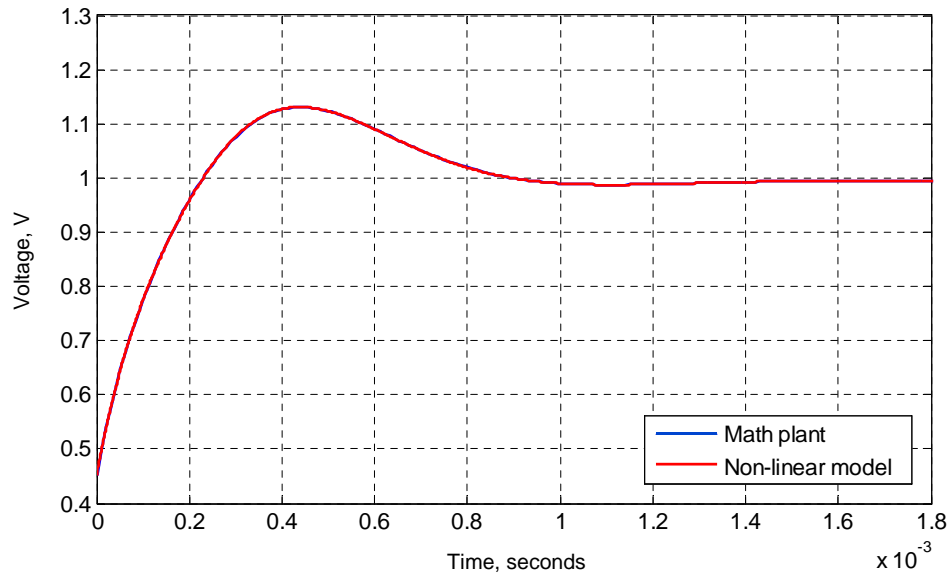
Fig. 5.14. Open loop FW plant step verification at 32krpm in generator mode with unlimited i_q^*.

From (5.17), it can be seen that there were a number of poles and zeroes that are very close to one another. The zeroes at 3044 and 290.1 are in the approximate locations of the poles at 2997 and 290.1 respectively. These pole and zero pairs are due to the cross linked dynamics of the converter functional equation. They can be assumed to cancel each other out and thus only the dominant poles and zeroes remain:

$$f_{fw\_nl\_32s} = \frac{0.45018(s+2.029\times10^4)(s+4449)(s^2+9339s+1.05\times10^8)}{(s^2+8884s+3.947\times10^7)(s^2+1.464\times10^4 s+1.102\times10^8)} \quad (5.18)$$

The pole zero movements are mapped out in Fig. 5.15 for operating speeds of 20krpm, 25krpm and 32krpm. It can be seen that the zero previously shown to be normally on the RHP during starter mode operation is now located on the LHP.

127

Similar zero movements were found for load impacts at a constant speed of 32krpm, as shown in Fig. 5.16. Once again, the positive zero position changes the most as it moves further towards the origin with increased load impact.

The trajectories of the dominant zero at different speeds can be seen in Fig. 5.17. The load demand was expressed in terms of i_q for consistency with the analysis in starter mode. Throughout all operating conditions in generator mode with unlimited i_q^*, the zero was located within the RHP. This indicates that the FW plant changes from non-minimum phase in starter mode to minimum phase in generator mode.
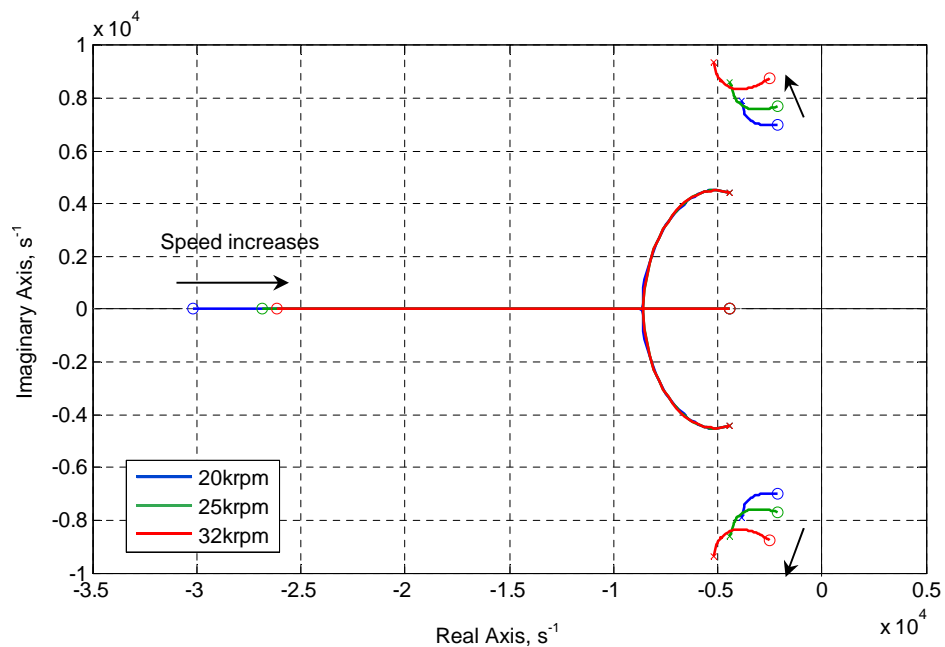
Fig. 5.15. Pole zero location as speed increases from 20krpm to 32krpm in generator mode with unlimited i_q^*.

The closed loop response of the derived FW plant with the previously designed FW controller was also analysed. The root loci at different speeds and loads are shown in Fig. 5.18 and Fig. 5.19 respectively. When k_{iv} increases, the poles remain within the LHP, indicating a more stable plant compared to the starter mode variant.
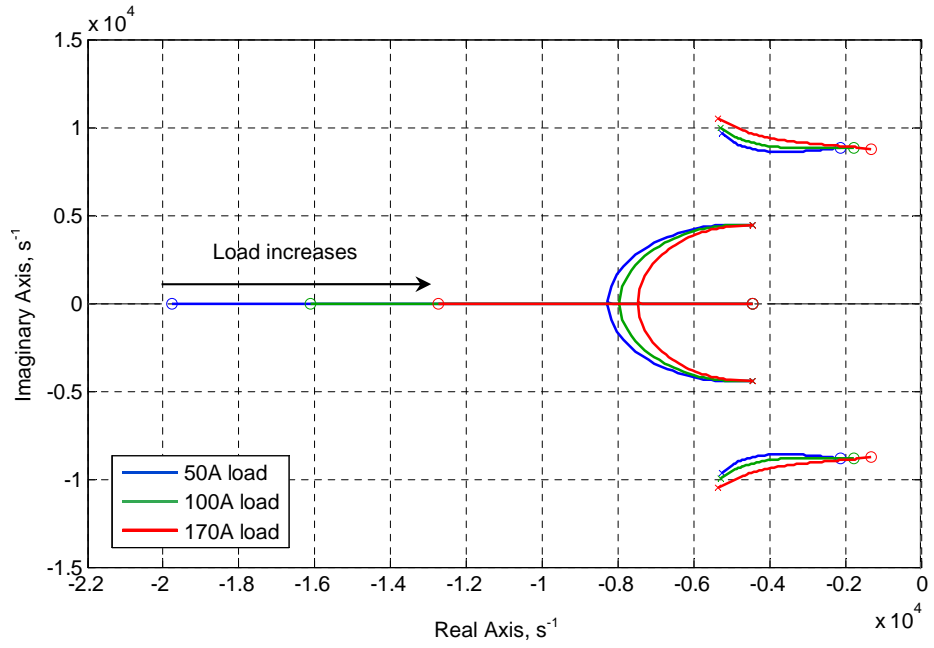
Fig. 5.16. Pole zero movement when load increases from 50A to 170A at 32krpm in generator mode with unlimited i_q^*.
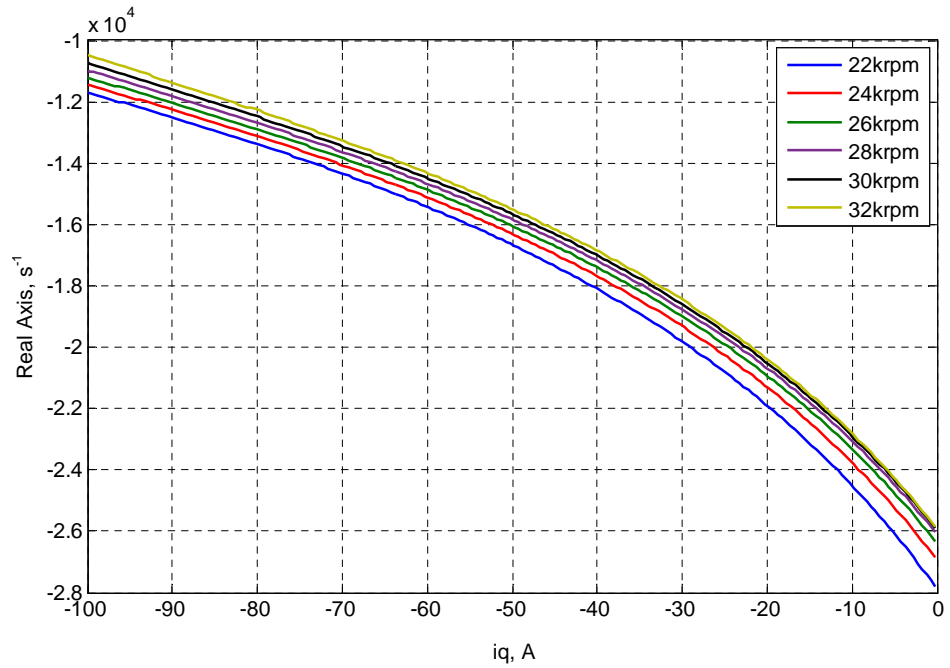
Fig. 5.17. Zero trajectories across load range at different speeds in generator mode with unlimited i_q^*.
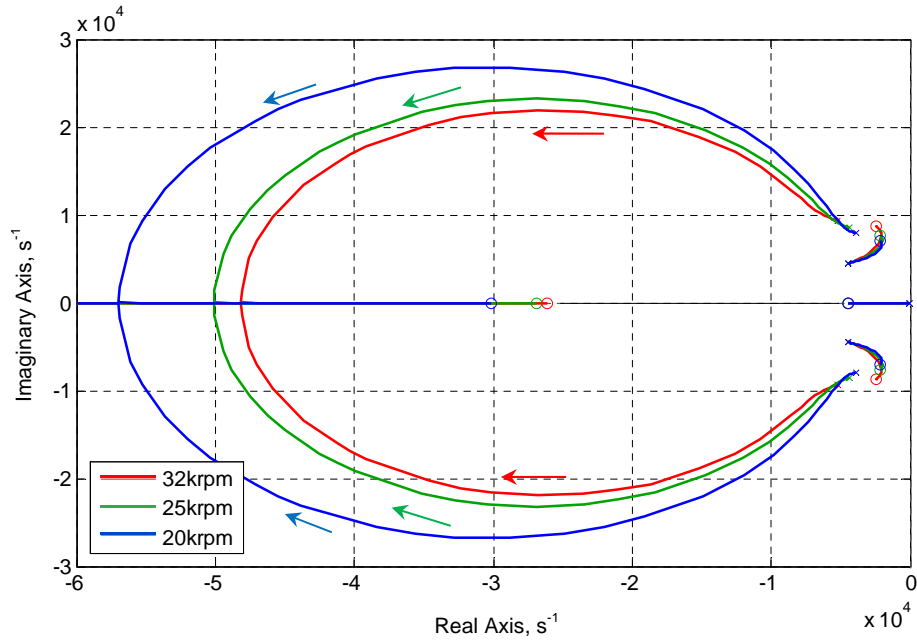
Fig. 5.18. Closed loop zero stability range at different speeds in generator mode with unlimited i_q^*.
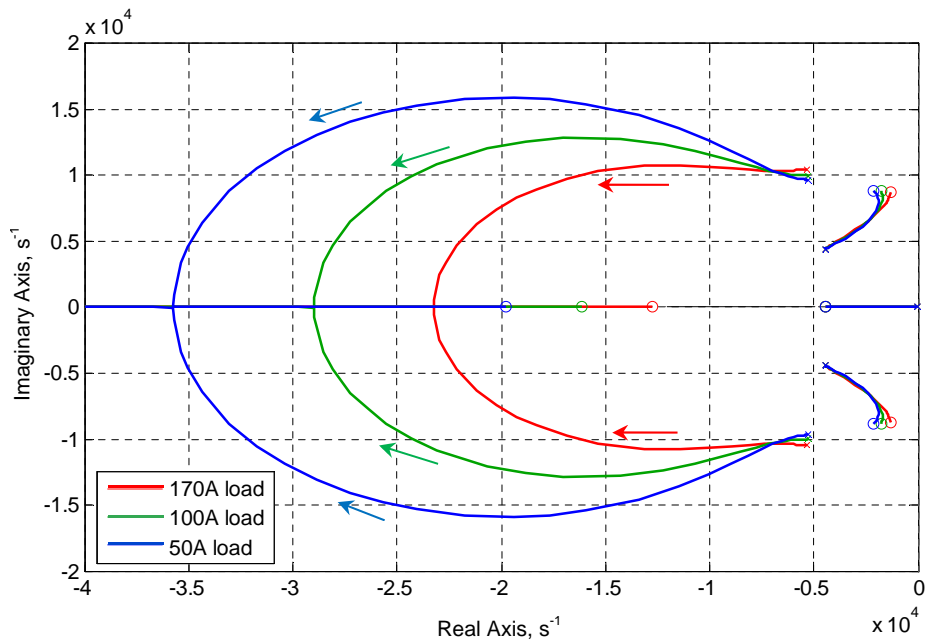
Fig. 5.19. Closed loop zero stability range at different loads operating at 32krpm in generator mode with unlimited i_q^*.

The selection of k_{pv} can be more flexible during operation in generator mode with unlimited i_q^*. Fig. 5.20 shows stable closed loop step responses even when k_{pv} is increased beyond the limit found in the previous Chapter. However as k_{pv} increases, the responses have more oscillations during the transient stages. Furthermore, the

settling time was not significantly influenced by the addition of k_{pv}. Hence, the FW control can continue to use the integral controller designed for starter mode as it is able to operate throughout the generator mode operating range.
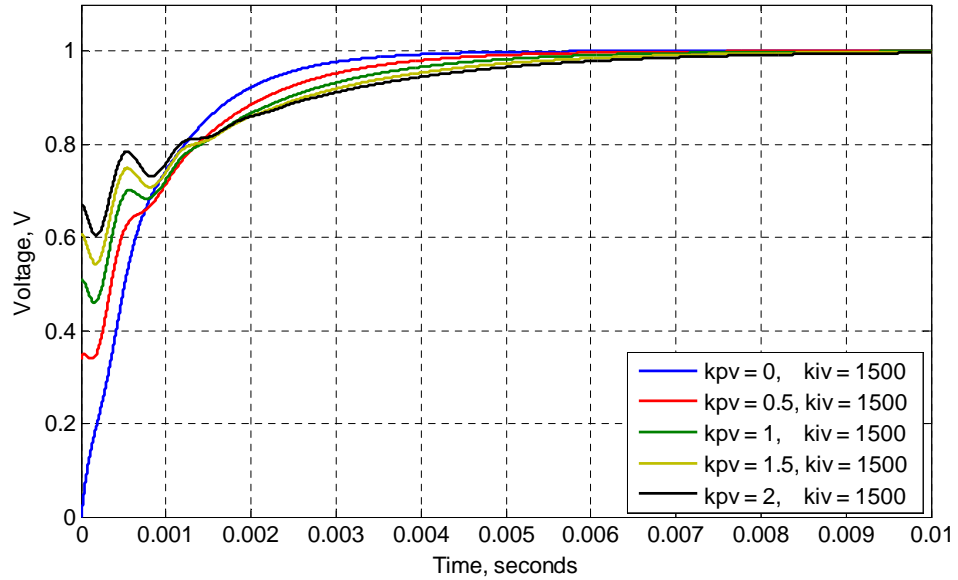
Fig. 5.20. Closed loop step response to $|V|^* = 1$V with $k_{iv} = 1500$ and different k_{pv} operating at 32krpm in generator mode with unlimited $i_q{}^*$.

5.3.2 Limited $i_q{}^*$ Case

In the previous Sub-section, the main assumption was that the S/G system only operates with unlimited $i_q{}^*$ during generator mode. The focus of this Sub-section is to gain an understanding of the FW plant when $i_q{}^*$ is limited. The findings can also be applied to other S/G systems which require FW to operate in generator mode when $i_q{}^*$ is limited.

Assuming that the S/G system does operate with limited $i_q{}^*$ during generator mode, the FW controller determines the control signal for both i_d and i_q controllers. The linearised block diagram of the plant in this case, along with FW controller, can be seen in Fig. 5.21. The difference between the FW plants in starter and generator modes is that for the latter the speed is assumed to be constant.
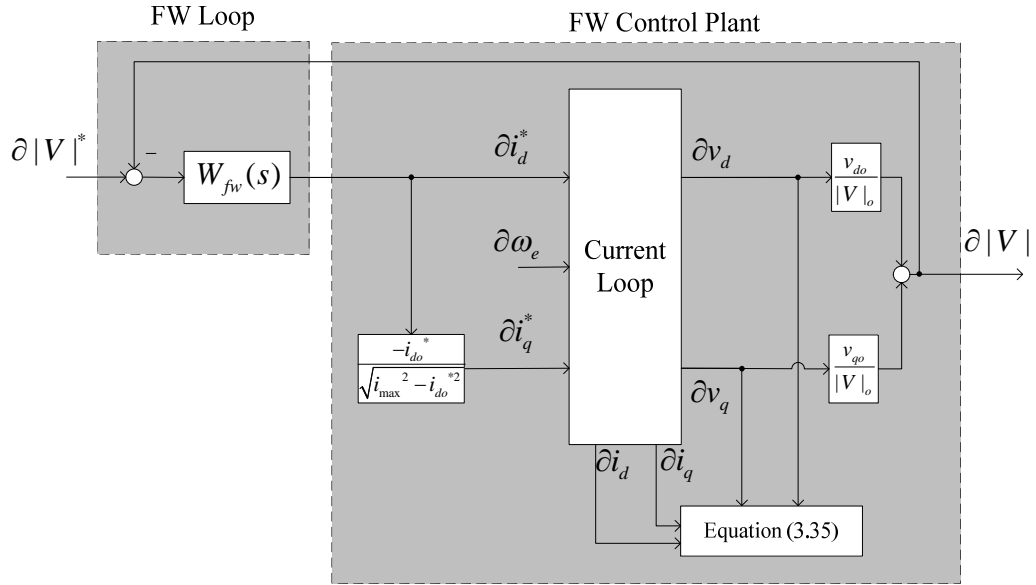
Fig. 5.21. Linearised block diagram for the FW plant analysis in generator mode with limited i_q^*.

Similar to the unlimited i_q^* case, f_{11} and f_{12} are the primary transfer functions that influence $\partial|V|$. ∂i_d^* determines the value of ∂i_q^* through the current limit (4.15). Since i_q^* is required to be always negative during generator mode, the output of (4.15) is set to be negative. It is then used to combine f_{11} and f_{12} yielding:

$$\frac{\partial|V|}{\partial i_d^*} = \frac{\left(a_{7l}s^4 + a_{8l}s^3 + a_{9l}s^2 + a_{10l}s + a_{11l}\right)}{|V|_o\, i_{qo}^*\left(L_q s^2 + \left(R_s + k_{pq}\right)s + k_{iq}\right)\left(L_d s^2 + \left(R_s + k_{pd}\right)s + k_{id}\right)} \tag{5.19}$$

The coefficients for each zero can be found in Appendix B. An operating point of 32krpm was selected to verify the plant against a non-linear equivalent in Matlab®/Simulink®. The chosen plant operating point was v_{do} = 155.87V, v_{qo} = 0.02V, $|V|_o$ = 155.9V, i_{do} = -367.9A, i_{qo} = -157.01A, ω_{eo} = 10048rad/s. This can be represented numerically as:

$$f_{fw\_l\_32} = \frac{0.87822(s + 2.358 \times 10^4)(s + 4449)}{(s^2 + 8884s + 3.947 \times 10^7)} \tag{5.20}$$

$f_{fw\_l\_32}$ can be reduced to second order transfer function as $L_d = L_q$ for the SPM machine. This simplifies the inner current closed loop transfer function. The structure then becomes the same as (4.19). Fig. 5.22 shows the open loop step response of the derived plant and the non-linear model.
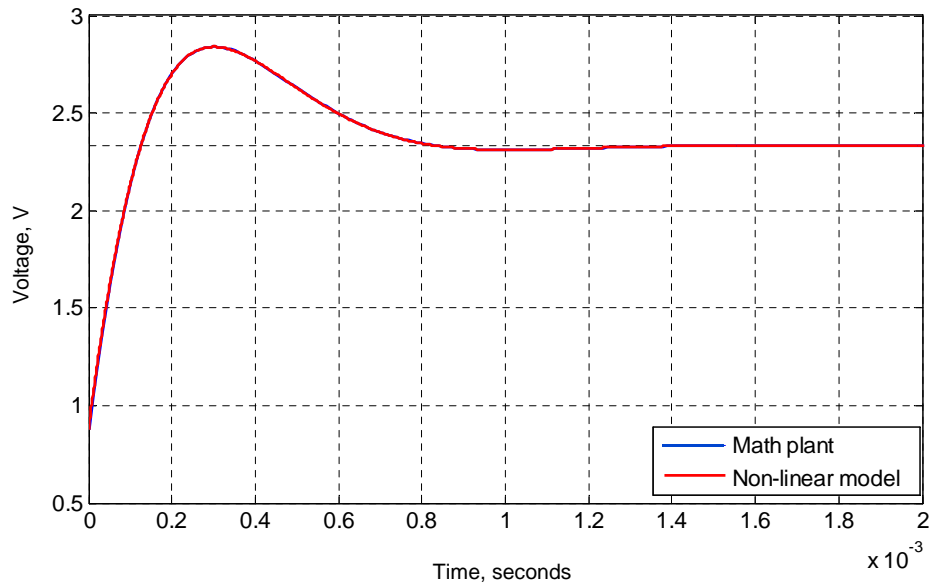
Fig. 5.22. Open loop FW plant step verification at 32krpm in generator mode with limited i_q^*.

The pole zero movements are shown in Fig. 5.23 and Fig. 5.24 at different operating points with respect to speed and load impact. At different speeds, the zero is located on the LHP which indicates it is minimum phase. Different load levels were achieved by varying i_{max} such that the required i_q limit was reached. The load variation results in the positive zero moving away from the origin as the load increases. The zero trajectories at different speeds and loads can be seen in Fig. 5.25.
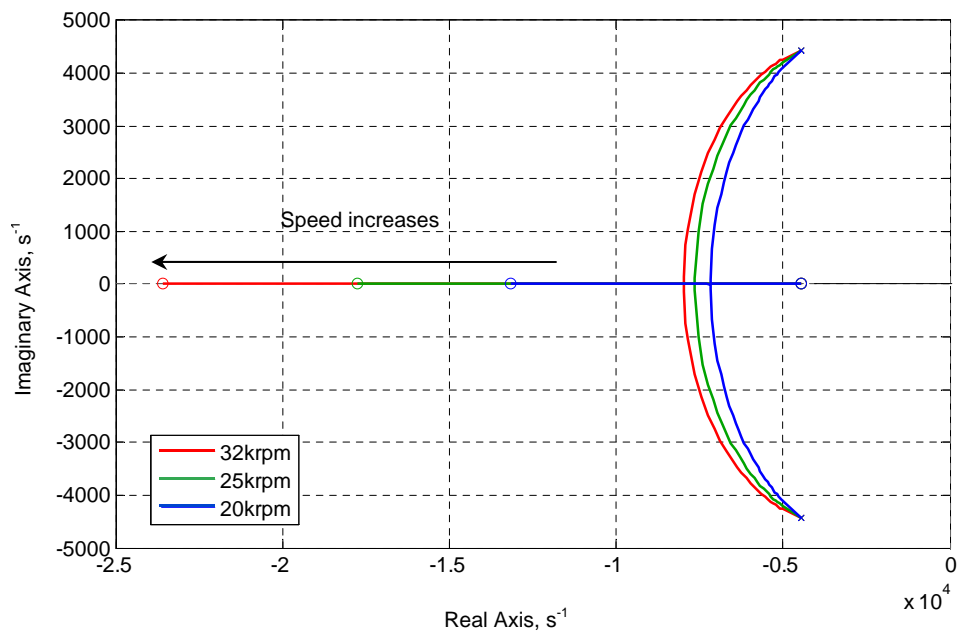
Fig. 5.23. Pole zero movement when speed increases from 20krpm to 32krpm in generator mode with limited i_q^*.
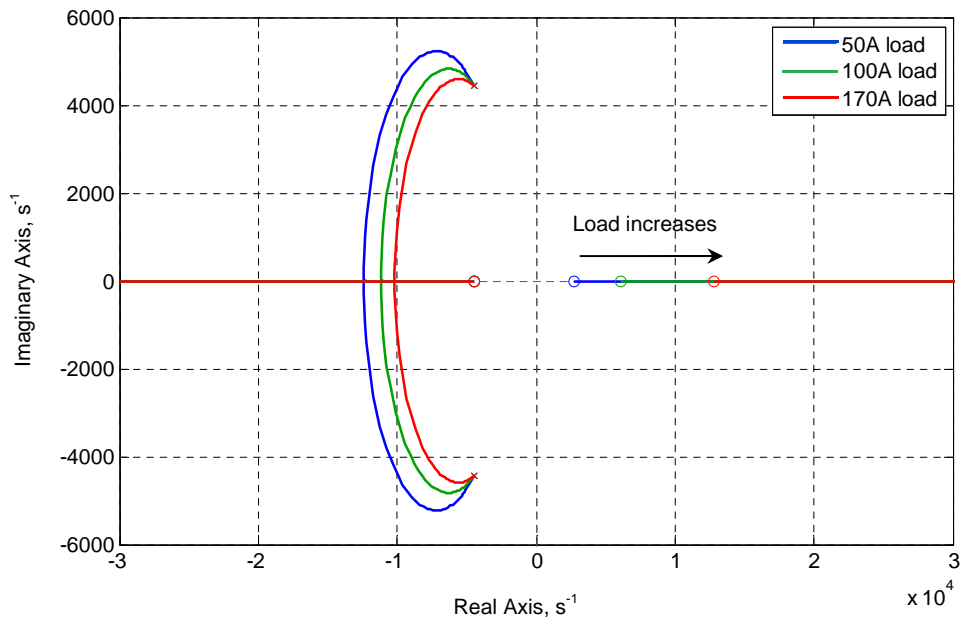
Fig. 5.24. Pole zero movement when load increases from 50A to 170A at 32krpm in generator mode with limited i_q^*.

The response of this zero is similar to response of the zero in equation (4.20) which was analysed during starter mode under limited i_q^* conditions. It can be seen that the zero is usually located in the RHP when i_q is less than 140A. There are limits to how much load can be sustained at each operating speed before the stability of the power system is influenced. In order to operate with maximum stator current, $i_{max} = 400A$, large i_q was required and the plant operated with LHP zeroes as observed in Fig. 5.23. If the load demand, i_L, is lower than 170A, i_{max} is reduced to reach the required operating point and the plant operates with RHP zeroes. The value of i_q was not equal to i_L due to additional currents contributed by i_d.

Since the FW plant operating in generator mode with limited i_q^* is non-minimum phase by nature, there is a limited range for the gain of the FW controller, as seen in Fig. 5.26. It was observed that the allowable k_{iv} range reduced as the load was reduced. At 170A load, the k_{iv} range was up to 3300 which met the requirement for the initially designed FW controller with $k_{iv} = 1500$. When the load was almost zero, the plant became uncontrollable as the k_{iv} range was almost zero. This therefore complicates the design of the FW controller, especially at small load conditions.
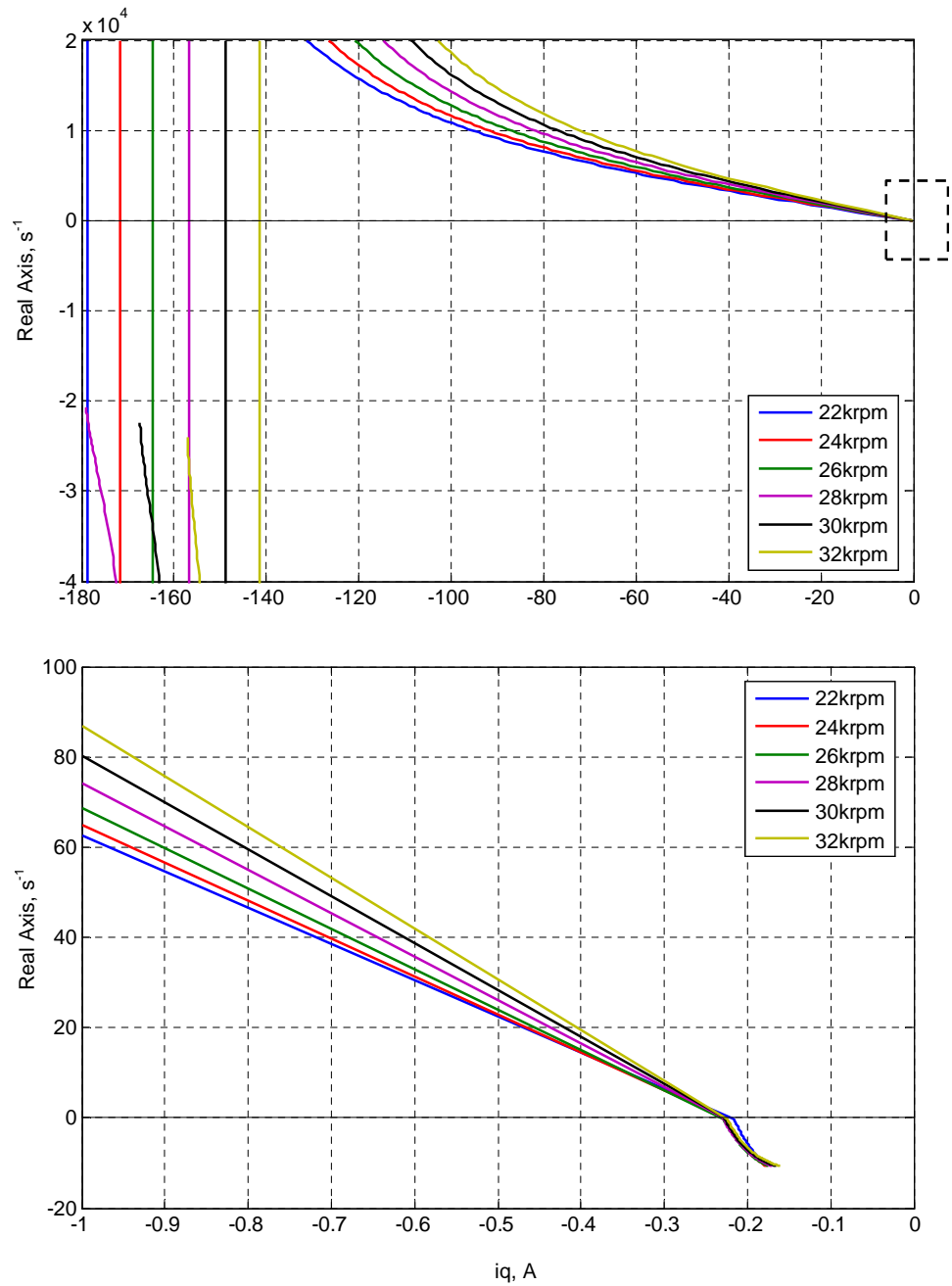
Fig. 5.25. Zero trajectories across the load range at different speeds (top) and zoomed area (bottom), in generator mode with limited i_q^*.
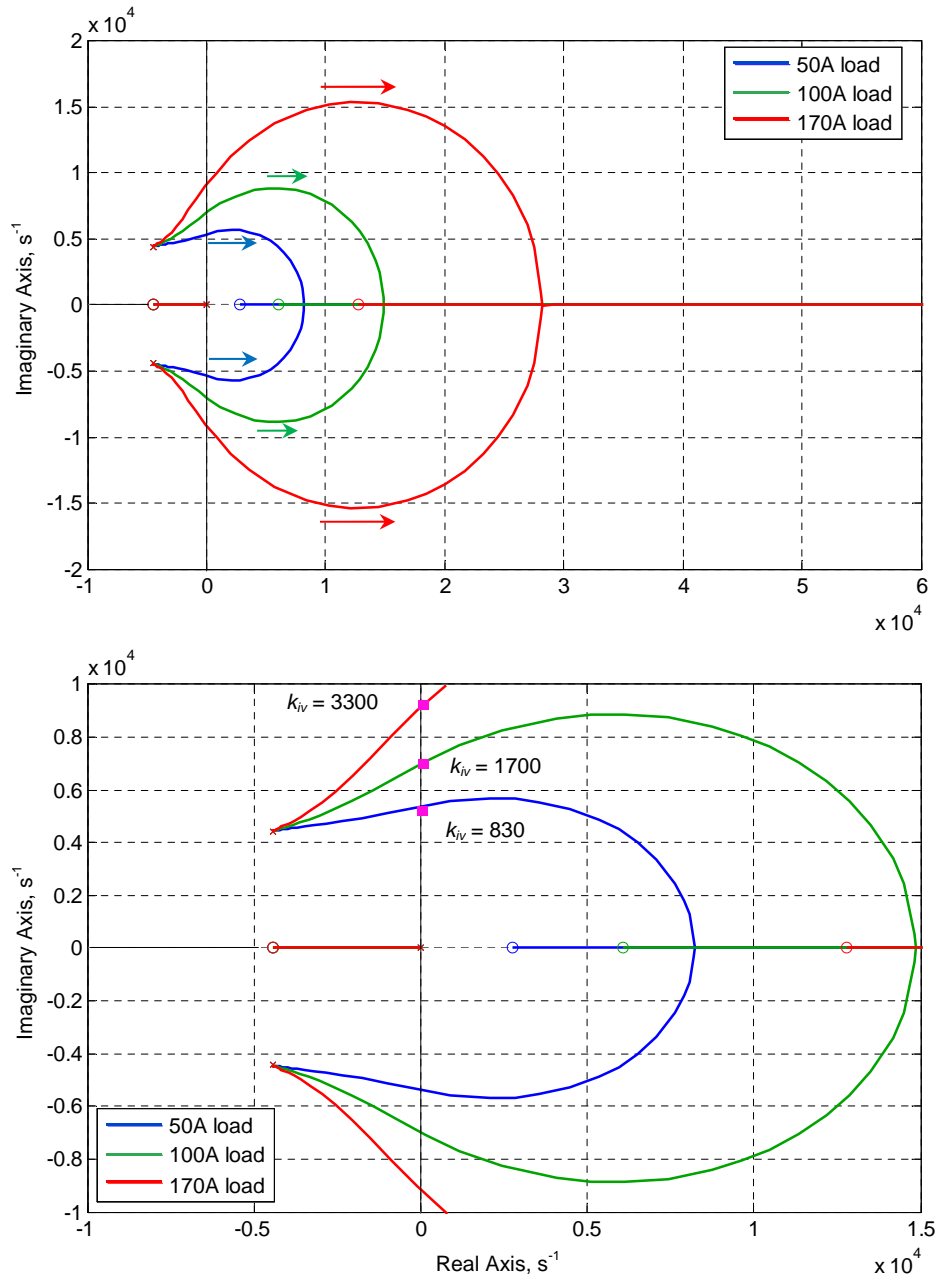
Fig. 5.26. Closed loop zero stability range at different loads at 32krpm (top) and zoomed area (bottom) in generator mode with limited $i_q{}^*$.

The range for k_{iv} at different loads and speeds was plotted using Routh-Hurwitz criterion with the closed loop transfer function (4.24). In order to satisfy the Routh criteria, the stable region was limited by $k_{iv\text{-}lmt3}$ and $k_{iv\text{-}lmt5}$ seen in Fig. 5.27. The k_{iv} range decreased significantly for smaller loads. At low i_q values, the k_{iv} range became negative with reference to $k_{iv\text{-}lmt5}$. The stable region was then overtaken by $k_{iv\text{-}lmt2}$, $k_{iv\text{-}lmt1}$, and $k_{iv\text{-}lmt4}$ respectively; this is shown as an average in Fig. 5.27 as i_q decreases to about -0.2A. Operating within this region will result in controller instability if k_{iv} is unchanged. Adaptive control is therefore required to adjust k_{iv} according to the load condition when operating in generator mode with limited i_q^*.

There is an unstable region highlighted in red between $i_q \approx$ -0.2A and 0A in Fig. 5.27. This i_q value occurs when the zero of the FW control plant crosses from the RHP to LHP, as shown in Fig. 5.25. The critical i_q value can be calculated using equation (4.20) by solving the equation when z_l and $v_d = 0$. This yields:

$$i_{qcrit-lmt} = \frac{R_s i_{do}}{\omega_e L_d} \tag{5.21}$$

This unstable region is due to the use of the dynamic limiter and can be explained through the effect of gradient variation between ∂i_q^* and ∂i_d^* in the linearised current limit equation (4.15). As ∂i_q^* approaches zero with some non-zero value of ∂i_d^*, the gradient rises infinitely. This high gradient value causes instability when operating with limited i_q^*. With reference to (5.19), the open loop gain of the FW plant becomes very large due the small i_{qo}^* which leads to output responses that cannot be regulated by the controller. A solution that could be considered to mitigate this is implementation of a current reference modifier that accounts for i_{max} and low load to prevent operation within this region. The concept of this solution will be explained and demonstrated in Section 5.3.4.
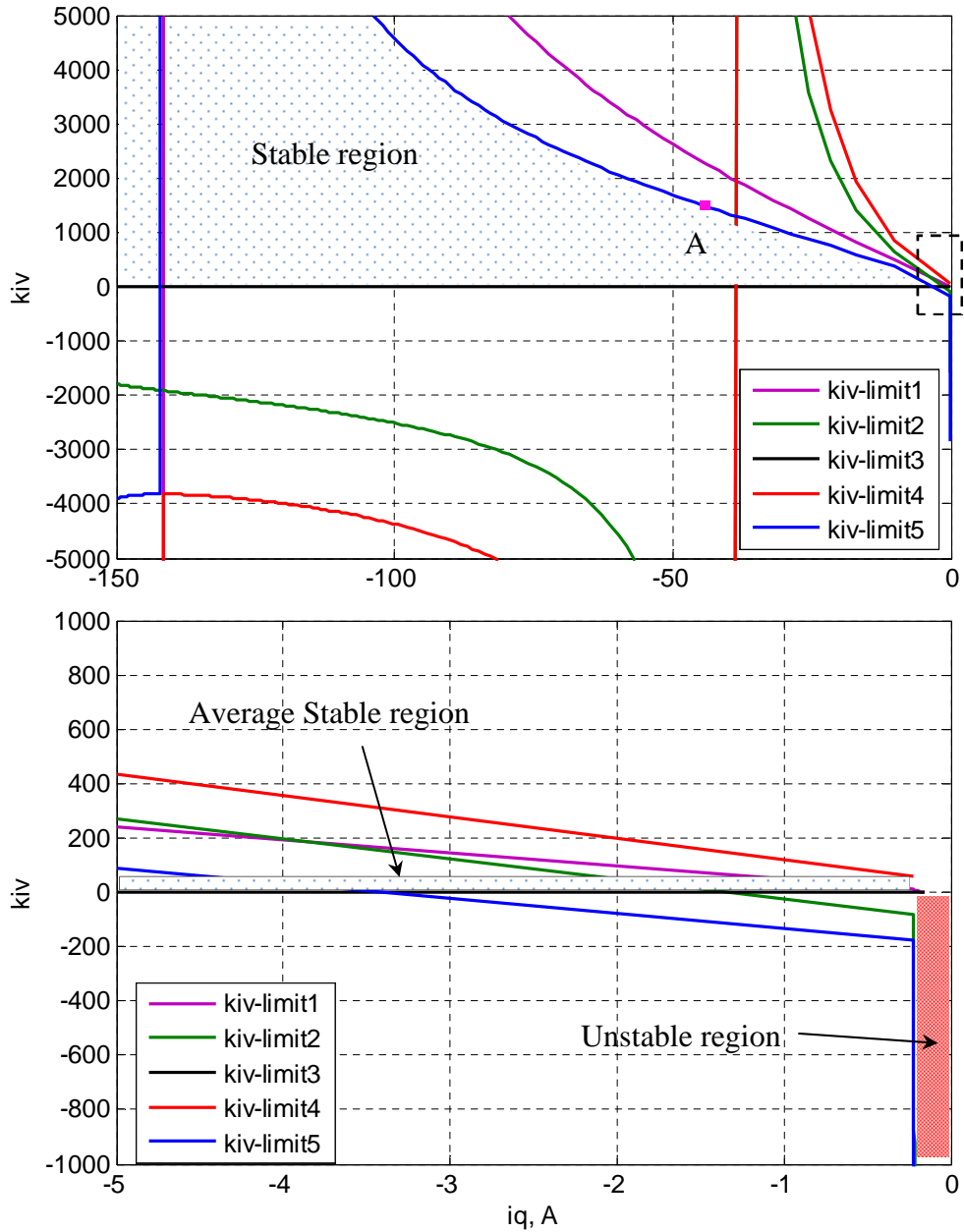
Fig. 5.27. Range of k_{iv} from $i_q = 0A$ to -150A operating at 32krpm (top) and zoomed area (bottom) for generator mode with limited $i_q{}^*$.

5.3.3 Adaptive FW Controller

In this Sub-section, the adaptive k_{iv} approach will be discussed and tested using a time-domain simulation of the S/G system. For the stable operating regions within generator mode, $i_q{}^*$ will be limited until the unstable region is reached. k_{iv} will then be adaptively set equal to half of $k_{iv\text{-}lmt5}$ when $k_{iv\text{-}lmt3} > 0$. A lower limit for $k_{iv\text{-}lmt5}$ is imposed so that the FW controller can still work within the average stable region covered by $k_{iv\text{-}lmt1}$, $k_{iv\text{-}lmt2}$, and $k_{iv\text{-}lmt4}$. In equation form they can be written as:

$$k_{iv-adapt} = \frac{1}{2} k_{iv-lmt5} \tag{5.22}$$

$$k_{iv-lmt5} > 100 \tag{5.23}$$

Fig. 5.28 shows stator current magnitude i_s and i_q when i_{max} is used to reduce the operating point while keeping k_{iv} constant. i_q becomes unstable at about -40A. This occurred around point A in Fig. 5.27 with $k_{iv} = 1500$. The results when utilising $k_{iv\text{-}adapt}$ can be seen in Fig. 5.29.
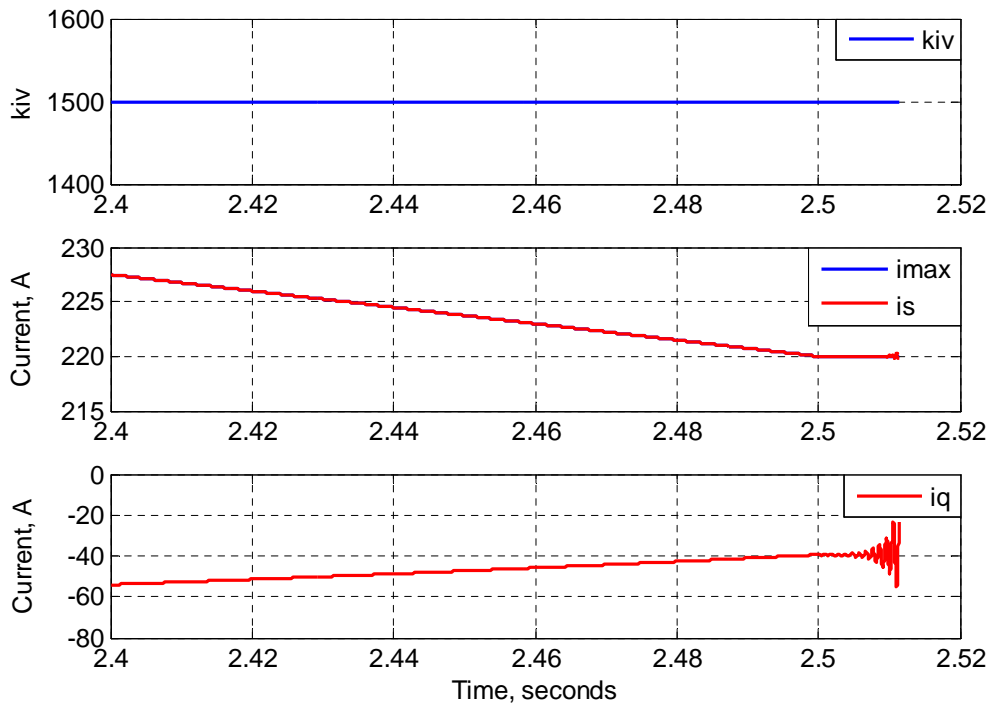
Fig. 5.28. i_s and i_q when i_{max} is reduced to 220A while $k_{iv} = 1500$.

i_{max} was increased up to 212A and the FW controller was still stable as shown by i_q. i_s closely follows i_{max} which indicates that the power system is operating with limited $i_q{}^*$. A step change of $i_{max} = 0.4$A was applied at $t = 2.8$s to show that the FW controller is still stable. This demonstrates the adaptive FW controller operates correctly and stably for the S/G system in generator mode with limited $i_q{}^*$.
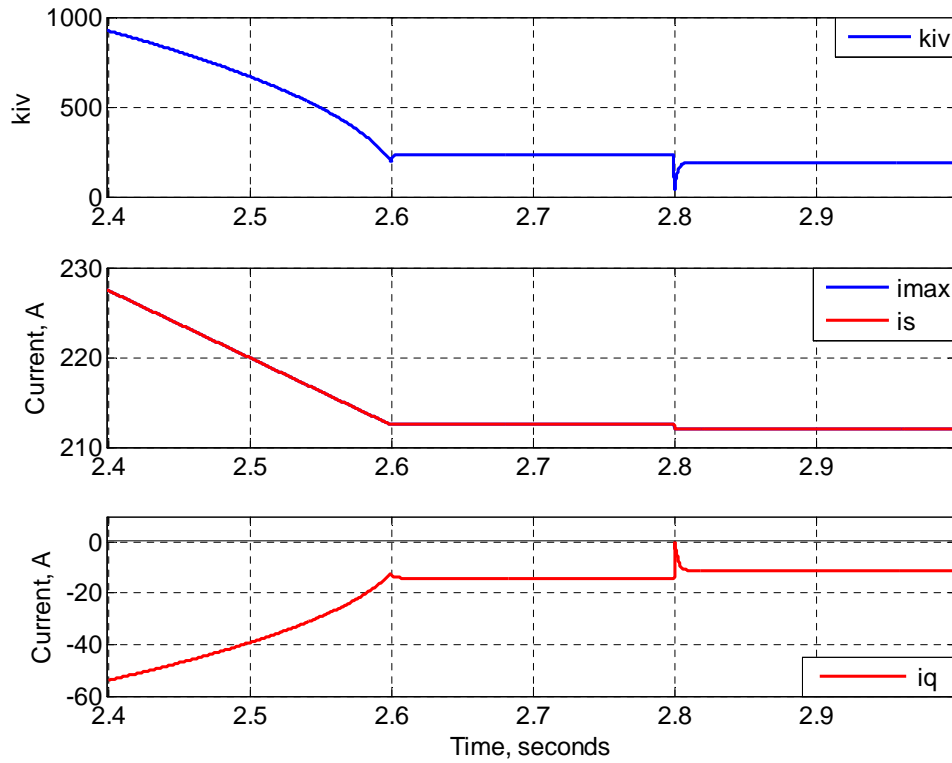
Fig. 5.29. i_s and i_q when adaptive k_{iv} is implemented.

5.3.4   Current Limit Modifier

Fig. 5.27 highlights that there is an unstable region when operating in generator mode with limited $i_q{}^*$. This region is from $i_{qcrt\text{-}lmt}$ to $i_q = 0$ due to the use of dynamic current limit. To address the issue, a novel method of current limiting is proposed: to modify the current limit equation in order to limit the gradient value of $\partial i_q{}^*/\partial i_d{}^*$ when $i_q{}^*$ is small and operating within generator mode with limited $i_q{}^*$. An alternative approach is to avoid operating within the unstable area which is defined by $i_{qcrt\text{-}lmt}$. To avoid the unstable region area by a sufficient margin and to satisfy the condition

of (5.21), i_{max} should be high enough such that the resultant i_q^* from the current limit equation (4.15) is more than twice the value of $i_{qcrt\text{-}lmt}$. This condition is fulfilled by:

$$i_{\max} > i_{lmt} \tag{5.24}$$

where

$$i_{lmt}{}^2 = i_d{}^{*2} + (2i_{qcrt-lmt})^2$$

The modified gradient results in a different current trajectory which can be observed using a current limit circle, as shown in Fig. 5.30. The gradient of the current limit trajectory is modified by the angle ϕ (the angle between the i_d^* and i_{max} vectors). The proposed limiting trajectory is then used in order to calculate i_q^*. The value of ϕ is the value at which $i_q^* = 2\ i_{qcrt\text{-}lmt}$ or when $i_{max} = i_{lmt}$ in order to give sufficient margin for the control to switch equation (4.15) to the modified current limit before reaching the unstable region.
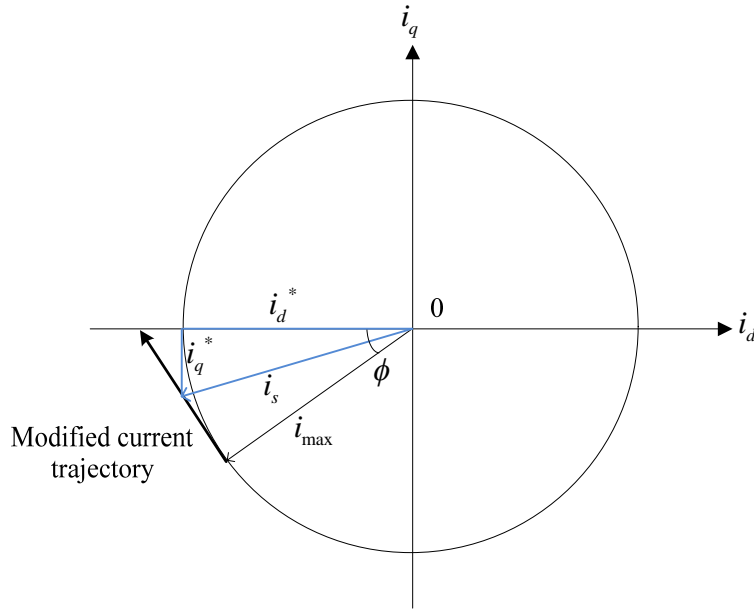
Fig. 5.30. Proposed current limit trajectory modifier.

Hence, using the equation for $i_{qcrt\text{-}lmt}$ and (5.22) with reference to Fig. 5.30:

$$\tan(\phi) = \frac{2R_s}{\omega_e L_d} \tag{5.25}$$

By applying trigonometric analysis to the blue-line triangle in Fig. 5.30:

$$-i_{\max}{}^2 = i_d{}^{*2} + i_q{}^{*2} \tag{5.26}$$

$i_q{}^*$ is calculated from the modified current trajectory as:

$$i_{\max} \sin(\phi) i_q{}^* = -i_{\max}{}^2 - i_d{}^{*2} \tag{5.27}$$

$$i_q{}^* = -\frac{i_{\max}}{\sin(\phi)} - i_d{}^* \tan(90 - \phi) \tag{5.28}$$

The equivalent small signal model is found to be:

$$\frac{\partial i_q{}^*}{\partial i_d{}^*} = -\tan(90 - \phi) \tag{5.29}$$

which gives a constant value for a given operating point.

Fig. 5.31 shows the boundary limit $k_{iv\text{-}lmt5}$ for different speeds when using the current limit (4.15). $k_{iv\text{-}lmt5}$ was used as a reference point representing all the other k_{iv} limits that bordered around $i_{qcrt\text{-}lmt}$. It can be seen that the border of the unstable region for different operating speeds was always around the same point; at about 0.23A. This limit occurs at $i_{qcrit\text{-}lmt}$ and this was confirmed by (5.21). Once the current limit modifier is applied, the borders at the different operating speeds have shifted very close to $i_q = 0$A, as seen in Fig. 5.32, which effectively eliminates the unstable region. This perfectly illustrates the capability of the current limit modifier to increase the FW controller stability when functioning in generating mode with limited $i_q{}^*$. The unstable region is very small for the S/G system in comparison to the maximum current limit of 400A; hence the advantage of this method will be demonstrated in Chapter 7 on a power system with a much smaller power rating.
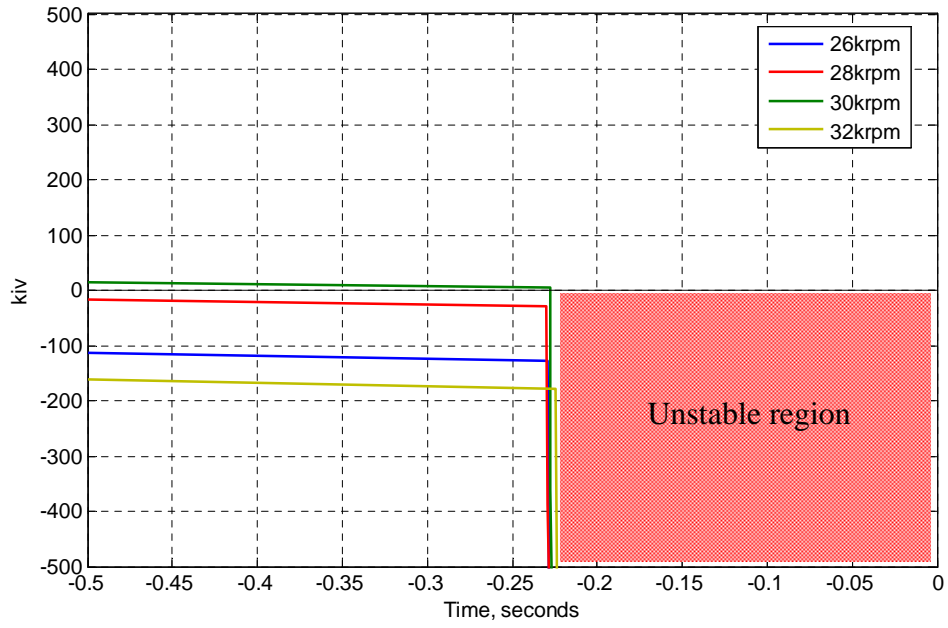
Fig. 5.31. $k_{iv\text{-}lmt5}$ at different operating speeds.
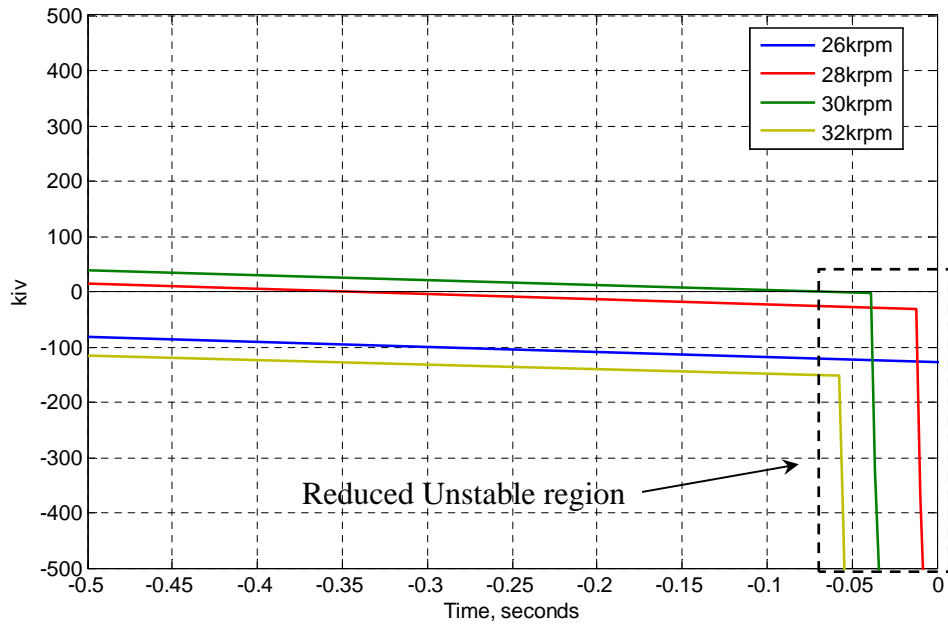
Fig. 5.32. $k_{iv\text{-}lmt5}$ after current limit modifier is applied.

The key findings from the analysis of the FW plant in generator mode are as follows:

- The FW plant is minimum phase when operating with unlimited i_q^* in generator mode as opposed to non-minimum phase when operating in starter mode. This is due to the change of direction in power flow. For the limited i_q^* case, the nature of the FW plant means it is non-minimum phase when i_q is below 140A and is minimum phase for larger values of i_q.

- The FW controller has a greater gain stability range in generator mode compared to starter mode due to the minimum phase FW plant. The FW controller design is therefore more crucial for stable operation in starter mode. The only exception to this is when operating with limited i_q^* in generator mode.

- The FW plant in generator mode with limited i_q^* has a very small gain range. Furthermore this range is proportional to the load demand. There is an unstable region when i_q is very small (~0.2A) due to the negative k_{iv} range. This instability region is due to the very high gradient between ∂i_q^* and ∂i_d^* when operating at very small i_q. An adaptive FW controller based on speed and load demand has been proposed in order to solve this issue. The application of the adaptive controller within the S/G system was successfully demonstrated in Matlab®/Simulink®. A novel method was also proposed to eliminate the unstable region by modifying the current limit trajectory. The current reference modifier improves the controller stability by preventing the power system from reaching the low load operating points.

5.4   Analysis of the Generator Mode Control Scheme

This Section details additional analysis which was performed on the designed outer loop controllers in generator mode. Fig. 5.33 shows a time domain simulation of the S/G power system with the DC link controller and the previously designed FW controller from Chapter 4. During the simulation the S/G speed is set at 32krpm and initially the power system was not subjected to any load. At 0.005s intervals, i_L was increased to 50A, 100A and 170A respectively and then removed in reverse order. It can be seen that E_{dc} reduces to 264V, 258V, and 250V for each step of load

respectively. The i_{dc} controller was therefore able to regulate the active power required for the loads. $/V/^*$ was determined by E_{dc} and the FW controller ensured that $/V/$ was regulated accordingly. The demanded value of i_s was very high due to the level of i_d required for FW purposes at 32krpm. Negative i_q was observed due to the power flow direction being towards the DC bus. The overall control performance was shown to be satisfactory for generator mode operation.
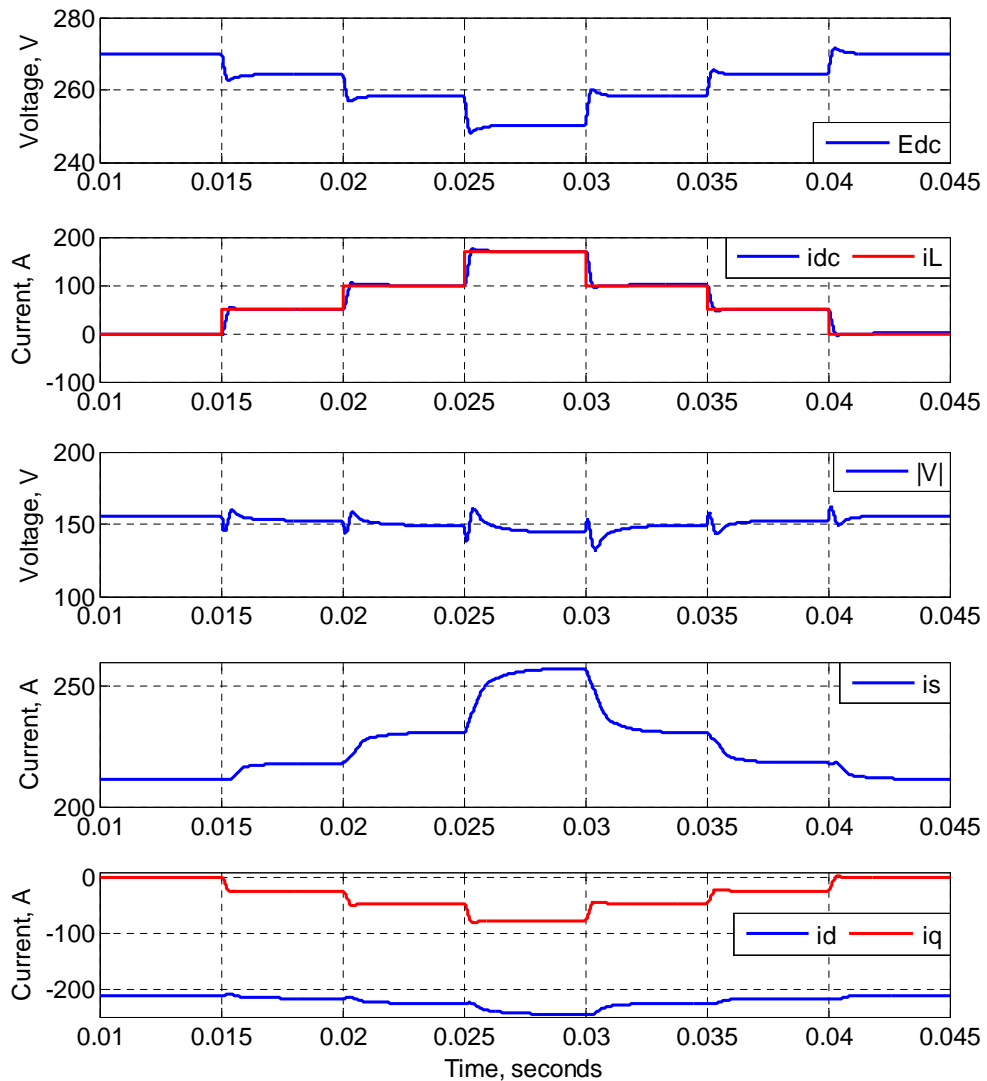
Fig. 5.33. Time domain simulation results of the S/G system with designed controllers in generator mode.

The main points arising from the overall control analysis and design for the S/G system in generator mode can be summarised as follows:

- The application of the direct current FW control methodology to the S/G system introduces two distinct operating conditions that can exist during dynamic operation. Depending on the operational requirements, these cases were identified to be limited and unlimited i_q^*. The difference between the cases is defined by the control signals for the current loop which are determined by the outer loop controllers. Independent control signals for i_d^* and i_q^* can be obtained from their respective loops during unlimited i_q^* operation. However the control signals for i_d^* and i_q^* are determined by the FW controller during limited i_q^* operation. The behaviour of the S/G system can be significantly different during these two operational cases. Therefore both cases and must be examined during the control design phase.

- Non-minimum phase plant characteristics are present for both FW and i_{dc} control. This imposes a limit on the controller gain range as the plant poles move to the RHP resulting in system instability. This limit determines the allowable range for the controller gain which will ensure stable operation with both limited and unlimited current in both starter and generator modes.

- The plant contains a dominant zero which determines the stability system. The position of this zero changes depending on the operating speed and load.

- Designing the control based on the worst case operating point enables the controller to work throughout the required operating range. In this study the worst case operational points for both modes of operation were identified to be at the highest operating speed and full load (20krpm with 40Nm load for starter mode and 32krpm with 170A load for generating mode).

- The use of linear controllers for FW and i_{dc} control is possible throughout both modes of S/G operation. However care has to be taken when designing the proportional term within the PI controller.

- The most critical stage for FW control design is associated with operation in generator mode with limited i_q^*. The stable range for the controller gain decreases in proportion to the amount of load. Adaptive gain controllers and current reference modification is therefore required to mitigate this problem if the S/G has to operate within this region. It has been shown that the FW controller can therefore be designed based on operation in starter mode with limited i_q^* as this is the most influential and restricted operating condition.

5.5 Conclusion

It has been shown that the transition of the investigated S/G system from starter to generator mode requires a change in the control scheme. DC link current has to be controlled instead of speed in order to meet the electrical load demanded from the DC bus. Droop control, which is commonly used on terrestrial grid systems, was applied as part of the control scheme for potential parallel operation with multiple generator sources. The control plant for the DC link current was derived and it has been shown that the plant is non-minimum phase. The DC link controller was designed based on the worst case operating point for generator mode. The DC link controller gain range was shown to be less critical than the FW controller because of the assumption that the S/G system would only operate with unlimited i_q^*. The droop coefficient defined for the S/G power system performed well with the designed DC link controller and met the high DC voltage transient limit requirements of MIL-STD-704F. The FW plant was re-derived with appropriate equations for generator mode in order to investigate any changes in stability response compared to the analysis performed in Chapter 4. The FW plant changed from non-minimum in starting mode to minimum phase when operating in generation mode; hence the closed loop gain stability margin was increased. Further analysis of the FW plant during limited i_q^* showed that the plant is non-minimum phase when i_q is below 140A and is minimum phase for larger values of i_q. When i_q^* is limited the FW plant has a very restricted gain range which is proportional to the load demand. It was found that there is an unstable region when i_q is very small (~0.2A) and the k_{iv} range reduces to zero. This unstable region was found to be due to the very high gradient between ∂i_q^* and ∂i_d^* when operating at very small i_q. An adaptive FW controller based on speed and load demand was utilised in order to ensure stable operation up to the unstable region. The k_{iv} range used by the adaptive controller was calculated using the Routh-Hurwitz criterion. The adaptive FW controller was successfully demonstrated on a non-linear model in Matlab®/Simulink®. A novel method involving the modification of the current limit trajectory was proposed in order to eliminate the unstable region. A current reference modifier was considered in order to improve controller stability by limiting the gradient of the current limit; thus preventing the power system from reaching the unstable low load operating points.

Chapter 6   Applicability of Predictive

Control for Starter-Generator System

6.1   Introduction

In the previous Chapters, the control design for the S/G system based on an AFE-fed PMM was completed. It has been shown that the performance requirements can be met using linear (PI) controllers and that a fast dynamic response can be achieved for the DC link control. From control theory it is known that in cascade control structures the achievable external loop bandwidth is limited by the bandwidth of internal loop, i.e. the *dq* current loops in this S/G system. The main purpose of the AEGART system is to operate in future MEA electrical power system architectures with multiple sources running in parallel. In addition, it must be capable of providing a very fast response to DC power demands from on-board loads. A fast i_{dc} response will ease the on-board power sharing and power management tasks. In the previous Chapters, traditionally designed PI controllers were employed for the inner current loops. Due to practical considerations and from experience in the field the bandwidths of these loops cannot exceed 800-1000Hz. Indeed, the targeted bandwidth of the i_{dc} control loop should not exceed 400-500Hz, otherwise severe interactions between the loops can occur which will degrade the control performance. A straight forward approach is to further increase the bandwidths of the inner current loops. However, referring back to Section 3.6, the effect of the digital delay also has to be taken into account as there is a limit to the allowable inner current loop bandwidth. Therefore, in order to respond quickly to the fast changes in power demand coming from newly introduced electrical loads (can be well within 1ms); an alternative to PI control strategy for the internal loops will be investigated in this Chapter.

Among the wide selection of control methods available such as sliding mode, linear quadratic regulators, and adaptive controllers, model predictive control is a technique that can provide very fast control response. It is categorised as a non-

causal controller as it relies on future states from the system to perform its control and thus is able to overcome the digital delay.

This Chapter aims to look at the applicability of model predictive control for the S/G power system in order to attempt to achieve much faster inner current loop dynamics and hence allow for more flexibility in the design of outer loop controllers. This type of control will be reviewed in order to assess its applicability within the S/G system. Model predictive control will be utilised for the inner current loops however the outer loops will continue to contain PI controllers for disturbance rejection. The control performance will be tested and compared with the full PI control scheme over the operational range of the S/G.

6.2   Model Predictive Control

Model predictive control (MPC) is known as receding horizon control or moving horizon control, and was introduced in the 1960s as an advanced process control technique that is different from the classic proportional plus integral plus derivative (PID) controller [144, 145]. It is similar to linear H_2 and H_∞ optimal control [146] but is solved within a finite horizon rather than an infinite horizon. Additionally, MPC can compute its solution online while reading the current state of the controlled plant instead of considering all of the states. Because of this, MPC is usually implemented in the discrete domain while considering the switching states of the power converter.

Initially MPC was used in process industries to control multivariable slow dynamic plants [126, 146]. Then it was investigated with faster dynamic systems such as automotive traction control and eventually to power converters and drive systems [126, 147]. MPC has been getting more attention of late as a solution for the control of power converters due to its fast dynamic performance, multivariable control, ease of constraint implementation and absence of signal modulation schemes. It is also capable of handling non-minimum phase systems and non-linear dynamics [126, 127, 146, 148, 149]. The non-minimum phase dynamics can be managed by avoiding the selection of corresponding future states. The advantage of MPC lies in its ability to predict future states over a defined time horizon based on

the measured present states and control inputs. For a power converter, this information is optimised within a cost minimisation function that determines the converter switching states for the next sampling period. The most suitable switching state is selected and sent to the converter. Since a converter has a finite number of switching states, the optimisation stage and the time it takes can be reduced. The process of prediction and cost minimisation is repeated for every sampling period [126, 127]. A flow diagram summarising the process can be seen in Fig. 6.1.
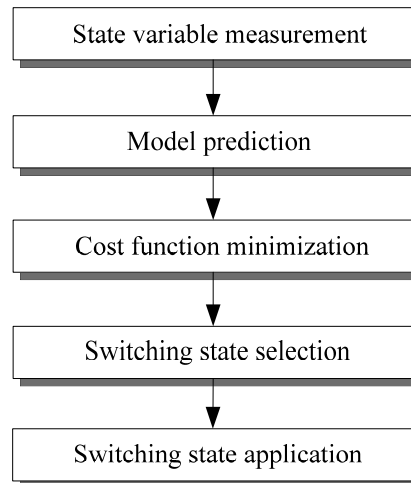
Fig. 6.1. Generalised MPC flow diagram.

There are disadvantages of using MPC as well. Obviously since MPC is a model based control strategy, its performance largely depends on the accuracy of the model. Furthermore, the lack of a modulation scheme results in a switching state applied across the whole switching period. It may therefore result in larger ripples in controlled variables with slow switching frequencies. Large ripples in current and voltage outputs from power converters have high harmonic content and hence have lower output power quality.

The use of MPC within drive systems have been covered in [126, 150-153]. Preindl implemented MPC for torque control of a PMM drive system [150]. The torque reference was provided by a speed PI regulator and i_d was utilised for MTPA operation. State observers were used to compensate for possible noise and modelling error. The same author also looked at direct speed control using MPC in [151]. The study demonstrated the validity of the proposed control scheme which also incorporated MTPA and FW operation. Similar work was also done by Bolognani in

[152]. The paper highlighted the use of MPC as a multivariable controller rather than being part of the conventional cascade control structure. In addition, the paper also detailed the controller design process for MPC when applied to electrical machine drive systems. MPC has also been investigated for S/G systems in [154]. This paper looked at the use of MPC within a multilevel converter for stator current control. The aim of the paper was to achieve lower current ripple for S/G systems that have low inductances. Significant current ripple reduction was achieved through the proposed converter topology and control scheme. Moreover, the resultant reduction in current ripple also indirectly reduced the size of the required filters. However, the exact amount of current ripple reduction which was due to the proposed MPC method alone is unclear.

A recent variant of the MPC method was introduced with an intrinsic SVM scheme called Modulated Model Predictive Control (M^{2}PC) with the aim of improving the performance of traditional MPC in terms of power quality. This method was proposed by Tarisciotti and studies have been performed in [155-158]. The aim of this method is to improve the output power quality of the system while maintaining the advantages of MPC with an intrinsic modulator. SVM was selected as the intrinsic modulator due to is efficient use of selected voltage vectors for finite switching power systems [156]. This resulted in less total harmonic distortion (THD) and switching losses from the output waveforms. Simulation and experimental results showed significant improvements in terms of power quality compared to the standard MPC control method. The advantage offered by M^{2}PC may be crucial in meeting power quality and voltage regulation standards such as MIL-STD-704F in aircraft power systems. In [158], the AC current ripples of a seven-level H-bridge were reduced due to the presence of the modulator. Similar power quality could be achieved using the standard MPC control method at the cost of increasing the switching frequency of the converter. The demonstration of different E_{dc} and i_d control has also been presented in [156]. M^{2}PC has also been investigated on IM based drive system with matrix converter [159]. The main control scheme had inner current controlled M^{2}PC and a speed outer loop. Better current output waveforms were observed when compared to the similar control scheme with inner current MPC control.

Two variations of M^{2}PC have been derived and investigated, one based on dead beat control [155] and the other was based on cost function ratio [158, 159] to determine the duty cycles for the SVM. Dead beat control is a variant of predictive control where the output converter voltage reference is calculated based on the model. This allows the controlled variable to reach its required reference during the next sampling period. Dead beat control also has advantage of providing a fast dynamic response, but requires a modulator to work and system constraints cannot be included directly [126]. In M^{2}PC, dead beat control is used to predict the voltage vectors required at each switching state. The cost function then selects the optimal voltage vectors for the modulation scheme and the output is sent to the power converter. Cost function ratio based M^{2}PC works by calculating multiple cost functions for each voltage vector and then selecting the optimal vector for the modulation scheme. Both methods offer the advantage of better power quality due to the intrinsic modulator; however a performance comparison has yet to be reported in literature.

More research is required to analyse the use of M^{2}PC within drive systems. The inherent advantages of fast dynamic response and reduced current ripple could potentially contribute to controller stability enhancement and hence reduction in aircraft overall weight by means of smaller passive filters. In this Chapter, M^{2}PC will be investigated as potential control strategy for the inner current loop of the S/G power system before other options are considered (multivariable control with FW, speed, and DC link voltage). The outer loop will remain with PI based controllers, as established in the previous Chapters. Together this will therefore form a hybrid control scheme. The control performance of both MPC and M^{2}PC will be considered in order to determine the better predictive control method for the S/G power system. The hybrid control scheme will also be compared with the full PI control scheme. Finally, system parameter variation will be conducted to determine the robustness of the hybrid control scheme.

6.3 Control Approach

The working principle of MPC is illustrated in Fig. 6.2, where k is the current instant time, t, in the discrete domain and e is the e-th number of sampling steps from

k. The states of a system are measured at time k. These values are then used to predict the future switching states up to step $k + e$ by using the model of the system. An optimisation cost function, J_c, is used over the prediction horizon to determine the optimum control signals [145]:

$$J_c = \min \sum_{e=1}^{N} w_{x_e} \left(r_e - x_e \right)^2 + \sum_{e=1}^{N} w_{u_e} \Delta u_e^2 \qquad (6.1)$$

where N is the number of state variables, x_e is the e-th state variable, r_e is the e-th reference variable, and u_e is the e-th error of the predicted variables, w_{xe} is the weighting factor for the error between the state variables to their reference, and w_{ue} is the weighting factor for the error of the predicted variables. The utilisation of the cost function forms a predicted trajectory (red) if the state values at k are used throughout the prediction horizon. However, at time instant $k + 1$, if the prediction is performed with the state values at $k + 1$ a more appropriate trajectory is formed (blue). In general, the greater number of steps that are performed with updated states, the more accurate the prediction. Eventually, the measured state will follow the predicted trajectory and hence reach the desired state.
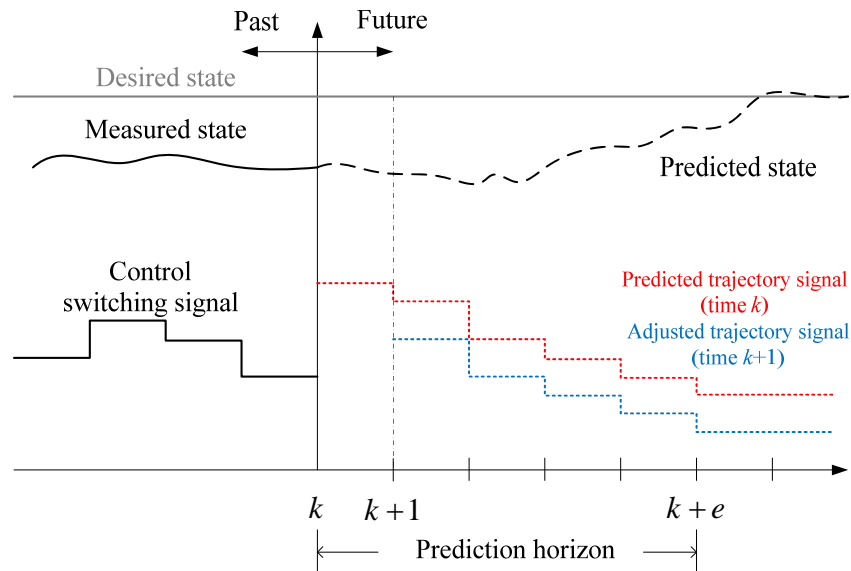
Fig. 6.2. Working principle of MPC [160].

The application of MPC to the S/G system is similar to a drive system. Depending on the type of control scheme, for example FOC or DTC, the appropriate model equations of the controlled system are used. For the S/G system studied here,

as detailed in Chapter 2, FOC is utilised. In order to implement MPC into the FOC for the S/G system, i_d and i_q are regulated in order to produce appropriate switching signals. This modified control structure is illustrated in Fig. 6.3. The outer loop control is retained in order to address the disadvantage MPC's delayed response to disturbances. The required prediction model can be based on the machine voltage equations in the dq frame. The currents are predicted from the finite number of switching combinations of the power converter. The cost function selects the most optimal switching state for the next sampling period based on the error between the predicted dq currents and their reference values. The selected switching state is then sent to the power converter and the cycle is repeated. The following explanation will detail the MPC based inner current loop control design for the S/G system.
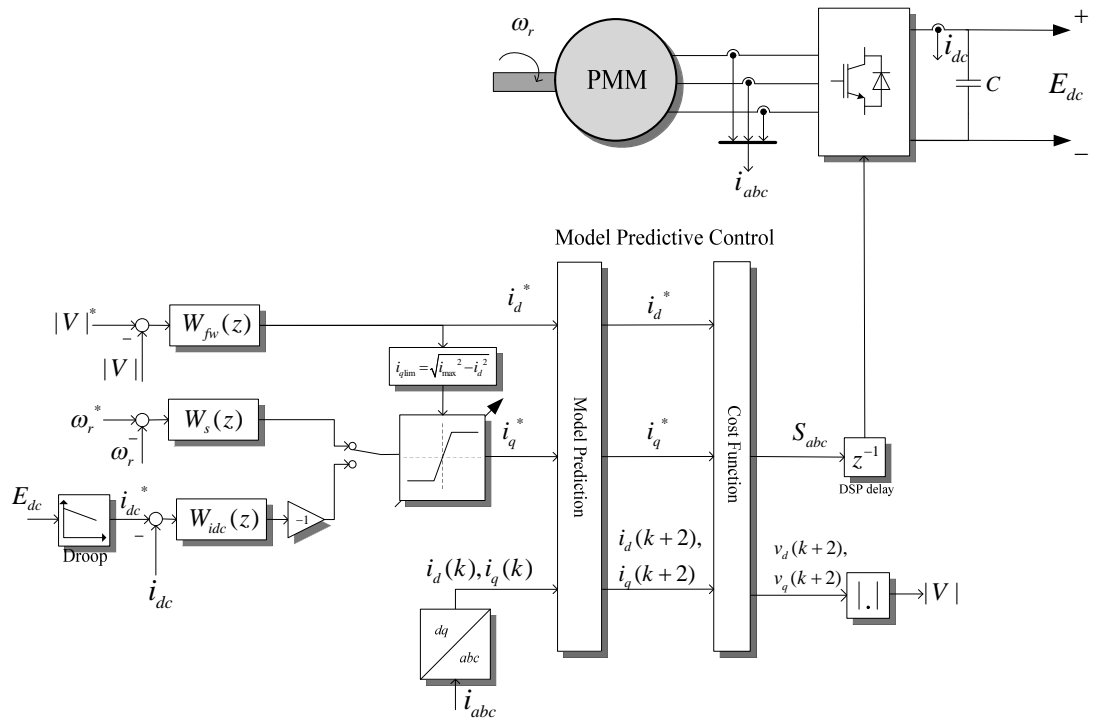
Fig. 6.3. Hybrid PI – MPC scheme.

For the investigated S/G system, the model equations are based on the PMM electrical equations (3.14) and (3.15). The derivative terms within these equations were discretised using the forward Euler method. It was assumed that the state variables remain constant throughout the sampling period, T_s.

$$\frac{di(t)}{dt} \approx \frac{i(k+1)-i(k)}{T_s} \tag{6.2}$$

The discrete model for the PMM can therefore be derived as:

$$v_d(k) = R_s i_d(k) + \frac{L_d(i_d(k+1) - i_d(k))}{T_s} - L_q \omega_e(k) i_q(k) \tag{6.3}$$

$$v_q(k) = R_s i_q(k) + \frac{L_q(i_q(k+1) - i_q(k))}{T_s} + L_d \omega_e(k) i_d(k) + \psi_m \omega_e(k) \tag{6.4}$$

Neglecting the impedance of the transmission line between the AFE and PMM, $v_{d,q}$ can be related to the switching states of the AFE in the dq frame, $S_{d,q}$, and E_{dc}, by the following equation:

$$v_{d,q} = E_{dc} k_{dq} S_{d,q} \tag{6.5}$$

The dq transformation matrix can be applied to transform the relevant three-phase state variables into the discrete domain:

$$\begin{bmatrix} x_d(k) \\ x_q(k) \end{bmatrix} = k_{dq} \begin{bmatrix} x_a(k) \\ x_b(k) \\ x_c(k) \end{bmatrix} \tag{6.6}$$

$$k_{dq} = \frac{2}{3} \begin{bmatrix} \cos(\theta(k)) & \cos\left(\theta(k) - \frac{2\pi}{3}\right) & \cos\left(\theta(k) + \frac{2\pi}{3}\right) \\ -\sin(\theta(k)) & -\sin\left(\theta(k) - \frac{2\pi}{3}\right) & -\sin\left(\theta(k) + \frac{2\pi}{3}\right) \end{bmatrix} \tag{6.7}$$

Since a computational delay is always present in the practical system, the control output calculated at the time instant k can only be applied at the time instant $k+1$. This one step delay can be avoided by predicting values two steps ahead. Equations (6.3) and (6.4) can be re-arranged for two step prediction to give:

$$i_d(k+2) = -\frac{R_s T_s i_d(k+1)}{L_d} + i_d(k+1) + \frac{\omega_e(k+1) T_s L_q i_q(k+1)}{L_d} + \frac{T_s v_d(k+1)}{L_d} \tag{6.8}$$

$$i_q(k+2) = \begin{bmatrix} -\dfrac{R_s T_s i_q(k+1)}{L_q} + i_q(k+1) - \dfrac{\omega_e(k+1) T_s L_d i_d(k+1)}{L_q} \\ + \dfrac{T_s v_q(k+1)}{L_q} - \dfrac{\psi_m \omega_e(k+1) T_s}{L_q} \end{bmatrix} \tag{6.9}$$

Now the equations are established, according to (6.1), the cost function, g_{MPC}, can be defined as:

$$g_{MPC} = \left| i_d^* - i_d^i (k+2) \right| + \left| i_q^* - i_q^i (k+2) \right| \qquad (6.10)$$

The currents are predicted considering all possible switching states. In this study a two-level converter is utilised and so as such eight switching states are possible, as listed in Table 6.1. This assumes that an inverted pair of signals is provided to the two switches connected to each converter leg. The switching state for $k + 2$ that gives the smallest cost function is selected and applied at the next sampling period.

Table 6.1. Two level converter possible switching states.

i	S_a	S_b	S_c
1	0	0	0
2	1	0	0
3	1	1	0
4	0	1	0
5	0	1	1
6	0	0	1
7	1	0	1
8	1	1	1

The whole process for MPC can be summarised using a flow diagram as shown in Fig. 6.4.

6.3.1 Modulated Model Predictive Control

In general, M²PC follows the same prediction pattern except with the addition of another stage for SVM. M²PC includes a suitable modulation scheme that aids in the cost function minimisation of the control algorithm. Since SVM uses a modulator, two active voltage vectors (v_1, v_2) are required for M²PC operation instead of just one. The two active vectors are selected from all the possible adjacent vector pairs using a modified cost function that considers the current prediction and duty cycles, d. The duty cycles determine the appropriate ratio for the four selected vectors within each sampling interval, as shown in Fig. 6.5. The SVM then applies the appropriate switching states over a series of modulation steps, m_s. Fig. 6.6 shows the proposed hybrid PI-M²PC. v_1 and v_2 are the two predicted active voltage vectors while v_{01} and v_{02} are the two zero voltage vectors.

Measure $i_{abc}(k), E_{dc}(k), \omega_e(k)$

Calculate $i_{dq}(k+1), \theta(k+1)$

$i = 1$

Calculate $i_{dq}^i(k+2)$

Calculate g_{MPC}

$i = i+1$

$i > 8?$

No

Yes

Choose i based on smallest g_{MPC}

Apply $S^i(k+2)$
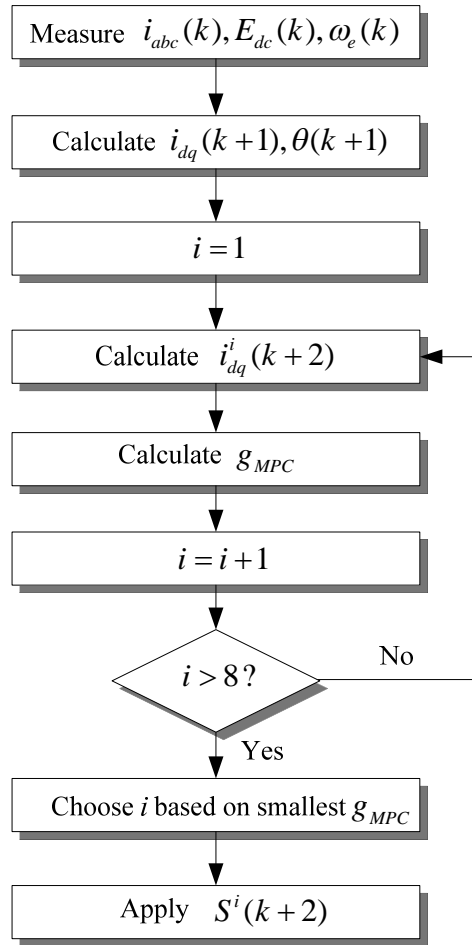
Fig. 6.4. MPC flow diagram for each sampling period.

v_{01} v_1 v_2 v_{02} v_2 v_1 v_{01}

v_a

E_{dc}

T_s

v_b

E_{dc}

T_s

v_c

E_{dc}

T_s

0.25   0.5   0.5   0.5   0.5   0.5   0.25
$d_0 T_s$ $d_1 T_s$ $d_2 T_s$ $d_0 T_s$ $d_2 T_s$ $d_1 T_s$ $d_0 T_s$
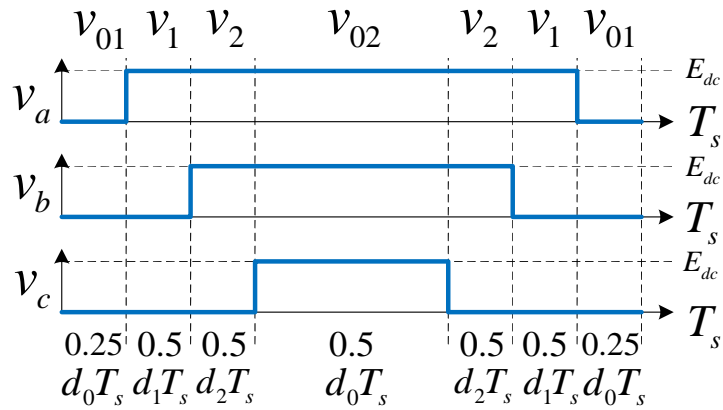
Fig. 6.5. M^{2}PC typical switching pattern [155].

The two active vectors are calculated based on (6.8) and (6.9), and these are used to predict $i^i_{d,q}(k+2)$ and $i^j_{d,q}(k+2)$. The variables with superscript i and j use switching state vectors in the order [1,2,3,4,5,6] and [2,3,4,5,6,1] respectively. The zero vector

157

currents, $i^0_{d,q}(k+2)$ are calculated using (6.3) and (6.4) with $v_{d,q} = 0$. Since SVM is used, equation (6.5) can be re-arranged to give:

$$v_d = E_{dc}\left[d_1 S_d^i + d_2 S_d^j \right] \tag{6.11}$$

$$v_q = E_{dc}\left[d_1 S_q^i + d_2 S_q^j \right] \tag{6.12}$$

where d_1 and d_2 are the duty cycles for v_1 and v_2 respectively. $S^i_{d,q}$ and $S^j_{d,q}$ are the switching states in dq frame.
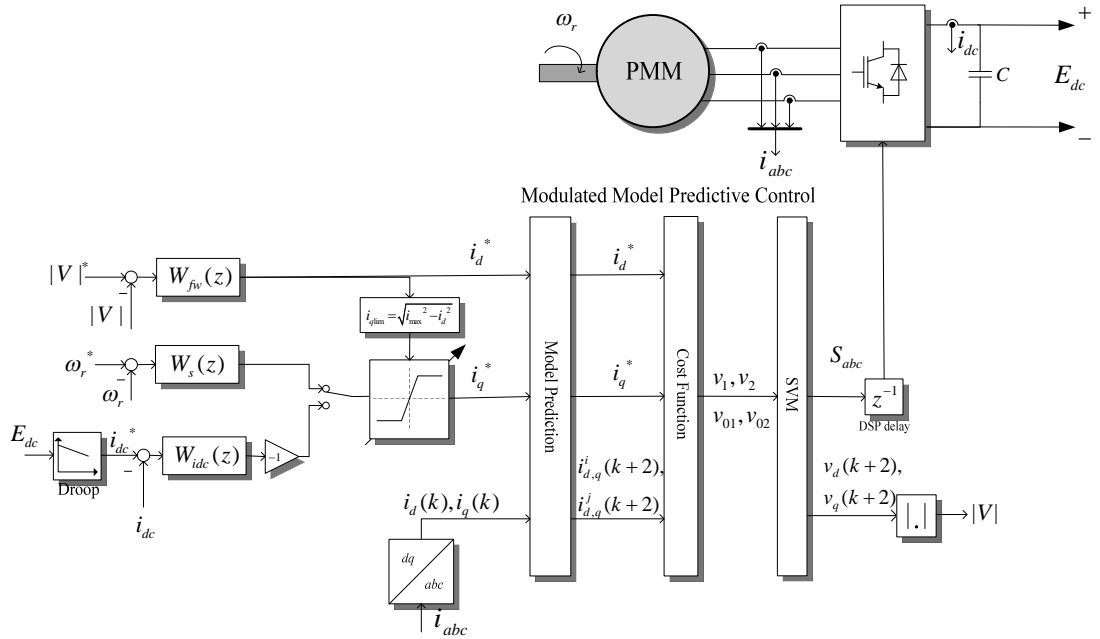
Fig. 6.6. Hybrid PI – M^{2}PC scheme.

The type of M^{2}PC used in this study is based on the dead beat control variation; hence the voltage reference for the model also has to be predicted. If $v_{d,q}^{\ *}(k+1)$ are considered as references for (6.11) and (6.12), then d_1 and d_2 can be solved simultaneously:

$$d_1 = \frac{v_q^*(k+1)S_d^j - v_d^*(k+1)S_q^j}{E_{dc}\left(S_d^j S_q^i - S_d^i S_q^j \right)} \tag{6.13}$$

$$d_2 = \frac{-v_q^*(k+1)S_d^i + v_d^*(k+1)S_q^i}{E_{dc}\left(S_d^i S_q^j - S_d^j S_q^i \right)} \tag{6.14}$$

158

The zero vector currents are compared with the reference currents assuming that the predicted $i_{d,q}(k+1)$ is equal to $i_{d,q}{}^*$:

$$\Delta i_d\left(k+1\right) = i_d^0\left(k+1\right) - i_d^*$$

(6.15)

$$\Delta i_q\left(k+1\right) = i_q^0\left(k+1\right) - i_q^*$$

(6.16)

$v_{d,q}{}^*$ can then be predicted to be equal to the voltage change across the inductances:

$$v_d^*\left(k+1\right) = \frac{\Delta i_d\left(k+1\right)L_d}{T_s}$$

(6.17)

$$v_q^*\left(k+1\right) = \frac{\Delta i_q\left(k+1\right)L_q}{T_s}$$

(6.18)

The zero vector duty cycle can then be calculated using:

$$d_0 = 1 - d_1 - d_2$$

(6.19)

As stated previously, M^{2}PC requires two active vectors:

$$g_{M^2PC1} = \left|i_d^* - i_d^i\left(k+2\right)\right| + \left|i_q^* - i_q^i\left(k+2\right)\right|$$

(6.20)

$$g_{M^2PC2} = \left|i_d^* - i_d^j\left(k+2\right)\right| + \left|i_q^* - i_q^j\left(k+2\right)\right|$$

(6.21)

Together with d_1 and d_2, the general cost function, g_{M2PC}, can then be determined by:

$$g_{M^2PC} = d_1 g_{M^2PC1} + d_2 g_{M^2PC2}$$

(6.22)

The switching combination of $S^i{}_{d,q}$ and $S^j{}_{d,q}$ that offers the smallest g will therefore be applied in the three-phase frame during time intervals of d_1 and d_2 using the modulation scheme. The process in general is summarised in the flow diagram shown in Fig. 6.7.

6.4 **Simulation Results and Analysis**

After having derived the control structure for both MPC and M^{2}PC, they were both tested on the same non-linear Matlab®/Simulink® model used in the previous Chapters. The same system parameters were used, as given in Table 2.3 and Table 2.4. The full PI control scheme designed in the earlier Chapters was used as a benchmark model. The switching parameters used are listed in Table 6.2. The sampling frequency used for MPC was much faster than that used for the other two control methods. This was crucial in order for the current ripple to be comparable in all three cases. The modulation step is the ratio between the PWM carrier signal frequency and sampling frequency. The modulation frequency is the rate at which the control signals are sampled. Within the time domain simulations the modulation frequency was set to be much slower than the level typically used in microcontrollers for drive control systems in order to reduce simulation time. For example, the TMS320C6713 DSP processor can perform control signal modulation at up to 225 MHz [161].

Table 6.2. Converter switching parameters.

Parameter	Value
Sampling frequency for M^{2}PC and full PI	16kHz
Sampling frequency for MPC	150kHz
Modulation frequency, $1/T_m$	1.6MHz
Modulation step, $m_s = T_m/T_s$	100

6.4.1 Inner Current Loop Response

The inner current loops for the three control methods were tested with set reference values. Fig. 6.8 shows the current loop responses to a step of 20A for the three different control methods (PI, MPC, M^{2}PC).

Measure $i_{abc}(k), E_{dc}(k), \omega_e(k)$

Calculate $i_{dq}(k+1), \theta(k+1)$

$i = 1, j = 2$

Calculate $i_{dq}^{\{i,j\}}(k+2)$

Calculate g_{M^2PC1}, g_{M^2PC2}

Calculate d_0, d_1, d_2

Calculate g_{M^2PC}

$i = i+1, j = j+1$

Yes

$i > 6?$

No

Yes

Choose i based on smallest g_{M^2PC}

No

SVM

$m_s = m_s + 1$

$m_s > 100?$

Apply $S^{\{i,j\}}(k+2)$
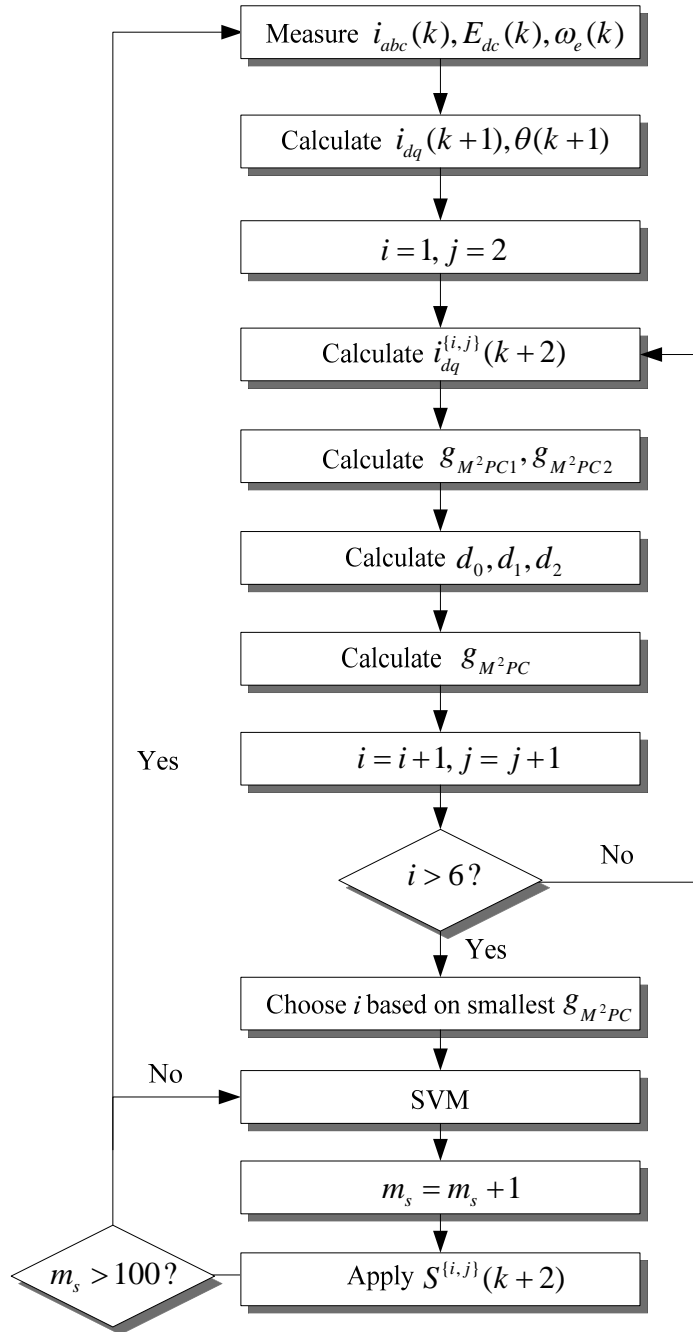
Fig. 6.7. M^{2}PC flow diagram.
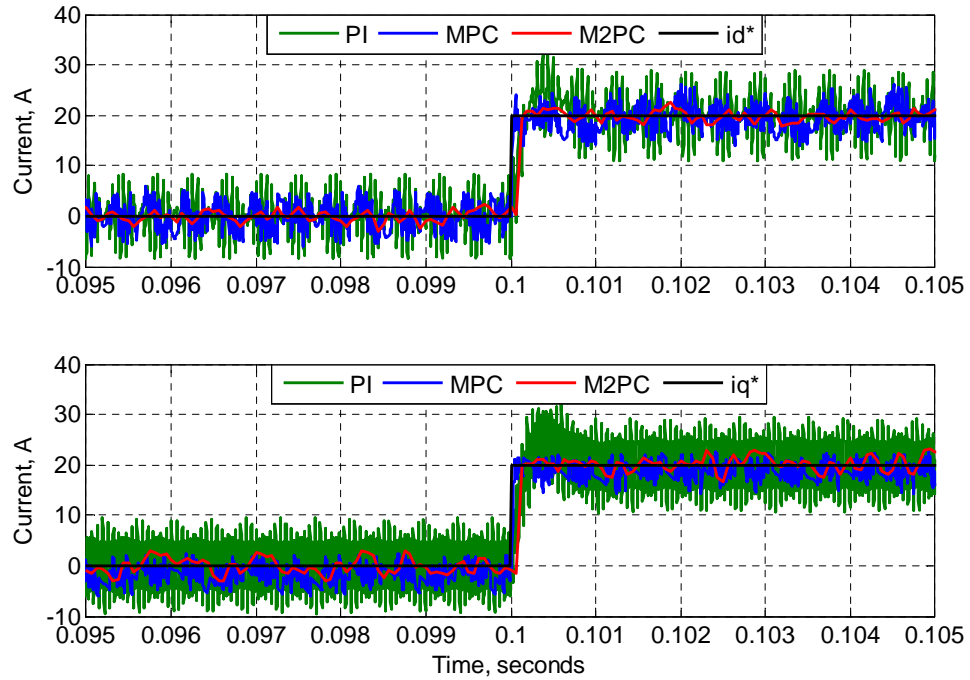
Fig. 6.8. Current responses to a step of $i_d{}^* = 20$A and $i_q{}^* = 20$A at $t = 0.1$s for the different control schemes operating at 8krpm.

The figure shows very fast control dynamics for all the control schemes. M²PC has the least ripple in comparison to the PI and MPC solutions. Despite the very fast sampling frequency, MPC still has a larger current ripple compared to M²PC. Due to the low inductance of the machine, the constant switching states across each sampling period resulted in a large change in current at high DC link voltage levels. The sampling frequency had to be increased significantly in order to reduce the ripple to be within a reasonable range. The modulation scheme within M²PC significantly reduces the ripple without the reliance on a high sampling frequency. As the use of a higher sampling frequency would contribute to more power losses, only M²PC was considered to be a viable alternate control strategy for the S/G system. M²PC was therefore selected for use in the hybrid control scheme.

6.4.2   Angle Compensation

Upon testing the M^{2}PC current loop at different speeds, it was found that there were some steady state errors that became worse as the operating speed was increased, as shown in Fig. 6.9. During the tests shown in Fig. 6.9, the operating speeds were all selected to be below ω_b, with no loads connected, so that both i_d and i_q were not influenced by other factors (FW, loads) other than their own current reference. Employing an outer loop PI may eliminate the steady state error, but if the error is significant, it may influence the performance of the control scheme.
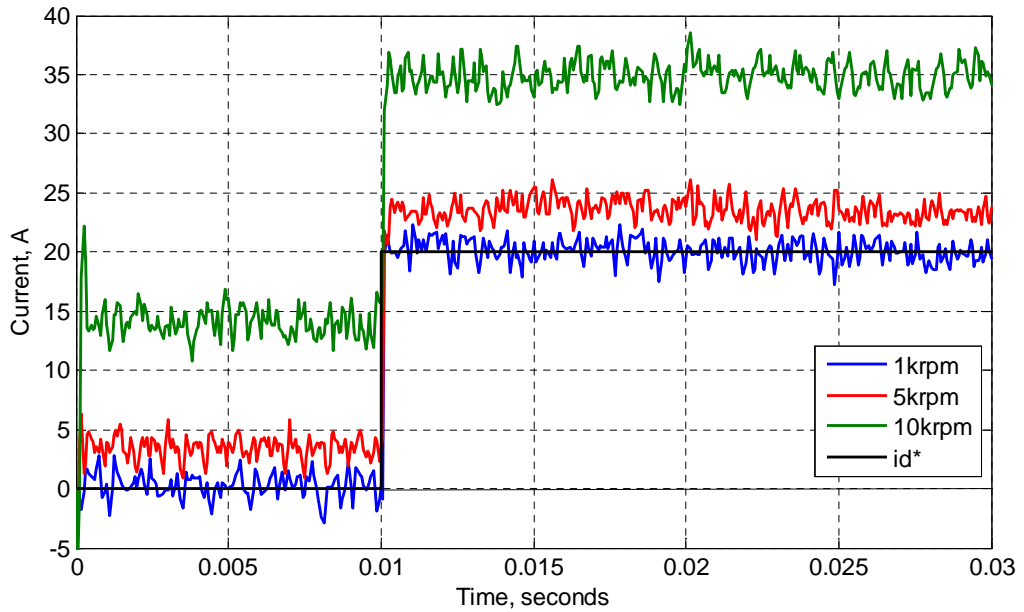
Fig. 6.9. i_d response to a step $i_d^* = 20$A at different operating speeds.

For drive systems that operate at high speeds, [153] highlights that the prediction of the electrical angle, θ, needs to be compensated. This is because θ is proportional to the machine rotor position, θ_r, and therefore there would be a difference between the predicted and actual rotor position depending on the speed, as shown in Fig. 6.10. The steady error becomes more apparent as the speed increases. In order to reduce this error, θ_r has to be compensated 1.5 sample periods ahead in order to obtain the mean rotor position after one sample delay. This can be represented by:

$$\theta(k+1) = 1.5 p \omega_r(k) T_s + \theta(k) \qquad (6.23)$$

163
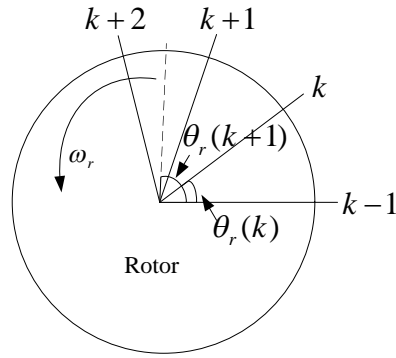
Fig. 6.10. Rotor position at different sampling intervals.

After adding the angle compensation to the time domain simulation, the steady state error was reduced, as seen in Fig. 6.11. Any remaining steady state error can be regulated by the outer loop PI controllers.
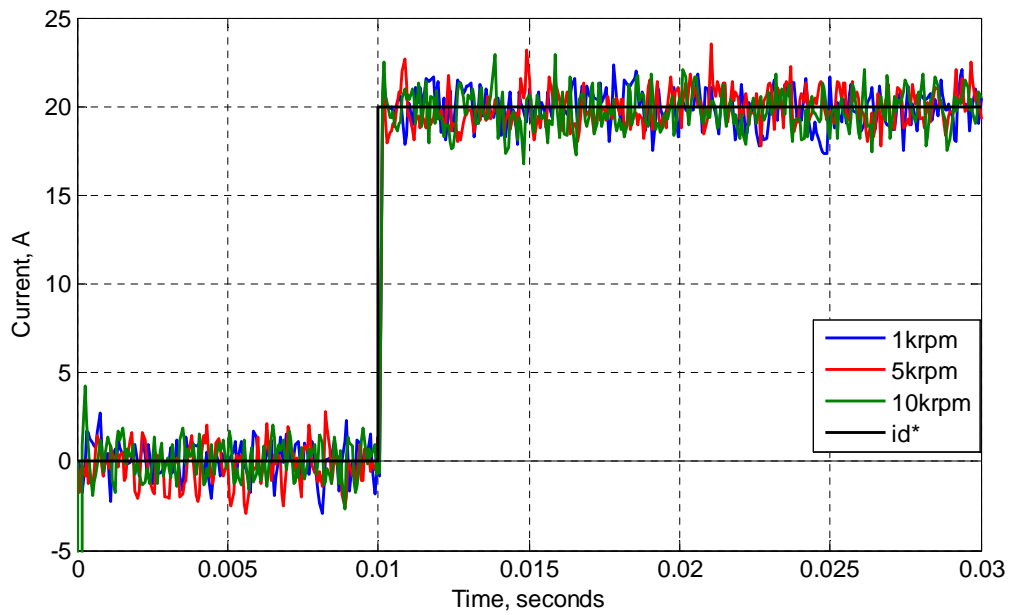
Fig. 6.11. i_d response to a step $i_d^* = 20$A at different operating speeds with angle compensation.

6.4.3 Steady State Operation

The inner current loop control was combined with the outer loop PI controllers to test the overall operation of the S/G system. Fig. 6.12 shows the responses of the key state variables during starter mode. The speed reference is set at 20krpm.
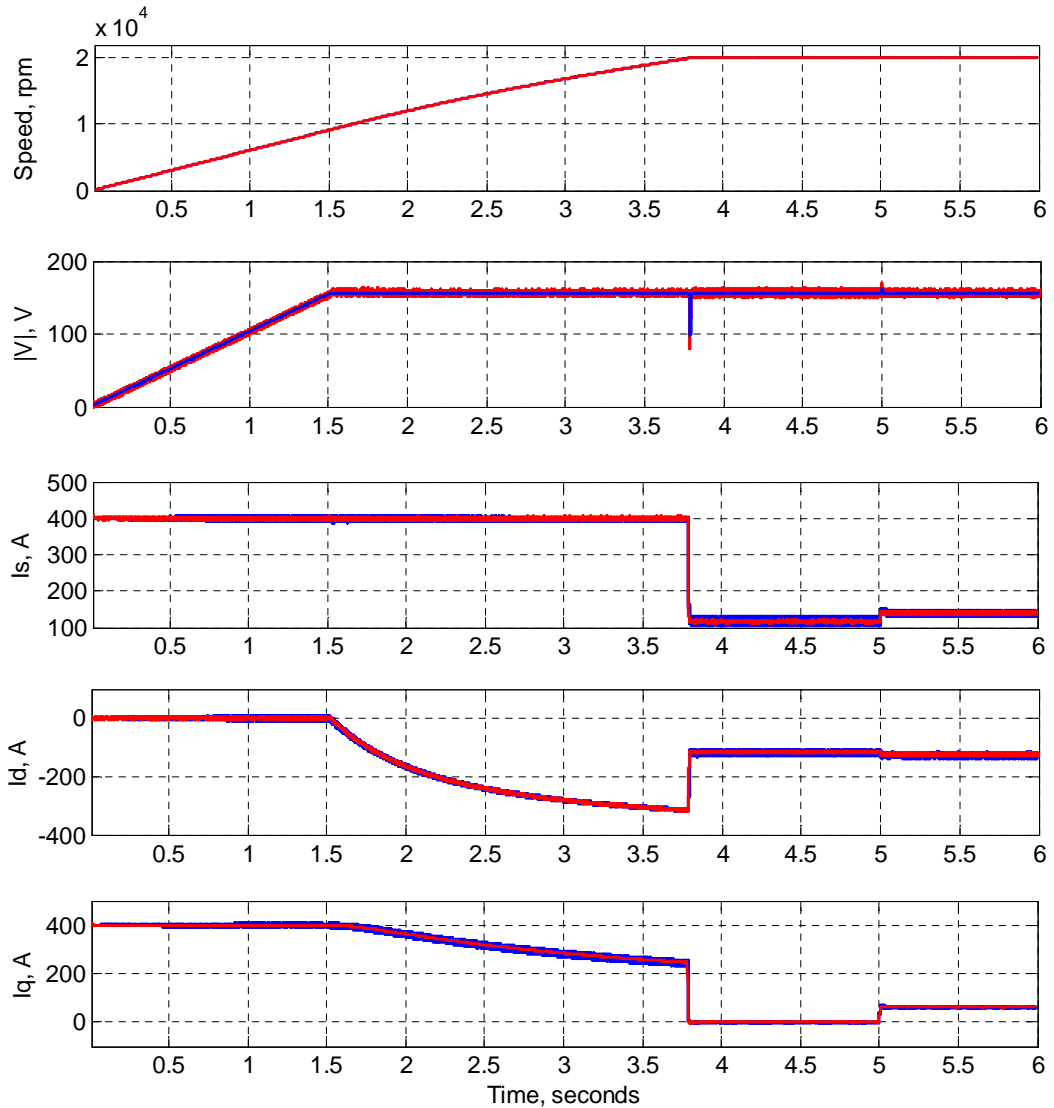
Fig. 6.12. Time domain simulation in starter mode up to 20krpm between the full PI (blue) and hybrid PI-M^{2}PC scheme (red).

The combined inertia of the machine and engine was reduced to $J = 0.103kgms^2$ for this simulation scenario in order to reduce the simulation time. FW was operational when $/V/$ reached its reference value of 155.9V by i_d injection into the machine, as clearly seen in the simulation results from $t \sim 1.5s$. Once the S/G system reached steady state, a load, T_L, of 10Nm was applied at $t = 5s$ and the responses can be seen in Fig. 6.13. The controlled variables $/V/$ and ω_r, which use outer loop PI based controllers, have zero steady state error upon T_L impact due to the integral terms present in their respective controllers. Using the hybrid PI-M^{2}PC scheme, significant dq current ripple reduction was observed throughout the simulation due to the use of M^{2}PC as part of the control structure.
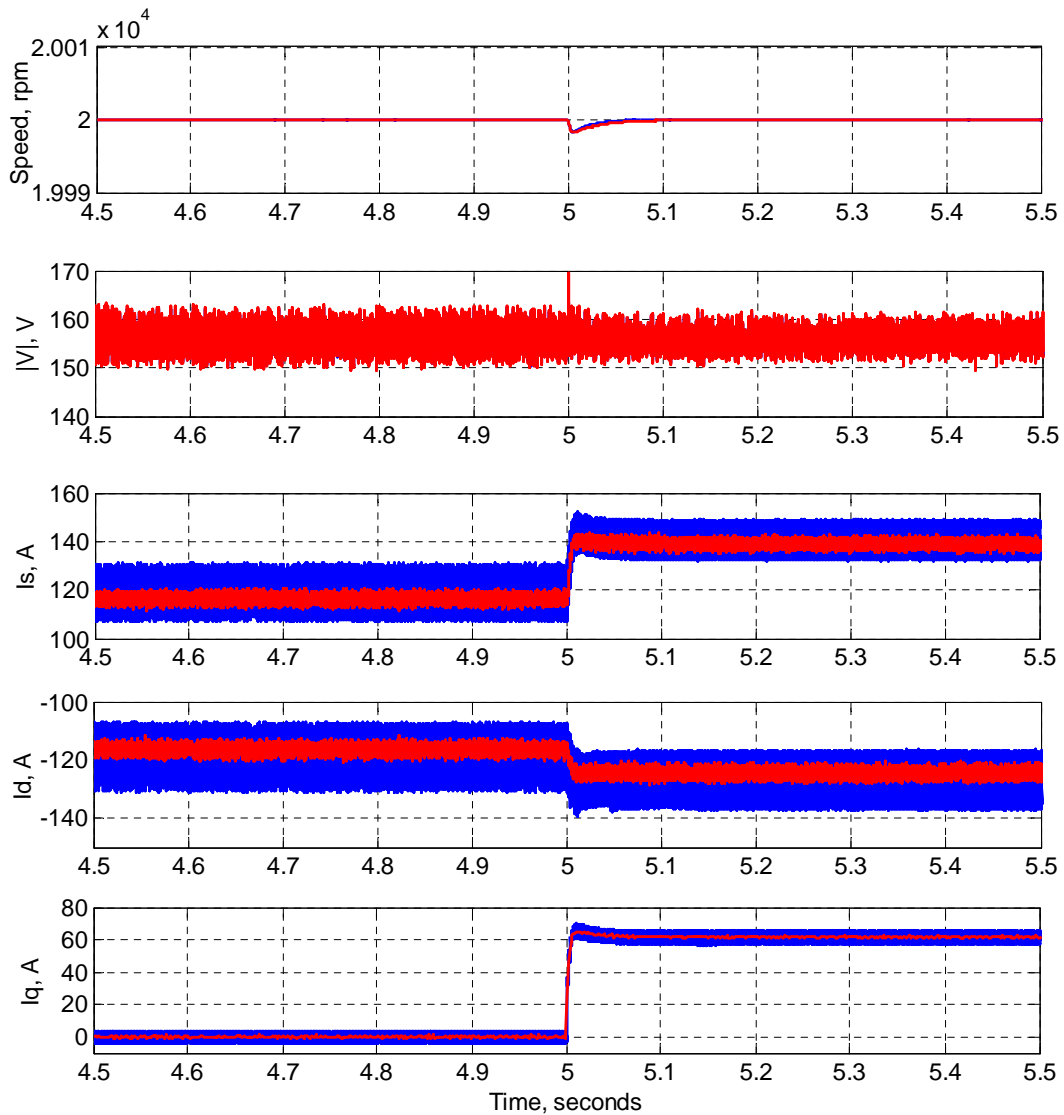
Fig. 6.13. Time domain simulation in starter mode with T_L = 10Nm at t = 5s operating at 20krpm between the full PI (blue) and hybrid PI-M^{2}PC scheme (red).

Fig. 6.14 shows the key state variable responses using the two control schemes in generator mode. During this simulation the DC link bus was subjected to load demands of 50A, 100A, 130A, and 170A in intervals of 0.03s. Both control schemes were able to operate with the subjected electrical loads at 32krpm. Significant reduction in the current and /V/ ripple was observed when using the hybrid PI-M^{2}PC. When the electrical loads were added, there was very little difference in the steady state ripple for E_{dc}. It can be seen that there was a more underdamped response for all of the state variables when using the hybrid PI-M^{2}PC scheme.
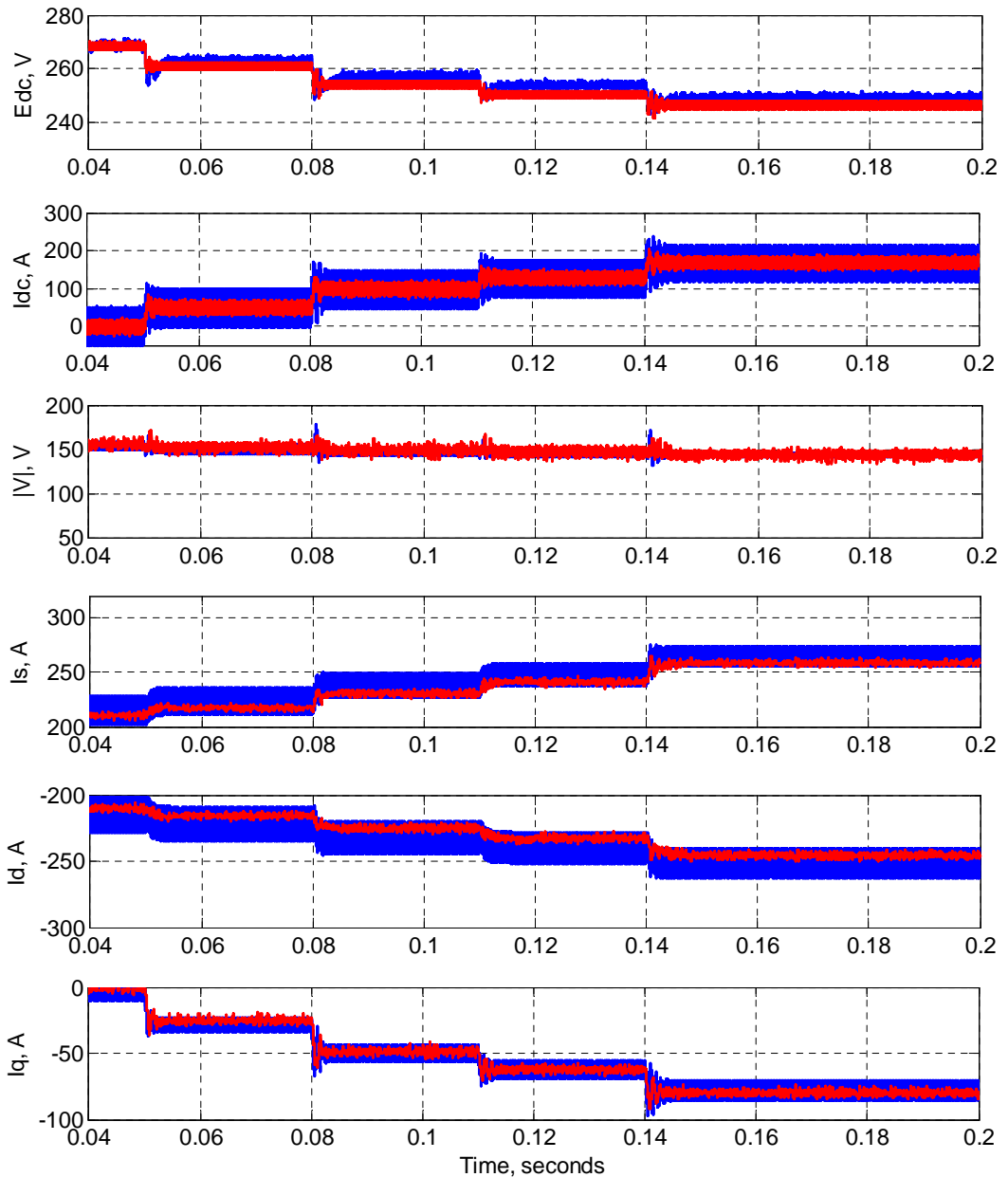
Fig. 6.14. Time domain simulation in generator mode operating at 32krpm between the full PI (blue) and hybrid PI-M^{2}PC scheme (red).

6.4.4   Outer Loop Controller Analysis with M^{2}PC

The stability range for non-linear MPC models can be very difficult to determine and analyse as it requires non-linear theorems such as Lyapunov stability [146]. This approach can be quite complex and is a subject of separate research. In this thesis the stability conditions are assessed by time-domain simulations. Steady state comparisons between the hybrid PI-M^{2}PC and full PI control schemes were

used to benchmark the controller stability performance. Fig. 6.15 shows the i_{dc} response for both control schemes to load demands of 50A (0.05s), 80A (0.08s), 110A (0.11s), 140A (0.14s), and 170A (0.17s) respectively.
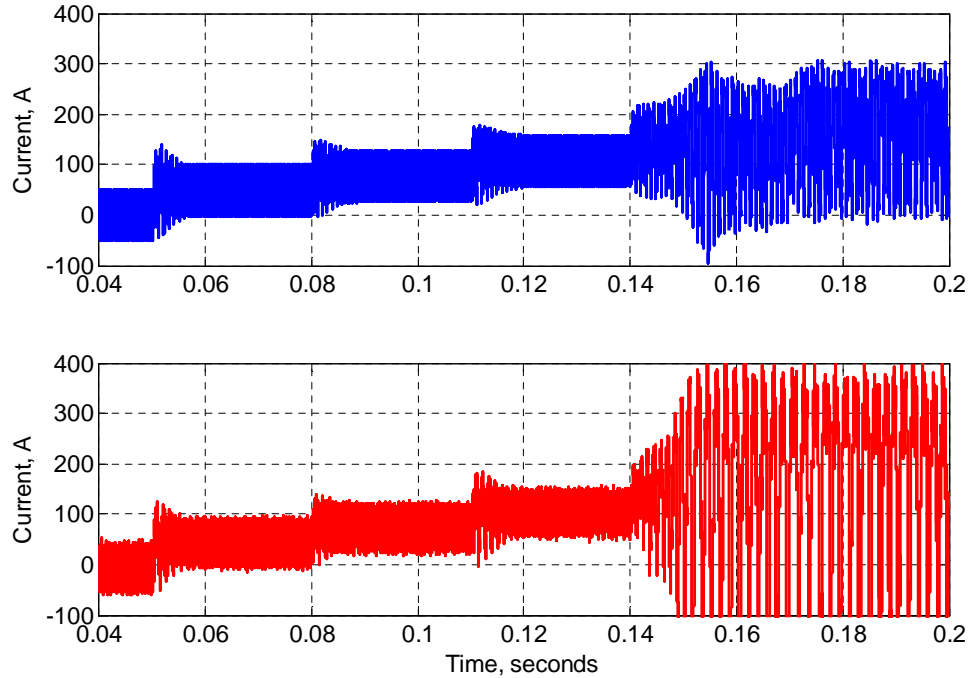
Fig. 6.15. i_{dc} response between the full PI (top, blue) with $k_{pi} = 0.2$, $k_{ii} = 1400$ and hybrid M^{2}PC (bottom, red) with $k_{pi} = 0.2$, $k_{ii} = 1800$.

It can be seen from Fig. 6.15 that i_{dc}, when controlled by the full PI scheme, became more oscillatory during the load step change to 140A after k_{ii} was increased from 200 to 1400. Note that the bandwidth of the i_{dc} controller around this k_{ii} value seen in Fig. 5.11 was very close to the inner current loop bandwidth. The hybrid structure showed a similar instability scenario when its i_{dc} controller had $k_{ii} = 1800$. When k_{ii} for the hybrid control was 1400 (similar to the full PI scheme), the responses were stable for every loading condition. The k_{pi} range was also compared for the two control schemes and the results are shown in Fig. 6.16. The full PI scheme became oscillatory when subjected to 140A load after k_{pi} was changed to 0.28. The hybrid control was still stable when k_{pi} was changed up to 0.5. This indicates that the faster inner current loop bandwidth provided by the use of M^{2}PC does improve the i_{dc} controller proportional and integral gain range.
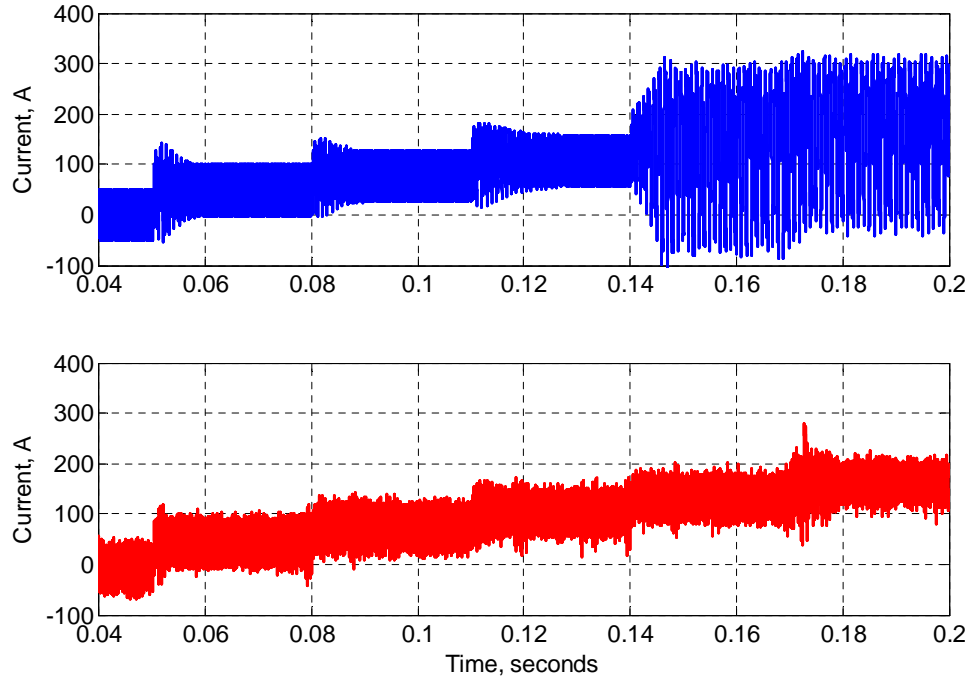
Fig. 6.16. i_{dc} response between the full PI (top, blue) with $k_{pi} = 0.28$, $k_{ii} = 200$ and hybrid M^{2}PC (bottom, red) with $k_{pi} = 0.5$, $k_{ii} = 200$.

6.4.5 Parameter Variation

For model based controllers such as MPC, it is important to assess the robustness of the technique towards parameter changes in the power system, especially if there are no parameter observer algorithms to adapt to the changes. Therefore, in order to test the robustness of the hybrid control scheme, parameter variation was introduced within the simulation model. Parameters that could change in actual drive systems due to operating temperature or other factors such as R_s, $L_{d,q}$, ψ_m, and C were assessed. Any significant changes in the state variables could then be observed through the dq currents along with the parameter difference from its nominal value.

In practise, the variation of R_s is based on the copper wire that is used for the machine windings. With respect to the operating temperature of the S/G system, R_s can increase by two to three times its nominal value. In order to fully evaluate the effect of R_s, larger variations than this were considered. Fig. 6.17 shows the i_q response when R_s was altered by 5, 10, 40, 70, and 100 times its nominal value

(1.058mΩ). The figure also shows the responses when subjected to a step in electrical load of 10kW at $t = 0.08$s. This was included in order to determine any differences before and after load impact. It can be seen that there was a difference in steady state values that are increasing (in the negative direction) as i_q had to compensate for the higher R_s. Even at 100 times the nominal value of R_s, the control was still stable.
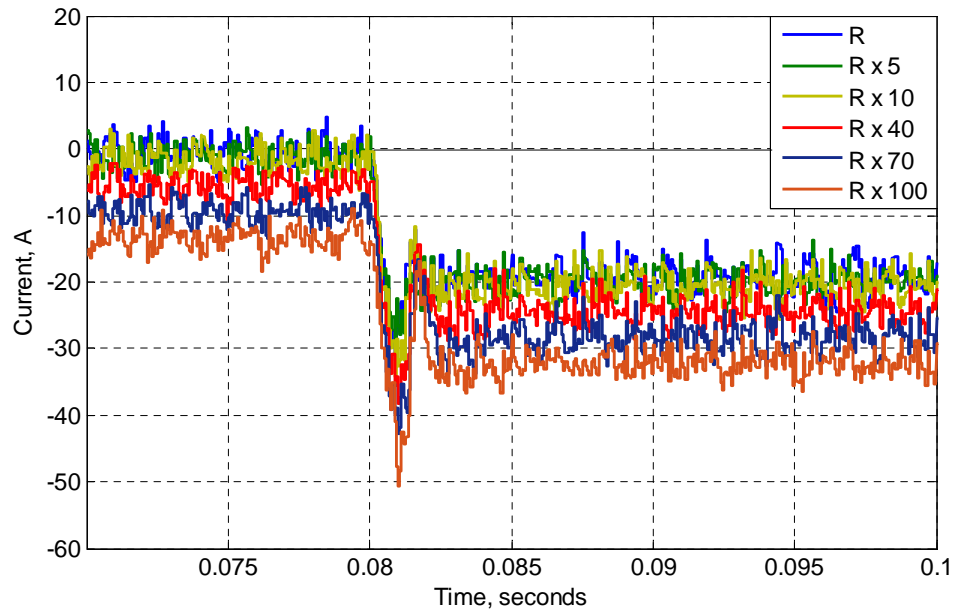
Fig. 6.17. i_q responses with different values of R_s operating at 32krpm.

Both L_d and L_q were reduced simultaneously in increments of 5% of their nominal value with the same load conditions as the R_s variation test. Both dq currents were found to be affected by the change in inductance, as can be seen in Fig. 6.18. Large ripples can be seen when the dq inductances were at 80% of the nominal value (99μH). The variation in L_d and L_q affects the accuracy of the model prediction and as such causes the different steady state values of i_d.
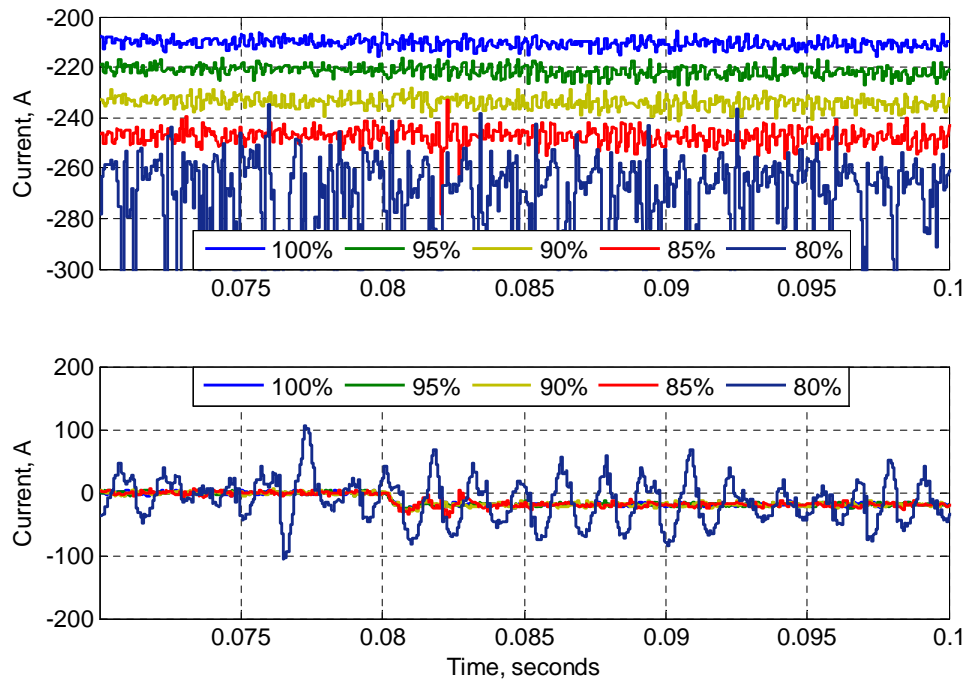
Fig. 6.18. i_d (top) and i_q (bottom) responses with different values of machine inductance operating at 32krpm.

ψ_m was reduced in increments of 5% of its nominal value. Both of the *dq* currents were observed and are shown in Fig. 6.19. The change of ψ_m resulted in different steady state results for i_d due to the decrease of back-emf. Less i_d was therefore required for FW. Large ripples were observed at 80% ψ_m when operating without load. After the load impact of 10kW, the large oscillations reduced and stability was restored. Fig. 6.20 shows i_q responses to changes of *C* when reduced by 20% increments. The reduction of *C* mainly affected the i_{dc} controller which explains the oscillations.

Overall, the influence of *L* and ψ_m variation imposed the most significant effect to the hybrid M^{2}PC control performance. A maximum change of 20% *L* or 25% ψ_m was required before the controller became unstable. Preliminary experiments were performed on the AEGART machine in order to determine the degree of parameter variation. Two factors were considered that could influence the machine parameters; operating speed and temperature. The machine R_s, L_d, L_q, and ψ_m were measured at different operating conditions. The most significant change for R_s was up to 5 times the nominal value due to operating speed variation. With respect to temperature, ψ_m varied up to 20% of the nominal value. L_d and L_q had very small variations (<5%)

which can be neglected. Comparing this information with the parameter variation range of the hybrid M^{2}PC, it showed that the AEGART system is able to adopt this control method without observers. In applications where the actual system parameters can vary beyond this range, observers can be used for parameter estimation such as Luenberger observer and Kalman filter [146].
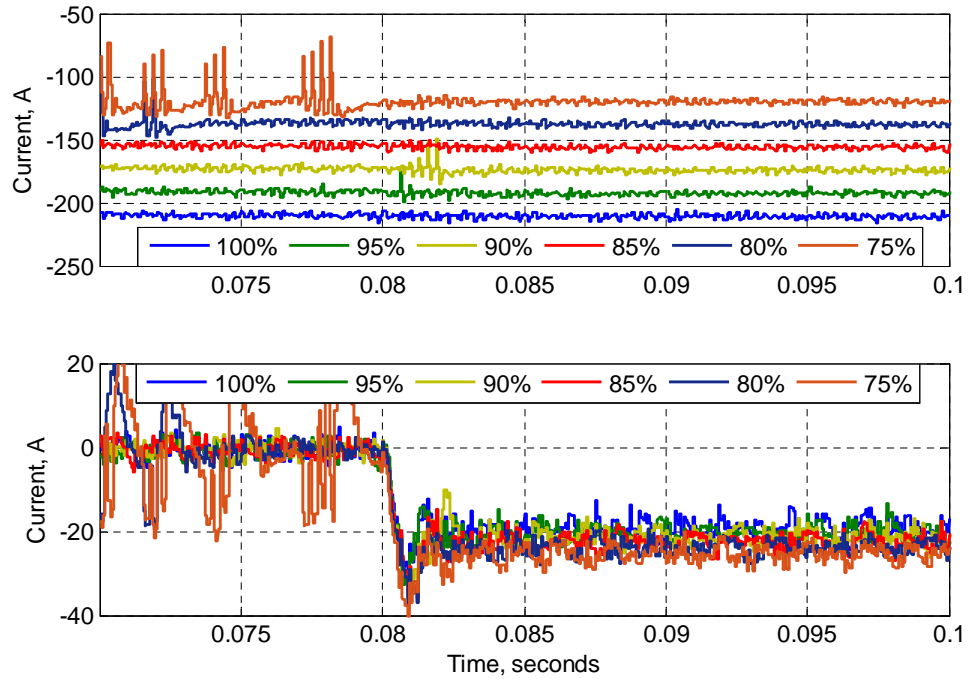
Fig. 6.19. i_d (top) and i_q (bottom) responses with different values of ψ_m operating at 32krpm.
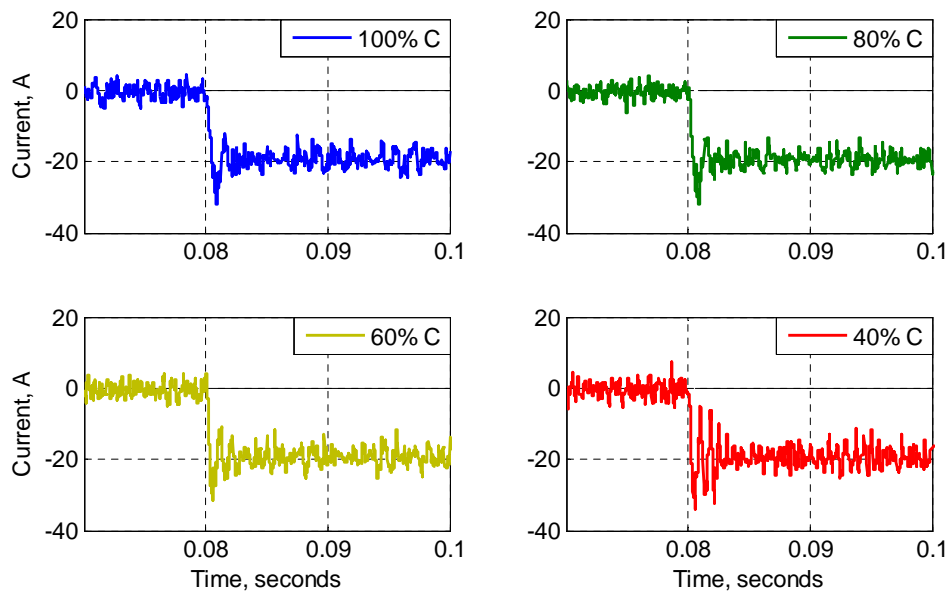
Fig. 6.20. i_q responses with different values of C operating at 32krpm.

The investigated use of MPC for S/G power systems can been summarised as follows:

- MPC can be successfully applied for inner current loop control due to its very fast dynamic. This would therefore allow a much faster outer loop controller to be used.

- A variant of MPC with an intrinsic modulation scheme, named M^{2}PC, can be utilised for the S/G system.

- M^{2}PC was found to provide very fast current loop dynamics in addition to reduced ripple; especially when compared to the MPC and PI based control schemes.

- The hybrid PI-M^{2}PC control scheme was defined and tested across the S/G operational conditions. In comparison to the full PI control solution, the hybrid scheme offered reduced current ripple. The downside was increased oscillations during the load transient periods.

- The i_{dc} controller stability range was found to be wider for the hybrid PI-M^{2}PC compared to the full PI scheme. Due to the faster dynamics of the inner current loop, it was found that the i_{dc} controller gains could be increased significantly in order to achieve higher bandwidths.

- Parameter variation tests showed that the hybrid control performance was most susceptible to the change of L and ψ_m within a variation of 20% and 25% respectively. Parameter observers are required to compensate for possible parameter variations beyond that range.

6.5 Conclusion

MPC was considered for the inner current loop of the S/G system to take advantage of its very fast dynamic response. This control method was investigated within this Chapter in order to assess its potential for improving the control performance of the S/G system. A variant of MPC called Modulated Model Predictive Control (M^2PC), which incorporates a modulation scheme as part of its control strategy, was also considered. The MPC and M^2PC schemes were derived and implemented for the *dq* current loop. The outer control loops were still controlled using the PI controllers designed in the previous Chapters. The performance of both MPC and M^2PC schemes was compared with the full PI control scheme. M^2PC showed reduced current ripple in comparison to MPC despite the MPC scheme utilising a much higher sampling frequency. As a result M^2PC was selected for detailed analysis. Differing steady state errors were found to be present for the M^2PC scheme depending on the operating speed. Angle compensation was therefore added as the model prediction was being affected by the speed of the PMM. This dramatically reduced the steady state error. The addition of the outer loop PI controllers then eliminated any remaining steady state error.

Overall, the hybrid PI-M^2PC scheme was found to be capable of S/G control operation. Moreover, it showed improvements in terms of reduced current ripple when compared to the conventional full PI control scheme. The stable gain range for the i_{dc} controller was also found to be wider for the hybrid PI-M^2PC scheme compared to the full PI control scheme. Parameter variation tests verified the robustness of S/G system when utilising the hybrid PI-M^2PC without any observer algorithms.

Chapter 7   Experimental Validation

7.1   Introduction

The core analytical findings reported in the previous Chapters can be summarised as below:

- The FW plant is non-minimum phase during both starter mode with unlimited i_q^* and generator mode with limited i_q^*. The i_{dc} plant is non-minimum phase during generator mode with unlimited i_q^*. For all other modes, the plant is minimum phase.

- The k_{iv} range limit for the FW controller was identified using the Routh-Hurwitz criterion across various operating speeds and loads. Limited k_{iv} is allowed when the control plant is non-minimum phase.

- A fixed value of k_{iv} can be selected for stable operation when considering both starter and generator modes at the highest speed and load demand, except when in generator mode with limited i_q^*. In this case, the stable k_{iv} range decreases according to the load demand. There is an unstable region at low load demand where the k_{iv} range becomes negative. A novel current limiting method was proposed to eliminate this unstable region. In the same operating condition (generator mode with limited i_q^*), an adaptive FW controller gain can be used to vary k_{iv} according to the load demand. This keeps the system within the stable operating region and provides good control performance.

- The i_{dc} plant is non-minimum phase and so the controller can be designed for the S/G system assuming the worst case operating point in generator mode.

- M^{2}PC can be used an alternative current control method for the S/G system. Reduced current ripple and much faster current control dynamics can be achieved using M^{2}PC.

This Chapter will report experimental verification of these key findings. For this purpose, a scaled model of the AEGART S/G system was designed and built. The

developed controllers will be adapted according to the rig parameters. The experimental results will be reported and compared with those theoretically expected.

7.2   Experimental Setup

In this Section, the experimental rig developed for the verification tests will be described. This rig is a scaled version of the AEGART system and was designed due to the unavailability of the AEGART S/G system which is currently undergoing testing at the facilities of the industrial partner. Nonetheless, the full PI control scheme will be used in the completed AEGART S/G system. The scaled model will allow for more extended tests including advanced concepts and future ideas that are deemed too risky to be performed on the actual S/G system.

Fig. 7.1 shows the block diagram for the experimental rig. In comparison to the investigated S/G power system, the role of the aircraft engine is replaced with a DC machine. A dedicated DC drive is connected to the DC machine which controls the machine speed/torque characteristics. The DC machine can be used to apply load torque or drive the PMM depending on starter or generator operation.
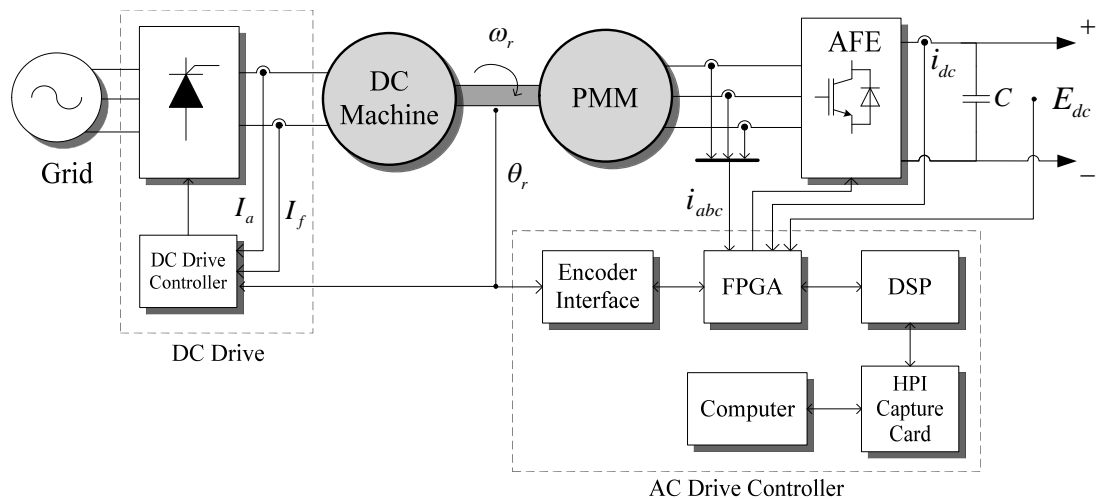
Fig. 7.1. Layout diagram for the experimental rig.

The main machine, which is used to represent the AEGART S/G, is a PMM powered by a two-level AFE. This is controlled by an AC drive controller. A digital signal processor (DSP) is used to implement the designed control scheme and control the PMM. i_{abc}, i_{dc}, and E_{dc} are measured using current and voltage sensors which transmit their data to a field programmable gate array (FPGA). Information about the PMM rotor position is decoded by the encoder interface board. The data is sent to the DSP in order for the control scheme to perform its functions. The output switching signals are sent to the AFE via the FPGA. The measured and calculated variables are sent to a computer via a HPI capture card [162]. Bi-directional communication is established through this card and additional commands from the computer can be sent through Matlab®.

Fig. 7.2 shows the overall prototype setup in the Aerospace Technology Centre at The University of Nottingham. The rig can be thought of two subsystems mechanically coupled together. The PMM with the two-level AFE and corresponding control equipment are considered to form an AC drive system. The other subsystem consists of a DC machine and its drive so hence forms a DC drive system. Both of these subsystems are controlled independently from each other although information on the communal shaft speed is shared.
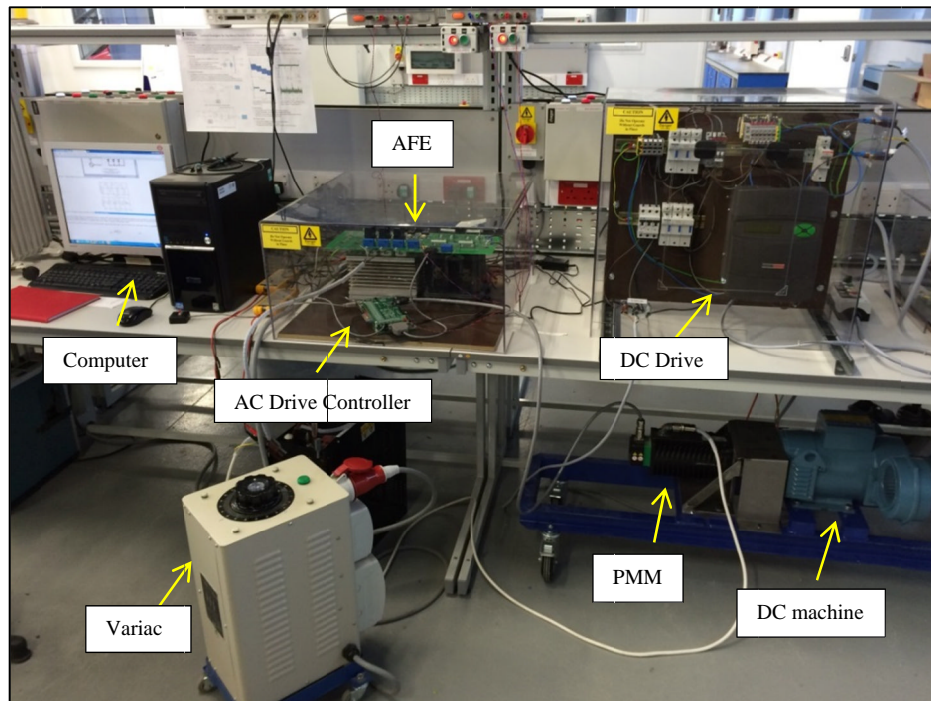
Fig. 7.2. Overall experimental setup.

The following Sub-sections contain detailed descriptions of each of prototype subsystems.

7.2.1 AC Drive System

The AC drive system is the main part of the test bench as it represents the AEGART S/G system. The designed control strategies are applied to this drive system via the AC drive controller. More details on the AC drive controller can be found in Appendix D. Fig. 7.3 shows the surface mounted permanent magnet synchronous AC servomotor used in this research work.
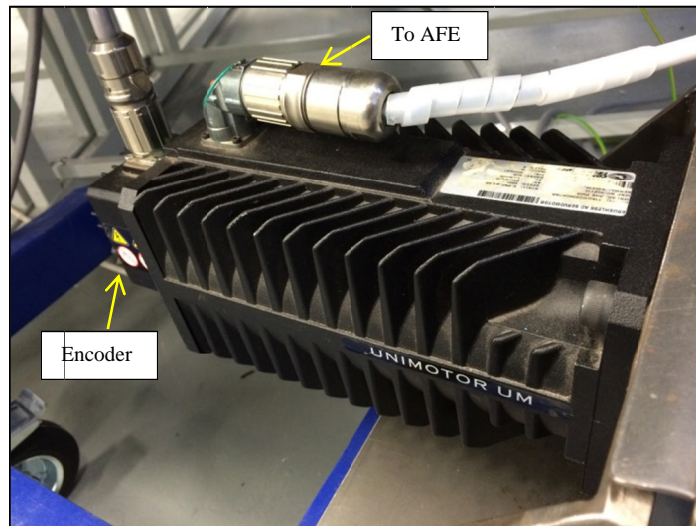
Fig. 7.3. Emerson UMC series PMM.

It was manufactured by Emerson (S/N 115UMC300CACAA [163]). The relevant machine parameters can be seen in Table 7.1. It is a six pole (three pole pair) machine with rated speed of 3krpm up to a maximum of 4krpm. The nominal power rating is 2.54kW and the rated torque is 8.1Nm (from 5A rated current). The machine has built-in encoder for rotor angle measurements and Hall effect sensors for machine start-up if required.

The AFE was constructed in-house based on the converter design by Dang in 2004 [164]. This can be seen in Fig. 7.4. The layout was determined by a custom made printed circuit board (PCB) which allows direct connection of various components of the power converter.

Table 7.1. Experimental rig PMM parameters.

Parameter	Value
Rated phase voltage	230V
Machine stator resistance, R_s	1.2Ω
Machine d-axis inductance, L_d	6.17mH
Machine q-axis inductance, L_q	8.379mH
Machine mutual flux, ψ_m	0.23Vs
Combine AC and DC machine inertia, J	0.0116kgm^2
Viscous damping, B	0.0015Nms
Mechanical friction, f_c	0.5372Nm

There are six slots for the power modules to be connected to the PCB with appropriate room for the gate drivers, sensors, and protection devices. Each slot can accommodate a single phase AC input. For this experiment, three slots were used in order to create a three-phase system and each was equipped with an IGBT module (SKM100GB12V), as can be seen in Fig. 7.5. The rated operational voltages and currents for the IGBT module are 600VAC and 100A respectively [165]. Each module has two IGBT switches. This therefore matches the required two-level converter topology. The gate drivers for each module interpret the control signals sent from the FPGA and convert them into PWM switching signals for the IGBTs. An appropriate heatsink was used to dissipate any heat generated by the IGBTs. Snubber capacitors were also connected to each IGBT modules in order to prevent voltage spikes caused by the switching effect.

Just beside the AC side of the converter is the DC link bus. Four 400V 4700µF electrolytic capacitors (KEMET ALS30 series) were used to form the overall DC bus capacitance [166]. The capacitors are arranged in parallel pairs with two capacitors in series within each pair. This therefore forms a capacitor bank with a maximum voltage of 800V and capacitance of 4700µF. The capacitors' primary function is to filter ripples caused by power switching. Discharging resistors were also connected in parallel to each of the capacitors in order to safely discharge any remaining voltage after power is removed.
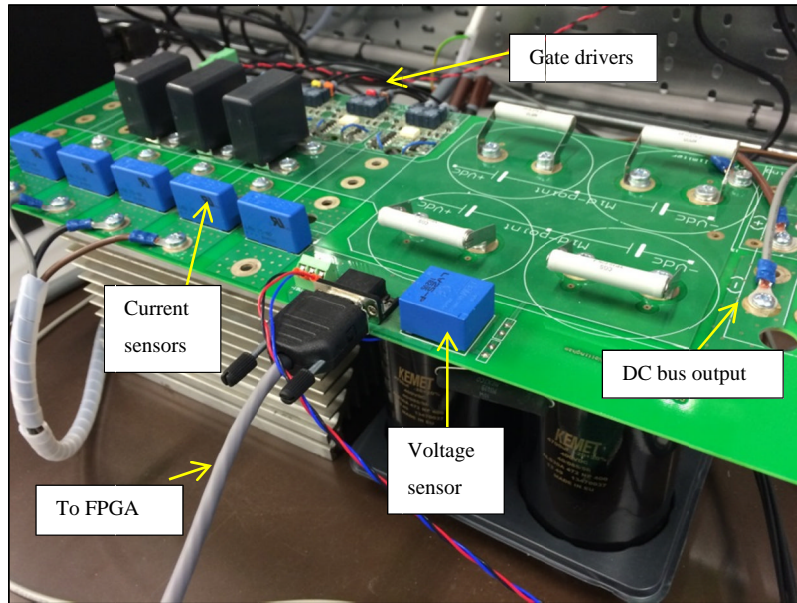
Fig. 7.4. Two level AFE for the AC drive system.

Sensors were used to measure the key variables for the designed control scheme. i_{abc}, i_{dc}, and E_{dc} were measured with the current and voltage transducers (LEM series) seen in Fig. 7.4. The PCB layout enables the sensors to be attached to the board and the measurements are sent to the DSP via the FPGA for control purposes.
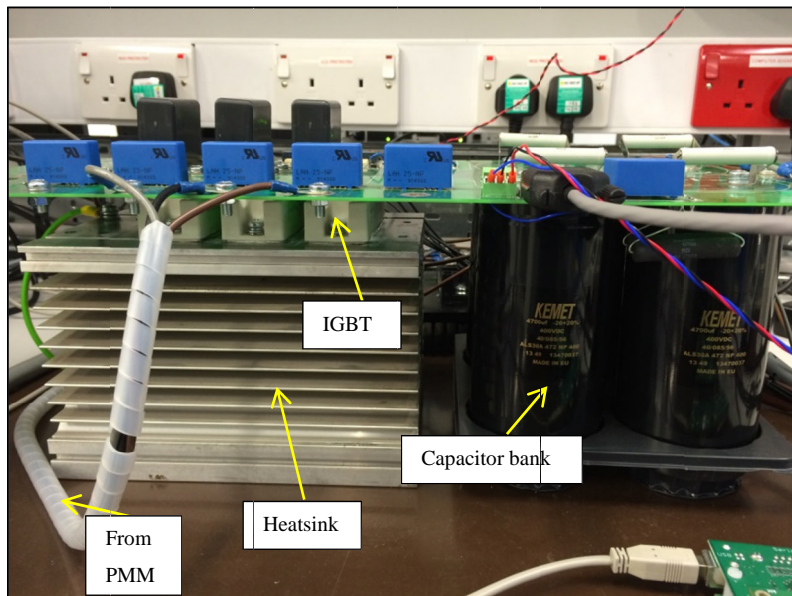
Fig. 7.5. Side view of the AFE.

During starter mode operation, the PMM is powered from the DC link via the AFE. A variable AC transformer (Variac) is used to supply power from the grid to the DC link. The AC power is rectified to DC using a diode rectifier as seen in Fig. 7.6. The voltage ripple on E_{dc} is filtered by the DC bus capacitors. During generator mode, the PMM is driven by the DC machine and the variac can be disconnected from the DC link. The electrical power accumulated in the DC link cannot be sent back to the grid; hence it is dissipated by the use of resistors, R_{dc}, that represent the electrical loads.
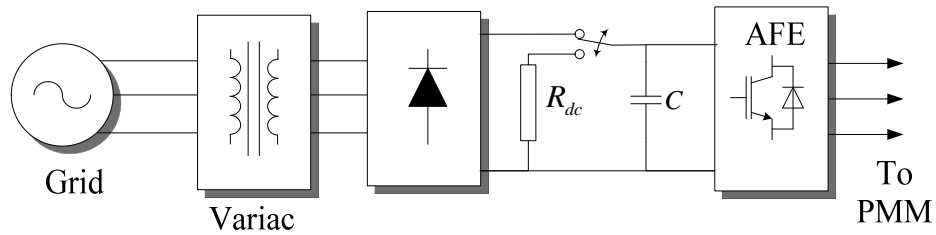
Fig. 7.6. Grid connection to the AFE DC bus for S/G operation.

The relevant operational parameters are summarised in Table 7.2.

Table 7.2. AFE parameters.

Parameter	Value
Total DC link capacitance, C	$4.7mF$
Rated AC current	$100A$
Rated AC voltage	$600V$
Maximum DC link voltage	$800V$

7.2.2 DC Drive System

In starter mode, the main function of the DC drive system is to provide a load torque to the PMM. In generator mode, the PMM has to be driven by the DC drive at constant speed. A DC brushed machine from TT Electric (LAK 2100-A) is selected for this purpose, as seen in Fig. 7.7. It is a two pole machine rated at 4.8kW capable of reaching a maximum speed of 5.5krpm [167]. More details about the DC machine can be found in Table 7.3. The DC machine was selected with such ratings in order to be able to drive the PMM up to its nominal speed (3krpm) and power (2.54kW)

ratings and beyond. A torsional rigid coupling was used to directly connect the shafts of both PMM and the DC machine for effective torque and speed transmission.
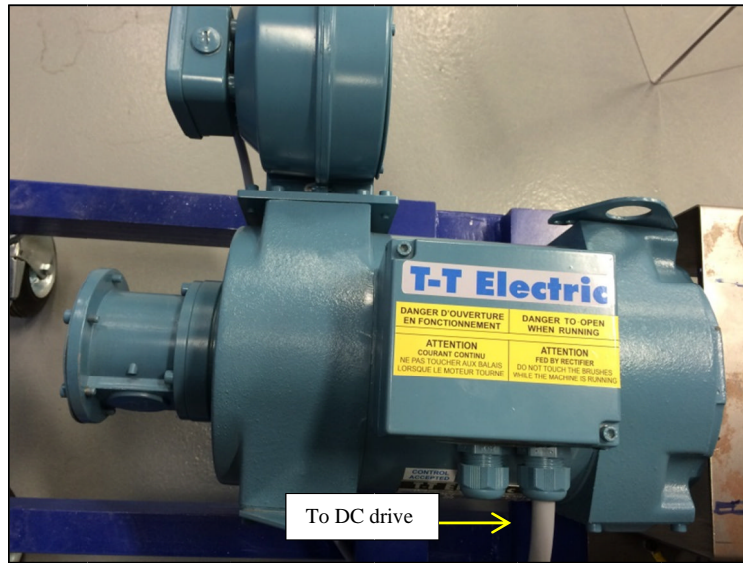
Fig. 7.7. TT electric DC brushed electrical machine.

Table 7.3. DC machine parameter.

Parameter	Value
Rated speed	$4.1krpm$
Rated torque	$11.2Nm$
Rated armature current	$12.6A$
Machine resistance	1.9Ω
Machine inductance	$15.4mH$

A commercially available DC drive (Sprint Electric PLX 10 [168]) is selected to control the DC machine, as seen in Fig. 7.8. The DC drive has a half-controlled active rectifier that converts the grid AC power into DC. The DC power can be controlled with its pre-built DC drive controller. The controller provides multiple functions such as speed or current control and can operate as a four quadrant drive. Built-in sensors are used to provide data for feedback control. The controller can be edited via an inbuilt LCD interface that is on the DC drive. Alternatively, the DC drive can be connected to a computer and the controller can be accessed via a software based interface. Fuses and contactors are used to protect the DC drive from

current surges and voltage spikes. The protection circuit is based on the recommended schematic from the drive manual. Overall, the DC machine power requirements are within the DC drive specifications which can be seen in Table 7.4.
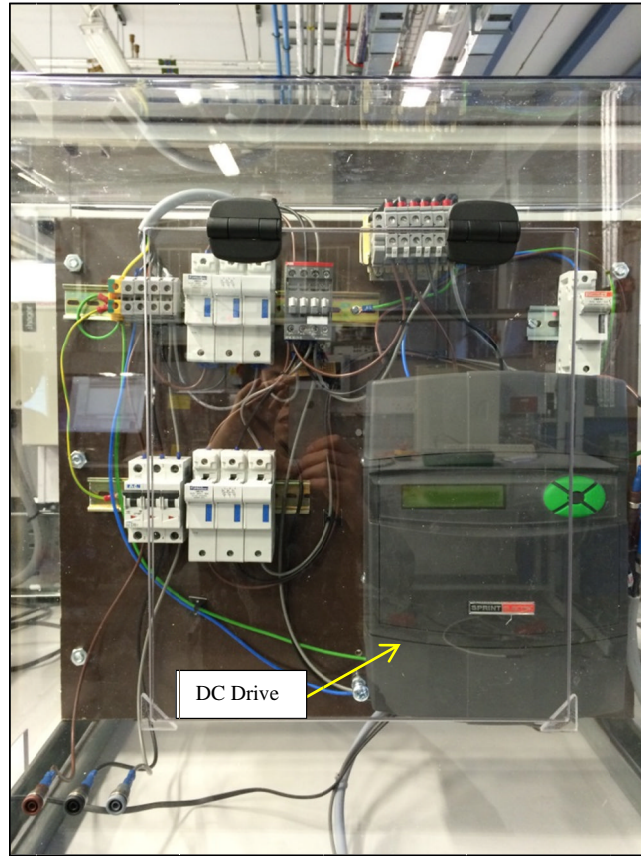
Fig. 7.8. Sprint Electric DC Drive with protection circuit.

Table 7.4. DC drive parameters.

Parameter	Value
Maximum power	*10kW*
Maximum armature current	24*A*
Maximum field current	8*A*

Torque output, as a load demand for the AC drive, can be achieved using speed-mode control of the DC machine. To prevent speed control conflict between the two subsystems, the DC drive speed reference is set to zero and the current output is limited. The limit is related to the amount of T_L required. This approach also prevents the test rig from experiencing uncontrolled acceleration should the AC

drive controller fail. For generator mode, the speed control of the DC drive can be set to the required speed reference value.

This Section has detailed the experimental rig and it has been established that the drive system can operate as a test bench for the AEGART S/G power system. The next Section will describe the capabilities of the drive system along with its controllers.

7.3   Experimental Rig Capabilities

As a smaller PMM is used within the test bench, the capabilities of the experimental AC drive system have to be investigated. The control design process detailed in Chapters 4 and 5 is repeated and the important findings are shown in this Sub-section.

The current and voltage operational limits of the drive system are determined based on the PMM requirements. The line-to-line AC voltage required is $415V_{rms}$ based on the rated phase voltage of $230V_{rms}$. The peak voltage value is therefore 586V which also correspond to the required voltage on the DC side. Hence E_{dc} is selected as 600V for operation of this drive system. The maximum current limit, i_{max}, is selected as 8A in order to sufficiently supply the rated current of 5A. The load demands (in terms of i_q) will therefore not normally exceed the rated current value. The AC voltage limit, $/V/_{max}$, is selected as $E_{dc}/\sqrt{3} = 346.4V$ due to the use of SVM modulation. However, a lower voltage limit is chosen below 346.4V to enable FW at an earlier stage. FW control will therefore be active when $/V/$ reaches 250V and above. These limits are chosen within the actual maximum limits with the purpose of control design verification.

Based on the PMM parameters and the selected limits, the voltage and current circles of this AC drive system are illustrated in Fig. 7.9. The blue circle is this current limit, while the dashed black lines are the voltage circles for speeds from 3.6krpm up to 4krpm. The base speed, ω_b, was found to be 3.321krpm and is represented by the green circle while the critical speed was found to be 3.452krpm shown by the red circle. This means that at $/V/ = 250V$, FW starts when the speed is

at 3.321krpm and FW is essential for speeds of 3.452krpm up until the maximum of 4krpm. The verification of FW control operation will use operating points in the middle of the FW speed range (between 3.6krpm and 3.8krpm).
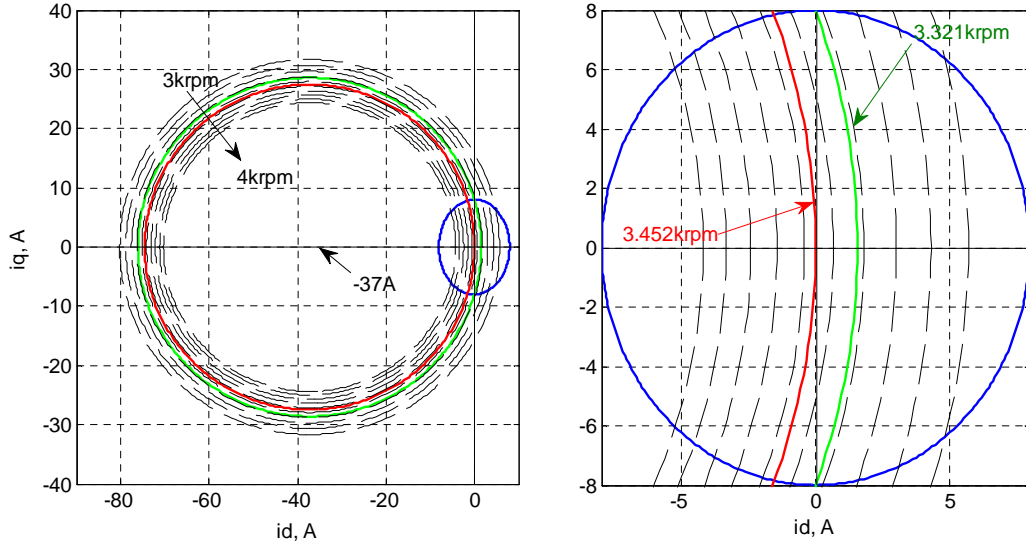
Fig. 7.9. Voltage and current limit circles of the experimental rig (left). Zoomed area of current limit circle (right).

Based on the PMM inductances, flux and inertia, the *dq* current and speed controllers can be designed as in Section 3.4.1 and 4.3 respectively. The tustin method is used to digitalise the controller with respect to the sampling frequency of 12.5kHz. Table 7.5 shows the controller gains which were designed to meet their respective bandwidths and damping ratios.

Table 7.5. Experimental rig PI controller values.

Parameter	Bandwidth	Damping ratio	Continuous Value	Discrete Value
i_d controller k_{pd} and k_{id}	200Hz	1	13.8, 9470	13.8, 0.7576
i_q controller k_{pq} and k_{iq}	200Hz	1	18.7, 12543	18.7, 1.0034
ω_r controller k_{pw} and k_{iw}	10Hz	0.5	0.7, 44	0.7, 0.0035

7.3.1 FW Controller Design

The FW controller for this AC drive system was designed according to the control design process proposed in this Thesis (Section 4.4 and 5.3). Using the derived FW control plants for S/G operation, the FW zero trajectories are shown in Fig. 7.10 and Fig. 7.11 for unlimited and limited i_q^* respectively. The zero trajectories for this PMM are similar to the AEGART PMM; having non-minimum phase characteristics in starter mode with unlimited i_q^* and generator mode with limited i_q^*.
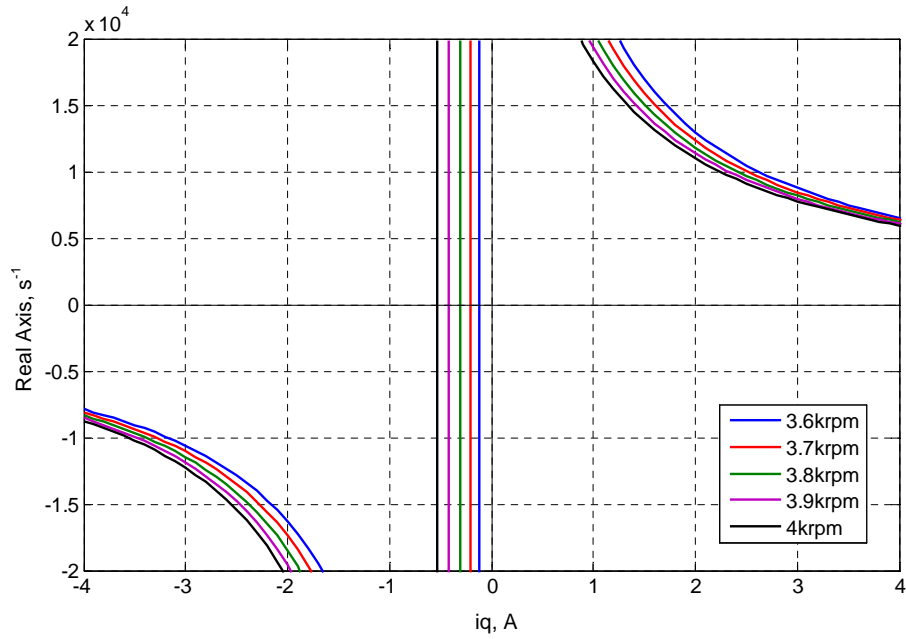
Fig. 7.10. Zero trajectories of FW plant during unlimited i_q^* case.
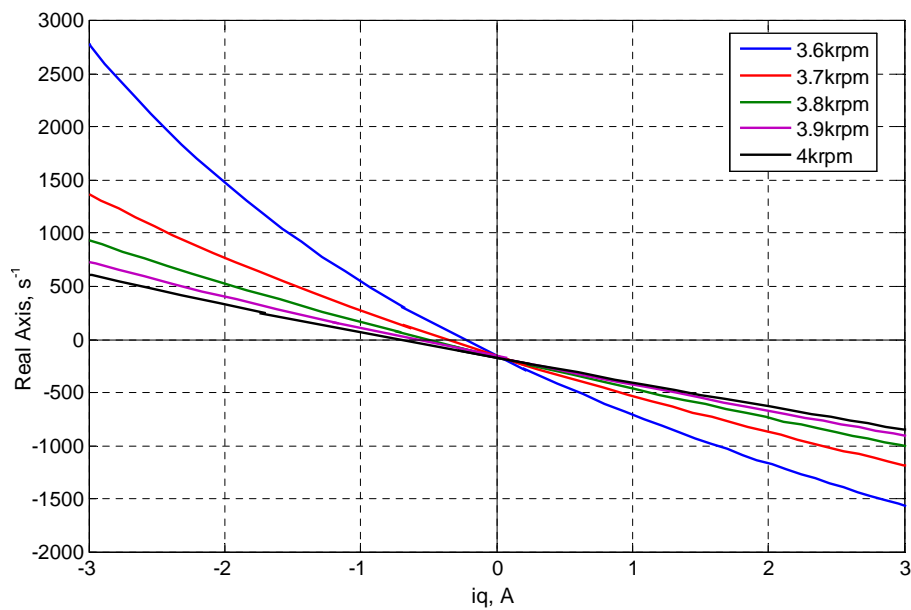
Fig. 7.11. Zero trajectories of FW plant during limited i_q^* case.

186

The FW controller gain range throughout the S/G operating range is determined using the Routh-Hurwitz criterion, as explained earlier in Section 4.5. Fig. 7.12 and Fig. 7.13 shows the k_{iv} range during both S/G modes for each $i_q{}^*$ dynamic limit case operating at 3.6krpm. The range of k_{iv} for stable operation is bounded by the five k_{iv} limits (4.29) to (4.33). The stable regions are highlighted in both of the figures. These are limited mainly by $k_{iv\text{-}lmt3}$ and $k_{iv\text{-}lmt5}$.
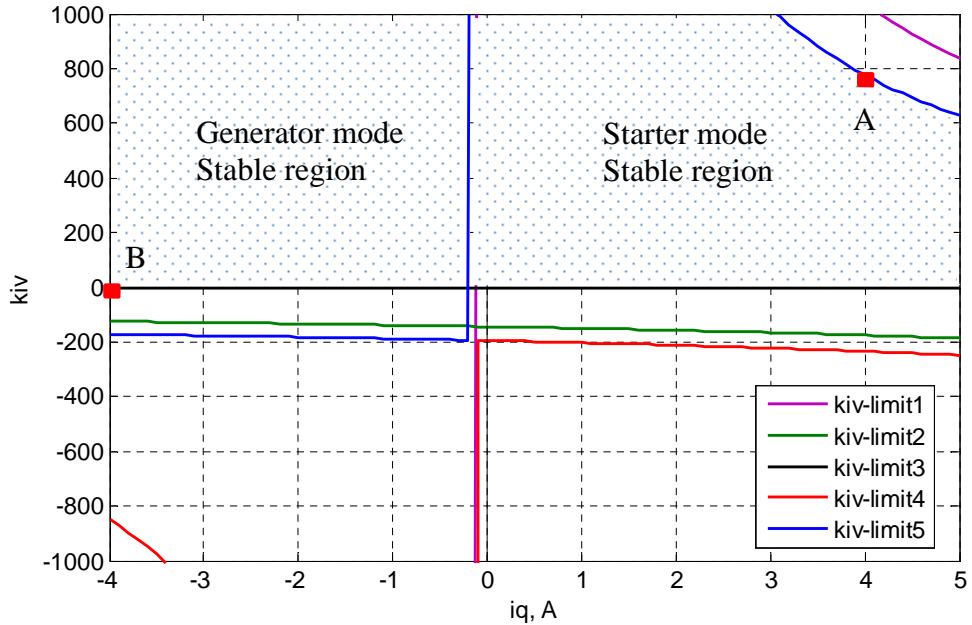
Fig. 7.12. Range of k_{iv} from i_q = -4A to 5A for unlimited $i_q{}^*$ at an operating speed of 3.6krpm.
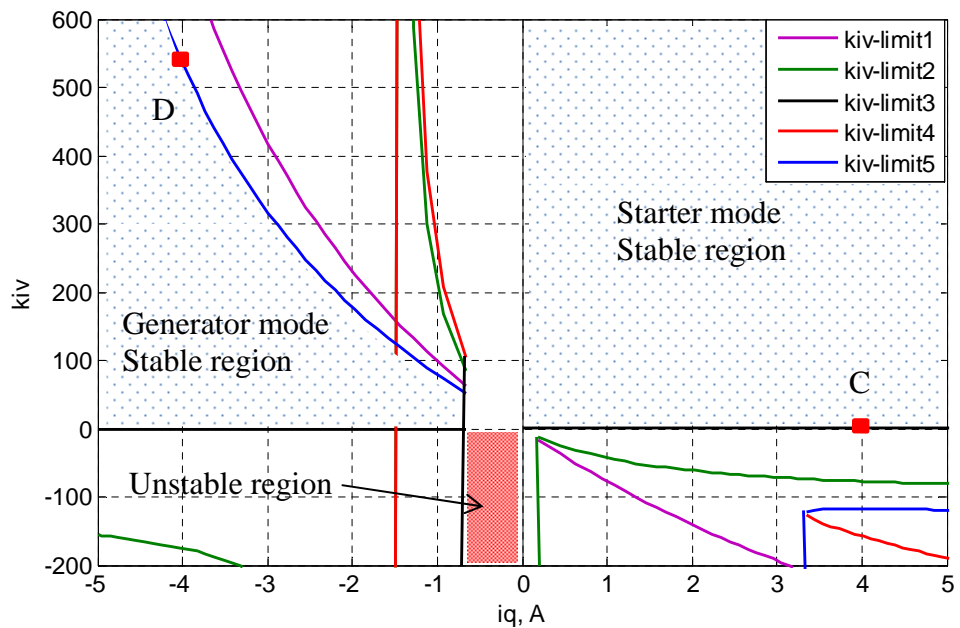
Fig. 7.13. Range of k_{iv} from i_q = -5A to 5A for limited $i_q{}^*$ at an operating speed of 3.6krpm.

If the AC drive system were used in same normal operational conditions as the AEGART power system (generator mode limited i_q^* is rarely reached), then the worst case operating point would be at 4krpm in starter mode with limited i_q^*. The FW controller under these conditions would have a gain range of up to 400. On this basis, the gain for the FW controller in the AC drive system was selected as $k_{iv} = 100$ in order to be safely within the specified limit. The resultant closed loop response is shown in Fig. 7.14.
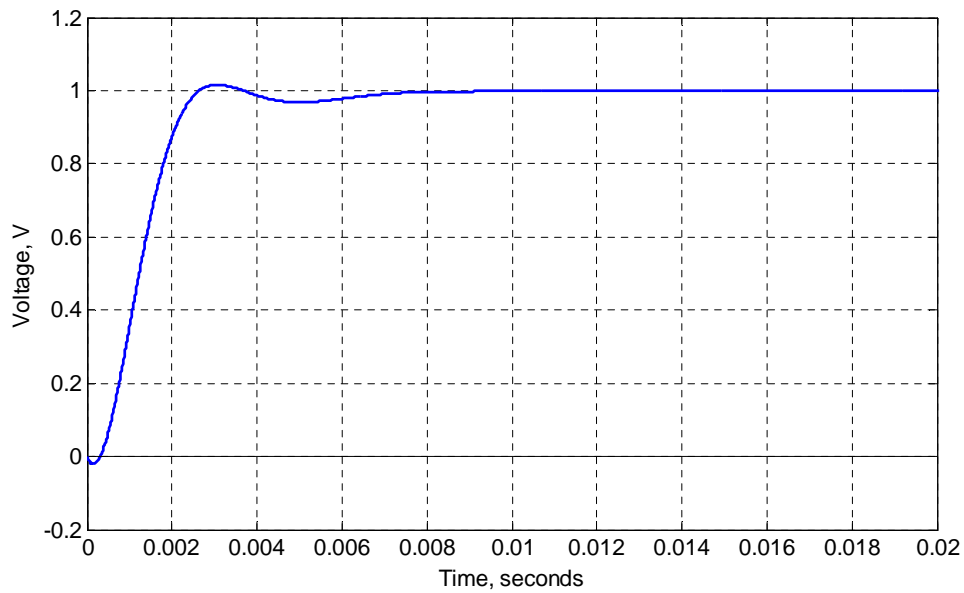
Fig. 7.14. Closed loop step response of designed FW controller ($k_{iv} = 100$) for the experimental rig.

When considering generator mode with limited i_q^*, the value of k_{iv} is critical (see Section 5.3.2) and a fixed controller gain may not be sufficient for stable operation. In Fig. 7.13, there is an unstable region at low i_q in generator mode (highlighted in red). The adaptive FW controller introduced in Section 5.3.3 will be used to operate within the stable region until the unstable area is reached. The current limit modifier proposed in Section 5.3.4 will then be implemented to eliminate the unstable region. The experimental results obtained using this technique will be shown in Section 7.4.

7.3.2 i_{dc} Controller Design

The i_{dc} controller is also designed with the control design process proposed in Section 5.2. The zero trajectories of the i_{dc} control plant at different speeds and load demands are shown in Fig. 7.15. Based on this figure, the worst case operating point is at 4krpm with 5A load. The i_{dc} plant at this operating point was therefore used for the design of the controller.
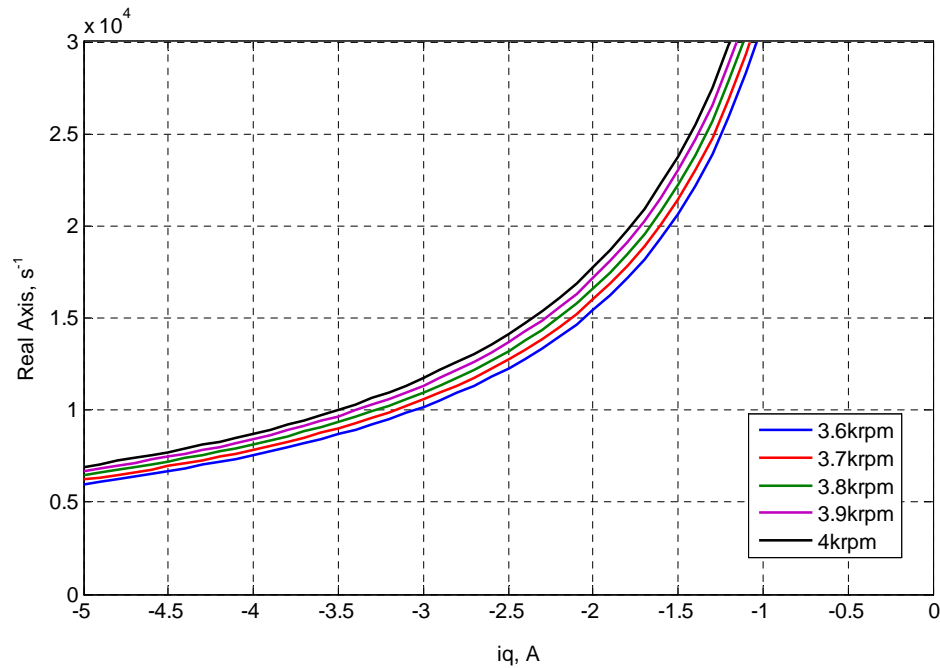
Fig. 7.15. Zero trajectories of i_{dc} plant during unlimited i_q^*.

The i_{dc} controller is designed based on root locus method at the worst operating case operating point. k_{pi} and k_{ii} are selected as 0.1 and 100 respectively and the closed loop step response can be seen in Fig. 7.16.
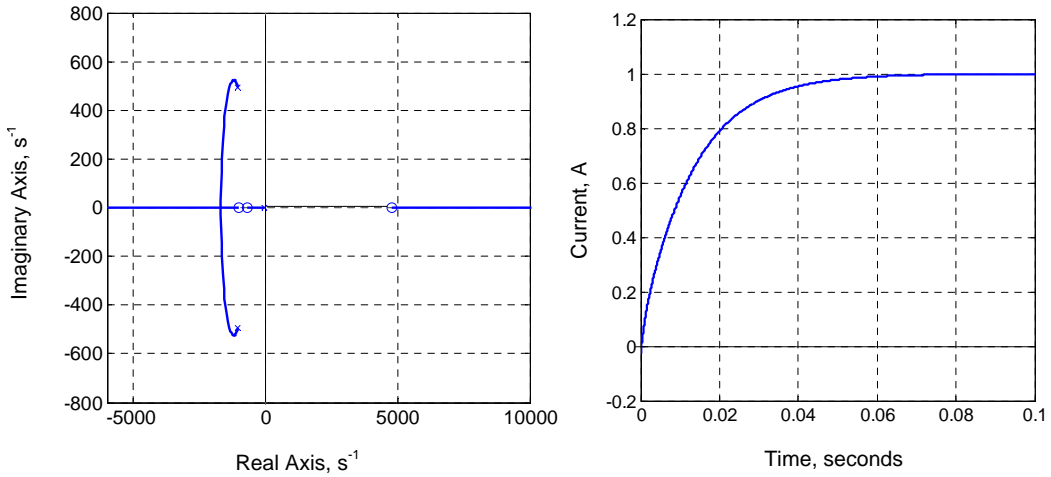
Fig. 7.16. Closed loop root locus (left) and step response (right) of i_{dc} plant with controller gains $k_{pi} =$ 0.1, $k_{ii} = 100$.

The droop control is adjusted according to the test bench DC link voltage and current levels. Table 7.6 shows the updated droop characteristics.

Table 7.6. Droop control parameters for the test bench.

Parameters	Values
Maximum DC link voltage, E_{dcmax}	610V
Minimum DC link voltage, E_{dcmin}	590V
Droop gain, k_{droop}	0.8
Maximum DC current at i_{dcmax}	8A

In summary, the FW and i_{dc} control plant characteristics for the test bench drive system are similar to the AEGART S/G power system. Hence, this test bench can be used to verify the main findings stated earlier in this Chapter. In addition, the following areas will also be verified using the test bench:

- Steady state operation of both S/G modes using the designed controllers.
- Application of M^{2}PC current loop control, as designed in Chapter 6.
- S/G operation with hybrid PI-M^{2}PC control.

7.4 Experimental Results

This section is divided into seven Sub-sections in order to verify each of the theoretical findings. The designed controllers are written in the C language and programmed into the DSP. A sampling frequency of 12.5kHz is selected for the control scheme.

7.4.1 Control Plant Verification

In this section, the plant characteristics of the derived FW and i_{dc} plants are verified using the test bench at different operating points, as summarised in Table 7.7. The inner current loops are used for this experiment without the outer loops. The current references are determined manually and the PMM is driven by the DC drive.

Table 7.7. FW and i_{dc} plant characteristics at different operating points.

Plant	FW		i_{dc}
Mode	Starter	Generator	Generator
Unlimited i_q^*	Non-minimum phase	Minimum phase	Non-minimum phase
Limited i_q^*	Minimum phase	Non-minimum phase	N/A

For the FW plant, a step change was applied to i_d^* and the output $/V/$ was observed. Fig. 7.17 shows the open loop response of $/V/$ to a step of $i_d^* = $ -2A in starter mode. i_q was set to 4A to ensure that the drive system is operating in starter mode. When i_q^* is unlimited, a small overshoot is observed when $/V/$ drops from 261V to 243V due to the step input. This indicates that the FW plant is non-minimum phase at that operating condition. When i_q^* is limited, as seen on the right of Fig. 7.17, the overshoot of $/V/$ is not present which establishes that the plant is minimum phase at that operating condition.
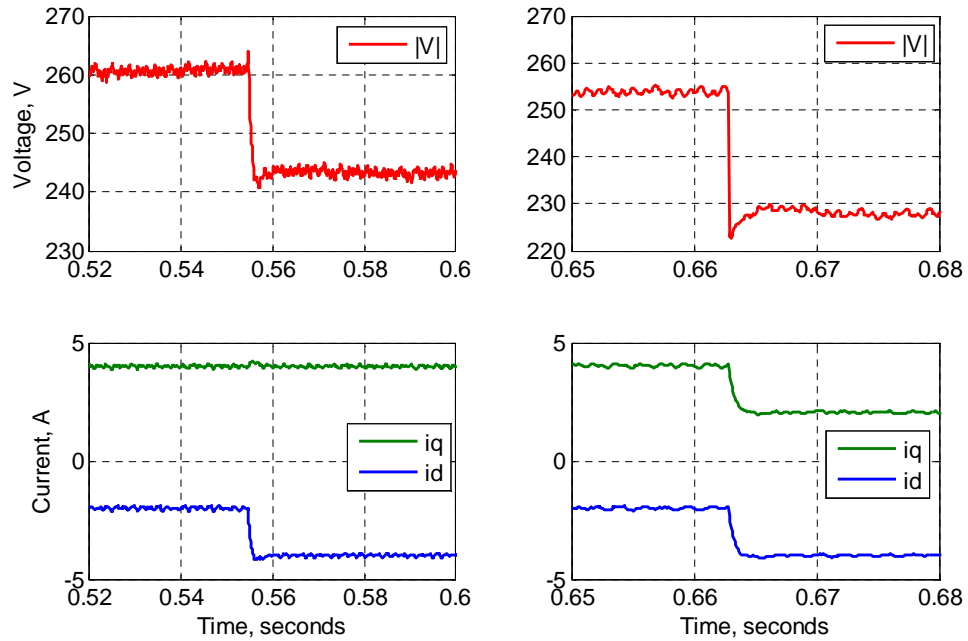
Fig. 7.17. FW plant in starter mode operating at 3.6krpm during unlimited (left) and limited (right) i_q^* cases.

A similar step response was obtained in generator mode for both current limit cases, as shown in Fig. 7.18. i_q was set to a negative value in order for the test bench to operate in generator mode. A step of $i_d^* = 2A$ was applied and clear difference was observed in the response of $|V|$ when i_q^* was limited compared to when i_q^* was unlimited. This showed that the FW plant is non-minimum phase when i_q is limited. The zero trajectories shown in Fig. 7.10 and Fig. 7.11 were also used to confirm the type of FW plant for each operating mode. These findings validate the derived FW plants (4.7), (4.19), (5.16), and (5.19).

The i_{dc} plant was also verified when operating in generator mode with unlimited i_q^*, as seen in Fig. 7.19. i_{dc} measurement was collected through the DSP and was sampled at 12.5kHz. A step change from $i_q^* = -4A$ to $-1A$ at $t \approx 0.735s$ shows the i_{dc} response has some initial overshoot which indicates its non-minimum phase nature. The ripples in the i_{dc} response are quite large due to the current sensor being located in between the power converter and the DC link capacitors. Despite this, the overshoot in the current step response confirms the derived i_{dc} plant (5.6).
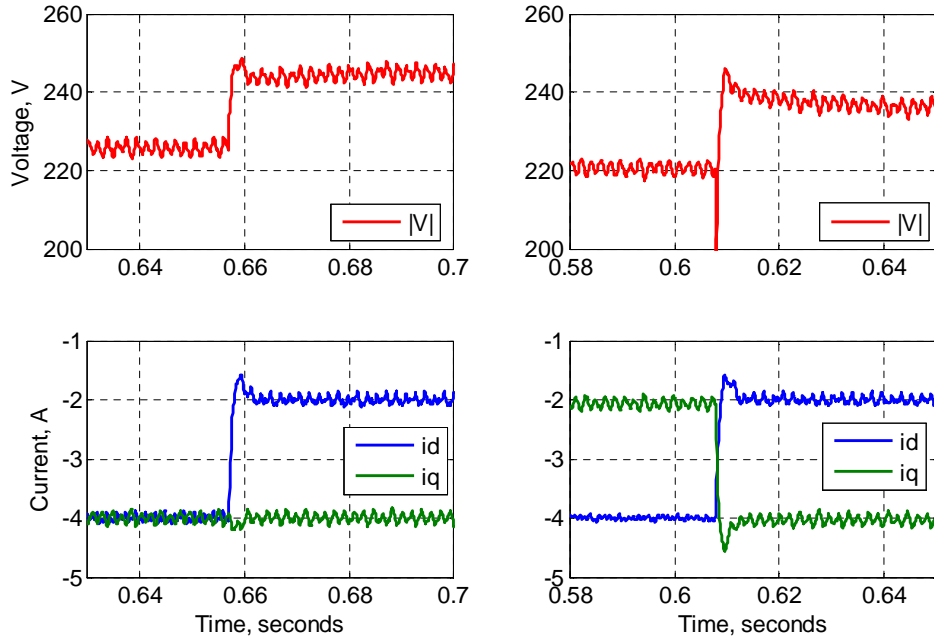
Fig. 7.18. FW plant in generator mode operating at 3.6krpm during unlimited (left) and limited (right) i_q^* cases.
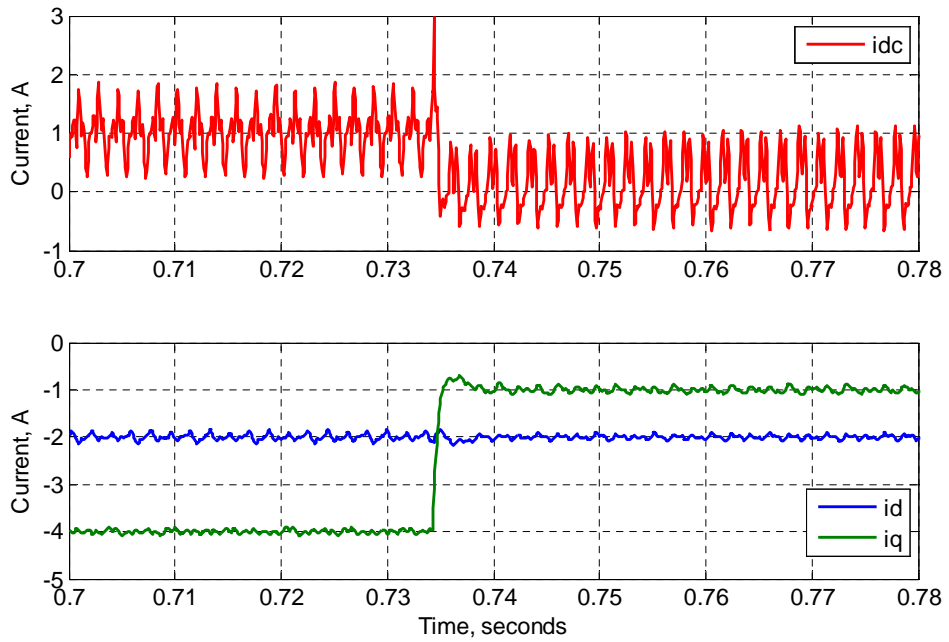
Fig. 7.19. i_{dc} plant in generator mode operating at 3.6krpm during unlimited i_q^* case.

7.4.2   FW Controller Gain Range Verification

In this Sub-section, the FW controller gain range during different operating modes and current limit cases will be verified. The gain range is defined by the $k_{iv\text{-}lmt5}$ boundary limit shown in Fig. 7.12 and Fig. 7.13. The stability limit for the FW controller integral gain, k_{iv}, will be investigated at selected points. These points are shown as A, B, C, and D in Fig. 7.12 and Fig. 7.13. In order to do this, the FW controller was included as part of the control scheme for the AC drive system. i_q^* was set manually in order to determine the operational mode; positive values for starter mode, negative values for generator mode. k_{iv} is then modified in order to exceed the gain limit at a specific operating point. Increased oscillations within the i_d and $/V/$ responses are expected, indicating instability in the FW controller. For the stable regions that are not limited by $k_{iv\text{-}lmt5}$, the k_{iv} step is just set to a large value.

7.4.2.1   Unlimited i_q^* Case

Fig. 7.20 shows the results of the k_{iv} step change when the drive system is operating in starter mode. A load demand of i_q = 4A was connected to ensure operation at point A in Fig. 7.12. The gain range at that point was found to be 750. The value of k_{iv} is initially set to 650 which is below the stability boundary limit, and then changed to 700 at about t = 0.44s. It can be seen that $/V/$ and i_d experienced increased oscillations which indicate instability after the k_{iv} step change. The instability occurred slightly below the expected gain range; this may be due to parameter variation within the PMM. Only the FW controller was affected as i_q was still stable.

The test was repeated under generating mode with i_q = -4A. In this case the system was operating at point B in Fig. 7.12. The gain range was not limited at that point and so k_{iv} was changed by a large margin in order to prove the theory in question. The results are shown in Fig. 7.21. k_{iv} is changed from 100 to 1000 at about t = 0.39s, and no significant change in $/V/$ or i_d ripple is observed.

The experimental results presented confirm the k_{iv} gain range at points A and B in Fig. 7.12. It also proves the non-minimum phase nature of the FW plant in starter mode with unlimited i_q^*.
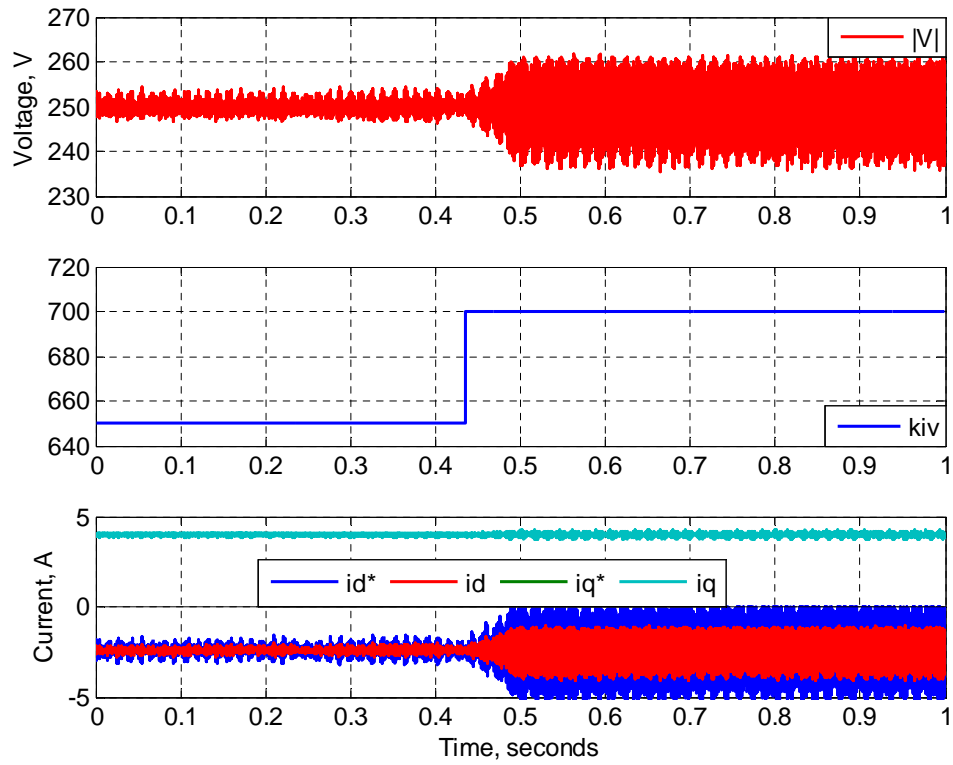
Fig. 7.20. k_{iv} range validation for starter mode unlimited $i_q{}^*$ operating at 3.6krpm.
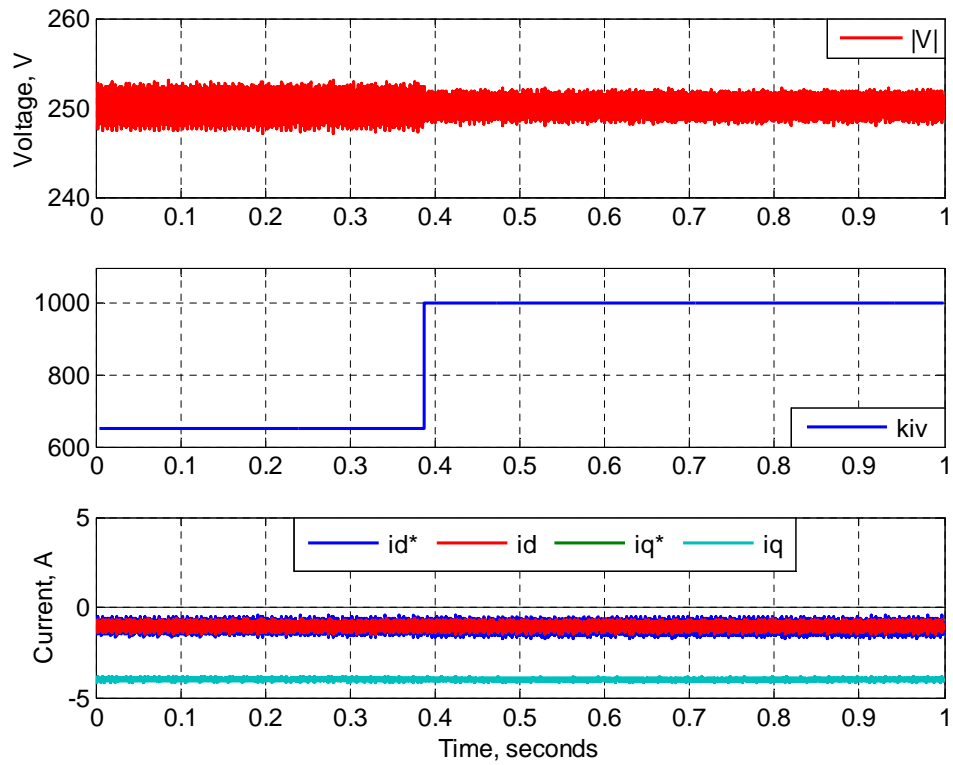
Fig. 7.21. k_{iv} range validation for generator mode unlimited $i_q{}^*$ operating at 3.6krpm.

7.4.2.2 Limited i_q^* Case

The test detailed in the previous Sub-section was also performed for limited i_q^*. The k_{iv} range at point C shown in Fig. 7.13 is not limited. At this point the S/G is in starter mode with limited i_q^*. i_{max} is reduced until the required operating point is reached where $i_q = 4A$. k_{iv} is changed to 1000 from an initial value of 100 at $t = 0.23s$ and the results can be seen in Fig. 7.22. Stable operation is observed despite the large change in k_{iv}.
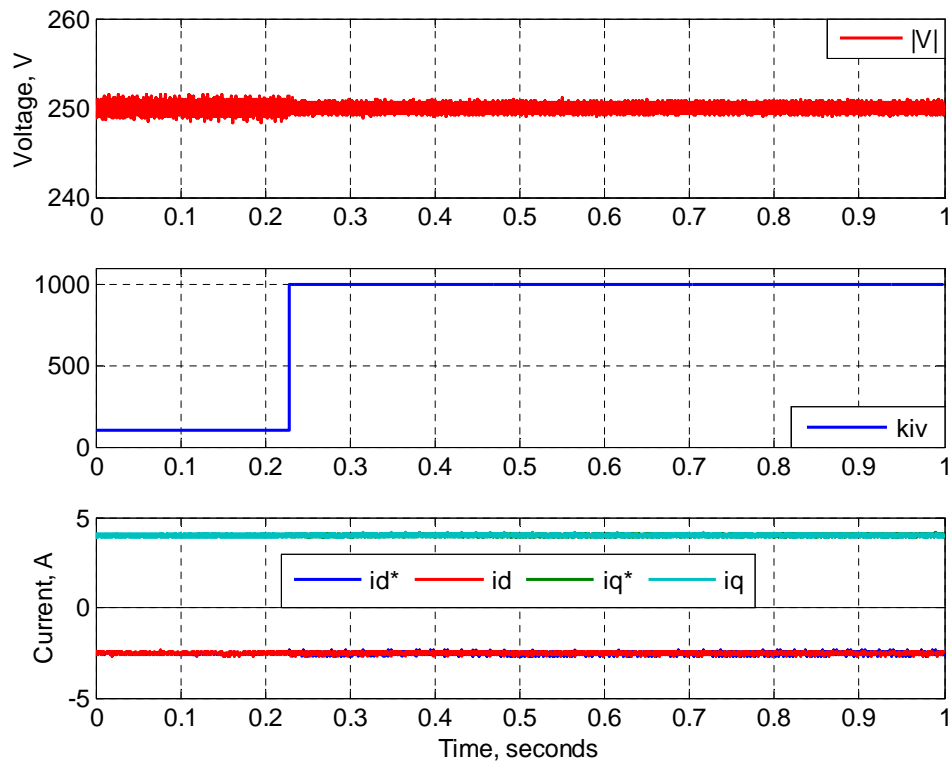
Fig. 7.22. k_{iv} range validation for starter mode limited i_q^* operating at 3.6krpm.

Point D was chosen as the point at which the k_{iv} range for generator mode operation with limited i_q^* would be verified. This point is shown in Fig. 7.13. At this point the gain limit was found to be 530. k_{iv} was therefore modified from 400 to 550 in order to observe the response of $|V|$ and i_d. The results are shown in Fig. 7.23. In addition to i_q, both $|V|$ and i_d became unstable after the step change at $t = 0.45s$. This is due to the reaction of the current limiter which changes i_q according to i_d. As i_d goes unstable, the increased oscillations reduce i_q. The reduction of i_q leads to an even smaller k_{iv} range limit which further degrades the stability of the whole control scheme. These results confirm the k_{iv} gain range in Fig. 7.13 for points C and D.

Non-minimum phase behaviour of the FW plant is also proven when operating in generator mode with limited i_q^*.
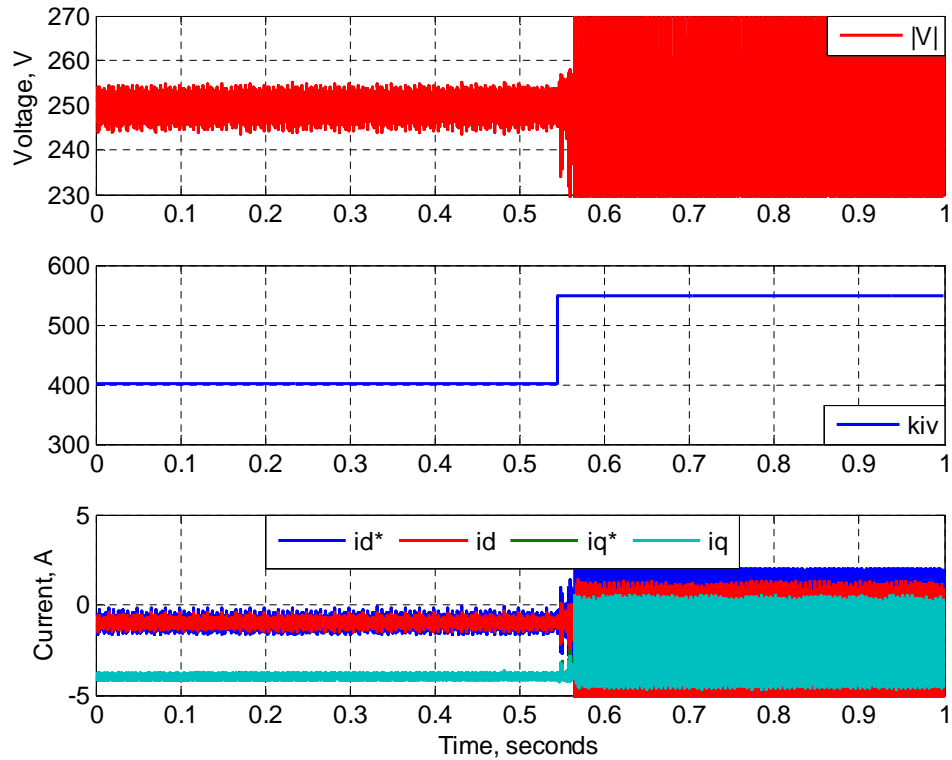
Fig. 7.23. k_{iv} range validation for generator mode limited i_q^* operating at 3.6krpm.

7.4.3   Current Limit Modifier

This experimental test was carried out in order to validate the effectiveness of the current limit modifier proposed in Section 5.3.4. The aim of the modifier is to eliminate the unstable area of operation shown in Fig. 7.13. The control structure is similar to that detailed in the previous Sub-section; inner current loops with outer FW controller. During the test, k_{iv} is initially set to a small value (15 in this case) in order to not trigger controller instability when approaching the unstable region. Then, i_{max} is gradually reduced to 1.7A so that there is sufficient current for i_d (FW) and i_q to be close to zero. At this operating point ($i_q < -0.7$A), instability can be observed in Fig. 7.24 before $t = 0.7$s. At time $t = 0.7$s, the current limit modifier is enabled instead of the dynamic current limit (4.15). The results show the *dq* currents stabilise after the current limit modifier is enabled. This test therefore proves that the proposed current limit modifier can eliminate the unstable operating area.
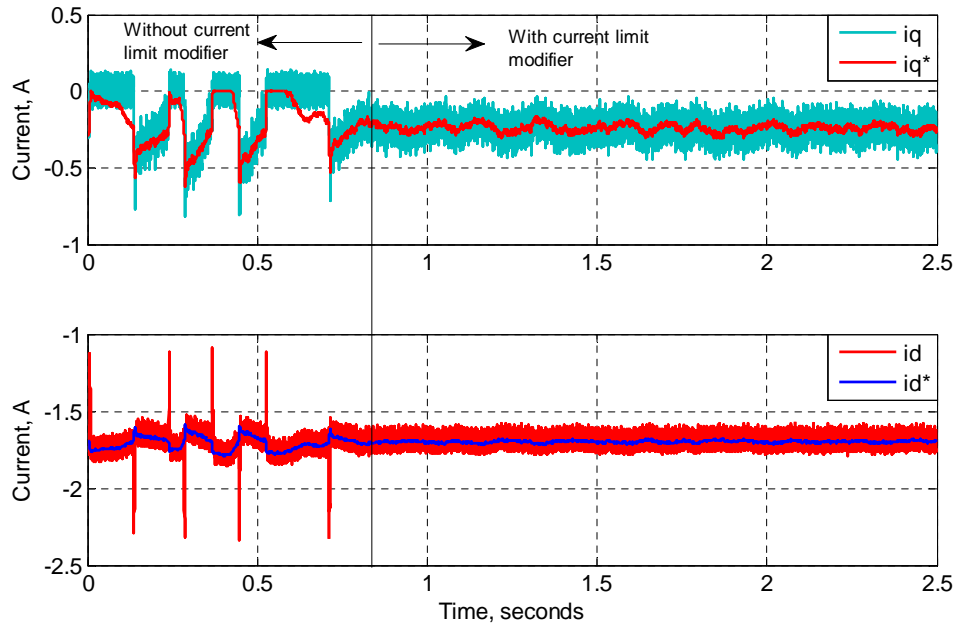
Fig. 7.24. *dq* currents operating at low i_q with and without current limit modifier.

7.4.4 Adaptive k_{iv} Gain Controller

If k_{iv} is set to a constant value of 100 throughout the load range, instability is bound to occur when i_q approaches zero. This experiment aims to prove this point with the addition of adaptive k_{iv} gain as a solution. An inner current loop and outer FW controller are used for this test. Fig. 7.25 shows the *dq* currents at different loads between -3A and 3A with limited i_q^*. For this test, i_{max} was decreased from 4A to 1.7A within 1s and remained fixed for a further 1s. After that, the operating mode was changed to starter mode at $t = 2.3$s and i_{max} was gradually increased from 1.7 A to 4.5 A. Between $t = 0.7$s and 2.3s, instability occurs within the control scheme, as indicated by the current oscillations in Fig. 7.25. When the operating point transitioned to starter mode (positive i_q), the system immediately stabilised.
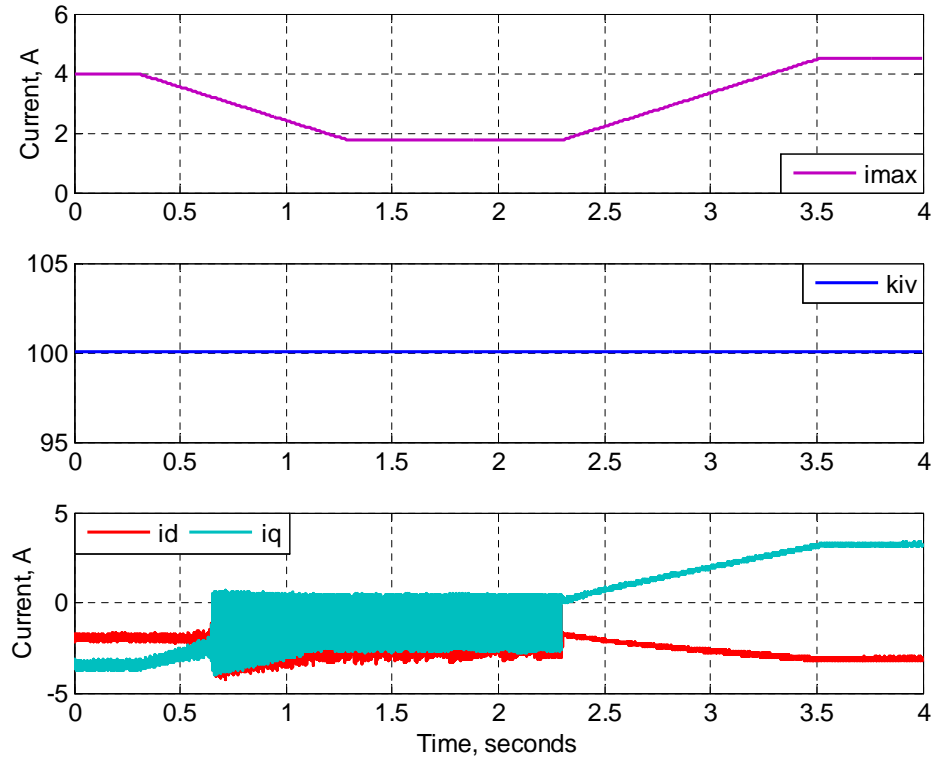
Fig. 7.25. *dq* currents when i_q varies from -3A to 3A with constant k_{iv} =100 in generator mode limited i_q^*.

The use of adaptive k_{iv} gain together with the current limit modifier will now be investigated for limited i_q^*. This technique has the potential to ensure smooth control performance across all values of negative i_q and even provide stable transition between generator and starter modes. The adaptive k_{iv} gain given in (5.22) was implemented using a lookup table in the test bench control scheme in order to reduce the computational complexity of the control algorithm. The lookup table for $k_{iv-adapt}$ provides an appropriate k_{iv} based on the operating speed and i_q. The upper and lower limits for k_{iv} are set to be 100 and 15 respectively.

Fig. 7.26 shows the *dq* currents when the adaptive k_{iv} and current limit modifier are used. It can be seen that the current oscillations that occurred between $t = 0.7$s and 2.3s in Fig. 7.25 were eliminated using this technique. The current limit modifier replaces the dynamic current limit when i_{lmt} is larger than i_{max}. This happens between $t = 1.2$s and 2.3s. As shown in the previous Sub-section, the current limit modifier stabilises the FW controller at low i_q during limited i_q^*. The remaining periods without oscillation are due to the adaptive k_{iv} algorithm. It can be seen in Fig. 7.26 that k_{iv} reduces as i_q increases. The results confirm the effective use of the adaptive

199

k_{iv} and the proposed current limit modifier to achieve stable FW control in generator mode with limited i_q^*.
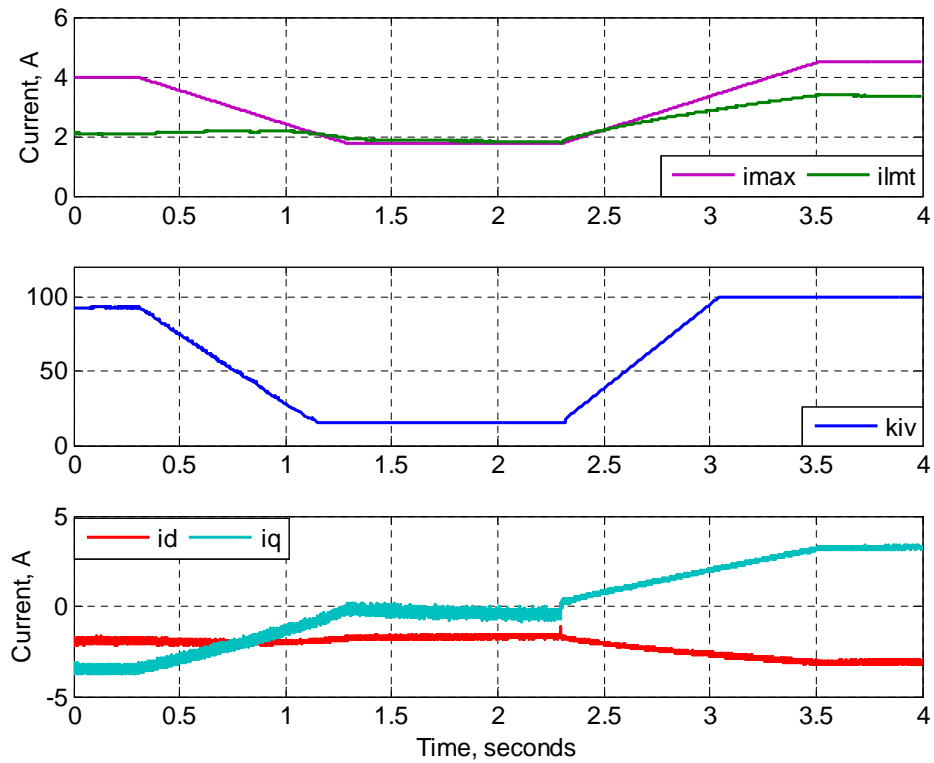
Fig. 7.26. *dq* currents when i_q varies from -3A to 3A with adaptive k_{iv} and current limit modifier in generator mode limited i_q^*.

7.4.5   S/G Operation Results

Once the controllers had been designed and verified, the whole S/G control scheme could be tested. Both speed and FW outer loop controllers were used in order to provide references for the inner current loops. Fig. 7.27 shows the key results from the AC drive system in start-up mode with the designed controllers.
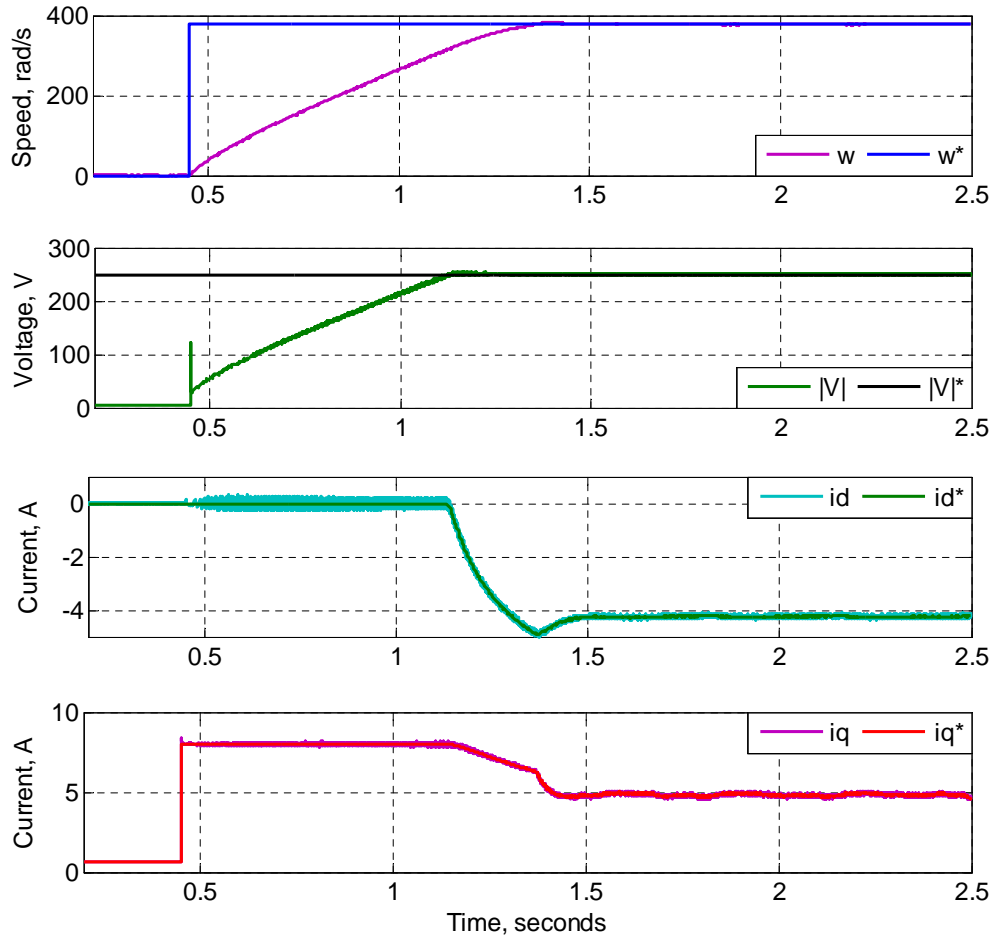
Fig. 7.27. Start-up mode from standstill to 3.6krpm (376.8rad/s) for the test bench AC drive system.

The non-zero i_q from to $t = 0$ to $t = 0.45$s is due to the 2Nm torque load which is initially applied by the DC machine. The speed controller for the AC drive therefore produces an equivalent i_q in order to compensate for this disturbance and maintain the speed at zero. The drive starts at stand still and is accelerated to 3.6krpm based on the speed reference at $t = 0.45$s. As the speed increases, $/V/$ also increases but is limited at $/V/_{max} = 250$V. i_d is demanded at $t = 0.6$s as a result of FW in order to regulate $/V/$. It can be seen from Fig. 7.27 that i_q reduces as i_d increases due to the use of the current dynamic limit. All of the variables are in steady state when the speed reaches the speed reference at $t = 0.9$s. Fig. 7.28 shows the same controlled variables when T_L dispatches at $t = 0.6$s. The outer loop controllers responded to the load change and the controlled variables are again regulated appropriately. This shows that the designed controllers are able to perform start-up operation without any issues.
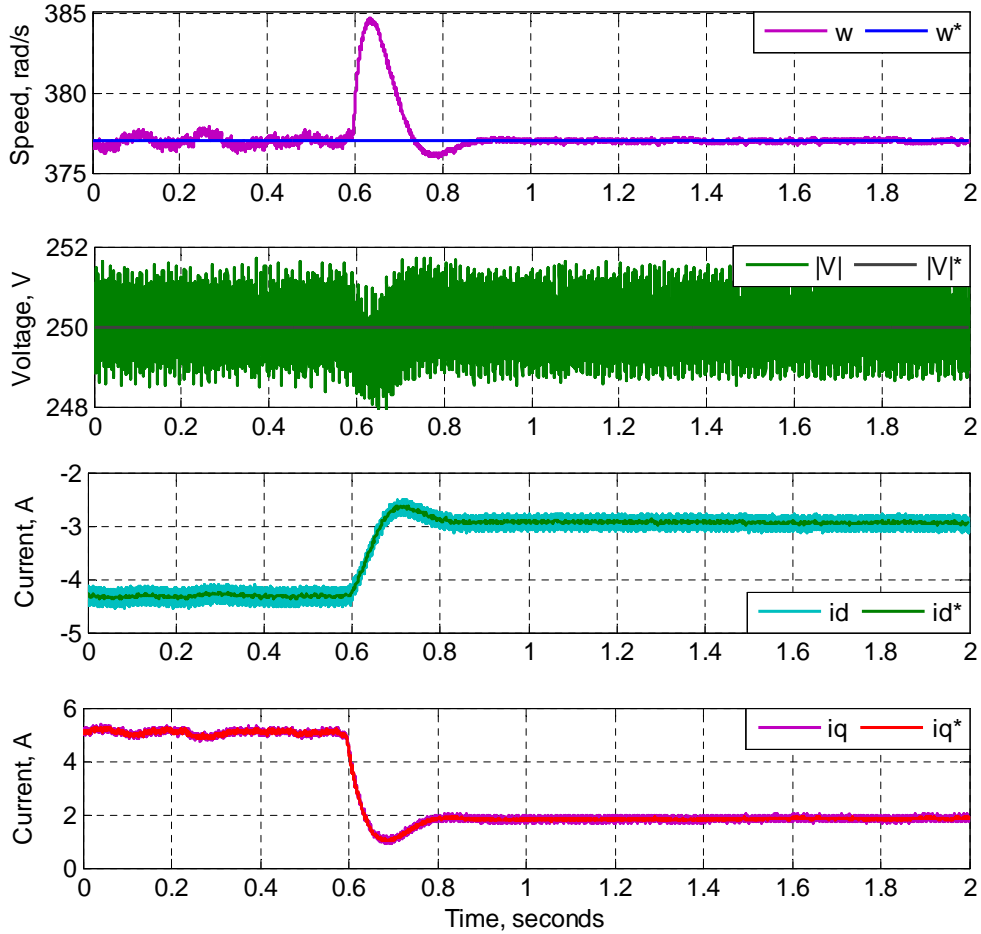
Fig. 7.28. Starter mode operating at 3.6krpm (376.8rad/s) and load dispatch at $t \approx 0.6$s for the test bench AC drive system.

In order to perform tests in generator mode, the speed controller has to be replaced with a DC link controller. Fig. 7.29 shows the time domain simulation of the power system in generator mode with the FW and DC link controllers. The operating speed was set to 3.7krpm with the help of the DC drive. A resistive load of 320Ω was connected to the DC link bus at $t \approx 0.64$s and E_{dc} drooped to 598V according to the droop gain in Table 7.6. At $t \approx 1.15$s, the load was disconnected from the DC link, and the control scheme responded to the load change and regulated the controlled variables accordingly, as seen in the left side of the figure. In this case, E_{dc} returned to 600V. This experiment confirms the designed controllers are capable of maintaining stable operation of the drive system during generator mode.
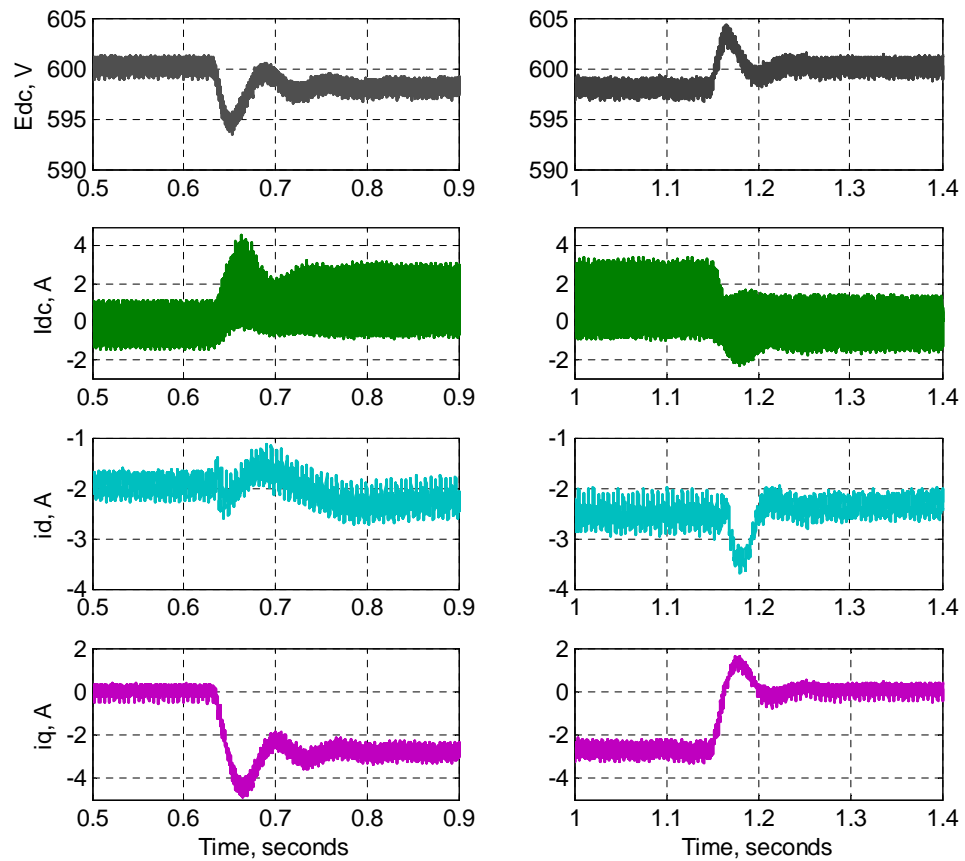
Fig. 7.29. Generator mode running at 3.7krpm (387.5rad/s) with load dispatch (left) and load impact (right) scenarios for the test bench AC drive system.

7.4.6   M^{2}PC Current Loop Control

The applicability of M^{2}PC was also investigated using the test bench. It was hoped that fast dynamics and *dq* current ripple would be observed in this test. M^{2}PC was implemented into the *dq* current loop control with the rig parameters introduced earlier in Section 7.2. The control was tested with a step input of 1A for the *dq* currents and the results can be seen in Fig. 7.30 and Fig. 7.31.
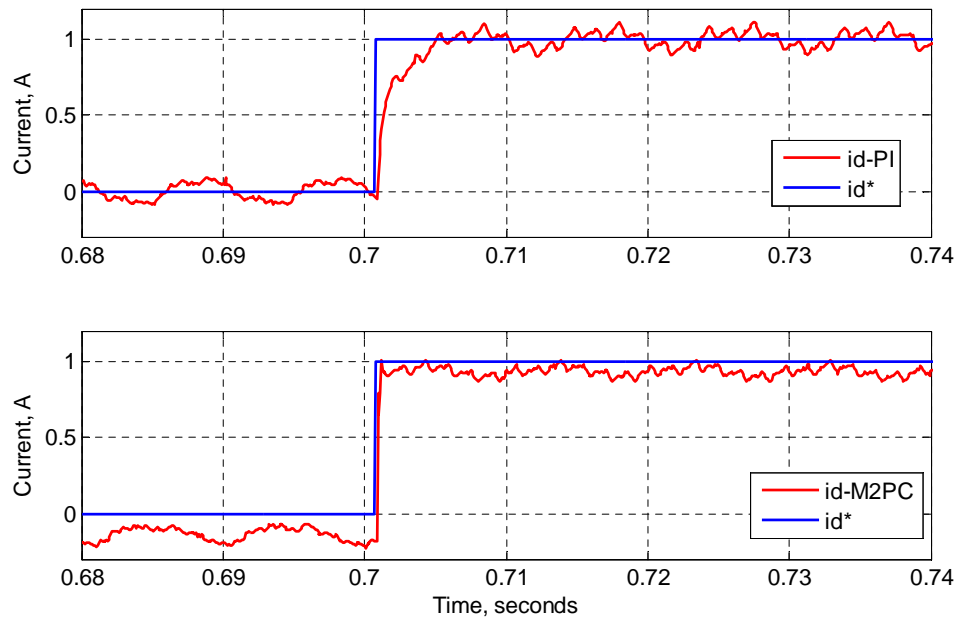
Fig. 7.30. i_d comparison between PI based (top) and M^{2}PC (bottom) inner current loop to $i_d{}^* = 1$A.
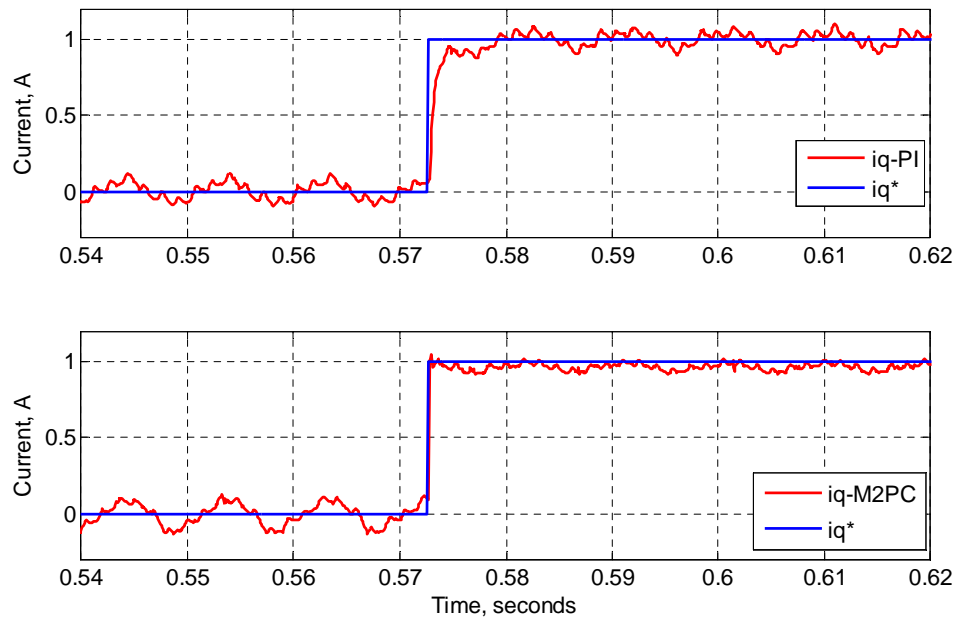
Fig. 7.31. i_q comparison between PI based (top) and M^{2}PC (bottom) inner current loop to $i_q{}^* = 1$A.

It can be seen from the figures above that a fast dynamic response was observed after one sampling period delay. However, there is some steady state error between the reference and measured dq currents. This may be due to discrepancies between the model used for prediction and the actual system parameters. This could be caused by parameter variation, as discussed in Chapter 6, or voltage drop across the power switches. This steady state error is not very significant and the use of outer loop PI controllers will compensate for this error. Fig. 7.30 and Fig. 7.31 also showed a comparison between the PI based inner current loops and M^{2}PC. It can be seen that the current ripple is slightly reduced when using M^{2}PC. This could be due to the much larger inductances on this PMM rig which could passively reduce the current ripple compared to the AEGART PMM. These results confirm the theoretical findings in Chapter 6 regarding the very fast control dynamics and reduced current ripple that can be achieved by the use of M^{2}PC.

7.4.7　Hybrid PI-M^{2}PC Operation Results

In order to perform this test the M^{2}PC current loop references were connected to the designed outer loop PI based controllers. As was the case for the full PI control scheme, the AC drive is driven from standstill to 3.6krpm as shown in Fig. 7.32. Once the speed reference is reached, FW is applied when $/V/ = 250$V. It can be seen from Fig. 7.32 that some steady state error exists for the dq currents but it is progressively reduced as the speed increases. During the acceleration from standstill to 3.6krpm, the full i_q of 8A was not demanded due to the observed steady state error. As a result, the torque output of the PMM was slightly less and this affected the time for the speed to reach steady state compared to the full PI control scheme.
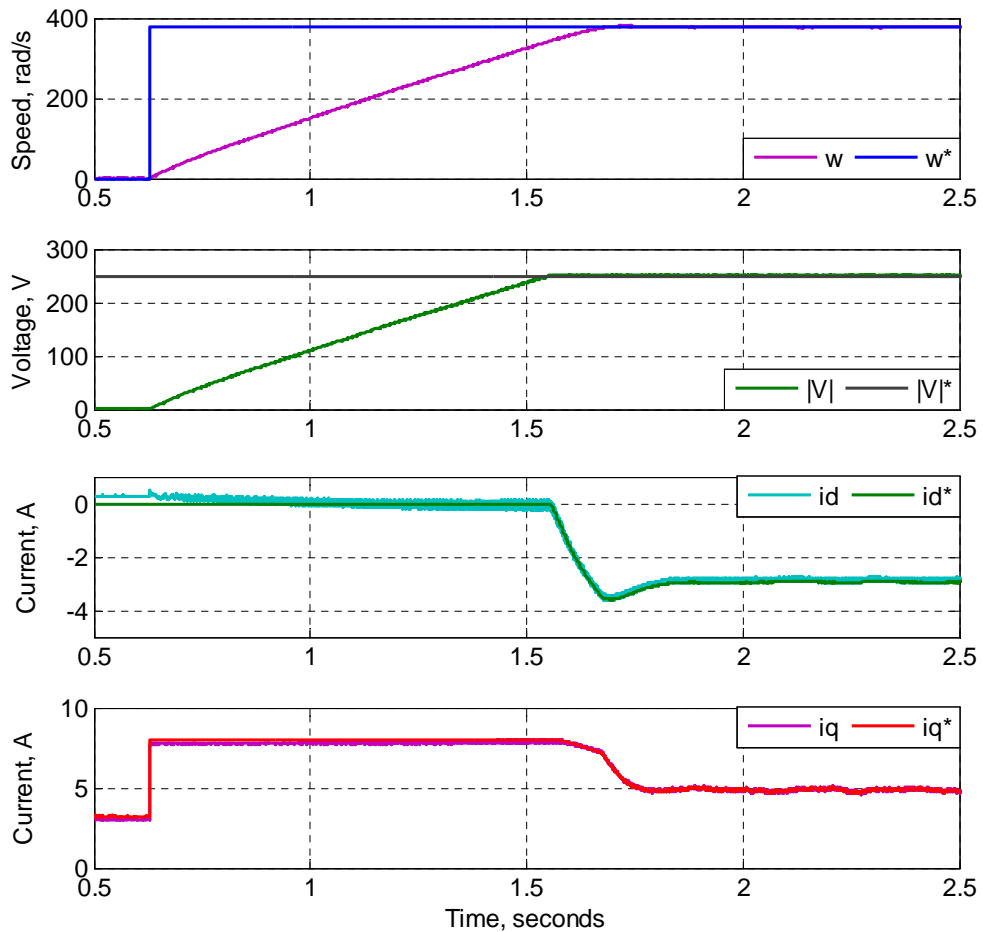
Fig. 7.32. Start-up mode from standstill to 3.6krpm (376.8rad/s) for the test bench AC drive system with hybrid PI-M^{2}PC.

A second test was performed on the hybrid PI-M^{2}PC system. In this case $T_L = 2$Nm was applied at the beginning of the test and it was dispatched at $t \approx 1.05$s at 3.6krpm, as seen in Fig. 7.33. The hybrid control scheme reacted to the load change and maintained the speed and $|V|$ according to their reference values. The dq current steady state errors were compensated by the outer loop PI controllers. This can be seen in Fig. 7.33 by the difference between the measured and reference values. Good performance of the hybrid control for starter mode was therefore demonstrated and verified by this test.
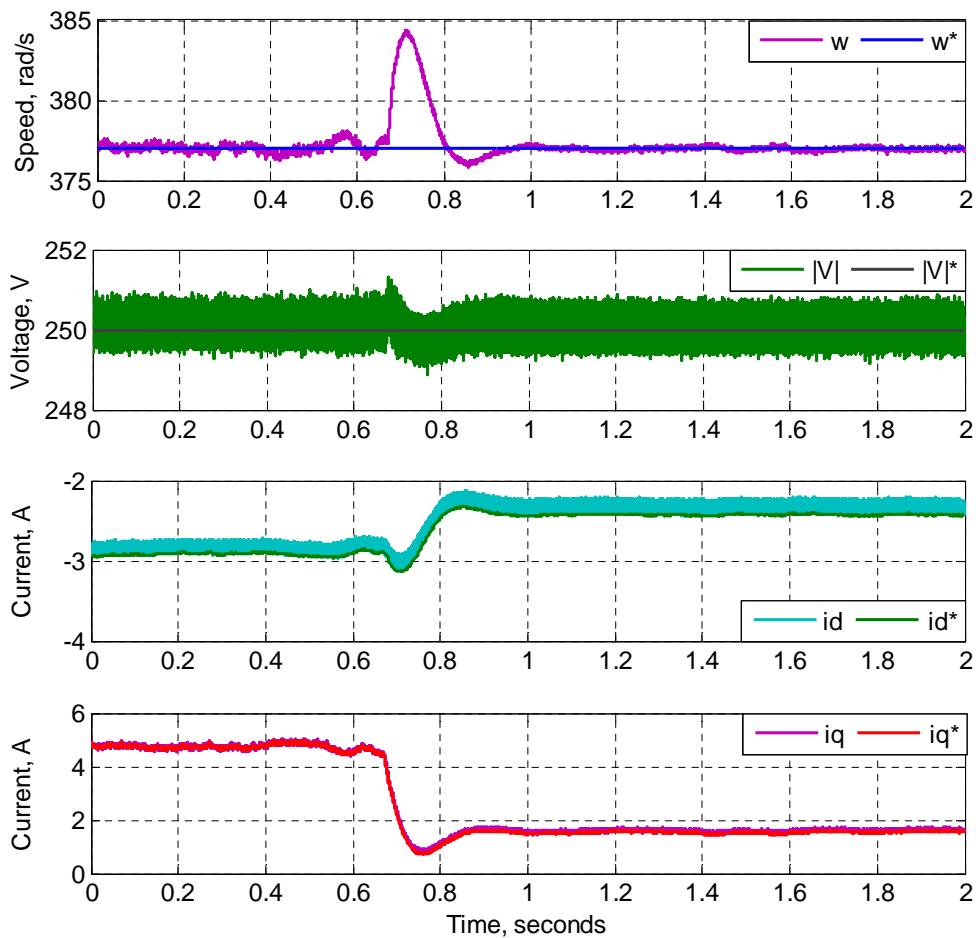
Fig. 7.33. Starter mode operating at 3.6krpm (376.8rad/s) and load dispatch at $t \approx 0.7$s for the test bench AC drive system with hybrid PI-M^{2}PC.

The hybrid PI-M^{2}PC scheme was also tested in generator mode. The test results can be seen in Fig. 7.34. The operating speed is set to 3.7krpm with E_{dc} drooping to 598V due to a connected resistive load of 320Ω at $t \approx 0.4$s. When the load is disconnected from the DC link, and the control scheme responds to the load change and regulates the dq currents accordingly. This experiment confirms the designed controllers are capable of stable control operation during generator mode.
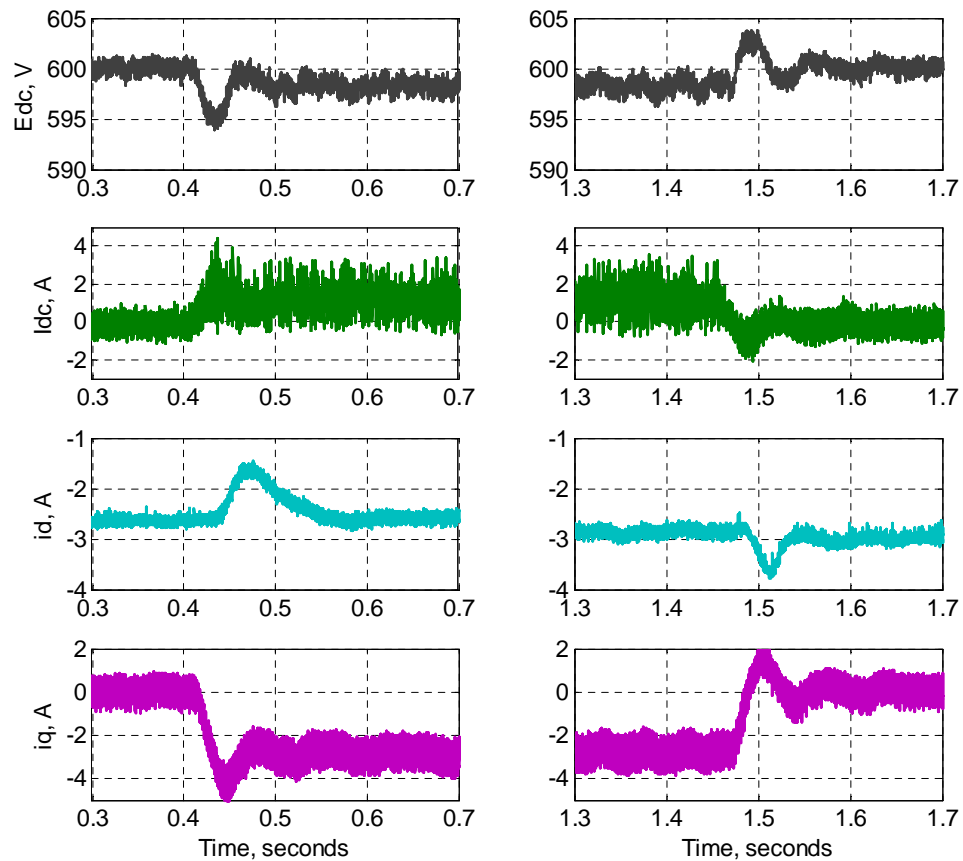
Fig. 7.34. Generator mode running at 3.7krpm (387.5rad/s) with load dispatch (left) and load impact (right) scenarios for the test bench AC drive system with hybrid PI-M^{2}PC.

7.5   Conclusion

This Chapter dealt with the experimental validation of the theoretical results accumulated from the previous Chapters. A prototype drive system was assembled and used as a test bench in order to resemble the functions of AEGART S/G system. The experimental setup was detailed with reference to the actual aircraft system. The control design concept in this Thesis was adapted to the experimental rig. Experimental results were produced to validate each of the theoretical findings. The experimental findings can be summarised as follows:

- The FW plant at different modes and current limit cases was verified by open loop step responses. The non-minimum phase properties expected from the analytical study were confirmed. The i_{dc} plant was also verified to be non-minimum phase when operating in generator mode with unlimited i_q^*.

- The FW controller integral gain range was verified at different modes and current limit cases. This was done by applying step changes in the value of the gain in order to move the system operating point from a stable region to unstable region. The values used were estimated by using the Routh-Hurwitz criterion.

- In generator mode with limited i_q^*, the FW controller gain range is critical as it is proportional to the load demand. An adaptive FW controller was introduced to change the controller gain according to the load demand and operating speed. An unstable region was identified at very low load demands due to the use of the dynamic current limiter. A novel current limit modifier was proposed which eliminated the unstable region. Improved control performance was achieved using both solutions in generator mode with limited i_q^*.

- Steady state operation in both starter and generator mode with the designed controllers was also tested. The results showed good control performance throughout the given operating range.

- M²PC was successfully utilised for inner current loop control. Fast dynamics and reduced current ripple were observed when compared with PI based control. This verified the analytical findings presented in Chapter 6. Some steady state error was present due to parameter difference and voltage drop across the power switches. This was eliminated by the use of outer loop PI based controllers.

- The hybrid PI-M²PC scheme was also shown to provide good control performance within both starter and generator mode.

Overall, the small signal analysis and proposed control design, along with the expected system performance, were successfully validated by the experimental results.

Chapter 8   Conclusion and Discussion

8.1   Conclusion

The trend of moving towards the development of MEA is driven by increased fossil fuel prices and stricter environmental policies. In addition, breakthroughs in power electronic systems and fault tolerant electrical machines support the advancement of MEA. The implementation of MEA will improve the aircraft empty-weight, drag, fuel efficiency, and hence reduce the aircraft's environmental impact. Some of the other advantages include improved reliability, easier prognostics and diagnostics, greater flexibility and reduced overall costs. Among the potential advancements for the MEA concept, the S/G scheme is the most significant improvement in the electrical power generation system. The S/G scheme involves using an electrical machine that functions as an aircraft engine starter, or a generator, depending on the aircraft flight profile. In conventional aircraft, starting and generation were typically distinct functions provided by separate systems. There are therefore obvious advantages in terms of weight and volume reduction when both starter and generator functions are provided by a single system. Therefore, the development of an electric S/G system is in the focus of many current research programs, including the AEGART project (part of EU FP7 CleanSky JTI, Systems for EcoDesign ITD) conducted at the University of Nottingham. This PhD project investigated control design aspects for the S/G system developed within this project.

The AEGART S/G system employs a surface mounted PMM connected to a three-level AFE which in turn is connected to the aircraft main bus. A PMM is utilised because of its high power density. A DC main bus is used in order to reduce the required number of cables which helps to reduce the aircraft weight. A VF topology was adopted due to its simplicity and because this can easily generate the required DC power with the help of an AFE. It also allows control of the PMM as a starter or generator with power flow to or from the aircraft electrical bus depending on the required mode of operation. The PMM and AFE designed within the

AEGART project were described in this Thesis along with its capabilities and operational limits. The work presented in this Thesis can be summarised as follows:

Based on the required S/G system operational modes, the general control requirements were outlined. It was shown that speed has to be controlled in starter mode while DC link voltage control is required in generator mode. For both modes, FW control is critical in order to maintain controllability of the power system. A detailed literature review was performed for selection of both the FW control approach and the DC link control method. For FW control, the direct current method was chosen for this application based on its given advantages.

Once the general control requirements were defined, the control design for the S/G power system was formulated. FOC was selected as the primary control method and the control structure was detailed according to the S/G operational modes. Two separate controllers were used to control speed and FW in starter mode. When operating the S/G system in generator mode, the speed controller was replaced with a DC link controller. The FW controller was active at all times for both modes of operation.

The core system plant was derived as a basis for the design of the S/G control scheme. The internal current control loops for the S/G were then designed and included into the core part of the control scheme. It was shown that the plant included non-linearities, hence small signal models were developed using the Taylor's series linearisation technique. In Chapter 3, the necessary control plant models were derived for each mode of operation. It was found that the plants for FW and DC link voltage control have cross-link dynamics due to feedforward terms within the PMM model. Furthermore, there were positive zeroes present within the derived plants which resulted in non-minimum phase characteristics. The designed controllers therefore had a limited stability range. These limits were investigated during the design phase of the FW and DC link voltage controllers.

The outer loop control design for the S/G system began in starter mode based on the plant models derived in Chapter 3. A speed controller was designed with the relevant plant in order to achieve the desired bandwidth and dynamic response. However, before designing the FW controller, the implementation of a direct current method into the control scheme required the investigation of two cases created by the

dynamic current limiter. Hence, two distinct control plants were derived for subsequent FW control design. It was shown that the plant properties were generally influenced by speed and load demand. The derived plants were discovered to be non-minimum phase during both unlimited i_q^* operation and when operating under maximum load with limited i_q^*. This limited the stability range of the FW controller. As a result, the Routh-Hurwitz criterion was used to analyse the stability range with respect to operating speed or load. The lowest gain range was found to occur at the highest operating speed with full load demand. It was also discovered that the response of the open loop plant was very sensitive towards the proportional gain of the FW controller, particularly for when operating with limited i_q^*. Additionally, it was shown that the wide speed range of the S/G system could cause more complications when using PI controllers; hence a pure integral controller was implemented for FW control.

The FW plant was then re-derived using the appropriate equations for generator mode in order to investigate any change in stability compared to that found in starter mode. It was found that the FW plant changed from non-minimum in starter mode to minimum phase in generator mode; hence the closed loop gain stability margin was increased. During operation in generator mode with limited i_q^*, the plant was found to be non-minimum phase and it was discovered that the gain range decreased according to the load. An unstable region was identified at very low load demands due to the use of the dynamic current limiter. The ratio between i_d and i_q when i_q approached zero became infinite and affected the control performance. Hence, solutions for stable FW control in generator mode were also considered. It was proposed that the FW controller gain could be adaptively changed according to the load demand and operating speed. A novel current limit modifier was proposed in order to eliminate the unstable region. For a given application, if operation of the S/G power system in generator mode with limited i_q^* is not possible then the FW controller could be designed based on the highest speed and load operating point in starter mode. Otherwise, adaptive gain control and a current limit modifier should be employed to ensure stable control performance throughout the S/G operational modes.

The transition of the investigated S/G system from starter to generator mode requires a change in the control scheme. At this transitional point, DC link voltage

control has to replace the speed control used in starter mode. In order to investigate the potential for future parallel operation of multiple S/G systems, droop control was included as part of the required DC link voltage control scheme. The control plant for i_{dc} was derived, with addition of the FW controller, as significant reactive power was found to affect the dynamics of the plant during generator mode. The plant models were established and it was shown that the i_{dc} plant was non-minimum phase. As with starter mode operation, it was found that caution was needed when modifying the proportional term within the i_{dc} controller as this could easily cause system instability. Overall, it was shown that the designed control scheme provides good control performance when the S/G transitions between starter and generator mode.

Analysis of the DC link controller showed that it was capable of fast i_{dc} control loop dynamics using a linear cascade control scheme. However, the small bandwidth difference between the i_{dc} and i_q control loops degraded the performance and caused some stability issues. MPC was therefore considered for the inner current loop control in order to take advantage of its very fast dynamic response. A variant of MPC called M^2PC, which incorporates a modulation scheme as part of its control to improve power quality, was also considered. M^2PC showed reduced current ripple compared to MPC. In addition, MPC had to operate at a much higher sampling frequency. As a result M^2PC was selected for further development. A hybrid PI-M^2PC scheme was then proposed for enhanced S/G control. The hybrid scheme showed reduced current ripple when compared to a full PI control scheme. Increased gain range was also observed for the i_{dc} controller when utilising the proposed hybrid control compared to the full PI control scheme. Parameter variation tests were conducted to gauge the robustness of the hybrid PI-M^2PC without any observer algorithms. The PMM inductances and mutual flux were found to affect the control performance of the hybrid control scheme. Observers would therefore be needed if the variation in system parameters within the S/G system was found to be significant.

Finally, the control design process for the S/G power system was tested on a prototype experimental rig. The experimental setup was explained in detail with reference to the AEGART S/G system. The controllers were adapted according to the specifications of the prototype and the key findings were reported. Experimental results were produced to validate each of the key theoretical findings. The presented

small signal analysis, proposed control design and expected system performance were successfully verified by the experimental results.

8.2   Future work

This research project has proposed a novel S/G system control concept. The achieved results met all key technical requirements and the research generated multiple possibilities for follow-on studies. The following bullet points outline potential future work that could be expanded from the research presented in this thesis:

- Full MPC control of S/G system: Alternative controllers could be considered such as type II compensators commonly used for power converter control. These compensators can be designed to cancel unwanted plant dynamics by placing a pole near the problematic zero. However, in the AEGART S/G power system the tendency is to have positive zeroes. It is very difficult to cancel the dynamics of positive zeroes without making the entire power system unstable. In practical applications, exact pole zero cancellation is also very difficult as the position of the zeroes may change due to system parameter variations and disturbances. The S/G system has a wide range of operating points so this could be a significant complication. Another solution that could be considered would be to use MPC to avoid non-minimum phase operating conditions. The predictive model can be utilised to predict future states several sampling periods ahead such that the non-minimum phase behaviour is avoided or reduced. Within this research, the fast control dynamics of MPC were only utilised for the inner current loops. Further work can be done to develop this method in order to utilise MPC for control of the main system outputs without the classic cascade loop structure. The implementation of such a technique may also simplify the control of multi-objective systems such as the S/G. There is ample literature on drive systems with such control strategies for motoring mode but research has yet to be done for generator mode.

- Parameter identification for MPC control strategies: One of the major disadvantages of using model based control is that changes in system parameters due to external factors, such as ambient operating temperatures, can have a significantly detrimental effect. Steady state error can be prominent when there are large variations in system parameters. Observers and adaptive models could be designed in order to respond to system parameter changes and update the predicted future states accordingly.

- Analysis of aircraft engine dynamics and its effects when coupled with the S/G power system: Throughout the analysis performed in this Thesis, the aircraft engine is assumed as an ideal load or speed source. In practical situations, this may not be always the case and the engine dynamics may have some effect on the stability of the S/G power system or vice versa. The interaction between the engine and the S/G system should therefore be further studied.

- Sensorless control of S/G system: Future work on sensorless control would allow the operation of the S/G system without the need of speed/position sensors. The speed can be estimated by observers using information such as the back-emf voltage obtained from the AC voltage sensors. This type of control offers advantages in terms of cost, reliability, and mechanical packaging for the electrical machine especially when the rotor is immersed in cooling fluids.

- Health monitoring, prognostics, and diagnostics for the S/G system: Studies could be performed on monitoring the reliability and end life of the S/G system components. The information required could be gathered based on actual flight operational temperatures and altitudes. This would provide important insight into the operational lifetimes of critical S/G components which could then be used to reduce maintenance downtime.

8.3 List of Publications

The reported research had generated the following publications:

[1]   S. Yeoh Seang, X. Linying, S. Bozhko, and G. Asher, "Stability analysis of aircraft electrical power system with active front rectifier system in generation channel," in *Power Engineering Conference (UPEC), 2013 48th International Universities'*, 2013, pp. 1-6.

[2]   S. S. Yeoh, F. Gao, S. Bozhko, and G. Asher, "Control design for PMM-based starter generator system for More Electric Aircraft," in *Power Electronics and Applications (EPE'14-ECCE Europe), 2014 16th European Conference on*, 2014, pp. 1-10.

[3]   Y. Seang Shen, Y. Tao, L. Tarisciotti, S. Bozhko, and P. Zanchetta, "Hybrid modulated model predictive control for the more electric aircraft generator system," in *Electrical Systems for Aircraft, Railway, Ship Propulsion and Road Vehicles (ESARS), 2015 International Conference on*, 2015, pp. 1-6.

[4]   G. Fei, S. Bozhko, S. Yeoh Seang, and G. Asher, "Control design for PMM starter-generator operated in flux-weakening mode," in *Power Engineering Conference (UPEC), 2013 48th International Universities'*, 2013, pp. 1-6.

[5]   G. Fei, S. Bozhko, Y. Seang, G. Asher, and P. Wheeler, "Stability of multi-source droop-controlled Electrical Power System for more-electric aircraft," in *Intelligent Energy and Power Systems (IEPS), 2014 IEEE International Conference on*, 2014, pp. 122-126.

[6]   Bozhko, S., Yeoh, S., Gao, F., Yang, T. et al., "Control Design for Electric Starter-Generator Based on a High-Speed Permanent-Magnet Machine Fed by an Active Front-End Rectifier," SAE Technical Paper 2014-01-2139, 2014, doi:10.4271/2014-01-2139.

[7]   S. Bozhko, Y. Seang Shen, G. Fei, and C. Hill, "Aircraft starter-generator system based on permanent-magnet machine fed by active front-end rectifier," in *Industrial Electronics Society, IECON 2014 - 40th Annual Conference of the IEEE*, 2014, pp. 2958-2964.

[8]   F. Gao, S. Yeoh, S. Bozhko, and G. Asher, "Coordinated control of a DC electrical power system in the more electric aircraft integrated with energy storage," in *Energy Conversion Congress and Exposition (ECCE), 2015 IEEE*, 2015, pp. 5431-5438.

Two papers were recently submitted to their respective conferences for consideration:

Rashed, M., Bozhko, S., Yeoh, S., Yang, T., Hill, C., "Flux Weakening Control of Permanent Magnet Electric Starter-Generator for Aircraft Applications," in *Power Electronics, Machines and Drives (PEMD 2016), 8th IET International Conference on*.

F. Gao, S. S.Yeoh, T. Yang, S. Bozhko, "Stability Analysis of A Permanent-Magnet Synchronous Generator Based Aircraft Starter/Generator System," in *Power Electronics and Applications (EPE 2016), 18th European Conference on*.

A journal paper is also under review:

> Rashed, M., Bozhko, S., Yeoh, S., Yang, T., Hill, C., "Flux Weakening Control of Permanent Magnet Machine Based Aircraft Electric Starter-Generator," in *Industrial Electronics, IEEE Transactions on*.

Appendix A   Inverse *dq* Transformation Convention

The three phase to *dq* frame transformation for field oriented vector control was explained in Section 3.2. The *dq* frame can be transformed back into three phase frame using the inverse *dq* transformation shown as:

$$
\begin{bmatrix} x_a \\ x_b \\ x_c \end{bmatrix} = k_{abc} \begin{bmatrix} x_d \\ x_q \end{bmatrix}
$$

(A. 1)

where the inverse *dq* transformation coefficient, k_{abc}, is defined as:

$$
k_{abc} = \begin{bmatrix} \cos(\theta) & -\sin(\theta) \\ \cos\left(\theta - \dfrac{2\pi}{3}\right) & -\sin\left(\theta - \dfrac{2\pi}{3}\right) \\ \cos\left(\theta + \dfrac{2\pi}{3}\right) & -\sin\left(\theta + \dfrac{2\pi}{3}\right) \end{bmatrix}
$$

(A. 2)

Appendix B   Linearisation Approach

The following Sub-sections show the coefficients of the derived i_{dc} and FW plants that were too large to be fitted with the core Thesis content.

B.1 i_{dc} Controller Plant in Generator Mode for $i_q{}^*$ Unlimited Case

$$\frac{\partial i_{dc}}{\partial i_q{}^*} = \frac{\left(k_{iq} + k_{pq}s\right)}{L_q s^2 + \left(R_s + k_{pq}\right)s + k_{iq}} \frac{-3CE_{dco}s\left(b_{1nl}s^4 + b_{2nl}s^3 + b_{3nl}s^2 + b_{4nl}s + b_{5nl}\right)}{\left(2CE_{dco}{}^2 s + 3i_{do}v_{do} + 3i_{qo}v_{qo}\right)\left(b_{6nl}s^3 + b_{7nl}s^2 + b_{8nl}s + b_{9nl}\right)}$$

where

$$b_{1nl} = i_{qo}L_d L_q \left|V\right|_o$$

$$b_{2nl} = \begin{bmatrix} i_{qo}k_{iv}k_{pd}L_d L_q v_{do} + i_{qo}k_{pd}L_q \left|V\right|_o + i_{qo}L_d R_s \left|V\right|_o + i_{qo}L_q R\left|V\right|_o \\ -i_{do}k_{iv}k_{pd}L_d L_q v_{qo} + L_d \left|V\right|_o v_{qo} - i_{do}L_d L_q \left|V\right|_o \omega_{eo} \end{bmatrix}$$

$$b_{3nl} = \begin{bmatrix} i_{qo}k_{id}k_{iv}L_d L_q v_{do} + i_{qo}k_{iv}k_{pd}\left(L_d + L_q\right)R_s v_{do} + i_{qo}k_{id}L_q \left|V\right|_o + i_{qo}k_{pd}R_s \left|V\right|_o \\ +i_{qo}R_s{}^2 \left|V\right|_o - i_{do}k_{id}k_{iv}L_d L_q v_{qo} - i_{do}k_{iv}k_{pd}\left(L_d + L_q\right)R_s v_{qo} + k_{iv}k_{pd}L_d v_{do}v_{qo} \\ -k_{iv}k_{pd}L_q v_{do}v_{qo} + k_{pd}\left|V\right|_o v_{qo} + R_s \left|V\right|_o v_{qo} - i_{do}k_{pd}L_q \left|V\right|_o \omega_{eo} - i_{do}L_q R_s \left|V\right|_o \omega_{eo} \end{bmatrix}$$

$$b_{4nl} = \begin{bmatrix} i_{qo}k_{id}k_{iv}\left(L_d + L_q\right)R_s v_{do} + i_{qo}k_{iv}k_{pd}R_s{}^2 v_{do} + i_{qo}k_{id}R_s \left|V\right|_o - i_{do}k_{id}k_{iv}\left(L_d + L_q\right)R_s v_{qo} - \\ i_{do}k_{iv}k_{pd}R_s{}^2 v_{qo} + k_{id}k_{iv}L_d v_{do}v_{qo} - k_{id}k_{iv}L_q v_{do}v_{qo} + k_{id}\left|V\right|_o v_{qo} + k_{iv}k_{pd}L_q v_{do}{}^2 \omega_{eo} - \\ i_{do}k_{id}L_q \left|V\right|_o \omega_{eo} + k_{iv}k_{pd}L_q v_{qo}{}^2 \omega_{eo} + i_{qo}k_{iv}k_{pd}L_d L_q v_{do}\omega_{eo}{}^2 - i_{do}k_{iv}k_{pd}L_d L_q v_{qo}\omega_{eo}{}^2 \end{bmatrix}$$

$$b_{5nl} = \begin{bmatrix} i_{qo}k_{id}k_{iv}R_s{}^2 v_{do} - i_{do}k_{id}k_{iv}R_s{}^2 v_{qo} + k_{id}k_{iv}L_q v_{do}{}^2 \omega_{eo} + k_{id}k_{iv}L_d v_{qo}{}^2 \omega_{eo} \\ +i_{qo}k_{id}k_{iv}L_d L_q v_{do}\omega_{eo}{}^2 - i_{do}k_{id}k_{iv}L_d L_q v_{qo}\omega_{eo}{}^2 \end{bmatrix}$$

$$b_{6nl} = L_d \left|V\right|_o$$

$$b_{7nl} = k_{iv}k_{pd}L_d v_{do} + k_{pd}\left|V\right|_o + R_s \left|V\right|_o$$

$$b_{8nl} = k_{id}k_{iv}L_d v_{do} + k_{iv}k_{pd}R_s v_{do} + k_{id}\ |V\ |_o + k_{iv}k_{pd}L_d v_{qo}\omega_{eo}$$

$$b_{9nl} = k_{id}k_{iv}R_s v_{do}$$

B.2 |V| Controller Plant in Generator Mode for i_q^* Unlimited Case

$$\frac{\partial|V|}{\partial i_d^*} = \frac{(k_{id} + sk_{pd})}{|V|_o\left(s^2 + (R_s + k_{pd})s + k_{id}\right)} \frac{\left(a_{7nl}s^5 + a_{8nl}s^4 + a_{9nl}s^3 + a_{10nl}s^2 + a_{11nl}s + a_{12nl}\right)}{\left(a_{13nl}s^4 + a_{14nl}s^3 + a_{15nl}s^2 + a_{16nl}s + a_{17nl}\right)}$$

where

$$a_{1nl} = 2CE_{dco}^2 L_d L_q v_{do} + 3CE_{dco}i_{qo}k_{pi}k_{pq}L_d L_q v_{do} - 3CE_{dco}i_{do}k_{pi}k_{pq}L_d L_q v_{qo}$$

$$a_{2nl} = \begin{bmatrix}
2R_s CE_{dco}^2 L_d v_{do} + 2CE_{dco}^2 k_{pq}L_d v_{do} + 3R_s CE_{dco}i_{qo}k_{pi}k_{pq}L_d v_{do} + 2R_s CE_{dco}^2 L_q v_{do} \\
+3RCE_{dco}i_{qo}k_{pi}k_{pq}L_q v_{do} + 3CE_{dco}i_{qo}k_{iq}k_{pi}L_d L_q v_{do} + 3CE_{dco}i_{qo}k_{ii}k_{pq}L_d L_q v_{do} \\
+3E_{dco}i_{qo}k_{droop}k_{pi}k_{pq}L_d L_q v_{do} - 3R_s CE_{dco}i_{do}k_{pi}k_{pq}L_d v_{qo} - 3R_s CE_{dco}i_{do}k_{pi}k_{pq}L_q v_{qo} \\
-3CE_{dco}i_{do}k_{iq}k_{pi}L_d L_q v_{qo} - 3CE_{dco}i_{do}k_{ii}k_{pq}L_d L_q v_{qo} - 3E_{dco}i_{do}k_{droop}k_{pi}k_{pq}L_d L_q v_{qo} \\
+3CE_{dco}k_{pi}k_{pq}L_d v_{do}v_{qo} - 3CE_{dco}k_{pi}k_{pq}L_q v_{do}v_{qo} - 3L_d L_q v_{do}\left(i_{do}v_{do} + i_{qo}v_{qo}\right) \\
+2CE_{dco}^2 L_d L_q v_{qo}\omega_{eo}
\end{bmatrix}$$

$$a_{3nl} = \begin{bmatrix}
2R_s^2 CE_{dco}^2 v_{do} + 2R_s CE_{dco}^2 k_{pq}v_{do} + 3R_s^2 CE_{dco}i_{qo}k_{pi}k_{pq}v_{do} + 2CE_{dco}^2 k_{iq}L_d v_{do} \\
+3R_s CE_{dco}i_{qo}k_{iq}k_{pi}L_d v_{do} + 3R_s CE_{dco}i_{qo}k_{ii}k_{pq}L_d v_{do} + 3R_s E_{dco}i_{qo}k_{droop}k_{pi}k_{pq}L_d v_{do} \\
+3R_s CE_{dco}i_{qo}k_{iq}k_{pi}L_q v_{do} + 3R_s CE_{dco}i_{qo}k_{ii}k_{pq}L_q v_{do} + 3R_s E_{dco}i_{qo}k_{droop}k_{pi}k_{pq}L_q v_{do} \\
+3CE_{dco}i_{qo}k_{ii}k_{iq}L_d L_q v_{do} + 3E_{dco}i_{qo}k_{droop}k_{iq}k_{pi}L_d L_q v_{do} + 3E_{dco}i_{qo}k_{droop}k_{ii}k_{pq}L_d L_q v_{do} \\
-3R_s^2 CE_{dco}i_{do}k_{pi}k_{pq}v_{qo} - 3R_s CE_{dco}i_{do}k_{iq}k_{pi}L_d v_{qo} - 3R_s CE_{dco}i_{do}k_{ii}k_{pq}L_d v_{qo} \\
-3R_s E_{dco}i_{do}k_{droop}k_{pi}k_{pq}L_d v_{qo} - 3R_s CE_{dco}i_{do}k_{iq}k_{pi}L_q v_{qo} - 3R_s CE_{dco}i_{do}k_{ii}k_{pq}L_q v_{qo} \\
-3R_s E_{dco}i_{do}k_{droop}k_{pi}k_{pq}L_q v_{qo} - 3CE_{dco}i_{do}k_{ii}k_{iq}L_d L_q v_{qo} - 3E_{dco}i_{do}k_{droop}k_{iq}k_{pi}L_d L_q v_{qo} \\
-3E_{dco}i_{do}k_{droop}k_{ii}k_{pq}L_d L_q v_{qo} + 3CE_{dco}k_{iq}k_{pi}L_d v_{do}v_{qo} + 3CE_{dco}k_{ii}k_{pq}L_d v_{do}v_{qo} \\
+3E_{dco}k_{droop}k_{pi}k_{pq}L_d v_{do}v_{qo} - 3CE_{dco}k_{iq}k_{pi}L_q v_{do}v_{qo} - 3CE_{dco}k_{ii}k_{pq}L_q v_{do}v_{qo} \\
-3E_{dco}k_{droop}k_{pi}k_{pq}L_q v_{do}v_{qo} - 3R_s L_d v_{do}\left(i_{do}v_{do} + i_{qo}v_{qo}\right) - 3k_{pq}L_d v_{do}\left(i_{do}v_{do} + i_{qo}v_{qo}\right) \\
-3R_s L_q v_{do}\left(i_{do}v_{do} + i_{qo}v_{qo}\right) + 3CE_{dco}k_{pi}k_{pq}L_q v_{do}^2\omega_{eo} + 2R_s CE_{dco}^2 L_d v_{qo}\omega_{eo} \\
+2CE_{dco}^2 k_{pq}L_d v_{qo}\omega_{eo} + 3CE_{dco}k_{pi}k_{pq}L_d v_{qo}^2\omega_{eo} - 3L_d L_q v_{qo}\left(i_{do}v_{do} + i_{qo}v_{qo}\right)\omega_{eo} \\
+3CE_{dco}i_{qo}k_{pi}k_{pq}L_d L_q v_{do}\omega_{eo}^2 - 3CE_{dco}i_{do}k_{pi}k_{pq}L_d L_q v_{qo}\omega_{eo}^2
\end{bmatrix}$$

$$
a_{4nl} = \begin{bmatrix}
2R_sCE_{dco}^2k_{iq}v_{do} + 3R_s^2CE_{dco}i_{qo}k_{iq}k_{pi}v_{do} + 3R_s^2CE_{dco}i_{qo}k_{ii}k_{pq}v_{do} \\
+3R_s^2E_{dco}i_{qo}k_{droop}k_{pi}k_{pq}v_{do} + 3R_sCE_{dco}i_{qo}k_{ii}k_{iq}L_dv_{do} + 3R_sE_{dco}i_{qo}k_{droop}k_{iq}k_{pi}L_dv_{do} \\
+3R_sE_{dco}i_{qo}k_{droop}k_{ii}k_{pq}L_dv_{do} + 3R_sCE_{dco}i_{qo}k_{ii}k_{iq}L_qv_{do} + 3R_sE_{dco}i_{qo}k_{droop}k_{iq}k_{pi}L_qv_{do} \\
+3R_sE_{dco}i_{qo}k_{droop}k_{ii}k_{pq}L_qv_{do} + 3E_{dco}i_{qo}k_{droop}k_{ii}k_{iq}L_dL_qv_{do} - 3R_s^2CE_{dco}i_{do}k_{iq}k_{pi}v_{qo} \\
-3R_s^2CE_{dco}i_{do}k_{ii}k_{pq}v_{qo} - 3R_s^2E_{dco}i_{do}k_{droop}k_{pi}k_{pq}v_{qo} - 3R_sCE_{dco}i_{do}k_{ii}k_{iq}L_dv_{qo} \\
-3R_sE_{dco}i_{do}k_{droop}k_{iq}k_{pi}L_dv_{qo} - 3R_sE_{dco}i_{do}k_{droop}k_{ii}k_{pq}L_dv_{qo} - 3R_sCE_{dco}i_{do}k_{ii}k_{iq}L_qv_{qo} \\
-3R_sE_{dco}i_{do}k_{droop}k_{iq}k_{pi}L_qv_{qo} - 3R_sE_{dco}i_{do}k_{droop}k_{ii}k_{pq}L_qv_{qo} - 3E_{dco}i_{do}k_{droop}k_{ii}k_{iq}L_dL_qv_{qo} \\
+3CE_{dco}k_{ii}k_{iq}L_dv_{do}v_{qo} + 3E_{dco}k_{droop}k_{iq}k_{pi}L_dv_{do}v_{qo} + 3E_{dco}k_{droop}k_{ii}k_{pq}L_dv_{do}v_{qo} \\
-3CE_{dco}k_{ii}k_{iq}L_qv_{do}v_{qo} - 3E_{dco}k_{droop}k_{iq}k_{pi}L_qv_{do}v_{qo} - 3E_{dco}k_{droop}k_{ii}k_{pq}L_qv_{do}v_{qo} \\
-3R_s^2v_{do}\left(i_{do}v_{do} + i_{qo}v_{qo}\right) - 3R_sk_{pq}v_{do}\left(i_{do}v_{do} + i_{qo}v_{qo}\right) - 3k_{iq}L_dv_{do}\left(i_{do}v_{do} + i_{qo}v_{qo}\right) \\
+3CE_{dco}k_{iq}k_{pi}L_qv_{do}^2\omega_{eo} + 3CE_{dco}k_{ii}k_{pq}L_qv_{do}^2\omega_{eo} + 3E_{dco}k_{droop}k_{pi}k_{pq}L_qv_{do}^2\omega_{eo} \\
+2CE_{dco}^2k_{iq}L_dv_{qo}\omega_{eo} + 3CE_{dco}k_{iq}k_{pi}L_dv_{qo}^2\omega_{eo} + 3CE_{dco}k_{ii}k_{pq}L_dv_{qo}^2\omega_{eo} \\
+3E_{dco}k_{droop}k_{pi}k_{pq}L_dv_{qo}^2\omega_{eo} - 3R_sL_dv_{qo}\left(i_{do}v_{do} + i_{qo}v_{qo}\right)\omega_{eo} \\
-3k_{pq}L_dv_{qo}\left(i_{do}v_{do} + i_{qo}v_{qo}\right)\omega_{eo} + 3CE_{dco}i_{qo}k_{iq}k_{pi}L_dL_qv_{do}\omega_{eo}^2 \\
+3CE_{dco}i_{qo}k_{ii}k_{pq}L_dL_qv_{do}\omega_{eo}^2 + 3E_{dco}i_{qo}k_dk_{pi}k_{pq}L_dL_qv_{do}\omega_{eo}^2 \\
-3CE_{dco}i_{do}k_{iq}k_{pi}L_dL_qv_{qo}\omega_{eo}^2 - 3CE_{dco}i_{do}k_{ii}k_{pq}L_dL_qv_{qo}\omega_{eo}^2 \\
-3E_{dco}i_{do}k_dk_{pi}k_{pq}L_dL_qv_{qo}\omega_{eo}^2
\end{bmatrix}
$$

$$
a_{5nl} = \begin{bmatrix}
3R_s^2CE_{dco}i_{qo}k_{ii}k_{iq}v_{do} + 3R_s^2E_{dco}i_{qo}k_{droop}k_{iq}k_{pi}v_{do} + 3R_s^2E_{dco}i_{qo}k_{droop}k_{ii}k_{pq}v_{do} \\
+3R_sE_{dco}i_{qo}k_{droop}k_{ii}k_{iq}L_dv_{do} + 3R_sE_{dco}i_{qo}k_{droop}k_{ii}k_{iq}L_qv_{do} - 3R_s^2CE_{dco}i_{do}k_{ii}k_{iq}v_{qo} \\
-3R_s^2E_{dco}i_{do}k_{droop}k_{iq}k_{pi}v_{qo} - 3R_s^2E_{dco}i_{do}k_{droop}k_{ii}k_{pq}v_{qo} - 3R_sE_{dco}i_{do}k_{droop}k_{ii}k_{iq}L_dv_{qo} \\
-3R_sE_{dco}i_{do}k_{droop}k_{ii}k_{iq}L_qv_{qo} + 3E_{dco}k_{droop}k_{ii}k_{iq}L_dv_{do}v_{qo} - 3E_{dco}k_{droop}k_{ii}k_{iq}L_qv_{do}v_{qo} \\
-3R_sk_{iq}v_{do}\left(i_{do}v_{do} + i_{qo}v_{qo}\right) + 3CE_{dco}k_{ii}k_{iq}L_qv_{do}^2\omega_{eo} + 3E_{dco}k_{droop}k_{iq}k_{pi}L_qv_{do}^2\omega_{eo} \\
+3E_{dco}k_{droop}k_{ii}k_{pq}L_qv_{do}^2\omega_{eo} + 3CE_{dco}k_{ii}k_{iq}L_dv_{qo}^2\omega_{eo} + 3E_{dco}k_{droop}k_{iq}k_{pi}L_dv_{qo}^2\omega_{eo} \\
+3E_{dco}k_{droop}k_{ii}k_{pq}L_dv_{qo}^2\omega_{eo} - 3k_{iq}L_dv_{qo}\left(i_{do}v_{do} + i_{qo}v_{qo}\right)\omega_{eo} \\
+3CE_{dco}i_{qo}k_{ii}k_{iq}L_dL_qv_{do}\omega_{eo}^2 + 3E_{dco}i_{qo}k_{droop}k_{iq}k_{pi}L_dL_qv_{do}\omega_{eo}^2 \\
+3E_{dco}i_{qo}k_{droop}k_{ii}k_{pq}L_dL_qv_{do}\omega_{eo}^2 - 3CE_{dco}i_{do}k_{ii}k_{iq}L_dL_qv_{qo}\omega_{eo}^2 \\
-3E_{dco}i_{do}k_{droop}k_{iq}k_{pi}L_dL_qv_{qo}\omega_{eo}^2 - 3E_{dco}i_{do}k_{droop}k_{ii}k_{pq}L_dL_qv_{qo}\omega_{eo}^2
\end{bmatrix}
$$

$$a_{6nl} = \begin{bmatrix} 3R_s^2 E_{dco} i_{qo} k_{droop} k_{ii} k_{iq} v_{do} - 3R_s^2 E_{dco} i_{do} k_{droop} k_{ii} k_{iq} v_{qo} + 3E_{dco} k_{droop} k_{ii} k_{iq} L_q v_{do}^2 \omega_{eo} \\ +3E_{dco} k_{droop} k_{ii} k_{iq} L_d v_{qo}^2 \omega_{eo} + 3E_{dco} i_{qo} k_{droop} k_{ii} k_{iq} L_d L_q v_{do} \omega_{eo}^2 \\ -3E_{dco} i_{do} k_{droop} k_{ii} k_{iq} L_d L_q v_{qo} \omega_{eo}^2 \end{bmatrix}$$

$$a_{7nl} = 2CE_{dco}^2 L_q + 3CE_{dco} i_{qo} k_{pi} k_{pq} L_q$$

$$a_{8nl} = \begin{bmatrix} 2R_s CE_{dco}^2 + 2CE_{dco}^2 k_{pq} + 3R_s CE_{dco} i_{qo} k_{pi} k_{pq} + 3CE_{dco} i_{qo} k_{iq} k_{pi} L_q \\ +3CE_{dco} i_{qo} k_{ii} k_{pq} L_q + 3E_{dco} i_{qo} k_{droop} k_{pi} k_{pq} L_q + 3CE_{dco} k_{pi} k_{pq} v_{qo} \\ -3L_q \left(i_{do} v_{do} + i_{qo} v_{qo} \right) - 3CE_{dco} i_{do} k_{pi} k_{pq} L_q \omega_{eo} \end{bmatrix}$$

$$a_{9nl} = \begin{bmatrix} 2CE_{dco}^2 k_{iq} + 3R_s CE_{dco} i_{qo} k_{iq} k_{pi} + 3R_s CE_{dco} i_{qo} k_{ii} k_{pq} + 3R_s E_{dco} i_{qo} k_{droop} k_{pi} k_{pq} \\ +3CE_{dco} i_{qo} k_{ii} k_{iq} L_q + 3E_{dco} i_{qo} k_{droop} k_{iq} k_{pi} L_q + 3E_{dco} i_{qo} k_{droop} k_{ii} k_{pq} L_q \\ +3CE_{dco} k_{iq} k_{pi} v_{qo} + 3CE_{dco} k_{ii} k_{pq} v_{qo} + 3E_{dco} k_{droop} k_{pi} k_{pq} v_{qo} \\ -3R_s \left(i_{do} v_{do} + i_{qo} v_{qo} \right) - 3k_{pq} \left(i_{do} v_{do} + i_{qo} v_{qo} \right) - 3CE_{dco} i_{do} k_{iq} k_{pi} L_q \omega_{eo} \\ -3CE_{dco} i_{do} k_{ii} k_{pq} L_q \omega_{eo} - 3E_{dco} i_{do} k_{droop} k_{pi} k_{pq} L_q \omega_{eo} \end{bmatrix}$$

$$a_{10nl} = \begin{bmatrix} 3R_s CE_{dco} i_{qo} k_{ii} k_{iq} + 3R_s E_{dco} i_{qo} k_{droop} k_{iq} k_{pi} + 3R_s E_{dco} i_{qo} k_{droop} k_{ii} k_{pq} \\ +3E_{dco} i_{qo} k_{droop} k_{ii} k_{iq} L_q + 3CE_{dco} k_{ii} k_{iq} v_{qo} + 3E_{dco} k_{droop} k_{iq} k_{pi} v_{qo} \\ +3E_{dco} k_{droop} k_{ii} k_{pq} v_{qo} - 3k_{iq} \left(i_{do} v_{do} + i_{qo} v_{qo} \right) - 3CE_{dco} i_{do} k_{ii} k_{iq} L_q \omega_{eo} \\ -3E_{dco} i_{do} k_{droop} k_{iq} k_{pi} L_q \omega_{eo} - 3E_{dco} i_{do} k_{droop} k_{ii} k_{pq} L_q \omega_{eo} \end{bmatrix}$$

$$a_{11nl} = 3R_s E_{dco} i_{qo} k_{droop} k_{ii} k_{iq} + 3E_{dco} k_{droop} k_{ii} k_{iq} v_{qo} - 3E_{dco} i_{do} k_{droop} k_{ii} k_{iq} L_q \omega_{eo}$$

B.3 $|V|$ Controller Plant in Generator Mode for $i_q{}^*$ Limited Case

$$\frac{\partial |V|}{\partial i_d{}^*} = \frac{\left(a_{7l}s^4 + a_{8l}s^3 + a_{9l}s^2 + a_{10l}s + a_{11l}\right)}{v_o i_{qo}{}^* \left(L_q s^2 + \left(R_s + k_{pq}\right)s + k_{iq}\right)\left(L_d s^2 + \left(R_s + k_{pd}\right)s + k_{id}\right)}$$

where

$$a_{7l} = -k_{pq}L_d L_q v_{qo} i_{do}{}^* + k_{pd}L_d L_q v_{do} i_{qo}{}^*$$

$$a_{8l} = \begin{bmatrix} -R_s k_{pq}L_d v_{qo} i_{do}{}^* - R_s k_{pq}L_q v_{qo} i_{do}{}^* - k_{pd}k_{pq}L_q v_{qo} i_{do}{}^* - k_{iq}L_d L_q v_{qo} i_{do}{}^* \\ +k_{pq}L_d L_q v_{do}\omega_{eo} i_{do}{}^* + R_s k_{pd}L_d v_{do} i_{qo}{}^* + k_{pd}k_{pq}L_d v_{do} i_{qo}{}^* \\ + R_s k_{pd}L_q v_{do} i_{qo}{}^* + k_{id}L_d L_q v_{do} i_{qo}{}^* + k_{pd}L_d L_q v_{qo}\omega_{eo} i_{qo}{}^* \end{bmatrix}$$

$$a_{9l} = \begin{bmatrix} -R_s^2 k_{pq}v_{qo} i_{do}{}^* - R_s k_{pd}k_{pq}v_{qo} i_{do}{}^* - R_s k_{iq}L_d v_{qo} i_{do}{}^* - R_s k_{iq}L_q v_{qo} i_{do}{}^* \\ -k_{iq}k_{pd}L_q v_{qo} i_{do}{}^* - k_{id}k_{pq}L_q v_{qo} i_{do}{}^* + R_s k_{pq}L_q v_{do}\omega_{eo} i_{do}{}^* + k_{pd}k_{pq}L_q v_{do}\omega_{eo} i_{do}{}^* \\ +k_{iq}L_d L_q v_{do}\omega_{eo} i_{do}{}^* + R_s^2 k_{pd}v_{do} i_{qo}{}^* + R_s k_{pd}k_{pq}v_{do} i_{qo}{}^* + R_s k_{id}L_d v_{do} i_{qo}{}^* \\ +k_{iq}k_{pd}L_d v_{do} i_{qo}{}^* + k_{id}k_{pq}L_d v_{do} i_{qo}{}^* + R_s k_{id}L_q v_{do} i_{qo}{}^* \\ + R_s k_{pd}L_d v_{qo}\omega_{eo} i_{qo}{}^* + k_{pd}k_{pq}L_d v_{qo}\omega_{eo} i_{qo}{}^* + k_{id}L_d L_q v_{qo}\omega_{eo} i_{qo}{}^* \end{bmatrix}$$

$$a_{10l} = \begin{bmatrix} -R_s^2 k_{iq}v_{qo} i_{do}{}^* - R_s k_{iq}k_{pd}v_{qo} i_{do}{}^* - R_s k_{id}k_{pq}v_{qo} i_{do}{}^* - k_{id}k_{iq}L_q v_{qo} i_{do}{}^* \\ + R_s k_{iq}L_q v_{do}\omega_{eo} i_{do}{}^* + k_{iq}k_{pd}L_q v_{do}\omega_{eo} i_{do}{}^* + k_{id}k_{pq}L_q v_{do}\omega_{eo} i_{do}{}^* \\ + R_s^2 k_{id}v_{do} i_{qo}{}^* + R_s k_{iq}k_{pd}v_{do} i_{qo}{}^* + R_s k_{id}k_{pq}v_{do} i_{qo}{}^* + k_{id}k_{iq}L_d v_{do} i_{qo}{}^* \\ + R_s k_{id}L_d v_{qo}\omega_{eo} i_{qo}{}^* + k_{iq}k_{pd}L_d v_{qo}\omega_{eo} i_{qo}{}^* + k_{id}k_{pq}L_d v_{qo}\omega_{eo} i_{qo}{}^* \end{bmatrix}$$

$$a_{11l} = -R_s k_{id}k_{iq}v_{qo} i_{do}{}^* + k_{id}k_{iq}L_q v_{do}\omega_{eo} i_{do}{}^* + R_s k_{id}k_{iq}v_{do} i_{qo}{}^* + k_{id}k_{iq}L_d v_{qo}\omega_{eo} i_{qo}{}^*$$

Appendix C   Simulation Models

Simulation analysis was primarily done with Matlab®/Simulink®. The following were the models created in Simulink to support this study.
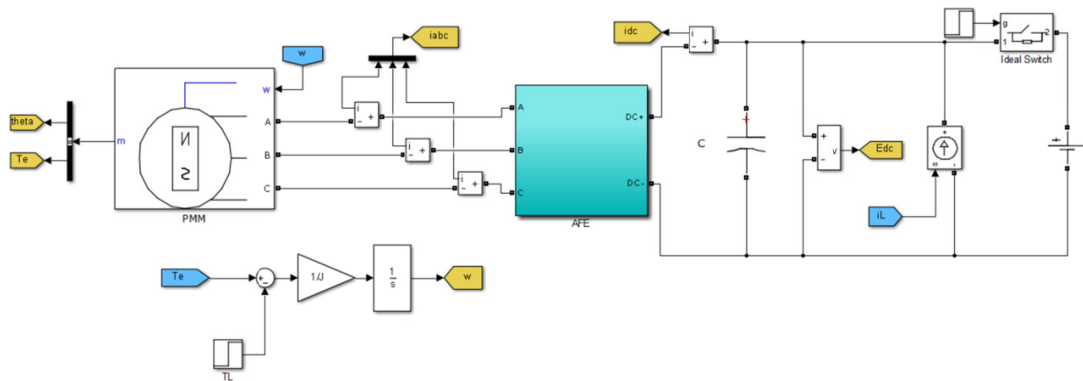
Fig. C. 1. S/G power system consisting of PMM, AFE, DC bus, and DC voltage source (for starter mode only).
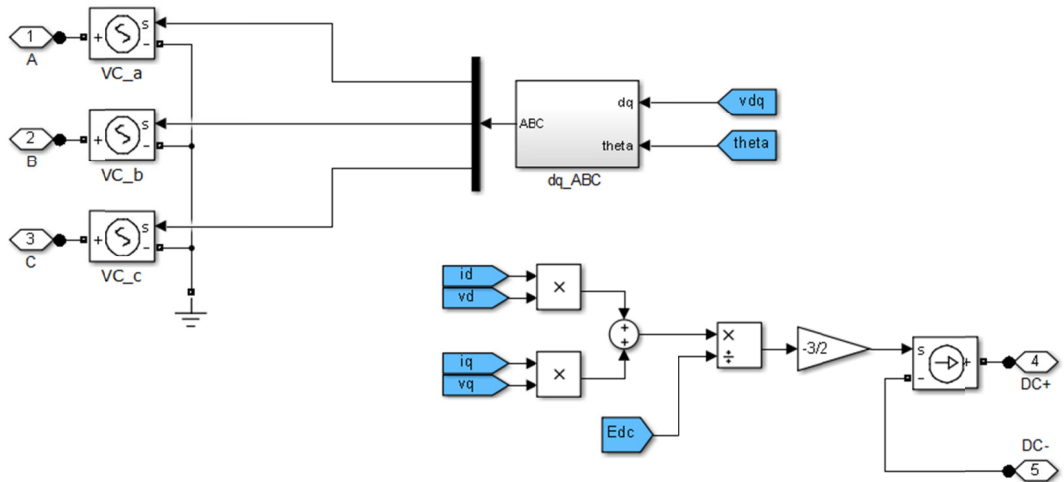
Fig. C. 2. Average model of AFE.
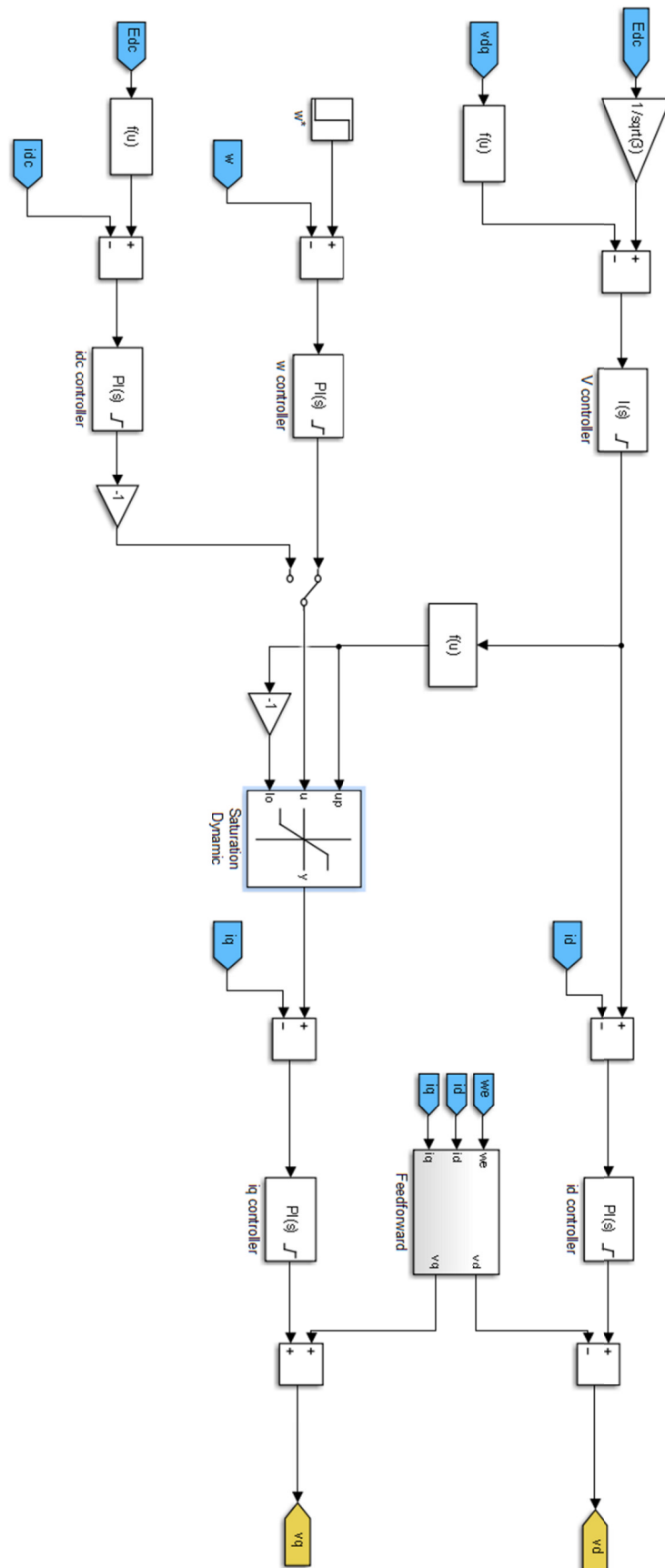
Fig. C. 3. Full PI control scheme for S/G system.

Appendix D   Experimental Rig Control Platform

The following are additional information about the experimental rig introduced in Chapter 7. They are details about the digital control platform that process information from the sensors and execute the control scheme for the AC drive system. The DSP, FPGA, interface board, and HPI capture card forms the control platform for the AC drive system shown in Fig. D.1. The DSP and FPGA works together to execute the control scheme, signal measurement and processing. An interface board is connected with the DSP and FPGA to obtain the rotor position information from the PMM encoder. The communication between the local computer and the digital control platform can be achieved through the HPI capture card.

In this research, the Texas Instrument TMS320C6713 DSP Starter Kit [161] shown in Fig. D.1 is used to as a processor to run the control scheme. The DSP processor can operate up to the frequency of 225MHz and perform eight operations at maximum per cycle. The control scheme is implemented in C and programmed into the DSP via the appropriate software on the computer.

Fig. D.2 shows the FPGA connected on top of the DSP processor. The control signal output from the DSP is sent to the FPGA which is used to interface the hardware by a hardware description language (HDL). This allows the data transfer between both components to be very fast (less than $10\mu s$ depending on DSP capabilities). The main functions of the FPGA in this AC drive system are pulse generation for PWM, online data measurement and conversion from the sensors, and hardware circuit protection for overcurrent/overvoltage.
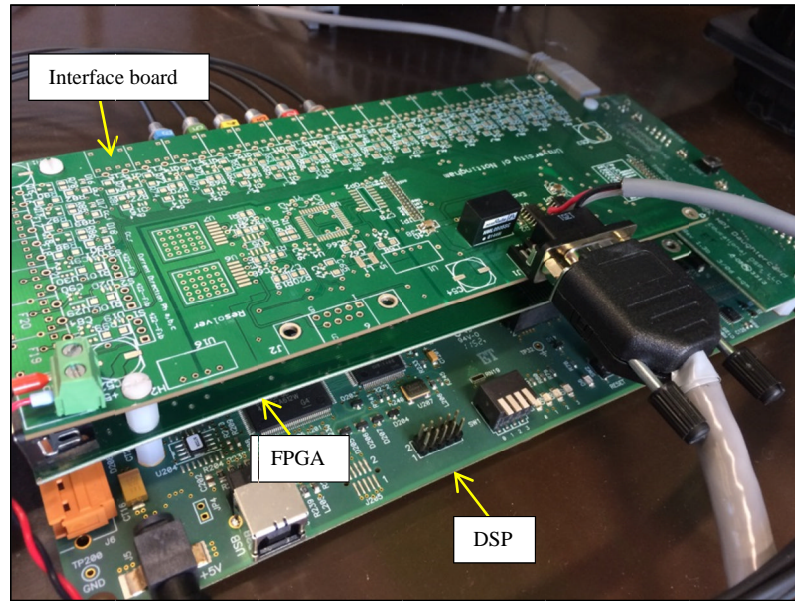
Fig. D.1. Overview of digital control platform.
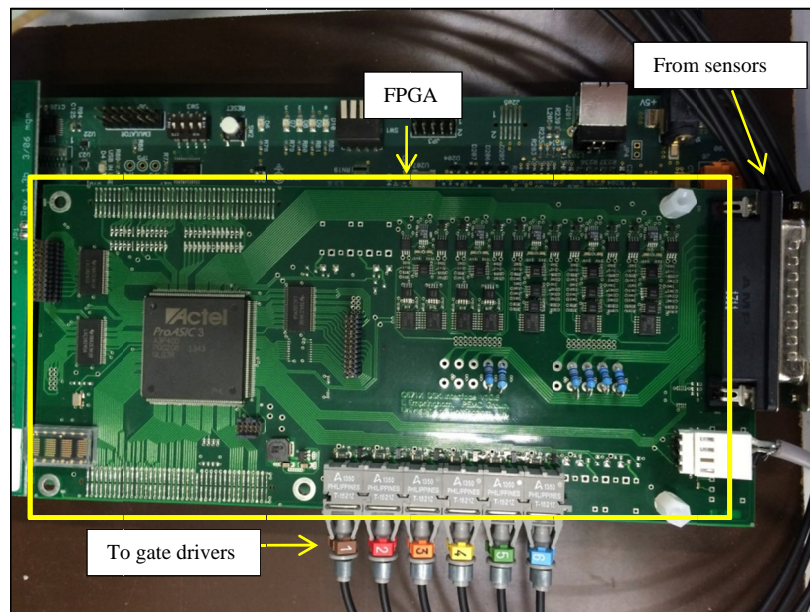
Fig. D.2. FPGA board designed by Dr. Empringham Lee.

An interface board is plugged onto the FPGA shown in Fig. D.3. This board provides interface for an encoder, resolver, and 21 additional optical connections. The six optical connections available on the FPGA are sufficient for this AC drive system, so only the encoder interface is used to obtain position information on the PMM rotor. Six signals are sent from the encoder to the interface; channel A, B, Z, and their respective inverse signals. Channel A and B are used to interpret the

position and rotating direction of the rotor. Channel Z is used to determine the position of the rotor that is aligned to the machine magnets that is useful for FOC.

A HPI capture card is connected to the DSP (see Fig. D.3) which interfaces to the computer. A host program interface is used in Matlab® where multiple commands can be sent to the HPI capture card. The card can be used to capture data sent to the DSP such as the measured and calculated variables. Commands can be sent to the control scheme through this card such as control reference value alterations.
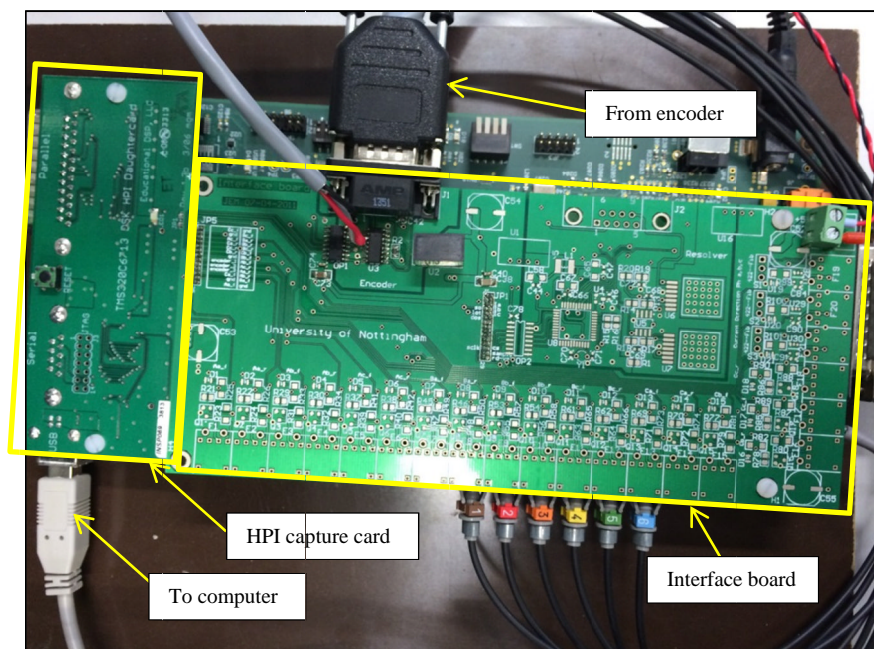
Fig. D.3. Interface board and HPI capture card.

References

[1]   J. Laurence K. Loftin. (1985). *The Evolution of Modern Aircraft*. Available: http://www.hq.nasa.gov/pao/History/SP-468/cover.htm. Accessed: 15/1/16

[2]   Airbus. *Onboard Well-being*. Available: http://www.airbus.com/aircraftfamilies/passengeraircraft/a380family/onboard-well-being/. Accessed: 16/1/2016

[3]   D. O. T. F. A. Administration. (2012). *Type Certificate Data Sheet No. A20WE*. Available: http://www.boeing.com/assets/pdf/commercial/airports/misc/A20WE.pdf. Accessed: 16/1/2016

[4]   S. J. Cutts, "A collaborative approach to the More Electric Aircraft," in *Power Electronics, Machines and Drives, 2002. International Conference on (Conf. Publ. No. 487)*, 2002, pp. 223-228.

[5]   M. Sinnett. (2007). *Saving Fuel and Enhancing Operational Efficiencies*. Available: http://www.boeing.com/commercial/aeromagazine/articles/qtr_4_07/AERO_Q407_article2.pdf. Accessed: 16/1/2016

[6]   A. F. Abdel-Hafez, A. J., "A Review of More-Electric Aircraft," in *ASAT-13*, Cairo, Egypt, 2009.

[7]   P. Wheeler and S. Bozhko, "The More Electric Aircraft: Technology and challenges," *Electrification Magazine, IEEE*, vol. 2, pp. 6-12, 2014.

[8]   A. Abdel-Hafez, *Power Generation and Distribution System for a More Electric Aircraft - A Review, Recent Advances in Aircraft Technology*, 2012.

[9]   X. Roboam, B. Sareni, and A. D. Andrade, "More Electricity in the Air: Toward Optimized Electrical Networks Embedded in More-Electrical Aircraft," *Industrial Electronics Magazine, IEEE*, vol. 6, pp. 6-17, 2012.

[10]   I. Moir and A. Seabridge, *Aircraft Systems: Mechanical, Electrical and Avionics Subsystems Integration*: Wiley, 2008.

[11]   Y. Tao, "Development of Dynamic Phasors for the Modelling of Aircraft Electrical Power Systems," Electrical and Electronic Engineering, University of Nottingham, 2013.

[12]   D. L. Faleiro, "Summary of the European Power Optimised Aircraft (POA) Project," *International Congress Of The Aeronautical Sciences*, 16/4/12 2006.

[13]   *More Open Electrical Technologies*. Available: http://ec.europa.eu/research/transport/projects/items/moet_en.htm. Accessed: 11/11/2015

[14]   *Clean Sky*. Available: http://www.cleansky.eu/. Accessed: 11/11/2015

[15]   C. Sky. *About Us*. Available: http://www.cleansky.eu/content/homepage/about-us. Accessed: 16/1/2016

[16]   M. J. Provost, "The More Electric Aero-engine: a general overview from an engine manufacturer," in *Power Electronics, Machines and Drives, 2002. International Conference on (Conf. Publ. No. 487)*, 2002, pp. 246-251.

[17]   S. Shoujun, L. Weiguo, D. Peitsch, and U. Schaefer, "Detailed Design of a High Speed Switched Reluctance Starter/Generator for More/All Electric Aircraft," *Chinese Journal of Aeronautics*, vol. 23, pp. 216-226, 2010.

[18]   M. Hirst, A. McLoughlin, P. J. Norman, and S. J. Galloway, "Demonstrating the more electric engine: a step towards the power optimised aircraft," *Electric Power Applications, IET*, vol. 5, pp. 3-13, 2011.

[19]   C. F. Taylor, *Aircraft Propulsion: A Review of the Evolution of Aircraft Piston Engines* vol. 1. Washington D.C: Smithsonian Institution Press, 1971.

[20]   R. Royce, *The Jet Engine*, 5th Edition ed. London, UK, 1996.

[21]   M. van der Geest, H. Polinder, J. A. Ferreira, and D. Zeilstra, "Machine selection and initial design of an aerospace starter/generator," in *Electric Machines & Drives Conference (IEMDC), 2013 IEEE International*, 2013, pp. 196-203.

[22]   M. E. Elbuluk and M. D. Kankam, "Potential starter/generator technologies for future aerospace applications," *Aerospace and Electronic Systems Magazine, IEEE*, vol. 12, pp. 24-31, 1997.

[23] T. Finken, M. Felden, and K. Hameyer, "Comparison and design of different electrical machine types regarding their applicability in hybrid electrical vehicles," in *Electrical Machines, 2008. ICEM 2008. 18th International Conference on*, 2008, pp. 1-5.

[24] R. Anbarasu, R. K. Gupta, N. D. Sharma, G. Gauthaman, A. K. Wankhede, P. H. Chavda, J. Nataraj, and B. Bhattacharjee, "Design and experimental investigation of high speed squirrel cage induction motor," in *Power Electronics, Drives and Energy Systems for Industrial Growth, 1996., Proceedings of the 1996 International Conference on*, 1996, pp. 920-926 vol.2.

[25] "MIL-STD-704F," in *Aircraft Electric Power Characteristics*, ed. United States of America: Department of Defense Interface Standard

2014.

[26] J. A. Rosero, J. A. Ortega, E. Aldabas, and L. Romeral, "Moving towards a more electric aircraft," *Aerospace and Electronic Systems Magazine, IEEE,* vol. 22, pp. 3-9, 2007.

[27] A. Boglietti, A. Cavagnino, A. Tenconi, and S. Vaschetto, "The safety critical electric machines and drives in the more electric aircraft: A survey," in *Industrial Electronics, 2009. IECON '09. 35th Annual Conference of IEEE*, 2009, pp. 2587-2594.

[28] C. R. Avery, S. G. Burrow, and P. H. Mellor, "Electrical generation and distribution for the more electric aircraft," in *Universities Power Engineering Conference, 2007. UPEC 2007. 42nd International*, 2007, pp. 1007-1012.

[29] D. Izquierdo, R. Azcona, F. del Cerro, C. Fernandez, and B. Delicado, "Electrical power distribution system (HV270DC), for application in more electric aircraft," in *Applied Power Electronics Conference and Exposition (APEC), 2010 Twenty-Fifth Annual IEEE*, 2010, pp. 1300-1305.

[30] B. H. Nya, J. Brombach, and D. Schulz, "Benefits of higher voltage levels in aircraft electrical power systems," in *Electrical Systems for Aircraft, Railway and Ship Propulsion (ESARS), 2012*, 2012, pp. 1-5.

[31] W. Shanshan and L. Yongdong, "Application and challenges of power electronics for variable frequency electric power system of more electric aircraft," in *Electrical Machines and Systems (ICEMS), 2011 International Conference on*, 2011, pp. 1-4.

[32] Y. Takahashi, K. Yoshikawa, M. Soutome, T. Fujii, M. Ichijyou, and Y. Seki, "2.5 kV-1000 A power pack IGBT (high power flat-packaged RC-IGBT)," in *Power Semiconductor Devices and ICs, 1996. ISPSD '96 Proceedings., 8th International Symposium on*, 1996, pp. 299-302.

[33] S. Muller, M. Deicke, and R. W. De Doncker, "Adjustable speed generators for wind turbines based on doubly-fed induction machines and 4-quadrant IGBT converters linked to the rotor," in *Industry Applications Conference, 2000. Conference Record of the 2000 IEEE*, 2000, pp. 2249-2254 vol.4.

[34] S. R. MacMinn and J. W. Sember, "Control of a switched-reluctance aircraft engine starter-generator over a very wide speed range," in *Energy Conversion Engineering Conference, 1989. IECEC-89., Proceedings of the 24th Intersociety*, 1989, pp. 631-638 vol.1.

[35] I. Alan and T. A. Lipo, "Starter/generator employing resonant-converter-fed induction machine. II. Hardware prototype," *Aerospace and Electronic Systems, IEEE Transactions on,* vol. 36, pp. 1319-1329, 2000.

[36] E. Richter and C. Ferreira, "Performance evaluation of a 250 kW switched reluctance starter generator," in *Industry Applications Conference, 1995. Thirtieth IAS Annual Meeting, IAS '95., Conference Record of the 1995 IEEE*, 1995, pp. 434-440 vol.1.

[37] S. R. Jones and B. T. Drager, "Sensorless switched reluctance starter/generator performance," *Industry Applications Magazine, IEEE,* vol. 3, pp. 33-38, 1997.

[38] G. Friedrich and A. Girardin, "Integrated starter generator," *Industry Applications Magazine, IEEE,* vol. 15, pp. 26-34, 2009.

[39] A. Griffo, D. Drury, T. Sawata, and P. H. Mellor, "Sensorless starting of a wound-field synchronous starter/generator for aerospace applications," *Industrial Electronics, IEEE Transactions on,* vol. 59, pp. 3579-3587, 2012.

[40] R. H. Williams, M. P. Foster, D. A. Stone, and S. R. Minshull, "Utilizing existing aircraft wound field generators for starter-generators," in *Power Electronics and ECCE Asia (ICPE & ECCE), 2011 IEEE 8th International Conference on*, 2011, pp. 691-696.

[41] B. S. Bhangu and K. Rajashekara, "Control strategy for electric starter generators embedded in gas turbine engine for aerospace applications," in *Energy Conversion Congress and Exposition (ECCE), 2011 IEEE*, 2011, pp. 1461-1467.

[42]   Cleansky.   *AEGART   Project   Summary*.   Available: http://cordis.europa.eu/result/rcn/143557_en.html. Accessed: 11/11/2015

[43]   S. Bozhko, Y. Seang Shen, G. Fei, and C. Hill, "Aircraft starter-generator system based on permanent-magnet machine fed by active front-end rectifier," in *Industrial Electronics Society, IECON 2014 - 40th Annual Conference of the IEEE*, 2014, pp. 2958-2964.

[44]   M. Degano, P. Arumugam, W. Fernando, Y. Tao, Z. He, J. B. Bartolo, S. Bozhko, P. Wheeler, and C. Gerada, "An optimized bi-directional, wide speed range electric starter-generator for aerospace application," in *Power Electronics, Machines and Drives (PEMD 2014), 7th IET International Conference on*, 2014, pp. 1-6.

[45]   Plexim. *Plexim: Electrical Engineering Software*. Available: http://www.plexim.com. Accessed: 20/2/2016

[46]   P. C. Krause, O. Wasynczuk, S. D. Sudhoff, and I. P. E. Society, *Analysis of electric machinery and drive systems*: IEEE Press, 2002.

[47]   M. Ahmad, *High Performance AC Drives: Modelling Analysis and Control*: Springer Berlin Heidelberg, 2010.

[48]   I. Takahashi and T. Noguchi, "A New Quick-Response and High-Efficiency Control Strategy of an Induction Motor," *Industry Applications, IEEE Transactions on,* vol. IA-22, pp. 820-827, 1986.

[49]   A.D. Karlis, K. Kiriakopoulos, D.P. Papadopoulos, and E. L. Bibeau. Comparison of the Field Oriented and Direct Torque Control Methods for Induction Motors used in Electric Vehicles.

[50]   M. Zordan, P. Vas, M. Rashed, S. Bolognani, and M. Zigliotto, "Field-weakening in high-performance PMSM drives: a comparative analysis," in *Industry Applications Conference, 2000. Conference Record of the 2000 IEEE*, 2000, pp. 1718-1724 vol.3.

[51]   B. Drury. (2009). *Control Techniques, Drives and Controls Handbook*. Available: http://digital-library.theiet.org/content/books/po/pbpo057e

[52]   L. Dongyun and N. C. Kar, "A review of flux-weakening control in permanent magnet synchronous machines," in *Vehicle Power and Propulsion Conference (VPPC), 2010 IEEE*, 2010, pp. 1-6.

[53]   T. M. Jahns, "Flux-Weakening Regime Operation of an Interior Permanent-Magnet Synchronous Motor Drive," *Industry Applications, IEEE Transactions on,* vol. IA-23, pp. 681-689, 1987.

[54]   F. Khatounian, E. Monmasson, F. Berthereau, E. Delaleau, and J. P. Louis, "Control of a doubly fed induction generator for aircraft application," in *Industrial Electronics Society, 2003. IECON '03. The 29th Annual Conference of the IEEE*, 2003, pp. 2711-2716 Vol.3.

[55]   Y. Xibo and W. Jiabin, "Stability and performance analysis of permanent magnet motors operating in flux-weakening region," in *Power Electronics and Motion Control Conference (IPEMC), 2012 7th International*, 2012, pp. 2542-2546.

[56]   H. Hannoun, M. Hilairet, and C. Marchand, "Experimental Validation of a Switched Reluctance Machine Operating in Continuous-Conduction Mode," *Vehicular Technology, IEEE Transactions on,* vol. 60, pp. 1453-1460, 2011.

[57]   R. Dutta, L. Chong, and M. F. Rahman, "Analysis of CPSR in motoring and generating modes of an IPM motor," in *Electric Machines & Drives Conference (IEMDC), 2011 IEEE International*, 2011, pp. 1474-1479.

[58]   N. V. Olarescu, S. Musuroi, C. Sorandaru, M. Weinmann, and S. Zeh, "Optimum current command algorithm for wide speed range and four quadrant operation of PMSMS drive without regenerative unit," in *Optimization of Electrical and Electronic Equipment (OPTIM), 2010 12th International Conference on*, 2010, pp. 704-709.

[59]   N. V. Olarescu, S. Musuroi, C. Sorandaru, M. Weinmann, and S. Zeh, "Optimum current control for wide speed range operation of PMSM drive without regenerative unit utilizing PWM-VSI overmodulation," in *Optimization of Electrical and Electronic Equipment (OPTIM), 2012 13th International Conference on*, 2012, pp. 612-617.

[60]   J. Wai and T. M. Jahns, "A new control technique for achieving wide constant power speed operation with an interior PM alternator machine," in *Industry Applications Conference, 2001. Thirty-Sixth IAS Annual Meeting. Conference Record of the 2001 IEEE*, 2001, pp. 807-814 vol.2.

[61]   S. Shinn-Ming and P. Ching-Tsai, "Voltage-Constraint-Tracking-Based Field-Weakening Control of IPM Synchronous Motor Drives," *Industrial Electronics, IEEE Transactions on,* vol. 55, pp. 340-347, 2008.

[62] P. Ching-Tsai and L. Jenn-Horng, "A robust field-weakening control strategy for surface-mounted permanent-magnet motor drives," *Energy Conversion, IEEE Transactions on,* vol. 20, pp. 701-709, 2005.

[63] Z. Yuan, X. Longya, Gu, x, M. K. ven, C. Song, and M. Illindala, "Experimental Verification of Deep Field Weakening Operation of a 50-kW IPM Machine by Using Single Current Regulator," *Industry Applications, IEEE Transactions on,* vol. 47, pp. 128-133, 2011.

[64] H. Taiyuan, L. Fei, L. Kezhen, F. Xiaocun, and Y. Zhongping, "Flux-weakening control of PMSM based on single current regulator and variable q-axis voltage," in *Electrical Machines and Systems (ICEMS), 2012 15th International Conference on*, 2012, pp. 1-6.

[65] C. Song, Z. Zheng, and X. Longya, "A Robust, Efficiency Optimized Flux-Weakening Control Algorithm for PM Synchronous Machines," in *Industry Applications Conference, 2007. 42nd IAS Annual Meeting. Conference Record of the 2007 IEEE*, 2007, pp. 1308-1314.

[66] X. Guo, X. Wen, F. Zhao, and Y. Wang, "The flux weakening control analysis and its PI controller of fuzzy self-adaptive design for PMSM," in *Electrical Machines and Systems (ICEMS), 2011 International Conference on*, 2011, pp. 1-4.

[67] G. Xinhua, W. Xuhui, Z. Feng, S. Xuelei, and Z. Xingming, "PI parameter design of the flux weakening control for PMSM based on small signal and transfer function," in *Electrical Machines and Systems, 2009. ICEMS 2009. International Conference on*, 2009, pp. 1-6.

[68] K. Sun and Q. Shu, "Field weakening operation control strategies of interior permanent magnet synchronous motor for electric vehicles," in *Control Conference (CCC), 2011 30th Chinese*, 2011, pp. 3640-3643.

[69] M. M. Bech, T. S. Frederiksen, and P. Sandholdt, "Accurate torque control of saturated interior permanent magnet synchronous motors in the field-weakening region," in *Industry Applications Conference, 2005. Fourtieth IAS Annual Meeting. Conference Record of the 2005*, 2005, pp. 2526-2532 Vol. 4.

[70] J. L. Shi, T. H. Liu, and S. H. Yang, "Nonlinear-controller design for an interior-permanent-magnet synchronous motor including field-weakening operation," *Electric Power Applications, IET,* vol. 1, pp. 119-126, 2007.

[71] S. Ji-Liang, L. Tian-Hua, and Y. Shih-Hsien, "Field Weakening with Nonlinear Controller Design for an Interior Permanent Magnet Synchronous Motor," in *IEEE Industrial Electronics, IECON 2006 - 32nd Annual Conference on*, 2006, pp. 1411-1416.

[72] J. Kang-Hwan, K. Soon-Hwan, P. Dong-Gyu, and K. Yoon-Ho, "Design of the sensorless speed control system for the PMSM based next generation high speed railway system," in *Power Electronics and ECCE Asia (ICPE & ECCE), 2011 IEEE 8th International Conference on*, 2011, pp. 1419-1424.

[73] Z. X. Fu, J. Xiang, W. C. Reynolds, and B. Nefcy, "Vector control of an IPM synchronous machine capable of full range operations for hybrid electric vehicle application," in *Industry Applications Conference, 2003. 38th IAS Annual Meeting. Conference Record of the*, 2003, pp. 1443-1450 vol.3.

[74] S. Pervin, Z. Siri, and M. N. Uddin, "Newton-Raphson based computation of id in the field weakening region of IPM motor incorporating the stator resistance to improve the performance," in *Industry Applications Society Annual Meeting (IAS), 2012 IEEE*, 2012, pp. 1-6.

[75] L. Lin, H.-w. Tang, J. Tang, and J.-T. Yin, "High performance control of IPMSM servo system based on dSPACE," in *Modelling, Identification and Control (ICMIC), Proceedings of 2011 International Conference on*, 2011, pp. 294-299.

[76] S. Morimoto, M. Sanada, and Y. Takeda, "Wide-speed operation of interior permanent magnet synchronous motors with high-performance current regulator," *Industry Applications, IEEE Transactions on,* vol. 30, pp. 920-926, 1994.

[77] P. Fajkus, B. Klima, and P. Hutak, "High speed range field oriented control for permanent magnet synchronous motor," in *Power Electronics, Electrical Drives, Automation and Motion (SPEEDAM), 2012 International Symposium on*, 2012, pp. 225-230.

[78] Y. Iwai, A. Ogawa, and A. Chiba, "Output DC voltage and power control of a flux strengthening IPM generator and a quick speed acceleration of a high speed SPM motor," in *Energy Conversion Congress and Exposition (ECCE), 2010 IEEE*, 2010, pp. 479-485.

[79] F. Aymen, H. Kraiem, and S. Lassaad, "Robust high speed control algorithm for PMSM sensorless drives," in *Systems, Signals and Devices (SSD), 2012 9th International Multi-Conference on*, 2012, pp. 1-6.

[80]   M. Tursini, E. Chiricozzi, and R. Petrella, "Feedforward Flux-Weakening Control of Surface-Mounted Permanent-Magnet Synchronous Motors Accounting for Resistive Voltage Drop," *Industrial Electronics, IEEE Transactions on,* vol. 57, pp. 440-448, 2010.

[81]   A. Ahmed, Y. Sozer, and M. Hamdan, "Flux weakening control for surface mount permanent magnet synchronous motor (PMSM) drives with rapid load and speed varying applications," in *Energytech, 2013 IEEE*, 2013, pp. 1-6.

[82]   A. Damiano, G. Gatto, I. Marongiu, A. Serpi, and A. Perfetto, "A novel flux-weakening approach for Surface-Mounted Permanent Magnet Synchronous Machines," in *Industrial Electronics Society, IECON 2013 - 39th Annual Conference of the IEEE*, 2013, pp. 2547-2552.

[83]   C. Song, Z. Zheng, and X. Longya, "Sliding-Mode Sensorless Control of Direct-Drive PM Synchronous Motors for Washing Machine Applications," *Industry Applications, IEEE Transactions on,* vol. 45, pp. 582-590, 2009.

[84]   C. Yuan, A. Bouscayrol, R. Trigui, and C. Espanet, "Inversion-based control of a PM electric variable transmission," in *Vehicle Power and Propulsion Conference (VPPC), 2011 IEEE*, 2011, pp. 1-6.

[85]   D. Wang, E. Liu, and H. Lin, "Permanent magnet synchronous motor driving single axis gyroscope stabilized platform based on field weakening vector control," in *Electrical Machines and Systems (ICEMS), 2013 International Conference on*, 2013, pp. 1298-1300.

[86]   M. Abroshan, J. Milimonfared, K. Malekian, and A. Rahnamaee, "An optimal control for saturated interior permanent magnet linear synchronous motors incorporating field weakening," in *Power Electronics and Motion Control Conference, 2008. EPE-PEMC 2008. 13th*, 2008, pp. 1117-1122.

[87]   K. D. Hoang, J. Wang, M. Cyriacks, A. Melkonyan, and K. Kriegel, "Feed-forward torque control of interior permanent magnet brushless AC drive for traction applications," in *Electric Machines & Drives Conference (IEMDC), 2013 IEEE International*, 2013, pp. 152-159.

[88]   C. Attaianese, V. Nardi, and G. Tomasso, "Vectorial torque control of permanent magnet AC (PMAC) machine drives in field weakening region," in *Advanced Motion Control, 2002. 7th International Workshop on*, 2002, pp. 257-262.

[89]   M. Abroshan, K. Malekian, J. Milimonfared, and B. A. Varmiab, "An optimal direct thrust force control for interior Permanent Magnet Linear Synchronous Motors incorporating field weakening," in *Power Electronics, Electrical Drives, Automation and Motion, 2008. SPEEDAM 2008. International Symposium on*, 2008, pp. 130-135.

[90]   M. F. Rahman, L. Zhong, and K. W. Lim, "A direct torque controlled interior permanent magnet synchronous motor drive incorporating field weakening," in *Industry Applications Conference, 1997. Thirty-Second IAS Annual Meeting, IAS '97., Conference Record of the 1997 IEEE*, 1997, pp. 67-74 vol.1.

[91]   G. Pellegrino, E. Armando, and P. Guglielmi, "Direct Flux Field-Oriented Control of IPM Drives With Variable DC Link in the Field-Weakening Region," *Industry Applications, IEEE Transactions on,* vol. 45, pp. 1619-1627, 2009.

[92]   W. Yingnan and U. Schafer, "Implementation of DTC for IPMSM with FPGA considering field weakening operation," in *Electrical Machines and Systems (ICEMS), 2011 International Conference on*, 2011, pp. 1-6.

[93]   F. Aymen and S. Lassaad, "BFO control tuning of a PMSM high speed drive," in *Electrotechnical Conference (MELECON), 2012 16th IEEE Mediterranean*, 2012, pp. 273-276.

[94]   A. Matsumoto, M. Hasegawa, and S. Doki, "A flux-weakening control method on Maximum Torque Control frame for IPMSM position sensorless control," in *IECON 2012 - 38th Annual Conference on IEEE Industrial Electronics Society*, 2012, pp. 1612-1617.

[95]   L. Ping-Yi and L. Yen-Shin, "Voltage Control Technique for the Extension of DC-Link Voltage Utilization of Finite-Speed SPMSM Drives," *Industrial Electronics, IEEE Transactions on,* vol. 59, pp. 3392-3402, 2012.

[96]   C. Capitan, "Torque Control in Field Weakening Mode," Institute of Energy Technology, 2009.

[97]   G. Fei, S. Bozhko, S. Yeoh Seang, and G. Asher, "Control design for PMM starter-generator operated in flux-weakening mode," in *Power Engineering Conference (UPEC), 2013 48th International Universities'*, 2013, pp. 1-6.

[98]   W. Yongxing, W. Xuhui, and Z. Feng, "A proposed control strategy of PMSM for deep field-weakening and square-wave mode," in *Electrical Machines and Systems (ICEMS), 2012 15th International Conference on*, 2012, pp. 1-6.

[99]   Z. Yuan, L. Fei, Z. Zheng, and X. Longya, "Direct voltage vector control for field weakening operation of PM machines," in *Power and Energy Conference at Illinois (PECI), 2010*, 2010, pp. 20-24.

[100]   W. Hatsuse, Y. Notohara, K. Ohi, K. Tobari, K. Tamura, C. Unoko, and Y. Funayama, "A stable field-weakening control using voltage phase operations in the high-power region," in *Power Electronics Conference (IPEC), 2010 International*, 2010, pp. 599-604.

[101]   D. Stojan, D. Drevensek, Z. Plantic, B. Grcar, and G. Stumberger, "Novel field weakening control scheme for permanent magnet synchronous machines based on voltage angle control," *Industry Applications, IEEE Transactions on,* vol. PP, pp. 1-1, 2012.

[102]   S. Kitamura and K. Kondo, "An enhanced torque control method of permanent magnet synchronous motor in the field weakening region," in *Electrical Machines and Systems (ICEMS), 2010 International Conference on*, 2010, pp. 781-786.

[103]   S. Bolognani, S. Calligaro, and R. Petrella, "Adaptive Flux-Weakening Controller for Interior Permanent Magnet Synchronous Motor Drives," *Emerging and Selected Topics in Power Electronics, IEEE Journal of,* vol. 2, pp. 236-248, 2014.

[104]   P. Vaclavek and P. Blaha, "Interior permanent magnet synchronous machine field weakening control strategy - the analytical solution," in *SICE Annual Conference, 2008*, 2008, pp. 753-757.

[105]   G. Gallegos-Lopez and S. Hiti, "Optimum Current Control in the Field-Weakened Region for Permanent Magnet AC Machines," in *Industry Applications Conference, 2007. 42nd IAS Annual Meeting. Conference Record of the 2007 IEEE*, 2007, pp. 2154-2160.

[106]   K. Jang-Mok and S. Seung-Ki, "Speed control of interior permanent magnet synchronous motor drive for the flux weakening operation," *Industry Applications, IEEE Transactions on,* vol. 33, pp. 43-48, 1997.

[107]   Z. Huawei, W. Xuhui, Z. Feng, Z. Jian, and M. Jinlei, "An improved flux-weakening strategy for field-oriented-controlled PMSM drives," in *Power Electronics and Motion Control Conference (IPEMC), 2012 7th International*, 2012, pp. 2353-2356.

[108]   S. Jong-Hwan, K. Jang-Mok, and S. Seung-Ki, "A new robust SPMSM control to parameter variations in flux weakening region," in *Industrial Electronics, Control, and Instrumentation, 1996., Proceedings of the 1996 IEEE IECON 22nd International Conference on*, 1996, pp. 1193-1198 vol.2.

[109]   D. S. Maric, S. Hiti, C. C. Stancu, and J. M. Nagashima, "Two improved flux weakening schemes for surface mounted permanent magnet synchronous machine drives employing space vector modulation," in *Industrial Electronics Society, 1998. IECON '98. Proceedings of the 24th Annual Conference of the IEEE*, 1998, pp. 508-512 vol.1.

[110]   K. Tae-Suk and S. Seung-Ki, "Novel anti-windup of a current regulator of a surface-mounted permanent-magnet motor for flux-weakening control," in *Industry Applications Conference, 2005. Fourtieth IAS Annual Meeting. Conference Record of the 2005*, 2005, pp. 1813-1819 Vol. 3.

[111]   P. Sandulescu, F. Meinguet, X. Kestelyn, E. Semail, and A. Bruyere, "Control Strategies for Open-End Winding Drives Operating in the Flux-Weakening Region," *Power Electronics, IEEE Transactions on,* vol. 29, pp. 4829-4842, 2014.

[112]   O. A. M. Mohamed Taha Elsayed, and Sherif Ahmed Zaid, "Simulation Study of a New Approach for Field Weakening Control of PMSM," *Journal of Power Electronics (JPE),* vol. 12 2012.

[113]   G. Clos, "Torque angle control of the permanent magnet synchronous machine at the voltage margin," in *Power Electronics and Applications (EPE), 2013 15th European Conference on*, 2013, pp. 1-9.

[114]   X. Song, X. Wen, and W. Cong, "Research on field-weakening control of multiphase permanent magnet synchronous motor," in *Electrical Machines and Systems (ICEMS), 2011 International Conference on*, 2011, pp. 1-5.

[115]   N. Trong Duy, G. Foo, T. King-Jet, and D. M. Vilathgamuwa, "Modeling and Sensorless Direct Torque and Flux Control of a Dual-Airgap Axial Flux Permanent-Magnet Machine With Field-Weakening Operation," *Mechatronics, IEEE/ASME Transactions on,* vol. 19, pp. 412-422, 2014.

[116] X. Zhuang, X. Wen, F. Zhao, H. Zhou, and B. Zhang, "A robust field weakening method for direct torque controlled PMSM drive system," in *Electrical Machines and Systems (ICEMS), 2011 International Conference on*, 2011, pp. 1-5.

[117] J. N. Radovan DOLEČEK, Ondřej ČERNÝ, "Traction Permanent Magnet Synchronous Motor Torque Control with Flux Weakening," 2009.

[118] Y. Sheng, W. Zhou, Z. Hong, and S. Yu, "Field weakening operation control of permanent magnet synchronous motor for railway vehicles based on maximum electromagnetic torque at full speed," in *Control Conference (CCC), 2010 29th Chinese*, 2010, pp. 1608-1613.

[119] S. D. Sudhoff, K. A. Corzine, and H. J. Hegner, "A flux-weakening strategy for current-regulated surface-mounted permanent-magnet machine drives," *Energy Conversion, IEEE Transactions on,* vol. 10, pp. 431-437, 1995.

[120] R. U. Lenke, R. W. De Doncker, K. Mu-Shin, K. Tae-Suk, and S. Seung-Ki, "Field Weakening Control of Interior Permanent Magnet Machine using Improved Current Interpolation Technique," in *Power Electronics Specialists Conference, 2006. PESC '06. 37th IEEE*, 2006, pp. 1-5.

[121] K. Tae-Suk, C. Gi-Young, K. Mu-Shin, and S. Seung-Ki, "Novel Flux-Weakening Control of an IPMSM for Quasi-Six-Step Operation," *Industry Applications, IEEE Transactions on,* vol. 44, pp. 1722-1731, 2008.

[122] L. Jae Hyuk, L. Jung Hyo, P. Jin ho, and W. Chung Yuen, "Field-weakening strategy in condition of DC-link voltage variation using on electric vehicle of IPMSM," in *Electrical Machines and Systems (ICEMS), 2011 International Conference on*, 2011, pp. 1-6.

[123] B. Bon-Ho, N. Patel, S. Schulz, and S. Seung-Ki, "New field weakening technique for high saliency interior permanent magnet motor," in *Industry Applications Conference, 2003. 38th IAS Annual Meeting. Conference Record of the*, 2003, pp. 898-905 vol.2.

[124] A. L. H. MAHMOUDI "FLUX-WEAKENING CONTROL OF PERMANENT MAGNET SYNCHRONOUS MACHINES," *Journal of Theoretical and Applied Information Technology,* vol. Vol 34. No. 2, 2011.

[125] L. Zhu, X. Wen, F. Zhao, L. Kong, and B. Zhang, "Deep field-weakening control of PMSMs for both motion and generation operation," in *Electrical Machines and Systems (ICEMS), 2011 International Conference on*, 2011, pp. 1-5.

[126] P. Cortes, M. P. Kazmierkowski, R. M. Kennel, D. E. Quevedo, and J. Rodriguez, "Predictive Control in Power Electronics and Drives," *Industrial Electronics, IEEE Transactions on,* vol. 55, pp. 4312-4324, 2008.

[127] J. Rodriguez, M. P. Kazmierkowski, J. R. Espinoza, P. Zanchetta, H. Abu-Rub, H. A. Young, and C. A. Rojas, "State of the Art of Finite Control Set Model Predictive Control in Power Electronics," *Industrial Informatics, IEEE Transactions on,* vol. 9, pp. 1003-1016, 2013.

[128] D. Zamecnik and I. Vesely, "Prediction control of Interior Permanent Magnet Synchronous Machine with field weakening," in *Intelligent Engineering Systems (INES), 2012 IEEE 16th International Conference on*, 2012, pp. 191-195.

[129] M. Preindl and S. Bolognani, "Model Predictive Direct Torque Control With Finite Control Set for PMSM Drive Systems, Part 2: Field Weakening Operation," *Industrial Informatics, IEEE Transactions on,* vol. 9, pp. 648-657, 2013.

[130] S. Yeoh Seang, X. Linying, S. Bozhko, and G. Asher, "Stability analysis of aircraft electrical power system with active front rectifier system in generation channel," in *Power Engineering Conference (UPEC), 2013 48th International Universities'*, 2013, pp. 1-6.

[131] J. M. Guerrero, J. C. Vasquez, J. Matas, L. G. de Vicuña, and M. Castilla, "Hierarchical Control of Droop-Controlled AC and DC Microgrids - A General Approach Toward Standardization," *Industrial Electronics, IEEE Transactions on,* vol. 58, pp. 158-172, 2011.

[132] M. C. Chandorkar, D. M. Divan, and R. Adapa, "Control of parallel connected inverters in standalone AC supply systems," *Industry Applications, IEEE Transactions on,* vol. 29, pp. 136-143, 1993.

[133] K. Visscher and S. W. H. de Haan, "Virtual synchronous machines (VSG's) for frequency stabilisation in future grids with a significant share of decentralized generation," in *SmartGrids for Distribution, 2008. IET-CIRED. CIRED Seminar*, 2008, pp. 1-4.

[134] A. Emadi, A. Khaligh, C. H. Rivetta, and G. A. Williamson, "Constant power loads and negative impedance instability in automotive systems: definition, modeling, stability, and control of power electronic converters and motor drives," *Vehicular Technology, IEEE Transactions on,* vol. 55, pp. 1112-1125, 2006.

[135] G. Fei, S. Bozhko, Y. Seang, G. Asher, and P. Wheeler, "Stability of multi-source droop-controlled Electrical Power System for more-electric aircraft," in *Intelligent Energy and Power Systems (IEPS), 2014 IEEE International Conference on*, 2014, pp. 122-126.

[136] G. Fei, S. Bozhko, G. Asher, and P. Wheeler, "An improved voltage compensation method for droop-controlled system in DC microgrid," in *Industrial Electronics Society, IECON 2014 - 40th Annual Conference of the IEEE*, 2014, pp. 1240-1246.

[137] G. Fei, G. Ye, S. Bozhko, G. Asher, and P. Wheeler, "Analysis of droop control methods in DC microgrid," in *Power Electronics and Applications (EPE'14-ECCE Europe), 2014 16th European Conference on*, 2014, pp. 1-9.

[138] A. Yazdani and R. Iravani, *Voltage-Sourced Converters in Power Systems*: John Wiley & Sons, Inc., 2010.

[139] J. R. Leigh, *Control Theory, 2nd Edition*: Institution of Engineering and Technology, 2004.

[140] S. Chapman, *Electric Machinery Fundamentals*: McGraw-Hill Companies,Incorporated, 2005.

[141] I. D. Landau and G. Zito, *Digital Control Systems: Design, Identification and Implementation (Communications and Control Engineering)*: Springer-Verlag New York, Inc., 2006.

[142] M. Gopal, *Control Systems: Principles and Design*: McGraw-Hill Education (India) Pvt Limited, 2002.

[143] D. G. Holmes and T. A. Lipo, *Pulse Width Modulation for Power Converters: Principles and Practice*: John Wiley & Sons, 2003.

[144] M. Morari and J. H. Lee, "Model predictive control: past, present and future," *Computers & Chemical Engineering,* vol. 23, pp. 667-682, 1999.

[145] K. S. Holkar and L. M. Waghmare, "An Overview of Model Predictive Control," *International Journal of Control and Automation,* vol. 3, 2010.

[146] E. F. Camacho and C. B. Alba, *Model predictive control*: Springer Science & Business Media, 2013.

[147] S. Mariethoz, M. Herceg, and M. Kvasnica, "Model Predictive Control of buck DC-DC converter with nonlinear inductor," in *Control and Modeling for Power Electronics, 2008. COMPEL 2008. 11th Workshop on*, 2008, pp. 1-8.

[148] S. Kouro, P. Cortes, R. Vargas, U. Ammann, and J. Rodriguez, "Model Predictive Control-A Simple and Powerful Method to Control Power Converters," *Industrial Electronics, IEEE Transactions on,* vol. 56, pp. 1826-1838, 2009.

[149] P. Zanchetta, P. Cortes, M. Perez, J. Rodriguez, and C. Silva, "Finite States Model Predictive Control for Shunt Active Filters," in *IECON 2011 - 37th Annual Conference on IEEE Industrial Electronics Society*, 2011, pp. 581-586.

[150] M. Preindl and S. Bolognani, "Model Predictive Direct Speed Control with Finite Control Set of PMSM Drive Systems," *Power Electronics, IEEE Transactions on,* vol. 28, pp. 1007-1015, 2013.

[151] M. Preindl and S. Bolognani, "Model Predictive Direct Torque Control With Finite Control Set for PMSM Drive Systems, Part 1: Maximum Torque Per Ampere Operation," *Industrial Informatics, IEEE Transactions on,* vol. 9, pp. 1912-1921, 2013.

[152] S. Bolognani, L. Peretti, and M. Zigliotto, "Design and Implementation of Model Predictive Control for Electrical Motor Drives," *Industrial Electronics, IEEE Transactions on,* vol. 56, pp. 1925-1936, 2009.

[153] M. Hyung-Tae, K. Hyun-Soo, and Y. Myung-Joong, "A discrete-time predictive current control for PMSM," *Power Electronics, IEEE Transactions on,* vol. 18, pp. 464-472, 2003.

[154] R. H. Williams, D. A. Stone, M. P. Foster, and S. R. Minshull, "Reduction of passive filtering in aerospace starter/generator systems using a multilevel converter with predictive current control," in *Power Electronics, Machines and Drives (PEMD 2012), 6th IET International Conference on*, 2012, pp. 1-5.

[155] L. Tarisciotti, P. Zanchetta, A. Watson, J. Clare, M. Degano, and S. Bifaretti, "Modulated Model Predictive Control (M2PC) For A 3-Phase Active Rectifier," *Industry Applications, IEEE Transactions on,* vol. PP, pp. 1-1, 2014.

[156] L. Tarisciotti, "Model Predictive Control for Advanced Multilevel Power Converters in Smart-Grid Applications," PhD, University of Nottingham, 2014.

[157] L. Tarisciotti, P. Zanchetta, A. Watson, J. Clare, S. Bifaretti, and M. Rivera, "A new predictive control method for cascaded multilevel converters with intrinsic modulation scheme," in *Industrial Electronics Society, IECON 2013 - 39th Annual Conference of the IEEE*, 2013, pp. 5764-5769.

[158]   L. Tarisciotti, P. Zanchetta, A. Watson, S. Bifaretti, and J. C. Clare, "Modulated Model Predictive Control for a Seven-Level Cascaded H-Bridge Back-to-Back Converter," *Industrial Electronics, IEEE Transactions on,* vol. 61, pp. 5375-5383, 2014.

[159]   M. Vijayagopal, L. Empringham, L. de Lillo, L. Tarisciotti, P. Zanchetta, and P. Wheeler, "Control of a direct matrix converter induction motor drive with modulated model predictive control," in *Energy Conversion Congress and Exposition (ECCE), 2015 IEEE*, 2015, pp. 4315-4321.

[160]   L. Dai, Y. Xia, M. Fu, and M. S. Mahmoud. (2012). *Discrete-Time Model Predictive Control*. Available: http://www.intechopen.com/books/advances-in-discrete-time-systems/discrete-time-model-predictive-control

[161]   T. Instruments. *TMS320C6713 DSP Starter Kit (DSK)*. Available: http://www.ti.com/tool/tmdsdsk6713. Accessed: 16/1/2016

[162]   L. Educational DSP. (2003). *DSK6XXXHPI Daughtercard*. Available: http://www.educationaldsp.com/stockproduct_dsk6xxxhpi.htm. Accessed: 16/1/2016

[163]   C. Techniques. *CTD Brushless Servo Motors*. Available: http://www.controltech.com.tr/Documents/CT%20Dynamics/Unimotor%20Manual.PDF. Accessed: 16/1/2016

[164]   D. H. Q. Si, "A new implementation of high frequency, high voltage Direct Power Converter," PhD, University of Nottingham, 2006.

[165]   Semikron. *SKM100GB12V*. Available: https://www.semikron.com/dl/service-support/downloads/download/semikron-datasheet-skm100gb12v-22892023. Accessed: 16/1/2016

[166]   Kemet. *Screw Terminal Aluminum Electrolytic Capacitors*. Available: http://www.kemet.com/Lists/ProductCatalog/Attachments/389/KEM_A4031_ALS30_31.pdf. Accessed: 16/1/2016

[167]   T. Electric. *DC Motors LAK 2080-2132* Available: http://www.t-telectric.com/pdf/lak2000.pdf. Accessed: 16/1/2016

[168]   S. Electric. *PLX Product Manual*. Available: http://www.sprint-electric.com/products/plx. Accessed: 16/1/2016